The University of
Nottingham

School of Civil Engineering

Centrifuge Modelling of Piled Embankments

Mr. Raveed Aslam

Supervisor

Dr. E. A. Ellis

GEORGE GREEN LIBRARY OF
SCIENCE AND ENGINEERING

Thesis submitted to The University of Nottingham

for the degree of Doctor of Philosophy

September 2008

ABSTRACT

It is becoming increasingly necessary to construct on land that was previously considered inappropriate for construction, such as soft clay. The properties of soft clay make it highly compressible and low in shear strength, meaning that bearing capacity failure and excessive settlement are of concern.

Piled embankments are a ground improvement technique that can provide a solution for this problem. Piled embankments have the ability to transfer the greater part of the embankment load and any surcharge to more competent material at greater depth due to the 'arching' concept. Consequently, the soft foundation soil has little direct impact on the performance of the embankment. The concept of 'arching' of granular soil over an area where there is partial loss of support from underlying strata has long been recognised in the study of soil mechanics (e.g. Terzaghi, 1943). However, a number of competing theories exist to quantify this behaviour in piled embankments.

In addition, the use of geotextile reinforcement in piled embankments placed above the pile caps in principle provides a number of technical as well as economical benefits. As the embankment fill is placed, tension is created in the reinforcement and it is the vertical component of this tension that transfers the embankment load onto the piles and reduces the load carried by the soft clay hence transferring the load of the embankment on to the piles.

Differential settlement can be a problem for piled embankments of low height. Significant differential settlement can cause undesirable effects on any structures constructed on the embankment. 'Arching' limits the amount of differential settlement in embankments and the use of geotextile geogrid can also potentially have additional benefits.

This thesis presents a series of centrifuge tests examining the performance of unreinforced and reinforced piled embankments constructed over soft subsoil in terms of

stress acting on the subsoil, and differential movement at the surface of the embankment. A large range of embankment heights are considered, and the results for stress on the subsoil are compared with existing predictive methods, allowing generic conclusions to be drawn regarding the predictions of various methods.

The effect of a 'working platform' below pile cap level and thus directly loading the subsoil is also considered, and used to examine the concept of a 'Ground Reaction Curve' (Iglesia et al, 1999) for arching in the embankment. In principle this can be used to consider compatibility of displacements at the base of the embankment, and thus improve design simultaneously considering the effect of arching in the embankment and underlying support from the subsoil and layers of reinforcement acting in tension.

Acknowledgements

Firstly I would like to thank my supervisor Dr E. Ellis for the opportunity to do a PhD, his excellent guidance and patience throughout the research. I have been extremely fortunate to have had a supervisor who, without his vast knowledge would not have made this possible and who always made the time and effort to respond to my queries. Under his supervision and teachings, I have improved as an engineer and gained new insight.

I would also like to thank all the technicians in the engineering laboratory, especially Craig Cox, Mike Langford and Andrew Maddison for their hard work and making the time spent in the laboratory so enjoyable.

I must mention Dr. James Walker for his friendship, help and much missed company. My brother Juneid Aslam, for all his support throughout the years, you are truly someone I can look up to. Oliver Leung for his friendship and help for putting all this together. A special thank you to Yan Yan, for her continuous encouragement and support.

I am greatly indebted to the EPSRC for their financial support.

List of symbols

Dimensions

h_e = thickness of embankment

h_w = thickness of working platform (piling mat)

h_s = thickness of subsoil

s = centre-to-centre spacing of pile caps

a = pile cap dimension

Vertical stress

σ_e = stress at base of embankment in areas between pile caps (acting on geogrid, or working platform, or subsoil)

σ_g = stress carried by geogrid (where this exists)

σ_w = stress at top of working platform, beneath geogrid

σ_s = stress at top of subsoil

Settlements

$\delta_{e,u}$ = uniform settlement at top of embankment

$\delta_{e,d}$ = differential settlement at top of embankment

δ_s = settlement at top of subsoil

$\delta_{s,n}$ = nominal calculated settlement of subsoil

δ_c = settlement at the embankment surface immediately above a pile cap

CONTENTS

CHAPTER 3

CENTRIFUGE MODELLING: EXPERIMENTAL TECHNIQUE

CHAPTER 7

CENTRIFUGE TEST DATA – REINFORCED PILED EMBANKMENT

CHAPTER 8

DISCUSSION OF RESULTS

CHAPTER 1

INTRODUCTION

In view of the fact that a large amount of construction is taking place to improve infrastructure in the United Kingdom and elsewhere in the world, it is becoming necessary to construct on land that was in the past considered inappropriate for construction, such as soft clay. The properties of soft clay make it highly compressible and low in shear strength, meaning that bearing capacity failure and excessive settlement are of concern. Due to time constraints and uncertainty of soft clay conditions, it is often not economic to allow the clay to gain stiffness and strength through consolidation, even if vertical drains and surcharging are used.

1.1 Pile supported embankments

A solution to this problem is to use a pile supported embankment (Figure 1.1) with a layer of reinforcement in between the piles and the embankment. Reinforced piled embankments are increasingly important as a construction method that reduces settlements, construction time and costs of embankments on soft soils. In this situation, the piles pass through the soft clay to transfer the greater part of the embankment weight to more competent material at greater depth. Construction can be done in a single stage without having to wait for the soft clay to consolidate as load transfer to the piles further reduces the settlement of the embankment. Consequently, the soft foundation soil has little direct impact on the performance of the embankment and the characteristics of the soil are considered only with regard to the type of piles used and their installation.

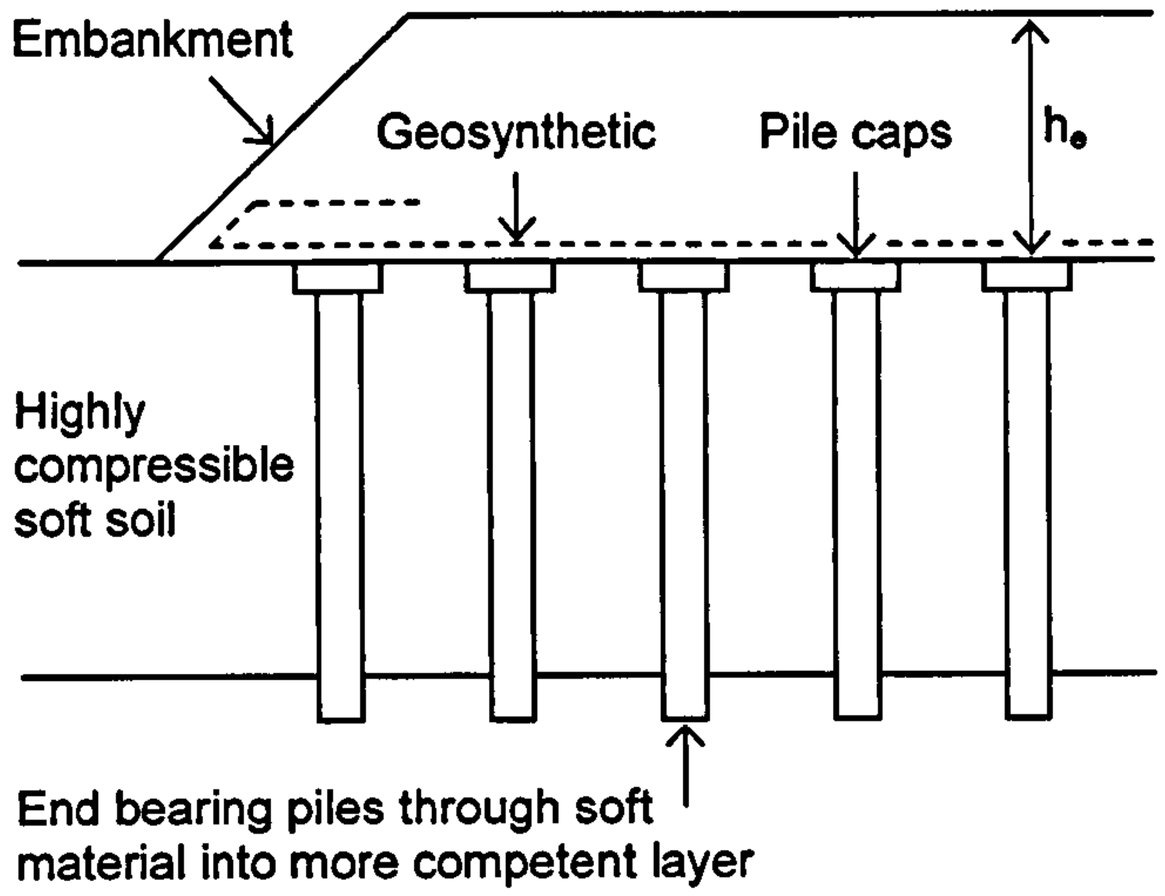

Figure 1.1 - Piled Embankment

1.2 Soil arching

As the embankment fill is placed, the soft foundation material begins to consolidate and settle causing differential movement between the relatively rigid piles and the soft foundation material. The embankment above the soft clay settles more than the piles. This develops shear stresses between the stationary piles and the downward moving embankment material. As a result shear stresses are generated in the embankment fill material, transferring the vertical stresses from the soft foundation material onto the piles. This effect is known as 'soil arching'. A number of competing theories exist to quantify this behaviour.

1.3 Geosynthetic reinforcement

The use of geosynthetic reinforcement in piled embankments in principle provides a number of technical as well as economical benefits. To allow a more economic design, a reinforcing material can be introduced between the piles and the embankment fill, meaning less costly piles with smaller pile caps can be placed further apart. Before the embankment fill is placed, the geosynthetic reinforcement is laid on top of the piles. As the embankment fill is placed, tension is created in the reinforcement and it is the vertical component of this tension that transfers the embankment load onto the piles and

reduces the load carried by the soft clay hence reducing the settlement of the embankment. The reinforcement material is commonly a polyester grid. However, the precise contribution which the reinforcement makes is not completely understood, and there is no single design approach in use.

1.4 Centrifuge apparatus

Numerical analysis has reached a level of sophistication and convenience in geotechnical engineering such that it can be used effectively for routine design. However, when design conditions are extreme or unfamiliar, rather than routine, or when response up to and including failure is required, their use is limited. In these cases, physical modelling of the whole system becomes the essential first step in understanding the event, and collecting data. Only then can the development of suitable methods of engineering analysis be undertaken.

Centrifuge testing concerns the study of geotechnical events using small-scale models subjected to acceleration fields of magnitude many times Earth's gravity. Scaled model experiments must be based on similarity laws derived from fundamental equations governing the phenomena to be investigated. Of critical importance in the present context is the stress/strain behaviour of granular soils, which is non-linear, and a function of stress level and stress history. In order to simulate the equivalent full scale 'prototype' accurately at small scale, the in situ stresses must be reproduced correctly in the model. In order to replicate these gravity induced stresses of a prototype in a $1/N^{th}$ scale model, it is necessary to test the model in a gravitational field N times larger than that of the prototype. Thus the dimensions and many of the physical processes can be scaled correctly if an N^{th} scale model is accelerated by N times the acceleration due to gravity.

1.6 Aims and objectives

The aim of the research presented was to contribute to the optimum design of piled embankments which will lead to a cost effective structure. The objectives needed to be achieved to satisfy the aim are:

- Accurately model a piled embankment in small scale centrifuge tests.
- Investigate the manner of vertical load transfer from the embankment fill and the associated settlement at the surface and at the subsoil level.
- Examine the effects of embankment height, pile spacing and stiffness of the subsoil on the efficacy of the vertical load transfer and embankment settlements.
- Consider the effects of the inclusion of a working platform and geosynthetic reinforcement on the efficacy of the vertical load transfer.

1.7 Methodology

The aims and objectives of this research will be fulfilled by modelling a piled embankment in a geotechnical centrifuge and by individually changing the variables listed in the objectives. The load exerted on the piles will then be measured to give the efficacy of the arching in the embankment fill and the surface settlement will be measured using photogrammetry. The obtained results will then be compared with results from current design procedures.

1.8 Layout of the report

This thesis consists of nine chapters. Chapter 1 has given a brief insight into the research topic.

Chapter 2 contains the literature review and summarises some of the work carried out by other researchers.

Chapter 3 is the methodology chapter and explains how the centrifuge tests were set up and performed.

Chapter 4 is the first of the four results chapters. Chapter 4 presents the findings from the piled embankment tests using a very soft subsoil material, with some discussion of the results.

Chapter 5 presents the findings from the piled embankment tests using a stiffer (but still 'soft') subsoil material, again with some discussion of the results.

Chapter 6 presents the findings from piled embankment tests where a 'working platform' was modelled at an elevation below the cap elevation. This material is not affected by arching, and loads the subsoil directly, potentially with undesirable effects.

Chapter 7 presents the findings from piled embankment tests for the first time considering the effect of geotextile reinforcement, in an idealised way.

Chapter 8 presents further discussion and analysis from the findings from Chapter 4 - 7, and systematic comparison with existing design methods for a range of embankment heights.

Chapter 9 presents conclusions of the thesis.

CHAPTER 2

LITERATURE REVIEW

2.1 Introduction

Construction of embankments on soft soils, often clays which have not experienced significant overconsolidation, presents two fundamental problems:

- The low strength of the underlying soil can significantly limit the load (embankment height) that can be applied for adequate safety against instability particularly in the short term;
- The high deformability and low permeability of the underlying soft soil can cause large settlements that develop slowly as pore water flows out and excess pore pressure dissipates (consolidation).

In geotechnics, ground improvement, in a broad sense, is the alteration of any property of soil and treatment of ground so that the soil strata may be strengthened to better serve engineering applications. There are a variety of ground improvement techniques involving mechanical and/or chemical processes that have been successfully implemented to overcome problems caused by the soft foundation soils.

In recent times, much emphasis has been given to piled embankments which normally also use reinforcement at the base. Although the soft soil may be slightly improved by construction of the piles which pass through it, the aim is actually to significantly reduce the load on it, and thus the stability is unlikely to be of concern. The method is also found to be generally effective in reducing settlement at the surface of the embankment.

Piled embankments on soft soils have been studied by a large number of authors but various aspects of the behaviour are not yet completely understood, and there is little consensus on which of the potential design methods available is most suitable. This

research aims to investigate principles behind the load transfer process in piled embankments and how they can be used effectively to reduce surface settlement.

2.2 Embankments in Civil Engineering

Embankments play a major role in infrastructure supporting roads and railways and buildings. Many are sited on soft soils generally clay or organic soils with high moisture content which are highly compressible and which can cause settlements at the surface of the embankment which impair the performance of the infrastructure.

These settlements are due to the weight of the embankment imposing a load on the subsoil which it cannot sustain. The way in which an embankment will be protected against instability and differential settlements will largely depend on local conditions but solutions to these settlement problems could include:

- Installing drainage systems,
- Loading the soil for a period before construction to consolidate it,
- Chemically treat compatible soils (e.g. Lime or cement),
- Reduce the load on the subsoil by using lightweight embankment fill (e.g. Expanded PolyStyrene (EPS) or Coal fly ash).

The first two methods do not eliminate settlement, but reduce the length of time for it to occur and may be used together.

Piled embankments can offer a quick and cost-effective method to construct on soft soil. Once the 'piles' (e.g. precast concrete piles, stone columns, or deep mix columns) have been installed, the embankment layer can be placed and the construction can continue immediately with minimal differential settlement.

2.2.1 Embankment Fill Material

The shear strength characteristics of the embankment fill are indicative of the ability of the material to support and transmit any loads imposed. A strong embankment fill will be able to redistribute concentrated external loads or arch over locally poor areas of the foundation. However, when a uniform load is applied on a relatively uniform foundation

soil which will often be the case, the strength of the fill will only benefit the stability of the embankment itself.

2.2.2 Vertical Stress in Embankment Foundations

As the scope of this research is limited to the analysis of the 'centre' of embankments and not the side slopes, one-dimensional consolidation will be considered, i.e. the deformation will only occur in the direction of the applied load (the vertical direction).

Embankments are constructed by placing and compacting successive layers of a fill material onto a foundation soil. The embankment self weight will cause compressive stress and associated strain in the foundation material. This strain is a normal phenomenon that occurs when any type of material is subjected to a stress and the associated settlements will probably not constitute 'failure'. Uniform settlements do not necessarily mean failure; problems arise when the settlement is non-uniform or when uniform settlement occurs near a rigid structure.

The reduction in volume of a soil mass (as water is expelled) resulting from the application of a load and the accompanying compressive stress and strain is called consolidation.

Prior to the placement of the embankment fill, the foundation material is in equilibrium, with the pore pressures hydrostatic. The effective stress in the soil cannot increase unless there is a compression of the soil skeleton. This requires the water to flow out of the pores which cannot occur instantly because the permeability of the soil is finite. In clay soils the permeability is very low, and hence this is a lengthy process.

Clay in one dimensional compression, such as the oedometer test, will consolidate and the voids ratio, *e*, will accordingly reduce as the water is expelled. The strength characteristics are related to the void ratio of the soil which can have an important influence on embankment construction.

Excess pore water pressure represents the portion of the embankment load carried by pore water pressure, which is initially high, but reduces as settlement occurs.

If the excess pore water pressure is significantly high, it can prevent the shear strength from increasing with increasing total confining stress which can cause the soft foundation layer to fail under increasing embankment load. Therefore, if the pore water pressure rises to a dangerous level during construction, it is best to halt the construction and allow the soft layer to consolidate until the pore water pressure returns to a safe value. It is for this reason embankments are sometimes constructed using multi-stage construction, to improve the soft soil, although this again adds significant time to the construction programme.

In this research the soft subsoil will be considered to deform one-dimensionally and virtually instantaneously. This idealisation will nevertheless allow the ultimate effect of subsoil settlement on a piled embankment to be observed with little compromise.

2.3 Piled Embankments

The benefit of piled embankments is their relatively short construction period, yet still generally significantly limiting any settlements. This is done by transferring the majority of the applied load due to the embankment self weight and any surcharge load, directly onto the pile caps and through the pile (or similar) foundations to a more competent underlying stratum. This leaves the clay layer which is largely unmodified except for the inclusion of the piles having to carry only a small proportion of the load.

After a piled embankment is constructed, the soft foundation material begins to consolidate and differential movement occurs between the relatively rigid piles and the soft foundation material. The fill material above the soft foundation settles more than the material above the piles. Because of its resistance to shearing, granular embankment fill has an inherent tendency to 'arch' over the subsoil between adjacent pile caps, transferring most of its self-weight and any other imposed load onto the pile caps. This transfer of load is commonly termed arching and is generally considered to be a fundamental aspect of behaviour in piled embankments. The remainder of this chapter will mainly concentrate on this concept.

2.4 Arching Concept

The following theory of arching considers the embankment soil to be a homogeneous material that is in an effective stress ('drained') condition, with zero pore pressure and hence total and effective stresses are equal. Also to simplify discussion of the concepts, the arching effect will initially be considered in a plane strain case.

2.4.1 Terzaghi's trapdoor

Terzaghi (1943) conducted early laboratory experiments, from which came the 'trapdoor' theory. Sand was placed above a platform that contained a narrow strip or trap door. Terzhagi showed that when the trapdoor was lowered slightly, the pressure on it reduced significantly whereas the pressure on the adjacent parts of the platform increased by the same amount (in terms of force).

As the trapdoor was lowered further, strains develop. The angularity of the particles means they begin to interlock with one another and a shearing stress is mobilised between the moving ('yielding') sand mass and the adjoining stationary sand mass.

Figure 2.1 shows a free body diagram showing the forces acting on a horizontal element of soil at some height above the trapdoor. A potential model of behaviour is that arching occurs through the shear stresses along the vertical soil prism planes at the edge of the void.

Assuming the vertical stress on a horizontal section at any depth z below the surface is σ_v, and the corresponding normal stress on the vertical surface of sliding (σ_h) is given by Equation 2.1, (for a frictional cohesionless soil) the shearing resistance of soil is determined by Equation 2.2.

$$\sigma_h = K\sigma_v \qquad \text{Eqn. 2.1}$$

$$\tau = \sigma_h \tan\phi \qquad \text{Eqn. 2.2}$$

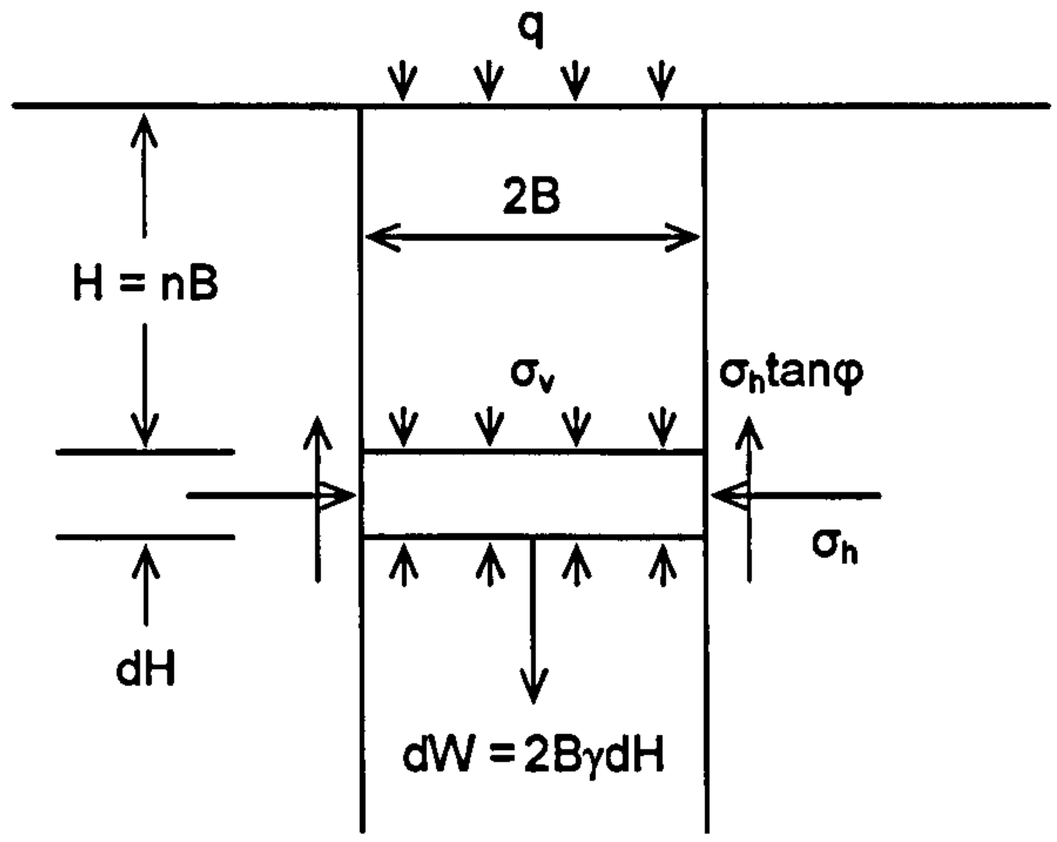

Figure 2.1 - Classical representation for soil above trapdoor differential elements

Figure 2.1 shows a rectangular soil element, having thickness *dH* and weight *dW*, that has a vertical stress applied to the top of its surface σ_v from the overlying material and any surcharge, *q*. Resisting the movement of the soil element due to the applied stress and the weight of the element itself is the soil layer beneath this element ($\sigma_v + d\sigma_v$) and the shear strength of the soil adjacent to the element (τ) acting on both sides of the element. When the element is in equilibrium, the sum of the forces indicated in Figure 2.1 acting on the slice of soil must equal zero and are expressed by the Equation 2.3

$$\frac{d\sigma_v}{dz} = \gamma - \frac{c}{B} - K\sigma_v \frac{\tan\phi}{B} \qquad \text{Eqn. 2.3}$$

Assuming cohesionless soil and no surcharge; Terzhagi (and later McKelvey, 1993) showed that by integrating the differential element from zero to a thickness z from the surface of the soil above the void, the equation to obtain the vertical stress is given by:

$$\sigma_v = \frac{B\gamma}{K\tan\phi}\left(1 - e^{-K\tan\phi\ z/B}\right) \qquad \text{Eqn. 2.4}$$

There is some uncertainty regarding the appropriate value of *K* to be used in this equation. However, if purely frictional soil on the point of failure on the vertical planes is considered then it follows (Handy, 1985) that

$$K = \frac{1 - \sin^2 \varphi}{1 + \sin^2 \varphi} \qquad \text{Eqn. 2.5}$$

Figure 2.2 shows the variation of σ_v (Equation 2.4) with depth derived using a variety of different K values. The unit weight of the fill is taken as 16 kN/m^3, and the friction angle as 30°. B is taken as 1 m.

The K values shown represent a range of numerical values as follows:

- $K = K_a = (1\text{-}\sin\varphi)/(1+\sin\varphi) = 0.33$ (the minimum active pressure coefficient)
- $K = K_0 = (1\text{-}\sin\varphi) = 0.50$ (the 'at rest' earth pressure coefficient)
- $K = (1\text{-}\sin^2\varphi)/(1+\sin^2\varphi) = 0.60$ (Handy, 1985)
- $K = 1.06(\cos^2\varphi + K_a\sin^2\varphi) = 0.88$ (Handy, 1985)
- $K = 1.0$

The vertical stress γz is also shown for comparison.

Not surprisingly the stress reduces as K increases. Each line appears to tend to its own asymptote as depth increases. It can be seen that the values (at 10 m) vary considerably from 25 - 70 kN/m^2 which implies that Equation 2.4 is very sensitive to the K value and also shows the importance of choosing an appropriate value.

Now consider the instance shown in Figure 2.3 (a), which is similar to Terzhagi's trapdoor. It shows a soil mass over a potential void (*a*-*b*) that may develop, and is assumed to have a width 2B. The base *ab* is assumed to be smooth so that $\tau_{xy} = 0$ at y = 0.

The elasticity solution to this problem was obtained by Finn (Thigpen, 1984) by using the slip line method for the plane strain condition. The vertical stress compared to the nominal overburden γH from Finn's analysis is plotted in Figure 2.3 (c). It is noted that the stress approaches infinity at the edge of the base, however, the Mohr-Coulomb failure criterion states that plastic flow would occur before this happens.

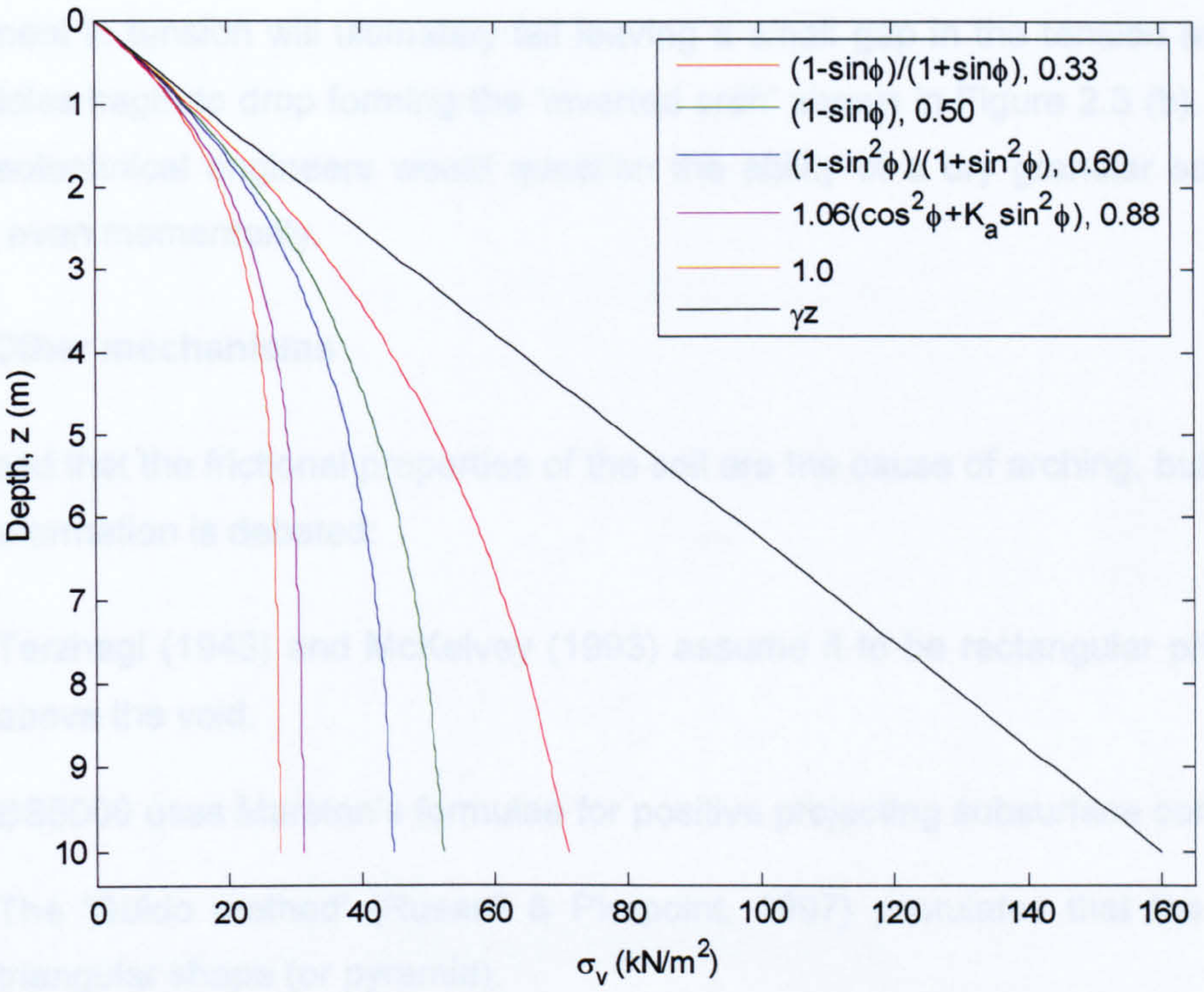

Figure 2.2 - Variation of σ_v with different K values

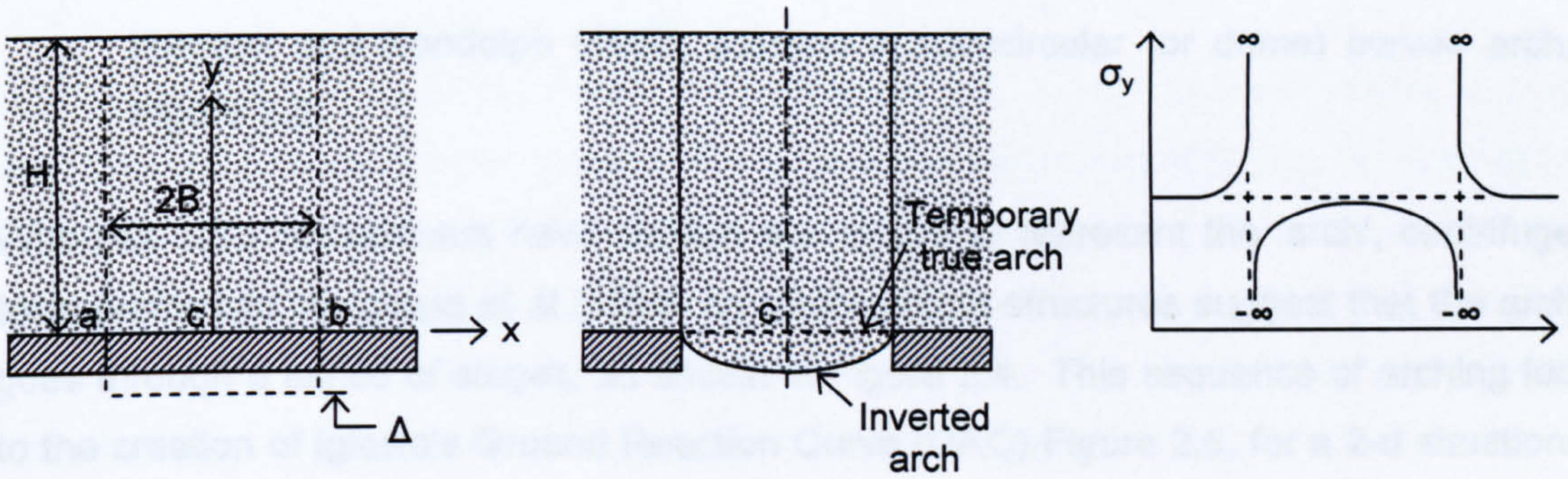

Figure - 2.3 Cross-section of a soil mass; (a) overlying the potential void, (b) inverted arch, (c) vertical stress distribution ((a) and (b) McKelvey, 1993 (c) Thigpen, 1984)

Thigpen (1984) states that as the base *ab* (Figure 2.3 (a)) yields, the compressive stress on the plane *ab* steadily reduces. McKelvey proposed that momentarily just after the base yields, the soil remains as it is, forming a 'true arch' and that the soil directly above the void is now in tension. According to Finn's elasticity solution a thin layer of soil

directly above the void space is in tension as a true arch. McKelvey then states that the soil element in tension will ultimately fail leaving a small gap in the tension arch as the soil particles begin to drop forming the 'inverted arch' shown in Figure 2.3 (b). However many geotechnical engineers would question the ability of a dry granular soil to carry tension, even momentarily.

2.4.2 Other mechanisms

It is agreed that the frictional properties of the soil are the cause of arching, but the mode of soil deformation is debated:

- Terzhagi (1943) and McKelvey (1993) assume it to be rectangular prism of soil above the void.
- BS8006 uses Marston's formulae for positive projecting subsurface conduits.
- The 'Guido method' (Russell & Pierpoint, 1997) postulates that the arch is a triangular shape (or pyramid).
- Carlsson (1987) and Han & Gabr (2002) assume a trapezoidal shape (which is in effect a truncated triangle or pyramid).
- Hewllett and Randolph (1988) assume a semicircular (or dome) curved arch, Figure 2.6.

Whereas other researchers have chosen one shape to represent the 'arch', centrifuge tests performed by Iglesia et al (1999) on underground structures suggest that the arch goes through a series of stages, as shown in Figure 2.4. This sequence of arching led to the creation of Iglesia's Ground Reaction Curve (GRC) Figure 2.5, for a 2-d situation. This is plotted as stress on an underground structure (normalised by the nominal overburden stress) as this varies with displacement of the structure roof (normalised by width of the structure).

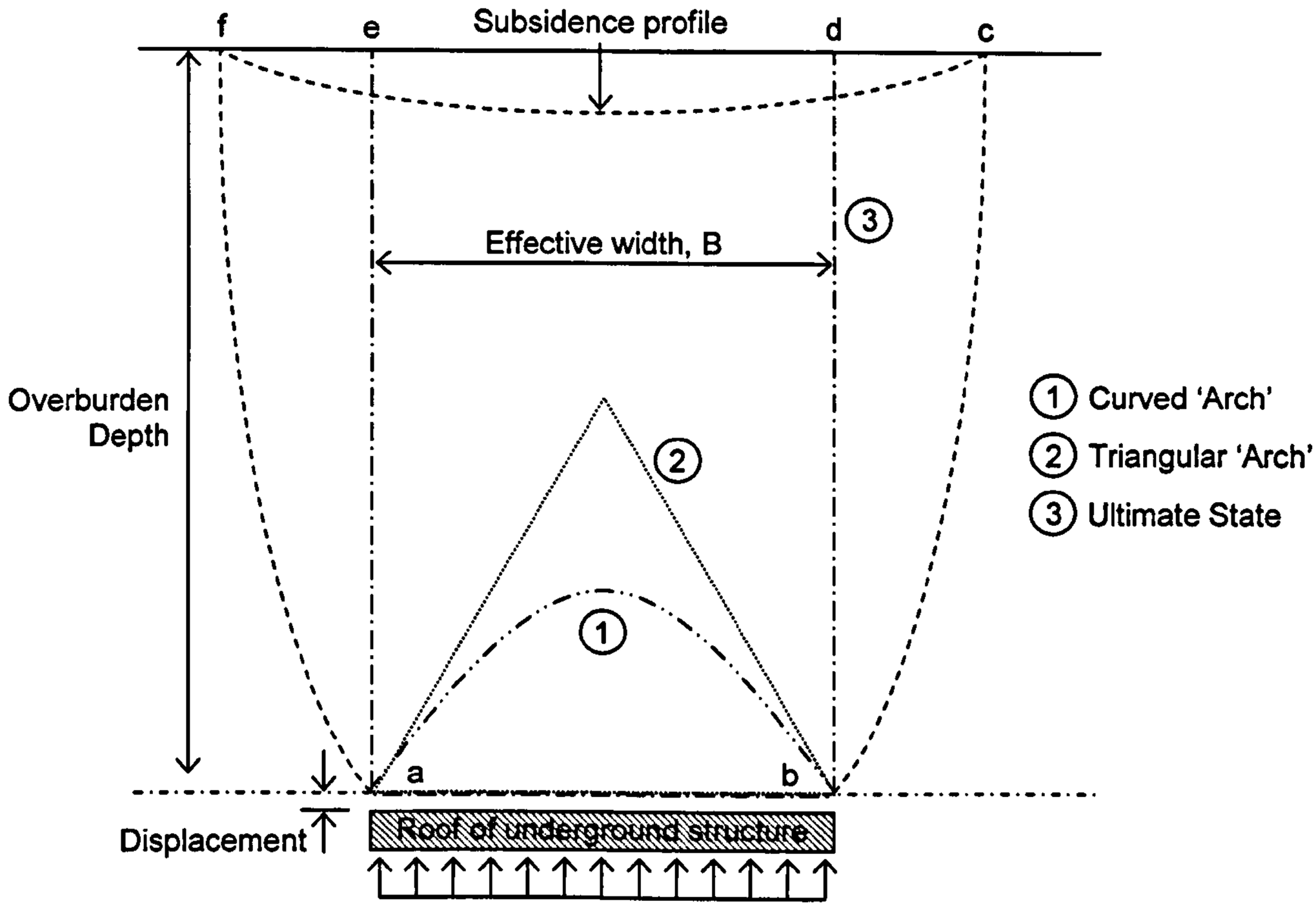

Figure 2.4 - Sequence of Arching (Iglesia et al, 1999)

Starting from the in situ stress state (p = 1 in Figure 2.5), as the roof of the underground structure deflects (similar to soft ground in between piles consolidating, or Terzhagi's trapdoor); Iglesia proposes that there is a rather sudden drop in load on the roof of the underground structure when the 'arch' begins to form, Figure 2.5. The rate of initial stress decrease is called the *modulus of arching* M_A (Figure 2.5). As the roof deflects further, the ground reaction curve no longer follows a straight line but tends towards a point of maximum arching (minimum load on the roof of the structure) after the *break point*, Figure 2.5.

The vertical load on the underground structure approaches a minimum value when the arch is in the shape of a curve, Figure 2.4. Iglesia et al (1999) proposed that maximum arching occurs when the relative displacement between the underground structure and the surrounding soil is about 2 - 6% of the effective width of the structure.

The loading recovery stage is the transition from the maximum arching phase to the ultimate state where the arch has become a prism with vertical sides as proposed by Terzhagi. Idealising this phase to be approximately linear, the rate of increase of the vertical load for an increase in displacement is the *load recovery index* λ. Based on centrifuge tests, Iglesia et al (1999) showed that the load recovery index increases with increasing B/D_{50} (D_{50} is the average particle size) and decreases with increasing H/B. At stage 3 (Figure 2.4) ultimate conditions are assessed using Terzaghi's equation for a vertical sided prism, Equation 2.4. This form of behaviour is 'brittle', and thus potentially of considerable importance (and concern) in design.

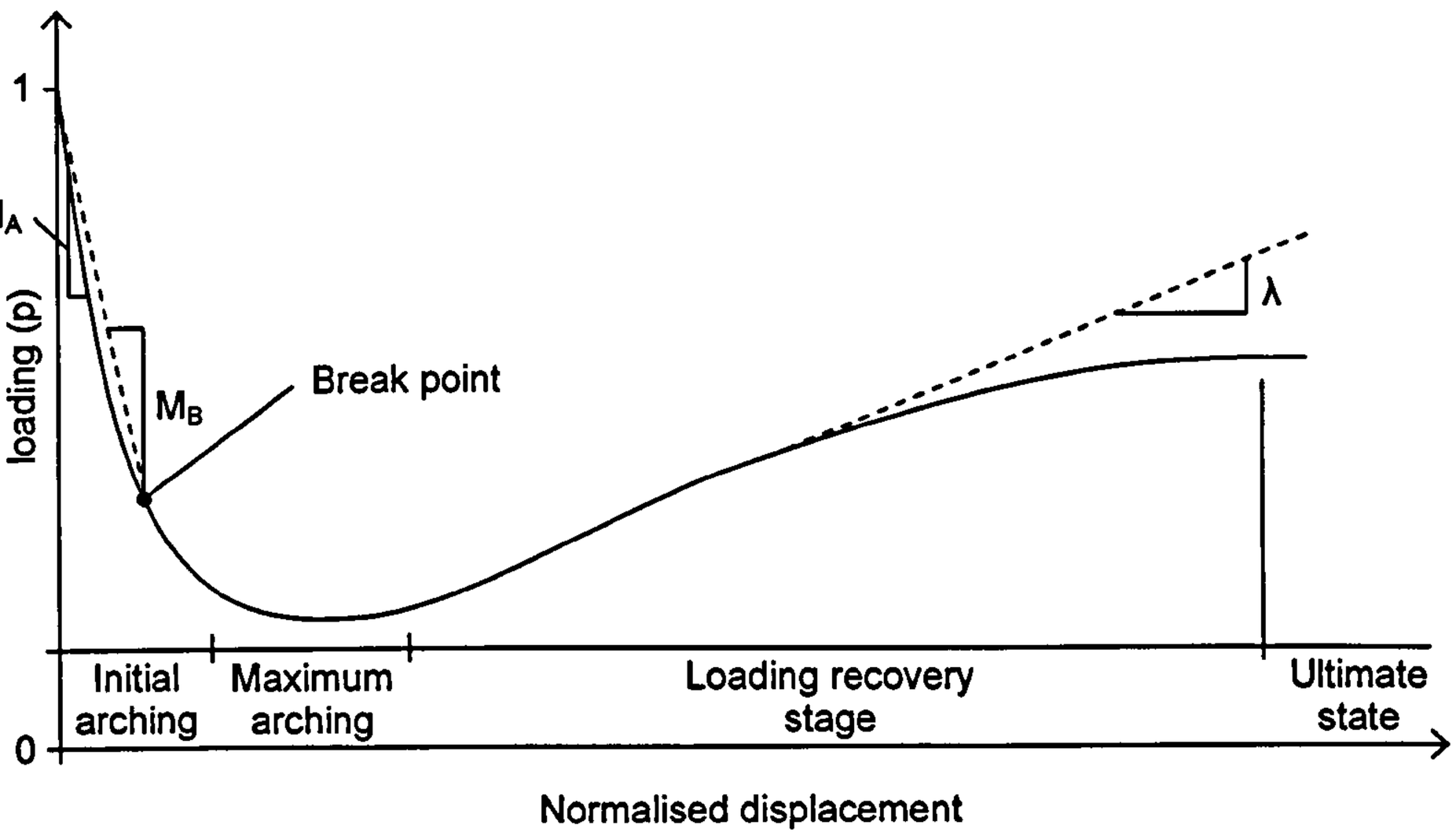

Figure 2.5 - Ground reaction curve (Iglesia et al, 1999)

Figure 2.4 shows the subsidence profile given by Finn's elasticity solution and Terzhagi. The dish or trough type subsidence profile develops as the soil yields and can be visualised as the wedges *aef* and *bcd* moving to the right and left respectively while the plane *ab* moves vertically down. Terzhagi proposes that the slope of each side of the depression is greatest where it intersects the surface of sliding. The distance between these steepest parts of the trough at the embankment surface are always greater than the width of the yielding strip. Hence, Terzhagi proposes that the surfaces of sliding must have a shape similar to that indicated in Figure 2.4 by the lines *af* and *bc*.

However, the problem of deriving the equations of the surfaces has not been solved so for simplicity Terzhagi assumed a sliding prism but maintained it is on the 'unsafe' side.

However, it must be emphasised that the stress beneath the arched element will rarely be zero, particularly if the overlying soil is cohesionless. Figures 2.3 (c) and 2.5 illustrate this. Hewlett & Randolph (1988) propose equations for a semicircular (2-d) or hemispherical (3-d) arch (Figure 2.5). Their equations indicate that the vertical stress at the 'crown' of the arch (where the horizontal stress is the major principle stress) is quite small. The stress on the subsoil beneath the arch is then due mainly to the weight of the 'infill' material beneath the arch. This will be considered further in Chapter 8.

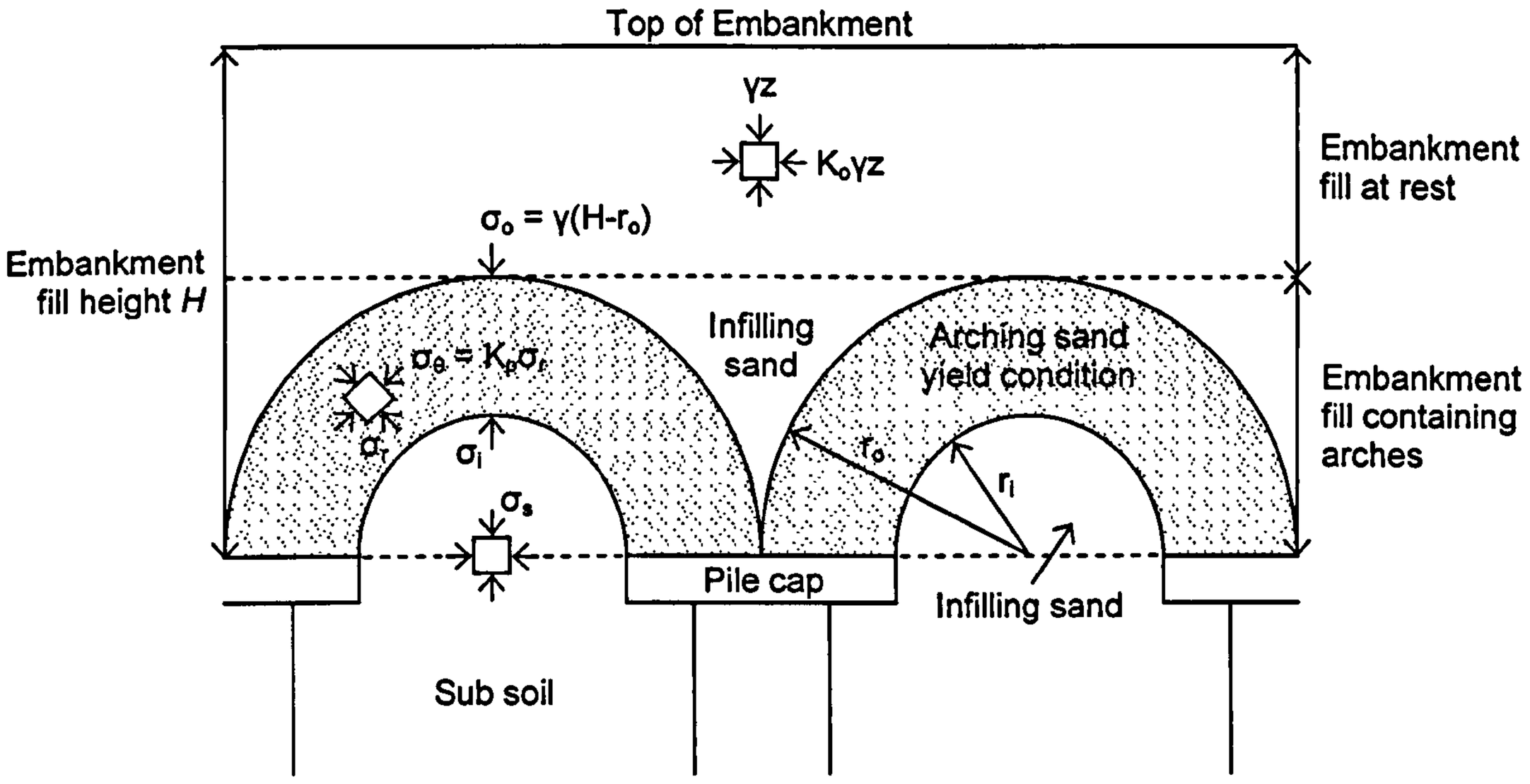

Figure 2.6 - Section through a piled embankment (Hewlett & Randolph, 1984)

2.5 Differential Settlement

Differential settlement depends on movement of the trapdoor (or void) and height above the trapdoor. Figure 2.7 shows that the differential settlement of the soil elements comprising the yielding soil prism above the void decreases as the vertical distance between a particular soil element and the void increases McKelvey (1993). McKelvey proposes that there will be a point where the differential settlement between the soil element and the adjacent soil is zero.

Based on Terzhagi's experiments, at elevations of more than about *5B* above the centreline (2.5 times the width of the void), lowering the trapdoor seems to have no effect at all on the sand. Hence, Terzhagi goes on to say, it can be assumed that the shearing resistance of the sand is mobilised only on the lower part of the vertical boundaries *ae* and *bd* of the prism of sand located above the yielding strip *ab* in Figure 2.4. From this, McKelvey stated that the plane of equal settlement will be approximately 1.5 - 2.5 times the width of the void.

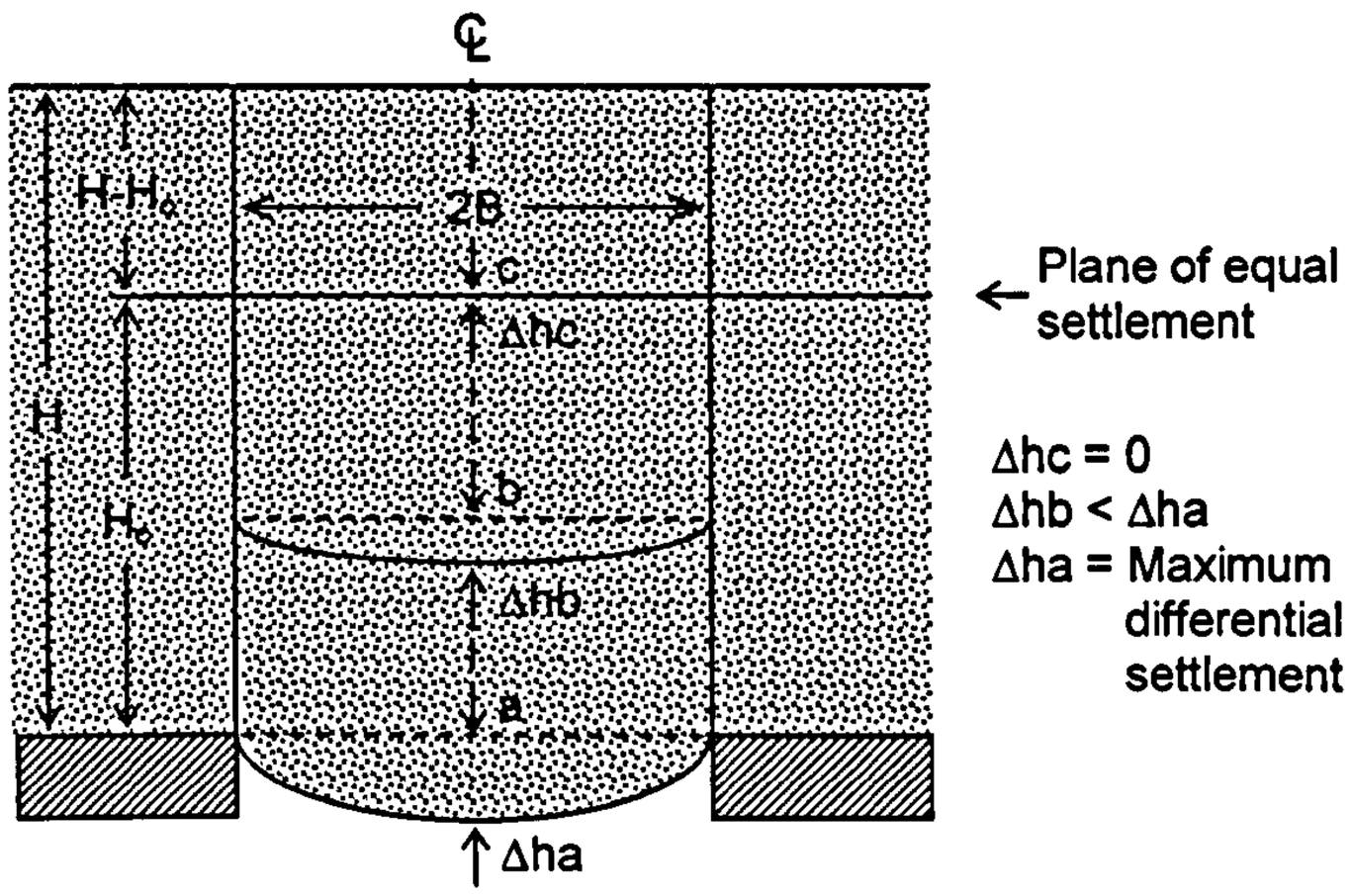

Figure 2.7 - Plane of equal settlement (McKelvey, 1993)

2.6 Geosynthetic reinforcement

Geosynthetic reinforcement allows the load of the embankment to be transferred on to the pile caps and can reduce settlement.

The Guido method (Russell & Pierpoint, 1997) is based on multiple layers of reinforcement. The method is actually based on studies of improvement of bearing capacity of soil by inclusion of multiple layers of geogrid, to give a 'load spread' angle of 45° for the 'improved' soil. There is some basis for this analogy since one potential mechanism of failure is by the pile caps 'punching' into the base of the embankment (Hewlett & Randolph, 1988). However, it is less clear how this relates to behaviour between the piles which is considered by Hewlett & Randolph using a separate mechanism. In this area the grids are more likely to act as a tension catenary.

Giroud et al (1990) incorporated the tension membrane theory with soil arching in order to design a method to determine the geosynthetic reinforcement required for a soil to span a void. The corresponding equations presented in BS8006 are based on research that has been performed with a geogrid lying across a long void. Giroud assumes the deflected shape of the geogrid across the void to be cylindrical with a circular cross section and with uniform strain. BS8006 assumes a uniform loading on the geogrid as shown in Figure 2.8. The BS8006 formulae will be considered further in Chapter 7.

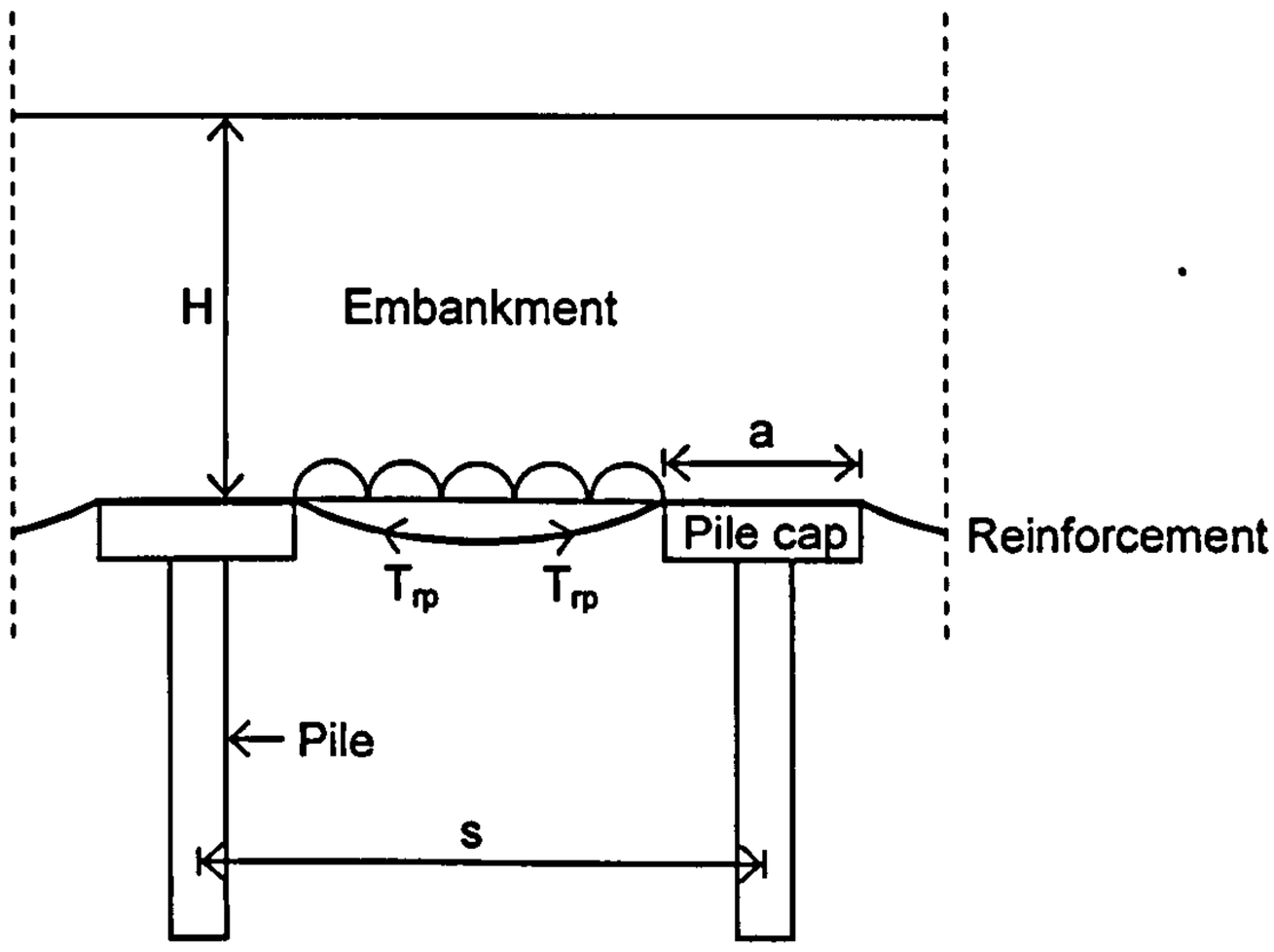

Figure 2.8 - Uniform loading on geotextile reinforcement

2.7 Numerical and analytical studies

A number of authors have undertaken numerical (e.g. Finite Element Modelling (FEM) and Fast Lagrangian Analysis of Continua (FLAC)) modelling of piled embankments on soft ground, using either plane strain, axisymmetric (this is potentially questionable) or full 3-d analyses. Often the results are compared with analytical studies, for instance using the various design methods available. Examples will be discussed below.

Russell & Pierpoint (1997) performed a study comparing the BS8006, Terzaghi, Hewlett & Randolph and Guido design methods using the A13 piled embankment and Second Severn trial embankments as examples. For the A13 embankment, the Terzaghi and Hewlett & Randolph methods gave the highest stress on the subsoil. BS8006 gave a

slightly lower value, but the Guido method was significantly lower at only about 20 % of the Terzaghi & Hewlett and Randolph methods. The tension in the geotextile reinforcement also reflected these observations. For the 2nd Severn trial embankment, BS8006 gave the highest stress on the subsoil, while the Terzaghi and Hewlett & Randolph methods gave 60 % of the BS8006 value and the Guido method only 10 %. Again the tension in the geotextile reinforcement followed a similar pattern.

Russell & Pierpoint (1997) also report 3-d numerical (FLAC) analyses and argued that only 3-d analysis can be used to reliably model piled embankments. Comparing the numerical analyses with the design methods for the A13 embankment, the numerical study gave subsoil stress approximately twice the value of the design methods referred to above (except Guido, which gave an unusually low value). However, the tension in the reinforcement had quite good correlation with the design methods (again except the Guido method, which gave an unusually low value).

For the Second Severn Crossing embankment, the numerical study gave slightly less susbsoil stress than the Terzaghi and Hewlett & Randolph methods and considerably less than the BS8006 method. Again the Guido method gave a much lower value. For the tension in the reinforcement, the numerical study gave considerably lower values than all the design methods and hence agreed reasonably well with the Guido method.

Kempton et al (1998) performed 2-d and 3-d numerical (FLAC) analyses of reinforced piled embankments with no subsoil. In both cases, the stress reduction ratio (SRR - defined as the ratio of the average vertical stress carried by the geosynthetic to the average vertical stress γh_e due to the embankment fill of height h_e) reduced as a/s and h_e increased and there is a point of 'full arching' after which point the load carried by the geogrid increases proportionally to h_e (a = pile cap width and s = pile spacing). The SRR increases with differential displacement, as does the maximum tension in the geogrid. The authors also show the SRR is higher in the 3-d case than the 2-d for a given a/s value. Therefore the differential settlement at the base of the embankment and the tension in the geogrid are underestimated in the 2-d case. Comparing the 2-d and 3-d FLAC analysis with the BS8006 design method, BS8006 overestimated the tension in the reinforcement in all 2-d cases and underestimated it in the 3-d cases. For a/s between 0.2 and 0.6 and with h_e/s between 0.6 and 1.4 the BS8006 reinforcement

tensions were approximately 30 % lower than the 3-d analysis. However, if load factors were used in the BS8006 equations, BS8006 would overestimate the tension in the geogrid by 30 % in both cases.

Han & Gabr (2002) performed a numerical study on reinforced piled embankments (using FLAC) and employed a 'unit cell' for a square pile cap arrangement that is assumed to be similar to a circle, and analytically modelled using axisymmetry. Springs are used to model the pile cap and subsoil vertical response. They reported common findings in terms of settlement and the effects of geotextile reinforcement. The authors showed that the embankment's ability to arch increases as h_e increases. The stiffness of the geogrid aids the transfer of load to the pile caps ('promotes arching'), but very high stiffnesses give diminishing return. They also found that the tension in the geogrid is greatest at the edge of the pile caps (as also discussed by Tonks & Hillier, 1998).

Russell et al (2003) presented a design method for piled embankments based on Terzaghi's approach to arching, verified using 3-d finite difference analysis. This design method will be considered in Chapter 8.

Stewart and Filze (2005) compared five existing methods: BS8006, Terzaghi, Hewlett & Randolph, Guido and the Carlsson design methods with numerical analysis (FLAC 3-d). The Carlsson design method is a 2-d approach that considers a wedge of soil whose cross-sectional area under the arching soil can be approximated by a wedge with an internal angle at the apex of the wedge equal to 30°. The Carlsson method adopts a critical height approach such that any additional overburden above the top of the wedge is transferred directly to the piles (thus the critical height is 0.5/tan15° = 1.87(s-a)).

Stewart and Filze (2005) showed that for all 5 methods, the SRR decreased with increasing a/s and h_e/s values. However, for a given geometry, the SRR values vary greatly from one method to another (e.g. for a/s = 0.25 and h_e/s = 4, the SRR from the Hewlett & Randolph is 12 times larger than the Guido method). They also claim the BS8006 design method to be the most sensitive to variations in the a/s than the others. For many of the a/s and h_e/s values considered, the Terzhagi, Hewlett & Randolph and Carlsson methods give similar SRR values. The Guido method gives very low values.

For the numerical analyses reported by Stewart and Filze, FLAC 3-d was used to model a reinforced piled embankment with two layers of reinforcement. The embankment geometry was h_e = 6.1m, a = 1.22m, s = 3.66m, the two geogrids had a combined stiffness of 2040kN/m. The stiffness of the subsoil was varied. Two SRR values were used: SRR_{top} which was defined as the normalised vertical load on top of the geosynthetic in the area outside of the pile cap and SRR_{net} which was defined as the normalised *net* vertical load on the geosynthetic in the area outside the pile cap. The numerical analysis showed that the SRR_{top} values decrease with increasing compressibility of the clay and increasing embankment fill stiffness whereas as the SRR_{net} increases and both values converge. Also, as the compressibility of the subsoil increases, the SRR_{net} and SRR_{top} approach the SRR values obtained from the Hewlett & Randolph and the Carlsson method.

Stewart and Filze (2005) claim that the compressibility of the ground between the piles has a large impact on the vertical load applied by an embankment to geosynthetic reinforcement in bridging layers in piled embankments. For this reason, they go on to suggest that the compressibility of the ground between the piles should be a factor in the design of piled embankments.

Naughton & Kempton (2005) again argue that piled embankment applications are a truly 3-d problem that cannot be simulated by 2-d or axisymmetric numerical analysis. Naughton & Kempton (2005) compared seven available design methods (one of which was the Kempfert et al's (2004) design method which is considered in more detail in chapter 8) and compared them using two different piled embankments geometries as examples. The design methods investigated were as Stewart and Filze (2005). Naughton & Kempton (2005) showed all design methods performed very differently in terms of their SRR and tension values in the reinforcement. But again, no systematic explanation was given as to why the behaviour was so different for the examples.

Cao et al (2006) modelled reinforced piled embankments and mainly focused on the efficacy of the embankment. A similar arrangement to the Han & Gabr (2002) axisymmetric 'unit cell' with springs is used to model the pile cap and subsoil response. Their findings showed the efficacy of the embankment decreased with increasing s/h_e values and increased with increasing a/s values. They also showed the shear strength

of the embankment fill only slightly increased the efficacy of the embankment and increasing the ratio of the pile - subsoil stiffness also increases efficacy. The usefulness of geotextile reinforcement was questioned as it reduces differential settlement and therefore in turn reduces the arching effect (see Chapter 6). However geotextile reinforcement does have the beneficial effect of transferring the load of the embankment onto the pile caps. The authors claim that overall geotextile reinforcement in piled embankments has no influence. However, Russell & Pierpoint (1997) have argued that assumptions of axisymmetry are not correct in the context of a square pile grid.

Yan et al (2006) modelled (plane strain) reinforced piled embankments in FLAC. The findings showed that the behaviour of reinforced and unreinforced piled embankments was markedly different. The inclusion of the geogrid resulted in an improved efficacy of the embankment, a reduction of differential and uniform settlement when settlements were large (0.3 to 1.0 m) and allowed a greater pile spacing (s) or smaller pile caps (a). Unsurprisingly therefore an increase in the number of layers of geogrid reinforcement also reduces settlement, particularly when s is in the region of 1.0 - 2.5 m. An increase in the tensile stiffness of the geogrid also has the same effect particularly at large s values. The authors went on to show that an increase in the stiffness of the subsoil and piles reduces the settlement of the embankment (up to 50 MPa for the piles). However, the authors do not attempt to relate these findings to more generic theory of arching or geogrid action.

He et al (2006) used Finite Element Modelling (FEM) to model piled embankments which had lime fly ash and EPS as part of the fill material. The authors modelled a piled embankment with 25 m long piles and with s = 3 m, and chose to vary a from 0.5 - 1.75 m and the embankment height (h_e) from 1 - 5 m. The FE analyses showed a stress reduction along the base of the embankment in between the pile caps and also showed that it is at its maximum at the edges of the pile caps. Regarding the use of EPS, He et al (2006) showed (using a 1 m thick layer of EPS as part of the embankment fill) that it can increase the efficacy of the embankment the closer it is to the pile caps. However, its influence decreases with an increasing a value.

He et al (2006) also used the Terzhagi's, Low et al's (1993), BS8006 and Hewlett and Randolph's design methods to analyse the embankments and compare their findings.

With regard to the efficacy of the embankment, the study showed that with Low's et al's method, there was no relationship with h_e whereas the BS8006 method shows a slight increase. With a = 0.5 m, the Hewlett and Randolph design method (surprisingly) shows a decrease with increasing h_e but increases when a = 1 and 1.75 m. The Terzhagi method showed an increase in efficacy with an increase in h_e. The authors concluded that the methods gave different results, but they did not comment on systematic variation in this respect.

Chen & Yang (2006) derived analytical solutions for a reinforced piled embankment involving deformation of the reinforcement and spring constants to represent the soft subsoil. They presented their results as 'allowable' embankment height, which increased with the pile diameter, and geogrid stiffness (up to a point), and subsoil stiffness. The allowable height reduced with the spacing between piles. However, by the authors own admission the method has a drawback since the ratio of stress on the pile caps compared to the soft soil is required as an *input* to the analysis.

Chen et al (2006) used the finite element package Plaxis and adopted a similar geometrical approach to Han & Gabr (2002), using axisymmetry. The findings showed that (unsurprisingly) the settlement of the embankment above the pile caps was less than the settlement between the pile caps. The authors used two different stiffness values for the subsoil and showed that settlement of the subsoil was greater for the softer subsoil. The stiffer subsoil (E_o' = 15 MPa) carried more of the embankment load but not in proportion to the increase in stiffness. They ultimately concluded that the uniform settlement of the embankment is mainly dependent on the (one dimensional) stiffness (E_o') of the subsoil.

2.8 Field studies and physical modelling

Some field and laboratory data is available and is described below. However, again the results do not tend to be conclusive.

Modelling at 1-g of arching in granular soil has been undertaken (e.g. Hewlett & Randolph, 1988). However, it is notable that it is the analytical solutions provided by Hewlett & and Randolph (1988) which have contributed most significantly in this field.

Wood (2003) monitored the construction of the A63 bypass that used a reinforced piled embankment that covered a very large area. The maximum allowable differential and uniform settlement were 1 in 500 and 75 mm respectively. s = 2.7 - 3.2 m and h_e = 4 - 9.5 m with a working platform (h_w) of 650 mm (below pile cap level). Settlements of 1 m were predicted on untreated ground. The main requirement of the embankment was to reduce the number of piles needed in order to reduce cost. Therefore piles of high stiffness were used in conjunction with geotextile reinforcement in order to increase s. The BS8006 design method was adopted. The embankment consisted of 400 mm thick Pulverised fly ash to minimise the load on the piles. The design adopted relied on the embankment fill transferring the majority of its load via arching and the geogrid. The BS8006 design method was ignored for the calculation of the load on the reinforcement and instead was calculated by estimating the efficacy of the embankment in supporting load arching naturally on to the piles as shown by Love & Miligan (2003) and Russell & Pierpoint (1997). The piled embankment met all the requirements of allowable settlement.

Kempfert et al (2004) performed 3-d 1:3 scale model tests to investigate the bearing and deformation characteristics of piled embankments. This was done using a 4 pile group in a rectangular grid and used peat as the subsoil. The reinforced and unreinforced embankments height was varied. Along with the physical tests, Kempfert et al (2004) also performed numerical (FEM) analysis. Based on the results from the tests and the view of the current design methods being 'simple', Kempfert et al (2004) developed a new theoretical design model for piled embankments. The design method will be considered in more detail in chapter 8.

Jenck et al (2006) performed 2-d small scale physical models. The embankment material was modelled using 3, 4 and 5 mm diameter steel rods. The subsoil was modelled using 0.15 m thick foam. The piles were made of steel and fixed to a steel frame. Two piles were modelled so that the behaviour in between could be monitored. The findings of Jenck et al (2006) are shown in Table 2.1.

Parameter	Load transfer	δ
h_e	++	++
a/s	++	++
E_0	-	+
J (geogrid)	+	+

Table 2.1 - Jenck et al's (2006) findings (Jenck et al, 2006)

In Table 2.1: '+' represents a positive influence, '++' a very positive influence and '-' represents a negative influence (depending on the increasing values of the parameters). As in the majority of studies increasing embankment height, pile cap area and geogrid stiffness improved arching, and hence reduced settlement. Increasing the subsoil stiffness reduced arching, but since the subsoil carried some of the embankment load settlement was reduced. However, Jenck et al (2006) did not attempt to quantify this behaviour, which had in any case been observed in a 1-g model which did not actually use soil for the embankment.

Lai et al (2006) analysed a full scale piled embankment reinforced with a hexagonal wire mesh (h_e = 6 m with, s = 1.5 m, a = 0.5 m). They found that the pore water pressure in the subsoil increased as soon as the piles were installed and significantly reduced after 70 days. The piles settled by 300 mm after the 1st year of which 40 % occurred during construction. However, if no ground improvement had been used, Lai et al (2006) predicted that there would have been more than 1000 mm.

2.9 Summary

A number of theories exist to quantify arching in a piled embankment. Many authors have compared the methods for specific geometries and noted that they give differing results. However, they tend to focus on one or two specific geometries, and compare the results with numerical analyses, but without commenting systematically on why this should be the case. It is also generally concluded that efficacy increases towards an asymptote of 1.0 for high embankments, whilst SRR decreases to an asymptote of 0. However, these observations apply to all methods, and thus do not assist in distinguishing between them.

CHAPTER 3

CENTRIFUGE MODELLING: EXPERIMENTAL TECHNIQUE

3.1 Introduction

3.1.1 Aim

The aim of the centrifuge test series was to model piled embankments representing plausible field situations and to gather data for comparison with present analytical methods. The tests would also give insight into soil-structure behaviour within the embankment layer.

3.1.2 Centrifuge modelling

Centrifuge modelling is useful for developing an understanding of the basic mechanical behaviour of large scale geotechnical systems. This can be done through direct physical analogy (scaling laws) and through verification and calibration of computer programs used for the subsequent analysis of prototype systems. Centrifuge modelling also finds use as a verifying supplement to conventional design and analysis techniques.

Centrifuge modelling is a powerful tool enabling the investigation of many geotechnical problems some of which were previously considered intractable. Centrifuge modelling concerns the study of geotechnical situations using small-scale models made of actual geotechnical materials subjected to acceleration fields of magnitude many times Earth's gravity. The fundamental mechanical behaviour of soil is highly non-linear and depends on the current (and previous) stress state. In order to simulate the equivalent full-scale 'prototype' accurately the in situ stresses must be reproduced correctly in the model. In order to replicate the gravity induced stresses in a $1/N^{th}$ scale model of the prototype, it is necessary to artificially increase gravity in the model by a factor of N. Thus many physical processes can be scaled correctly if an N^{th} scale model is accelerated by N

times the acceleration due to gravity. For a more complete discussion, the reader is referred to a more extensive text, such as Taylor (1995).

Table 3.1 summarises the most common scaling relationships between model-scale values and the equivalent full scale 'prototype'.

Parameter	Units	Scaling factor (prototype/model)
Acceleration (g)	m/s^2	$1/N$
Density	kg/m^3	1
Unit weight	N/m^3	$1/N$
Linear dimension	m	N
Area	m^2	N^2
Volume	m^3	N^3
Stress	N/m^2	1
Strain	Dimensionless	1
Force	N	N^2
Force/unit width	N/m	N

Table 3.1 - Centrifuge model scaling relationships

3.2 Test Programme

The centrifuge tests were all based on a prototype structure such as that shown in Figure 1.1 - a piled embankment constructed on soft clay, overlying a stiffer stratum. A 'unit cell' was assumed, Figure 3.1, with boundaries at the mid point between piles in a row. Such boundaries are lines of symmetry, and thus movement in the prototype at these locations would be expected to be in this plane but not normal to it. Thus these planes can be represented by frictionless rigid boundaries. In a 3-d finite element model this is feasible and the smallest possible 'unit cell' would be used, which would be half the centre-to-centre pile spacing along each side, and would incorporate one quarter of a pile cap. However, any integer multiple of this cell is equally valid, and such an

approach is often used in centrifuge modelling since the boundaries are never completely frictionless and hence behaviour may be undesirably affected here, but less so at the centre of the model. Figure 3.1 shows a grid of 3×3 piles as a 'unit cell' which actually comprises 36 of the smallest possible unit cells based on one quarter of a pile cap. Thus the 3-d effects associated with transfer of embankment load onto pile caps were correctly modelled. However, any effects associated with the side slopes of the embankment are not incorporated, and are not considered in this work.

Models were constructed on the lab floor at 1g, and then loaded on to the centrifuge and accelerated to 60g in 10g increments. Thus the 300 mm side length of the square model varied from 3 to 18 m at prototype scale. The behaviour at 30g gave the most plausible prototype dimensions, but additional information could potentially be obtained by also considering the other g levels

Figure 3.2 shows a 'cut through' projection of the general arrangement of the model; the specific arrangements and components are discussed below in Section 3.3.

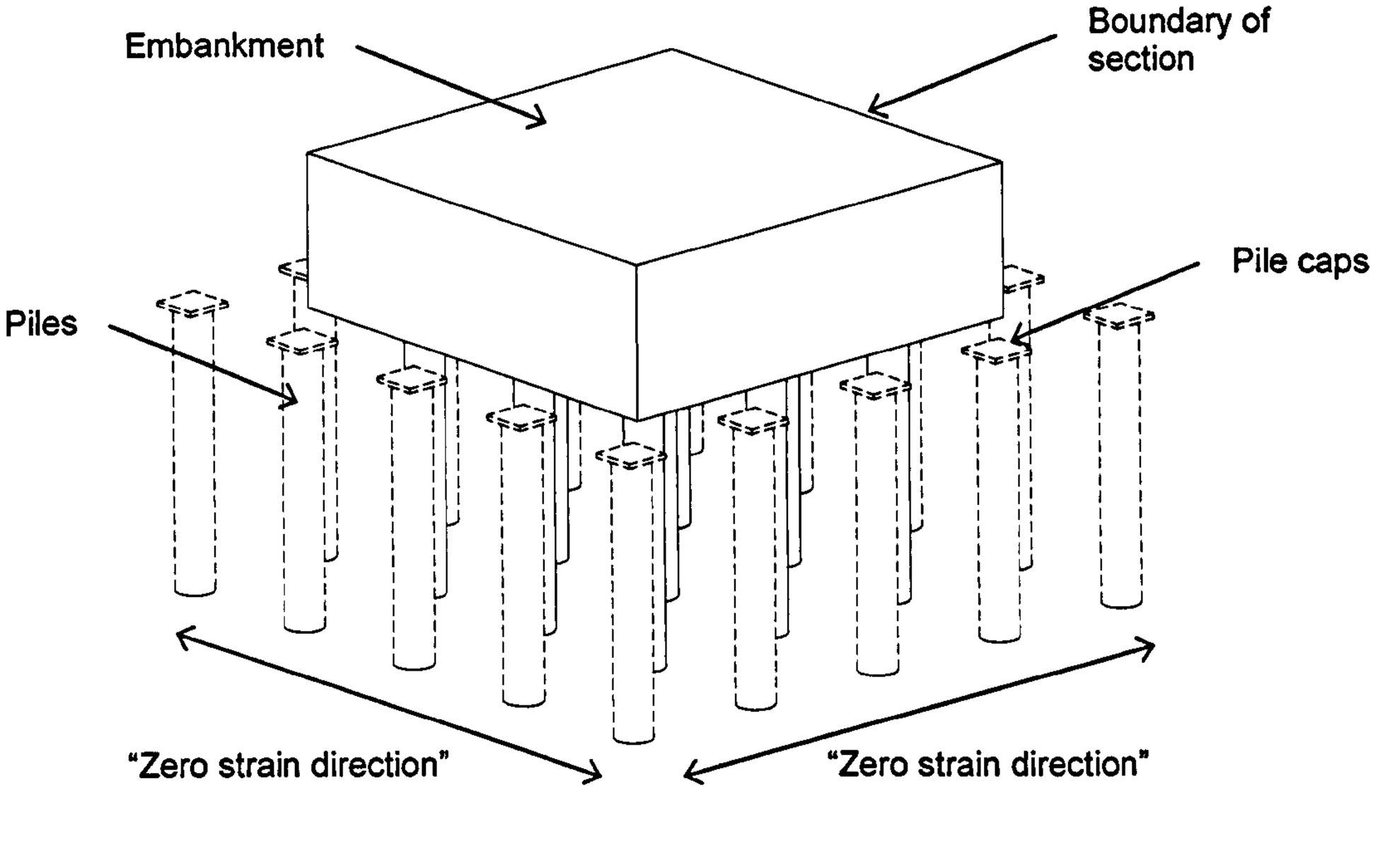

Figure 3.1 - 'Unit cell' assumed in centrifuge models

Initial tests refined the modelling technique, while later tests were designed to investigate the effects of variation of embankment thickness, pile spacing, stiffness of the subsoil and basal geotextile reinforcement. The granular embankment material also extended below pile cap level in some tests, modelling a working platform (piling mat) - such material cannot arch 'onto' the pile caps, and hence causes a significant load on the subsoil. All other model components remained unchanged throughout the test series, unless stated otherwise.

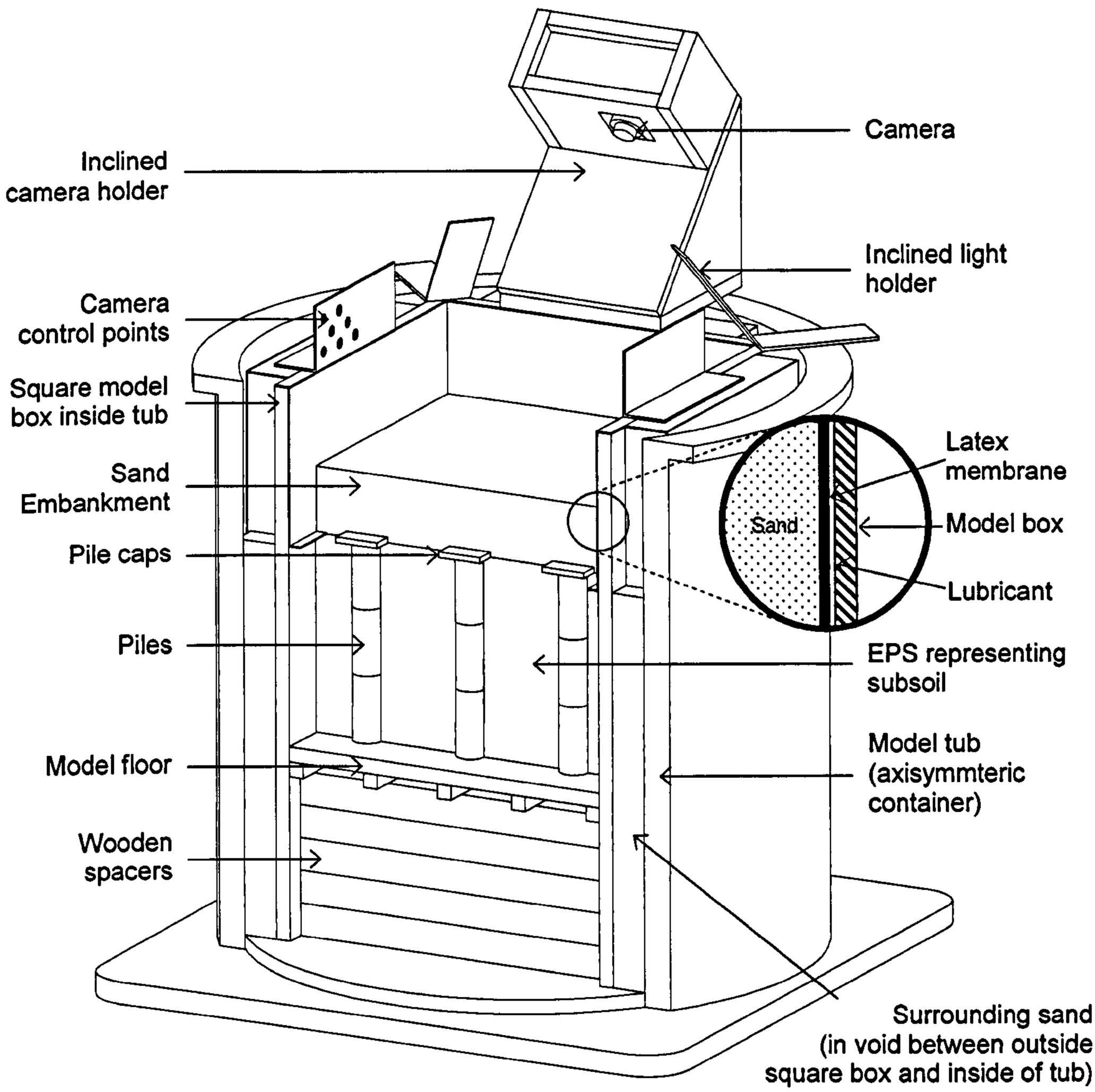

Figure 3.2 - Model projection

3.3 Test Equipment

3.3.1 NCG geotechnical centrifuge

Specific discussion of the Nottingham Centre for Geomechanics (NCG) geotechnical centrifuge can be found in Ellis at al (2006).

The centrifuge is essentially a 50g-T machine, with 2.0 m platform radius. Figure 3.3 shows the major components of the machine. The centrifuge was manufactured by Thomas Broadbent & Sons (Huddersfield, UK).

Coarse balancing of the payload is achieved by movement of a fixed counterweight (see Figure 3.3) using a detachable screw jack prior to centrifuge flight. 'In-flight' balancing of +/- 50 kgm is allowed by movement of oil in the tubular rotor arms from one side of the main axis to the other. The requirement to do this is based on very sensitive measurement of deflection of the support pedestal at the location of one of the legs. Services and data associated with the model are transmitted via slip rings at the top. As is common practice, the DAS (Data Acquisition System) cabinet is mounted on the central axis in a relatively low *g* environment (see Figure 3.3).

One end of the beam carries a swing cradle (suspended from a pivotal axis which is tangential to the beam, Figure 3.3). During the test, the platform "swings-up" so that the model is mounted horizontally. 'Vertical' and 'horizontal' in terms of the model now correspond to radial and tangential respectively in terms of the centrifuge arm. In this position, the model is subject to 2 acceleration fields. The Earth's gravitational field acts vertically downwards, whilst the radial acceleration field (Ng), due to centrifuge rotation acts in a horizontal plane, thus simulating a greatly increased gravitational field in the vertical model direction.

Since Ng » g, the vertical component of acceleration is generally neglected. The imposed acceleration is only truly 'vertical' (in terms of the model orientation) at the centreline of the model. At a distance of 100 mm either side of the centre, it is inclined at approximately 3.2° to the vertical, whilst at the edges of the model, the inclination increases to nearly 5°. However, this effect can generally be ignored (especially since the critical model components are normally situated near the centre of the package).

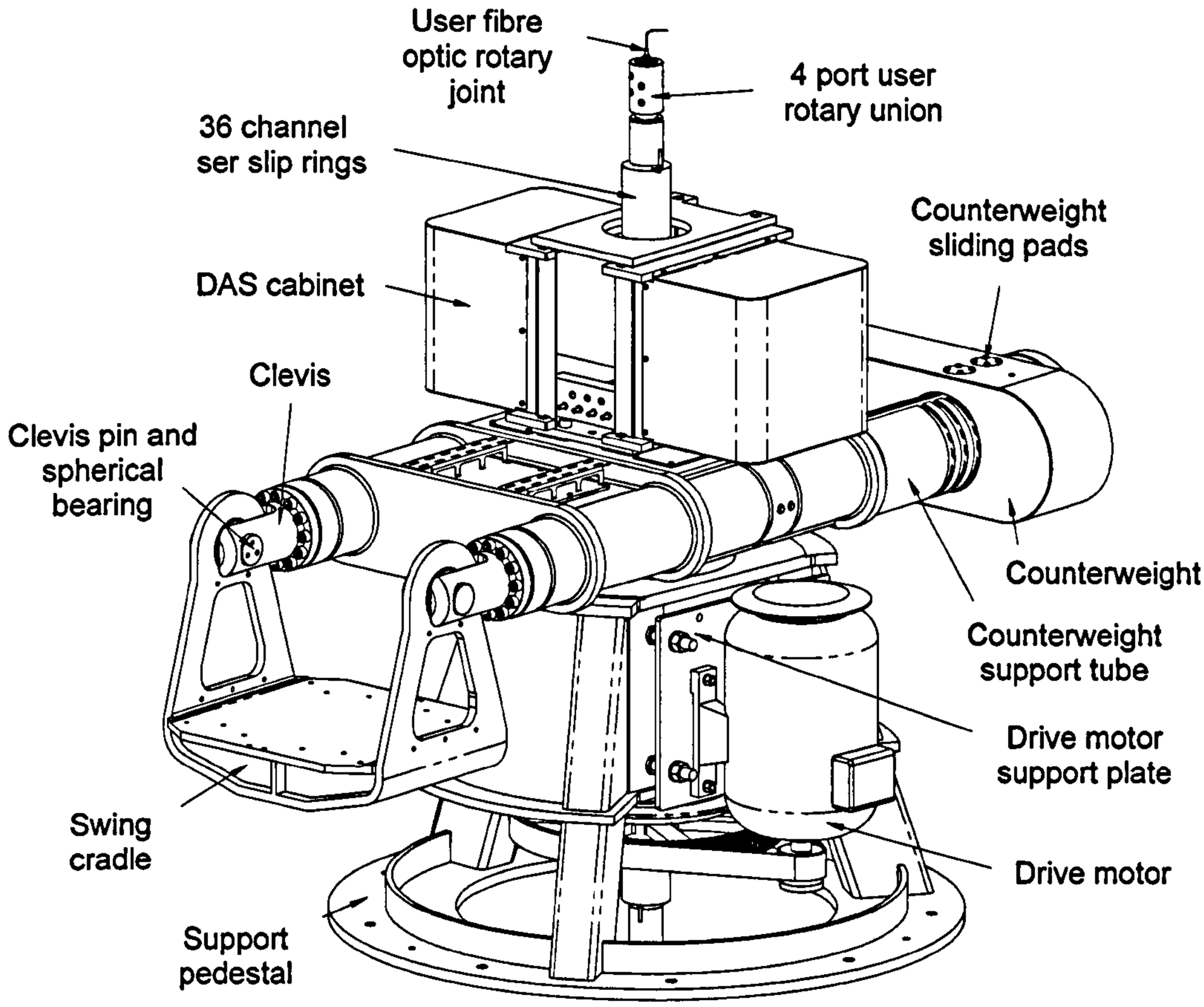

Figure 3.3 - Main machine components

Since the model (embankment) height is small when compared to the radius of the centrifuge arm, variation in the magnitude of radial acceleration with radius is also generally ignored. In these tests, in the worst case N increases from approximately 9.4 at the top of the embankment, to 10.6 at the pile cap level for a nominal acceleration N = 10. The chosen speed of centrifuge rotation ensured the required Ng level was at the mid-depth of the embankment. The total overburden stress at the base of the embankment is then 'correct'.

3.3.2 Model tub and box

The centrifuge "package" consists of the model, instrumentation, model box and model tub (axisymmetric container, see Figure 3.2). The model tub was provided by Broadbent and is made of steel, with 500 mm inner diameter.

The model is constructed within the 300 mm (internal dimension) square model box, which itself is contained in the tub and was manufactured within the Engineering Faculty workshops at the University of Nottingham. The model box represents a multiple unit cell (Figure 3.1), and is therefore square, as shown in Figure 3.4. It was manufactured using aluminium because of its light weight compared to steel, with the individual components glued together using araldite. The individual sides were then screwed together. Each box side was constructed from two aluminium plates separated by 38 mm, and joined by channel sections to act as a beam and give high stiffness in bending with minimum weight. The gap between the outer plate and inner diameter of the tub was filled with sand to approximately balance the pressure from the model soil on the inside, and thus there would have been little differential pressure to cause bending in any case. Figure 3.4 shows one side of the model box has holes cut out at the bottom. These holes allow the passage of wires so that they do not pass along and up the inside of the model box, interfering with the model's behaviour. To achieve a satisfactory unit cell, it is necessary to reduce side friction to an acceptably low level - see Section 3.3.7.

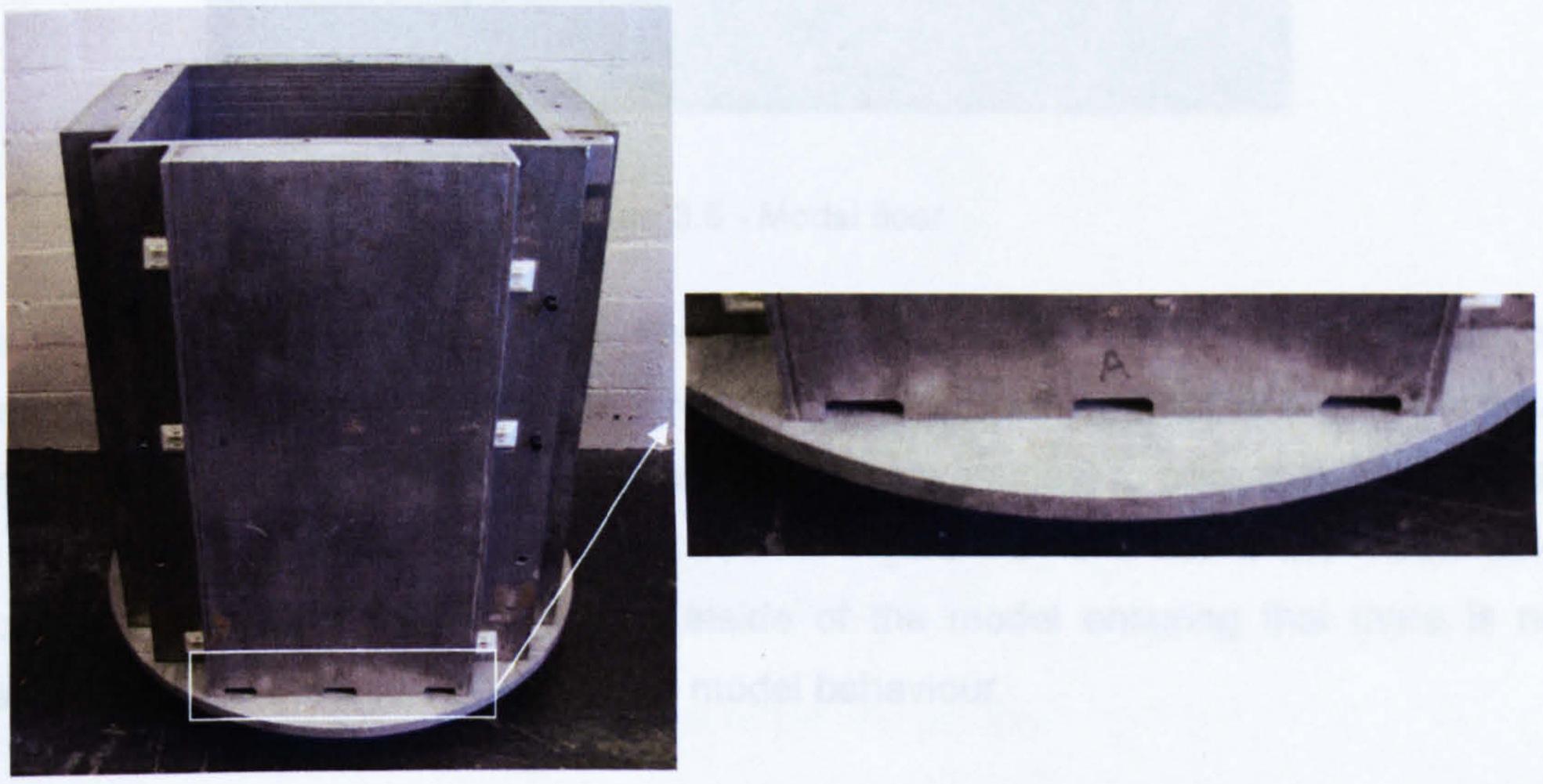

Figure 3.4 - Model box

Wooden spacers (sheets of plywood screwed together) of various thicknesses were placed under the model floor to lift the model so that the camera (Figure 3.2) had a good view of sand surface irrespective of the embankment thickness.

3.3.4 Model piles

Figure 3.5 shows the model floor on which the piles are positioned and which represents the surface of a stiffer stratum beneath the soft layer, where embedment of the piles is sufficient to give stiff bearing. In a real geotechnical situation the piles would need to be 'socketed' a few diameters into the stiffer stratum to exploit the full bearing capacity of this layer, but since the floor was practically completely rigid this was not necessary in the model.

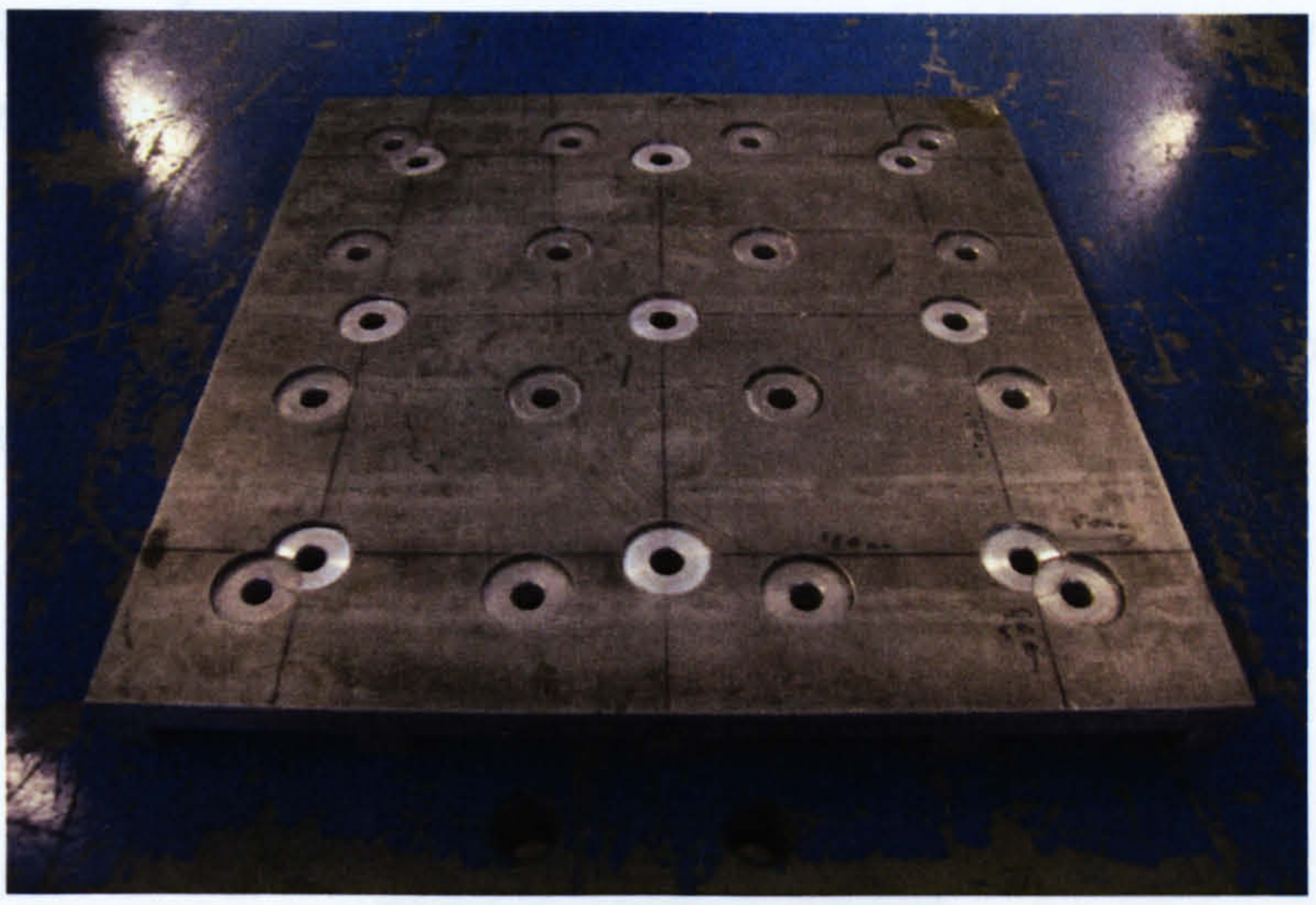

Figure 3.5 - Model floor

The model floor was made in the Engineering Faculty workshops and is made of aluminium plate. The piles locate in circular recesses machined out of the model floor with a hole in the centre to allow the wires (from strain gauges) to pass through beneath the model floor (which is supported on beams, Figure 3.2) and out of the model box. Thus no wires run through or on the inside of the model ensuring that there is no interference from the wire's presence on model behaviour.

During the test series, both '3 × 3' and '4 × 4' pile arrangements were used, as shown in Figure 3.5.

The piles were manufactured from aluminium tube and two types were used. The first type, capable of measuring axial load was made of 3 sections, one of which was a load cell section shown in Figure 3.6 (described in more detail in Section 3.4.1). The second type was an un-instrumented pile, not capable of measuring load, and was made from one section of 1/16" SWG aluminium tube (external diameter = 25.4 mm, wall thickness = 1.6 mm). Typically, loads in the piles were up to about 1 kN. This corresponds to a deformation of only about 0.02 mm in the pile, so they were effectively completely rigid.

The average axial stiffness of the piles along their length was *EA* = approximately 10 MN, which is equivalent to approximately 10 GN at 30g. Based on a Young's modulus of 30 GN/m^2 this would represent a concrete pile of approximate diameter 0.33 m. However, the piles were intended to represent inclusions of any nature which are effectively rigid compared to the surrounding soft soil.

The pile caps were made from aluminium and locate inside the piles. They are 30 mm square (*a*), equivalent to 0.9 m at 30g.

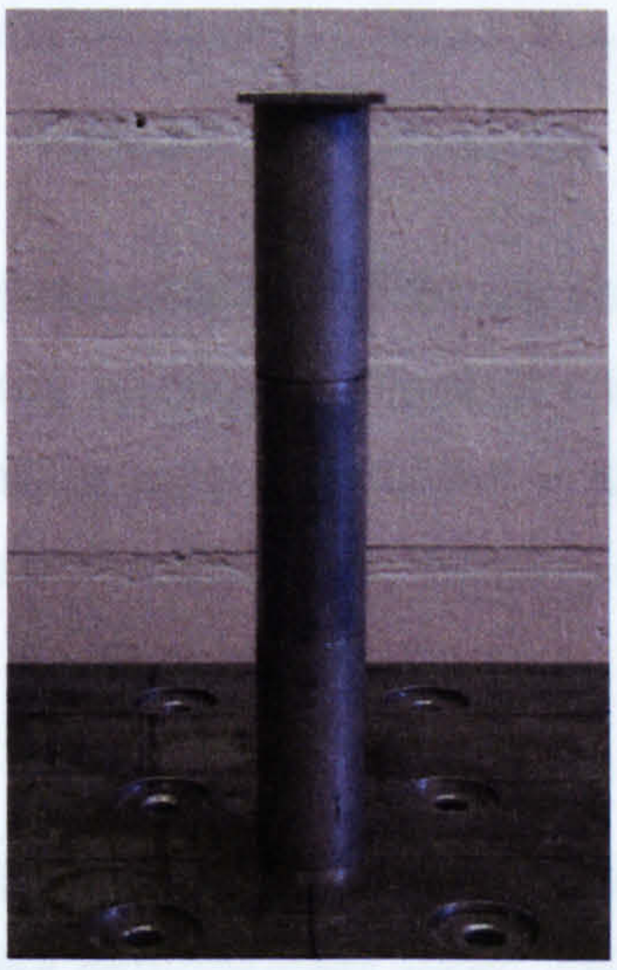

Figure 3.6 - Model pile with pile cap

3.3.4 Soft subsoil

Soil such as clay or peat is usually the type of material referred to as the 'soft subsoil' which piled embankments are constructed on. However, due to the complexity and time requirements to prepare clay to be used in the model tests, Expanded Polystyrene Styrofoam (EPS) was used to represent such a material.

The EPS was simply cut to size (initially with a hand saw, and then finished with a band saw) to fit in the model box and holes were drilled out to accommodate the piles. EPS proved to be a time efficient method of modelling the soft subsoil. Two types of EPS were used (Table 3.2), as supplied by Vencel Resil Ltd in 1 m cubes more normally used for lightweight embankment construction. The material was found to have quite consistent properties (probably at least as consistent as notionally identical soil samples) - see sample oedometer data in Appendix B.

EPS 'grade'	E_0 (MN/m^2)	Yield stress (kN/m^2)
EPS 70	1.7	70
EPS200	8.0	200

Table 3.2 - EPS properties

In the majority of tests the yield stress of the EPS was not exceeded, and thus the block could be reused, again improving efficiency. Appendix B gives data on repeatability of pre-yield behaviour. The E_0 values were considered to span a reasonable range of soft soil parameters. The thickness of the EPS was 180 mm, equivalent to 5.4 m at 30g.

3.4.5 Model embankment

Leighton Buzzard fraction C with a d_{50} of 0.5 mm and a peak friction angle of 35° (from shear box tests) was used for the embankment sand. The d_{50} of 0.5 mm was chosen so that there would be sufficient particles (at least 90) between adjacent pile caps to give representative arching behaviour. The embankment layer was constructed (Section 3.5.2) before the model was placed on the centrifuge swing.

3.4.6 Model reinforcement

Polyethylene or other polymers such as polypropylene or polyester are usually the type of material used as the basal reinforcement in piled embankments. Due to the centrifuge scaling laws, actual geogrid cannot be used as the aperture sizes and its strength and stiffness are too large. For this reason other materials (polyethylene grid - more commonly used for formwork lining) were used as 'model' geogrid.

The material was cut to size and held in a square aluminium clamp (Figure 3.7) and the model geogrid rested directly on the pile caps. The clamp maintained tension at the edges, as required for correct modelling of the 'unit cell'.

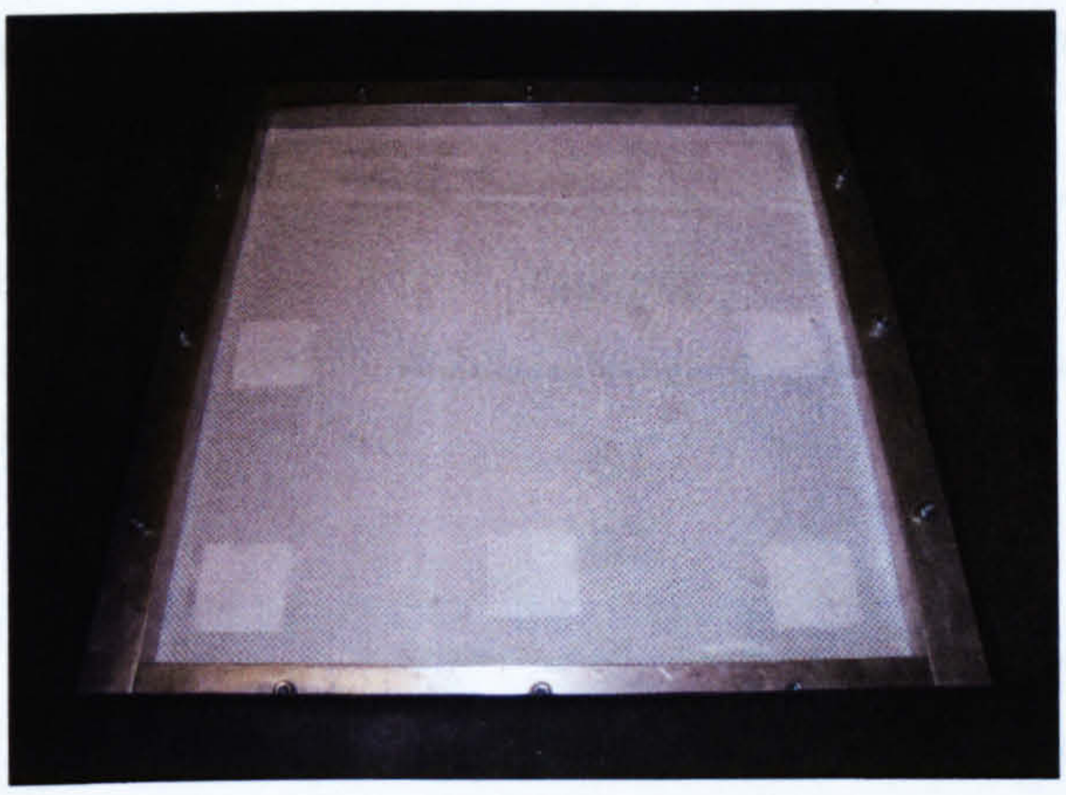

(a)

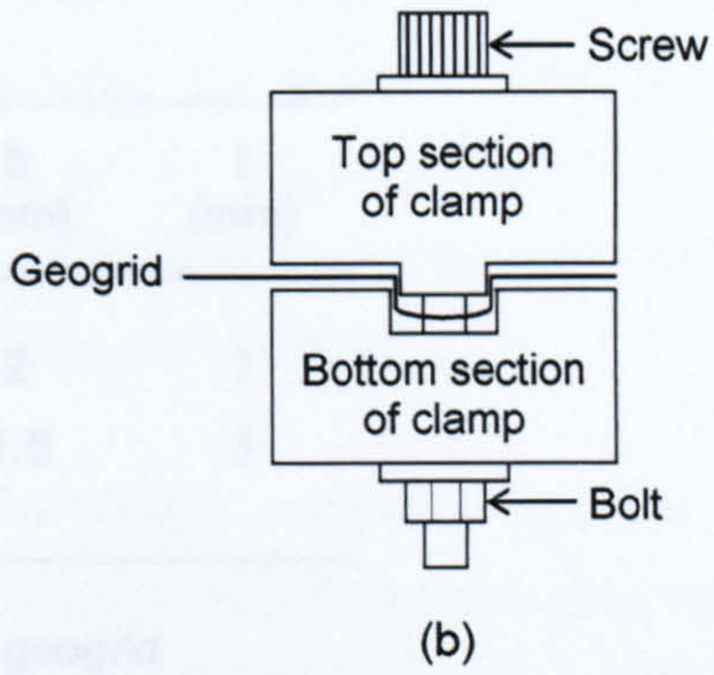

(b)

Figure - 3.7 Square clamp: (a) general view, (b) clamping mechanism

The geogrid shape and dimensions are shown in Figure 3.8 (a) whilst Figure 3.8 (b) shows photos of the grid.

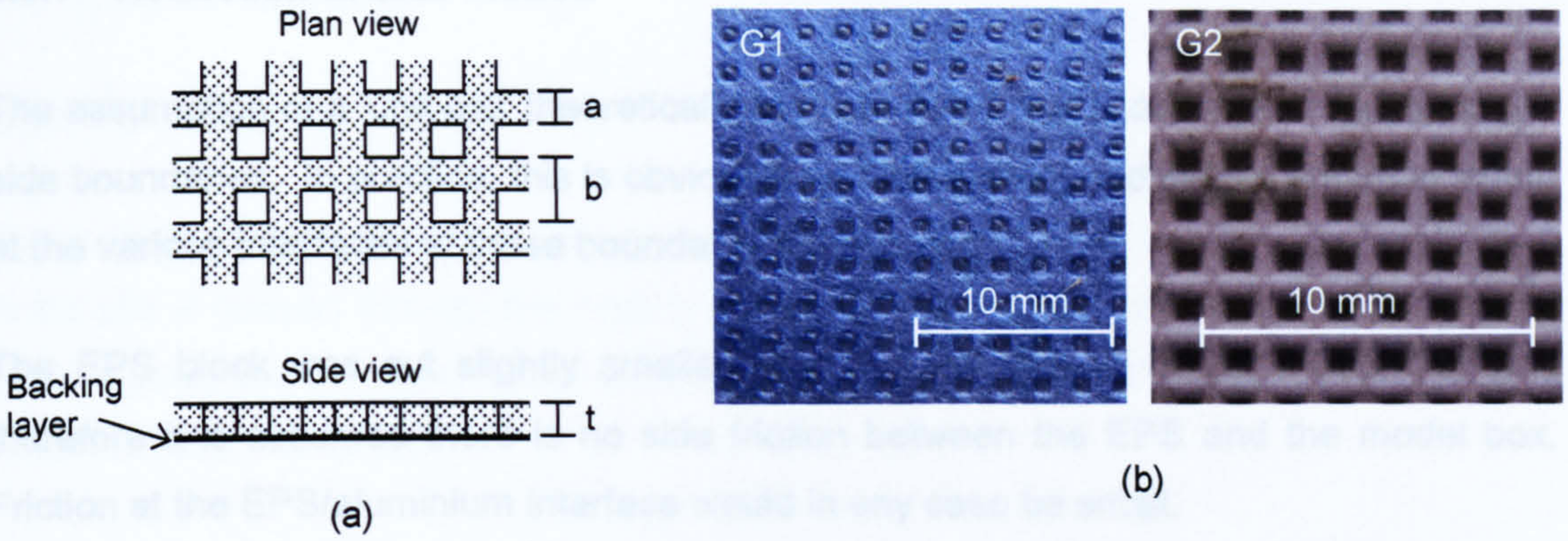

Figure 3.8 - Shape and dimensions of reinforcement (not drawn to scale): (a) Schematic view with dimensions (see Table), (b) Photos

The various dimensions of the geogrid are shown in Table 3.3

Geogrid	a (mm)	b (mm)	t (mm)
G1	1	2	1
G2	1	1.5	1

Table 3.3 - Dimensions of geogrid

Both materials actually had a 'grid' nature, with section $a \times t$, and square 'apertures' with size (b-a). However, these grids were fixed to a thin continuous plastic 'backing layer' (see Figure 3.8 (a)). Hence the 'apertures' provided a rough 'texture' on one side, whilst the other side was smooth due to the backing layer. The 'apertures' would not allow sand to pass through them, since the backing layer prevented this. The smooth side faced upwards, and thus was in contact with the base of the embankment. This allowed comparison of the behaviour of both model geogrids with a purely tensile reinforcement, which did not interact with the embankment in other ways.

The stiffness of these materials is considered in Chapter 7.

3.3.7 Reduction of side friction

The assumption of a 'unit cell' theoretically requires that there should be no friction at the side boundaries. In practice, this is obviously an idealisation, and potential friction acting at the various interfaces at these boundaries is discussed below.

The EPS block was cut slightly smaller than the dimensions of the model box and therefore it is assumed there is no side friction between the EPS and the model box. Friction at the EPS/aluminium interface would in any case be small.

More importantly, the embankment could show significant tendency for settlement and has interfaces on all box sides. To reduce the frictional resistance, latex and a silicone based lubricant was used as shown in Figure 3.2. The latex itself was sufficiently flexible (having a stiffness of approximately 1 kN/m width) that it would not restrict the sand movement, and from shear tests it was found that the greased side boundary offered only 5° frictional resistance compared to up to 25° for a normal sand/aluminium boundary. Using latex panels on all faces of the embankment, the estimated total side friction force was approximately 10 % of the embankment weight at 60g.

During construction of the model, the latex panels (which extended approximately 20 - 70 mm above and over the box sides) were secured by the clamping action offered by the control point mounts on three sides and the camera base on the other (see Figure 3.2). The panels were held against the side boundaries by adhesion within the greased interface. The latex panels also overlapped the EPS block by approximately 10 mm to ensure no sand from the embankment fell into any potential gaps. As the latex stiffness was sufficiently small, the clamped boundary caused little resistance to movement of the sand body since sufficient extension of the latex section above the sand embankment could occur with minimal tension in the latex.

3.5 Instrumentation

3.4.1 Model piles

Strain gauges were used to measure the load acting in the piles. The strain generated in the pile is relayed through the base to the foil where contraction (or extension) occurs; consequently the foil experiences a variation in resistance. This change in resistance is proportional to the strain.

The strain and hence the change in resistance to be measured was very small and therefore required the resistors to be arranged in the conventional Wheatstone bridge circuit form to convert it to a voltage output, Figure 3.9.

From Figure 3.9, assuming resistances of (Ω) are R_1, R_2, R_3 and R_4 and the bridge voltage (V) is E, the output voltage (V) e_o is obtained from Equation 3.1

$$e_o = \frac{R_1R_3 - R_2R_4}{(R_1 + R_2)(R_3 + R_4)}E \qquad \text{Eqn. 3.1}$$

Where:

e_o = Output voltage (V)
E = Excitation voltage (V)
R_1 = Gauge resistance (Ω)

As the resistance R_1 is the strain gauge and changes by ΔR due to the applied strain, the output voltage becomes:

$$e_o = \frac{(R_1 + \Delta R)R_3 - R_2R_4}{(R_1 + \Delta R + R_2)(R_3R_4)}E \qquad \text{Eqn. 3.2}$$

Nominally $R_1 = R_2 = R_3 = R_4 = R$, then:

$$e_o = \frac{R^2 + R\Delta R - R^2}{(2R + \Delta R)2R}E \qquad \text{Eqn. 3.3}$$

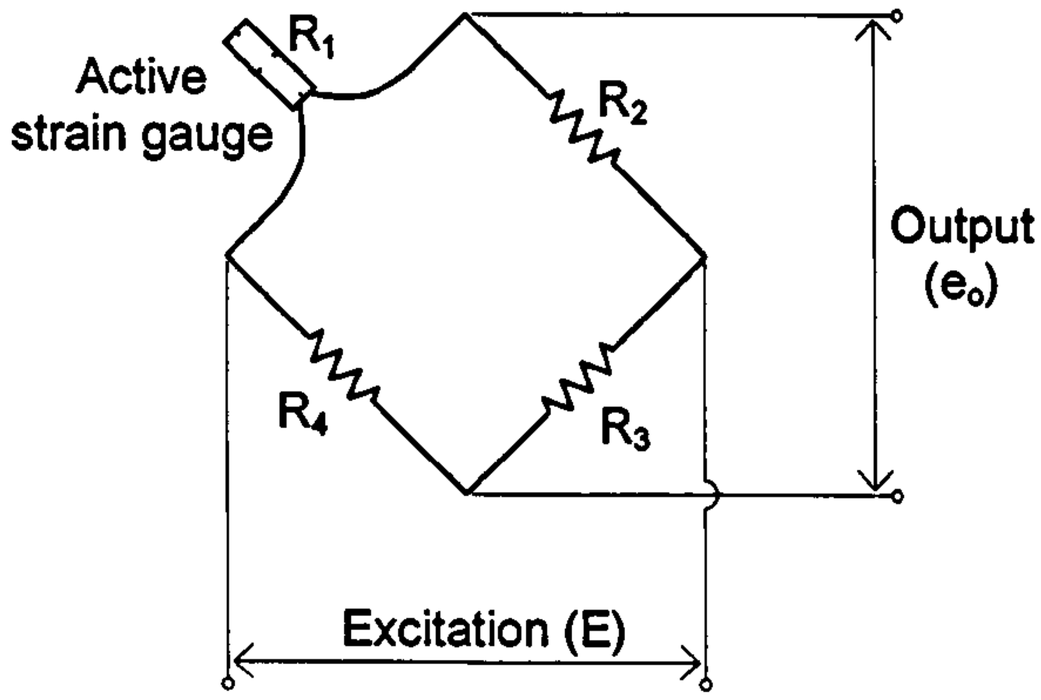

Figure 3.9 - Wheatstone bridge circuit arrangement

Since $R >> \Delta R$, Equation 3.4 gives the output voltage e_o that is proportional to the change in resistance, i.e. the change is in the applied strain on the pile Equation 3.5.

$$e_o = \frac{1}{4}\frac{\Delta R}{R}E \qquad \text{Eqn. 3.4}$$

The relative change in resistance resulting from strain is referred to as the 'gauge factor' (K):

$$\frac{\Delta R}{R} = K\varepsilon$$

Hence

$$e_o = \frac{1}{4}K\varepsilon\, E \qquad \text{Eqn. 3.5}$$

Orthogonal 4-Active-Gauge System

The system shown in Figure 3.9(a) has 4 strain gauges, one connected to each side of the bridge. This circuit improves output of strain-gauge transducers and improves temperature compensation as well as eliminating strain components other than the

target strain. This type of gauge arrangement was used to measure the pile strains in the tests.

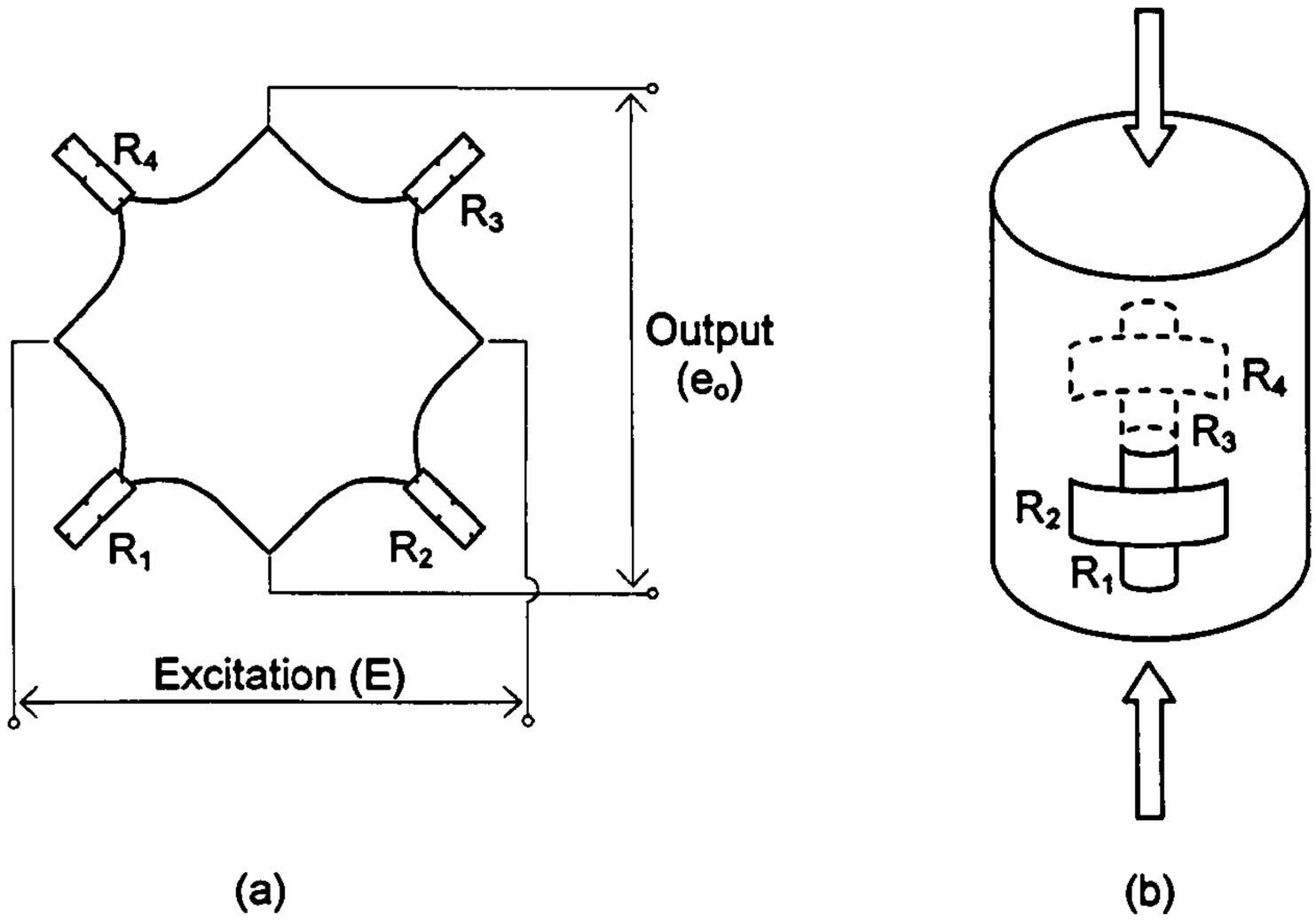

Figure 3.9 - Orthogonal 4-Active-Gauge System: (a) bridge, (b) rosette configuration

Figure 3.10 (b) shows how the orthogonal 4-active-gauge system that was attached to the inside walls of the aluminium piles, with two strain gauges (1 rosette) on each side forming the bridge.

When the strain is applied, the strain gauges R_1 and R_3 will be in compression and therefore increase in resistance (+ve) and gauges R_2 and R_4 will be in tension (due to Poisson's Ratio) and decrease in resistance (-ve). Hence the output can be calculated from Equation 3.6 below.

$$e_o = \frac{(1+v)}{2}\frac{\Delta R}{R}E = \frac{(1+v)}{2}K\varepsilon E \qquad \text{Eqn. 3.6}$$

Where

v = poisson's ratio

Axial Load Cell

The load cell sections of the model piles were fitted with a total of 4 rosettes of 2 orthogonal 350 Ω strain gauges configured to measure the axial load in the pile. As Figure 3.11 (a) and (b) show, the strain gauges were attached to the inside of the pile section. The piles were made from three different aluminium sections (which slotted into one another) and the strain gauges were attached to the top section. Figure 3.11 (b) shows the configuration used to make one axial load cell (ALC).

The diametrically opposite pairs of 2 rosette strain gauges each form a fully active four resistor bridge. The ALC has been treated as two separate fully active bridges (Equation 3.6) with the two voltage outputs averaged after the test to give one reading. This configuration has been found to perform better than the single bridge configuration as the two bridges 'compensate' each other if the load is eccentric. Poor repeatability of calibration was initially experienced with measurement on only one diametrically opposite pair (bridge), and this was assumed to be due to non-uniformity of stress in the model pile. Although theoretically introducing redundancy, averaging the output from a two bridge system gave a more 'distributed' measurement system and was found to give much better results.

The strain gauges are fixed to a section with relatively low thickness to maximise their output. However, the overall axial stiffness of the instrumented piles was similar to (about two-thirds of) the uninstrumented piles. As noted above the uninstrumented piles were effectively rigid, and thus the instrumented piles also were.

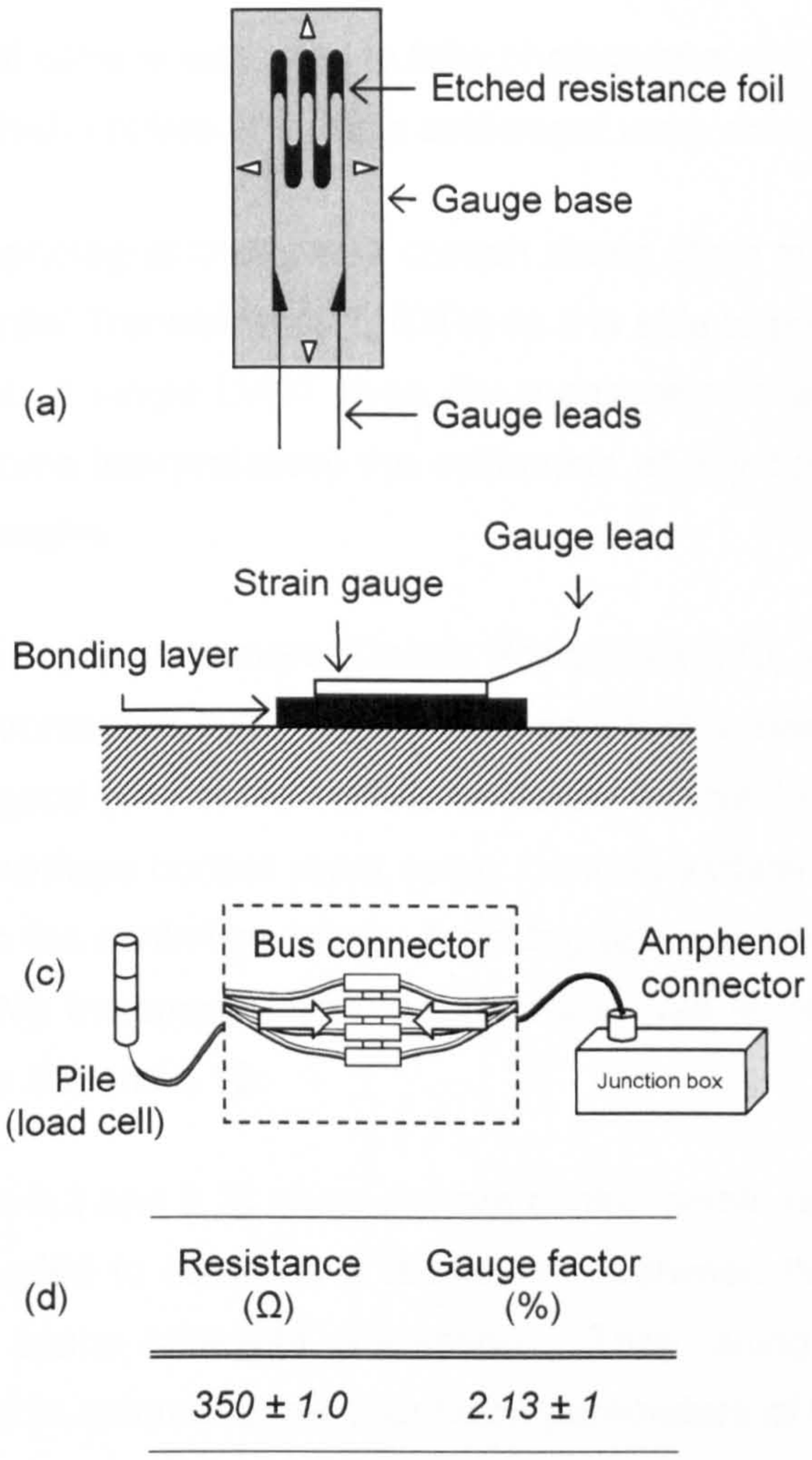

(d)

Resistance (Ω)	Gauge factor (%)
350 ± 1.0	*2.13 ± 1*

Figure 3.11 - Pile axial load cells: (a) Strain gauge application, (b) Pile - load cell configuration (dimensions in mm), (c) Load cell and amphenol connector, (d) Strain gauge type

3.4.2 In-flight photographic measurements

A digital camera was used to take photographs of the surface of the sand during the test, from which profiles of surface settlement were obtained.

Digital photogrammetry was chosen above other methods such as using Linear Variable Differential Transformers (LVDTs) as it is able to provide more data and is a non contact method. A single LVDT gives one measurement whereas photographs are able to give (with some interpretation) the settlement at any point that is visible on the sequence of photographs.

In these tests, a camera (Canon PowerShot S70) was held in an aluminium casing and was mounted on a 45° angled base so it had a reasonable coverage of the sand surface and a good view of the surface settlement. The camera was controlled in real-time from the centrifuge control room using Cannon software via a direct USB link (on the slip-rings to the centrifuge rotor). A photograph was taken before the test at 1g and again at every Ng increment. The sand surface was lit using 3 separate high intensity LEDs, Figures 3.2 and 3.12.

Figures 3.2 and 3.12 show camera control points (exterior orientation parameters) which are needed to establish a relationship between the 3-d model (object) space and the image space (absolute orientation). They, along with the collinearity equations, are needed to determine the orientation parameters of the camera with respect to the model coordinate system - this is called single photo resection. The collinearity equations are a common mathematical model used for the solution of the camera relative orientation parameters and model points. For a fuller description on this technique, see Schenk's (1999) book on Digital Photogrammetery.

The co-linearity equations are used to determine the absolute orientation and precise position of the camera in object space from the control point locations (whose positions in object space are known) on the images. This can also be used to account for any slight changes in camera orientation as g-level increases.

GeoPIV is a Matlab module which implements the principles of Particle Image Velocimetry (PIV) specifically for geotechnical applications. It was developed by researchers from the University of Cambridge (White et al, 2003).

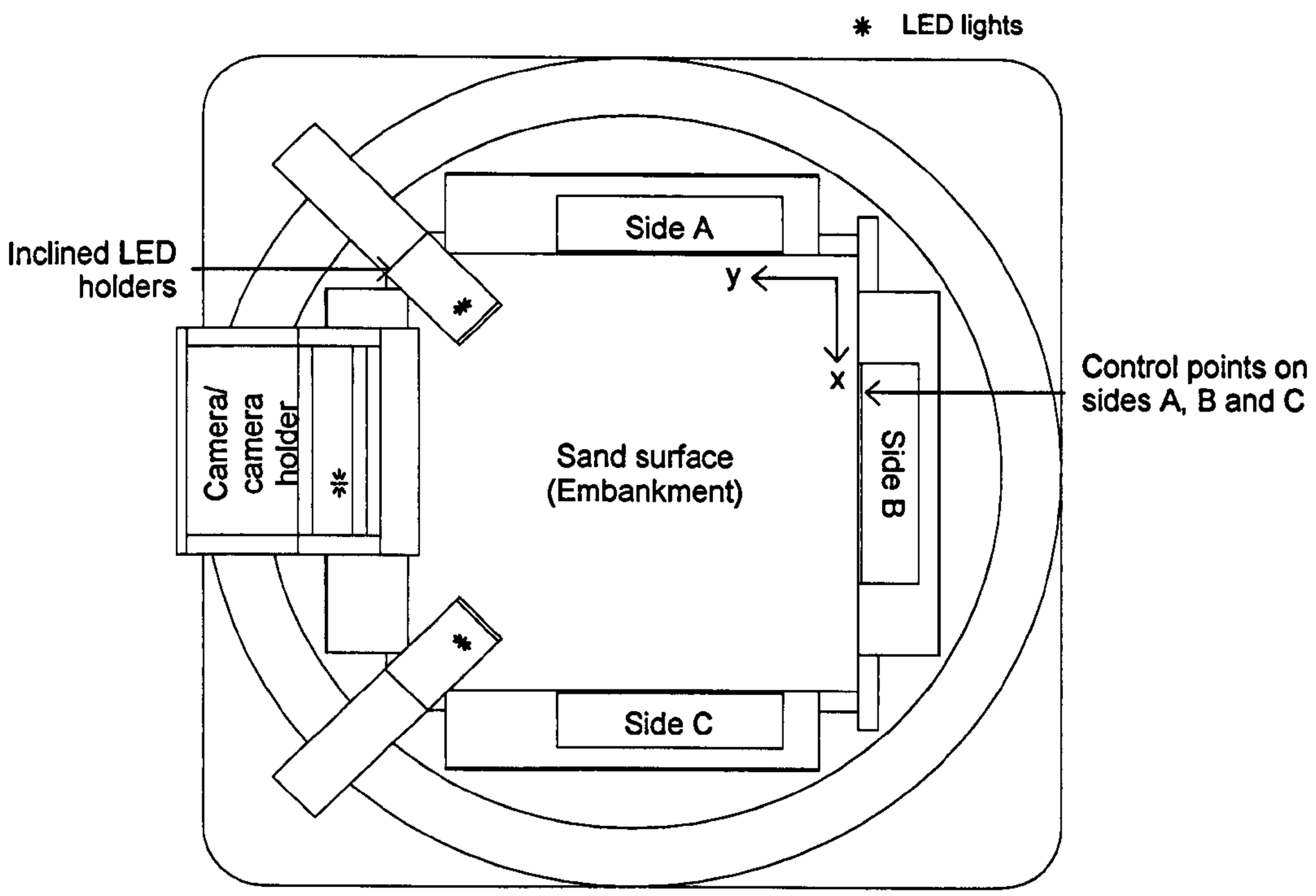

Figure 3.12 Top view of model

The principles of GeoPIV analysis are summarised in Figure 3.13. PIV operates by tracking the texture (variation in brightness) within an image of soil from one image to the next. The initial image, taken at 1g, is divided up into a mesh of PIV 'patches' as shown in Figures 3.13 and 3.14 (actual photograph taken from Test RA22). Considering a single patch located at (x_{1m}, y_{1m}) located on image 1, Figure 3.13, to find its displacement in the following image, a correlation between the patch extracted from image 1 at time t_1 and slightly larger patch from the same part in image 2 at time t_2 is carried out. The location at which the highest correlation is found indicates the displaced position of the patch (x_{2m}, y_{2m}). The location of the correlation peak can in principle be established to sub-pixel precision by fitting a bicubic interpolation around the highest integer peak. However, in this work the overall 'sensitivity' of reliable movement detection from the photogrammetric system was considered to correspond to about 0.1 - 0.2 mm - generally somewhat larger than one pixel on an image.

The GeoPIV software provides the movement of the patches in pixels from one photograph to another and so using the photogrammetry model; these 2-d movements in the images can be converted into settlement of the sand surface. In fact images from a minimum of 2 orientations are normally required to resolve 3-d movements, but the full collinearity equations can be considerably simplified if it is assumed that movement is purely vertical, and images from one camera are then sufficient. The software to convert movement in image space to object space (PIV3Danalysis) was developed in house at Nottingham, again using Matlab (Cox, 2005). The assumption that movement at the embankment surface is purely vertical seems reasonable in this situation.

This process allows a settlement value to be obtained for each of the 'patches' shown in Figure 3.14 at each g-level. The patch size and therefore the number of settlement (data) points, affects the computer processing time. Using smaller patches slows the analysis, but gives 'higher resolution' or more detailed settlement data. If the patches are too small the variation and uniqueness of texture within it will be reduced, and there is then increased risk that the software will not be able to correctly locate the patch in the second image.

As the magnitude of the overall settlement of the embankment surface increases (overall settlement is generally larger than the differential settlement of the embankment surface), the software will spend more time looking for and tracking an individual patch. For example, for small overall settlement, the patch would not have moved much between images so the software can quickly find the patch. However, when significant overall settlement of the embankment surface occurs, the software will take much longer in finding the patch. Therefore, in tests where significant overall settlement occurred (judged by eye before photograph processing) larger patch sizes were used. In 'normal' tests, a patch size of 50 × 50 pixels was used with a search zone of 100 pixels and had a process time of approximately 10 minutes. In tests where significant settlement occurred (working platform tests) a search zone of 200 pixels was used and had a process time of approximately 6 hours (was left to run overnight). 'Horizontal' centre-to-centre separation of pile caps on the image was of the order of 1000 pixels, and therefore even the larger patch size would have allowed differential settlement to be observed.

The movement of patches in image space was then converted to settlement data (Cox, 2005) and presented as a variety of plots (as shown in Section 4.1, Figure 4.3).

At high g-levels the settlement data appeared to be inherently gently curved along the x and y axes, Figure 3.15. This was assumed to be due to distortion of the camera CCD (sensor) under high g-loading. To remove the undesired curvature of the results, a 3rd order polynomial was fitted to the settlement data along the x and y axes, shown in Figure 3.15. This surface followed general curvature of the data, but not the shorter 'wavelength' differential movement associated with the square grid of 3 × 3 or 4 × 4 piles.

This surface was then removed from the raw settlement data to give a clearer representation of the differential movement.

Assuming the 'uniform' (and differential) settlement to be zero at the beginning of the test, the average value of the polynomial surface for each g-level was then taken as the corresponding 'uniform' settlement of the embankment surface. Results for both differential and uniform settlement will be presented in the later chapters.

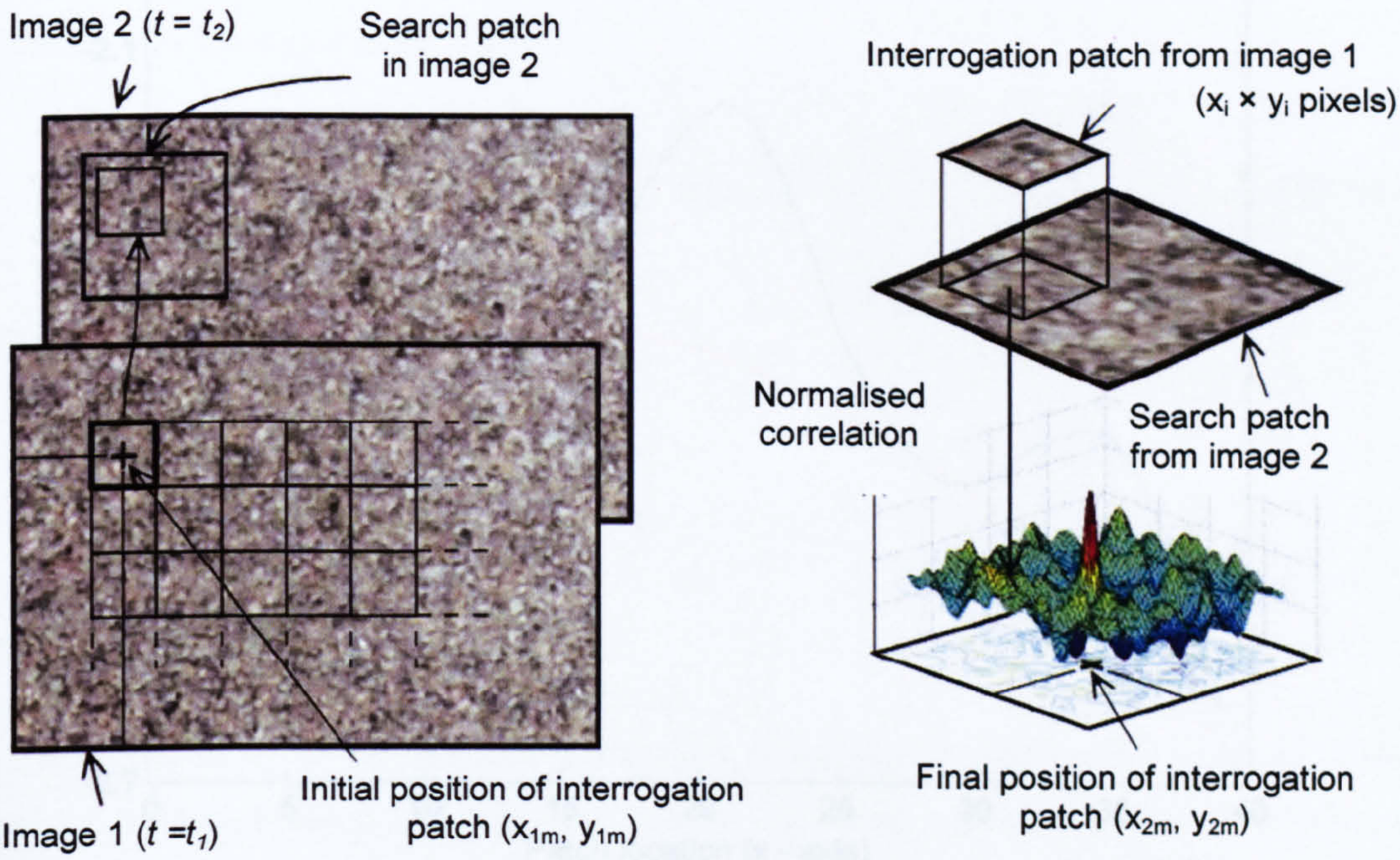

Figure 3.13 - Principles behind PIV analysis (White et al, 2004)

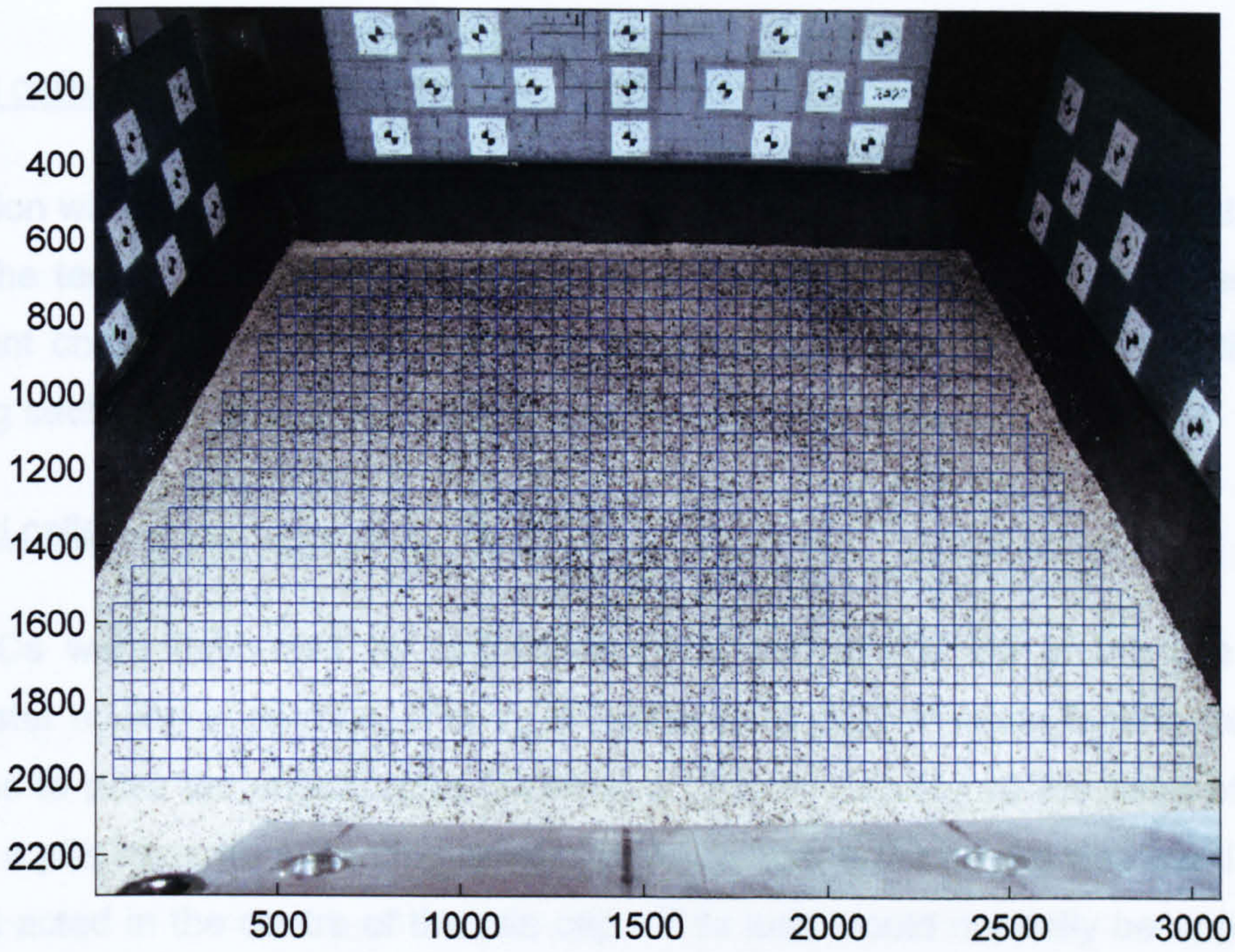

Figure 3.14 - Patch mesh for tests (photograph and mesh taken from Test RA22)

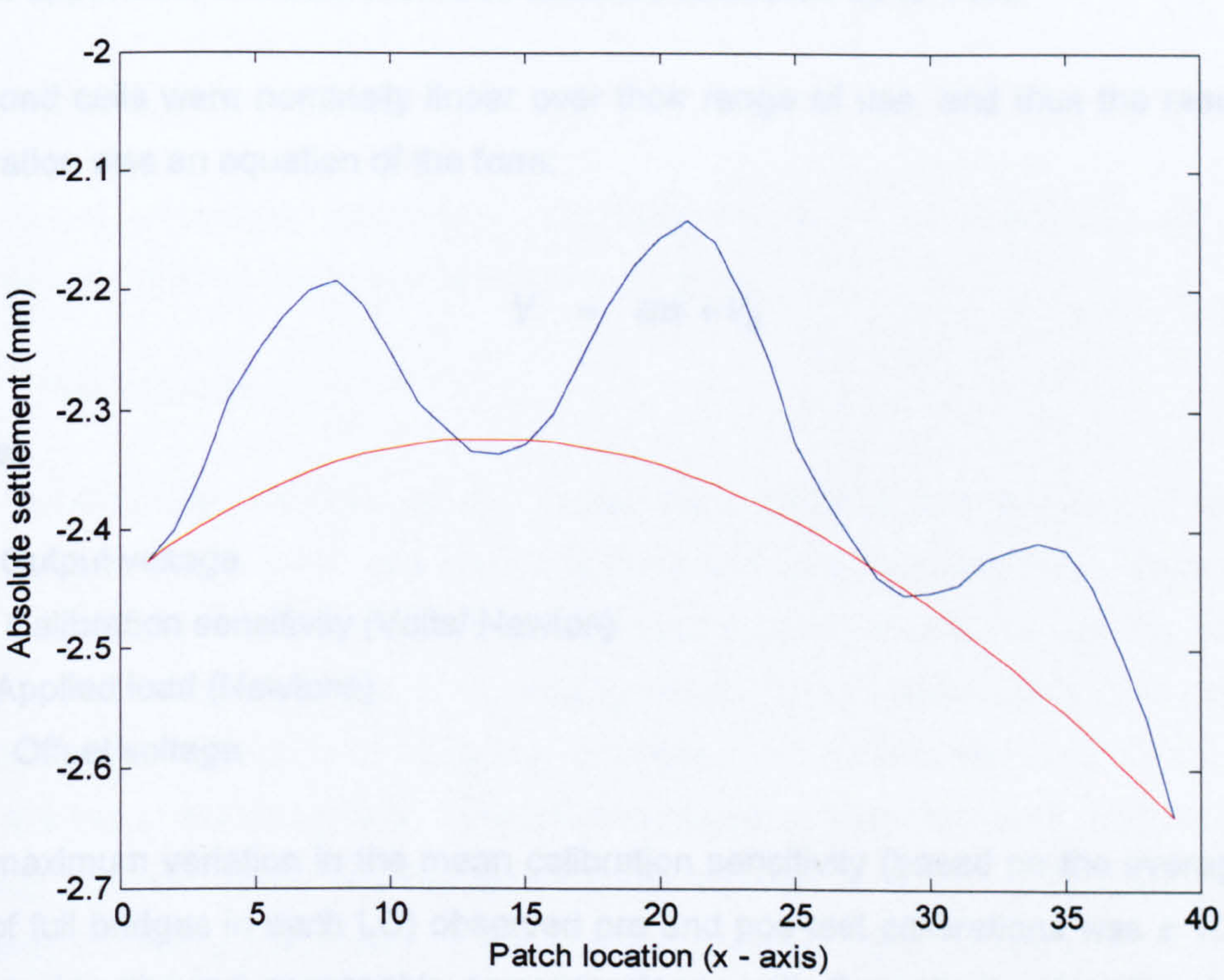

Figure 3.15 - Polynomial line fit (from test RA16)

3.4.3 Instrument calibration

General calibration procedures

Calibration was carried out using the signal conditioning and power supply that was used during the test. The load cells were calibrated at least once before each test, so that significant changes in instrumentation or amplifier behaviour would be identified. The following section gives details of consistency for the ALC instrumentation.

Pile load cells

The ALCs were calibrated by application of a load at the top of the pile using an Oedometer testing apparatus. The ALC rested on a custom made footing that allowed the wires to pass underneath and provided a uniform reaction to the base of the ALC. On top, a pile cap with a locating point hole machined at the centre was used to ensure the load acted in the centre of the pile cap. This load would normally be applied to the top plate of the oedometer sample. Large loads are readily obtained using a 11:1 lever on the apparatus, and thus the ALCs could be calibrated up to 1 kN.

The load cells were nominally linear over their range of use, and thus the result of the calibration was an equation of the form:

$$V = mx + V_0 \qquad \text{Eqn. 3.7}$$

where:

V = Output voltage
m = Calibration sensitivity (Volts/ Newton)
x = Applied load (Newtons)
V_0 = Offset voltage

The maximum variation in the mean calibration sensitivity (based on the average of the pair of full bridges in each LC) observed pre and pos-test calibrations was ± 10 % - the values also showed reasonable correspondence with theoretical calculation based on the gauge factor etc. Any variation observed in the offset voltage was of no

consequence in subsequent analysis due to the consideration of *changes* in axial load from the start of the test.

3.4.4 Supply voltages and signal conditioning

The instruments received power via conventional slip rings and transmitted data back (following digitisation) via a fibre optic rotary joint. Each channel is amplified and filtered by the electronics in the junction boxes close to the model payload such that the amount of signal noise on each channel is kept to a minimum. An amplification factor of 250 was used to increase the magnitude of small signals which would otherwise be severely corrupted by electrical noise.

3.4.5 Data acquisition system

In total, 20 - 30 instrumentation signals were monitored and logged (including a g meter on the swing) using the software Acqlipse, at a rate of 1 Hz. However this measurement was the result of averaging the previous 100 readings taken at 100 Hz. This was done to further reduce any effect of noise on the signal.

3.5 Model preparation

The model preparation procedure was designed to be as repeatable as possible. Differences between the tests are described below.

3.5.1 Sub structure

The 'substructure' consists of the model floor (representing the top of the stiffer underlying stratum), piles, pile caps and EPS and is constructed first. The ALC piles were first installed on the model floor with their cables passing through the designated holes in the chosen 4 × 4 or 3 × 3 arrangement. The uninstrumented piles were then installed in the remainder of the holes. Purpose cut EPS was then pushed into position from the top of the pile group. The different types of tests (i.e. piled embankment and working platform tests) require different thicknesses of EPS. Pile caps were now installed (following placement of the working platform sand on top of the EPS in the relevant tests).

Once the substructure was constructed, it was placed into the model box. Depending on the depth of the embankment, if the model required raising up into the camera's view, then wooden spacers were placed in the model box before placing the model substructure.

3.5.2 Sand embankment

The granular embankment was modelled using Leighton Buzzard fraction C with a uniform grading and a d_{50} of 0.5 mm. The maximum and minimum void ratios (e) were found to be:

e_{min} = 0.552
e_{max} = 0.802

Silicone grease and latex panels were attached to the inside of the box sides to reduce friction. The embankment was then formed by pluviation of sand directly into the model box from a line hopper. The sand was poured at a constant rate and from a constant height of approximately 1 m to ensure homogeneity and to provide a relatively dense sample. The maximum and minimum relative density ($I_D = (e_{max} - e)/(e_{max} - e_{min})$), as measured in each test from the calculated density of the resulting samples (using G_s= 2.65) were 1.0 and 0.7 respectively. The sand layer was then levelled off at the surface and black coloured sand with similar particle size to Fraction C was sprinkled on top to give the sand surface more 'visual texture'. This made it easier for the GeoPIV software to track the sand surface.

3.6 Test procedure

Once the model was assembled and loaded on the centrifuge swing, it was taken up to 60g in increments of 10g. The load cell data was on continuous capture, from before the centrifuge began to rotate and until when it stopped. A photograph was taken at each g-level in order to obtain settlement at each g increment.

After the test, the model was disassembled and the EPS was stored for later use (unless it had yielded during the test). The model components were inspected to check for any damage.

Figures 3.16 - 3.20 show photographs of a typical model during its construction.

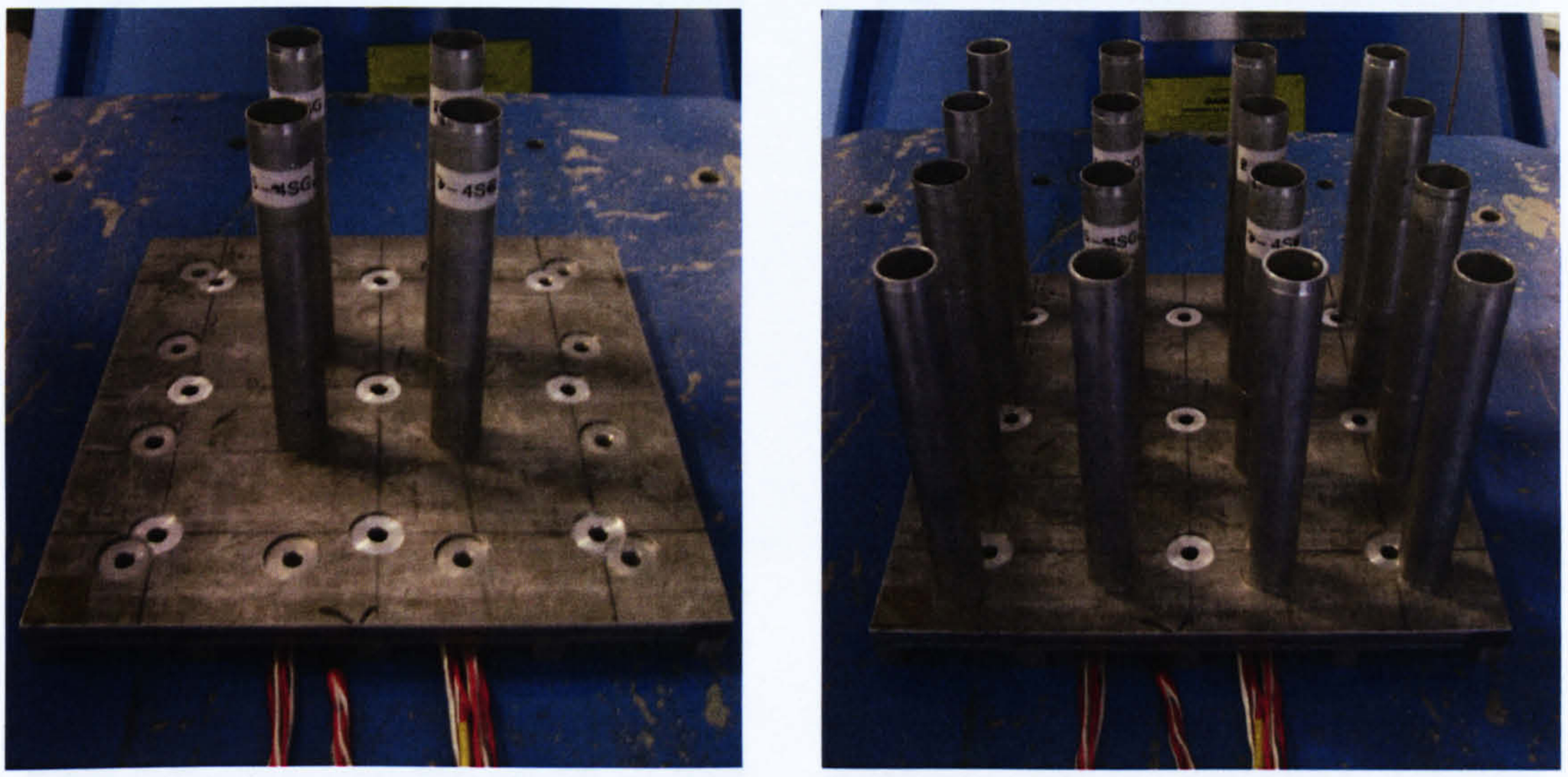

(a) (b)

Figure 3.16 - Model piles: (a) Instrumented piles only, (b) Instrumented piles together with non instrumented piles

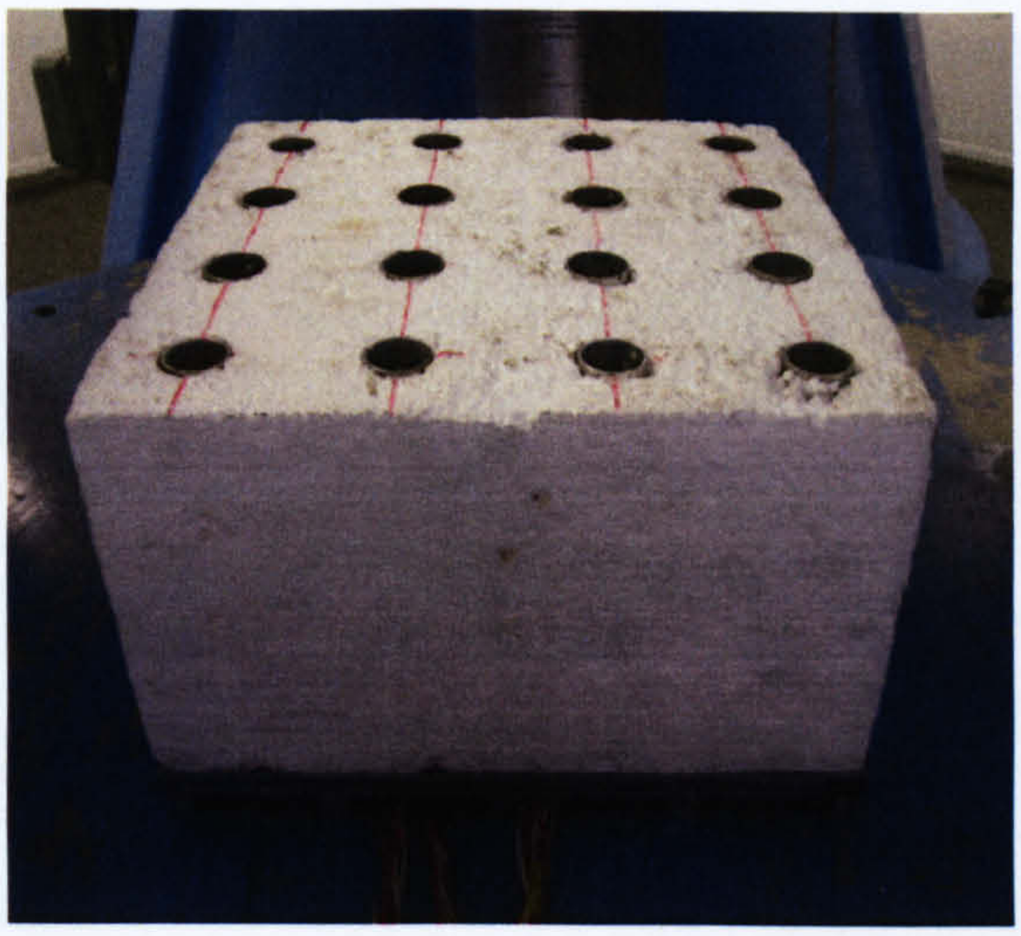

Figure 3.17 - Substructure (without pile caps)

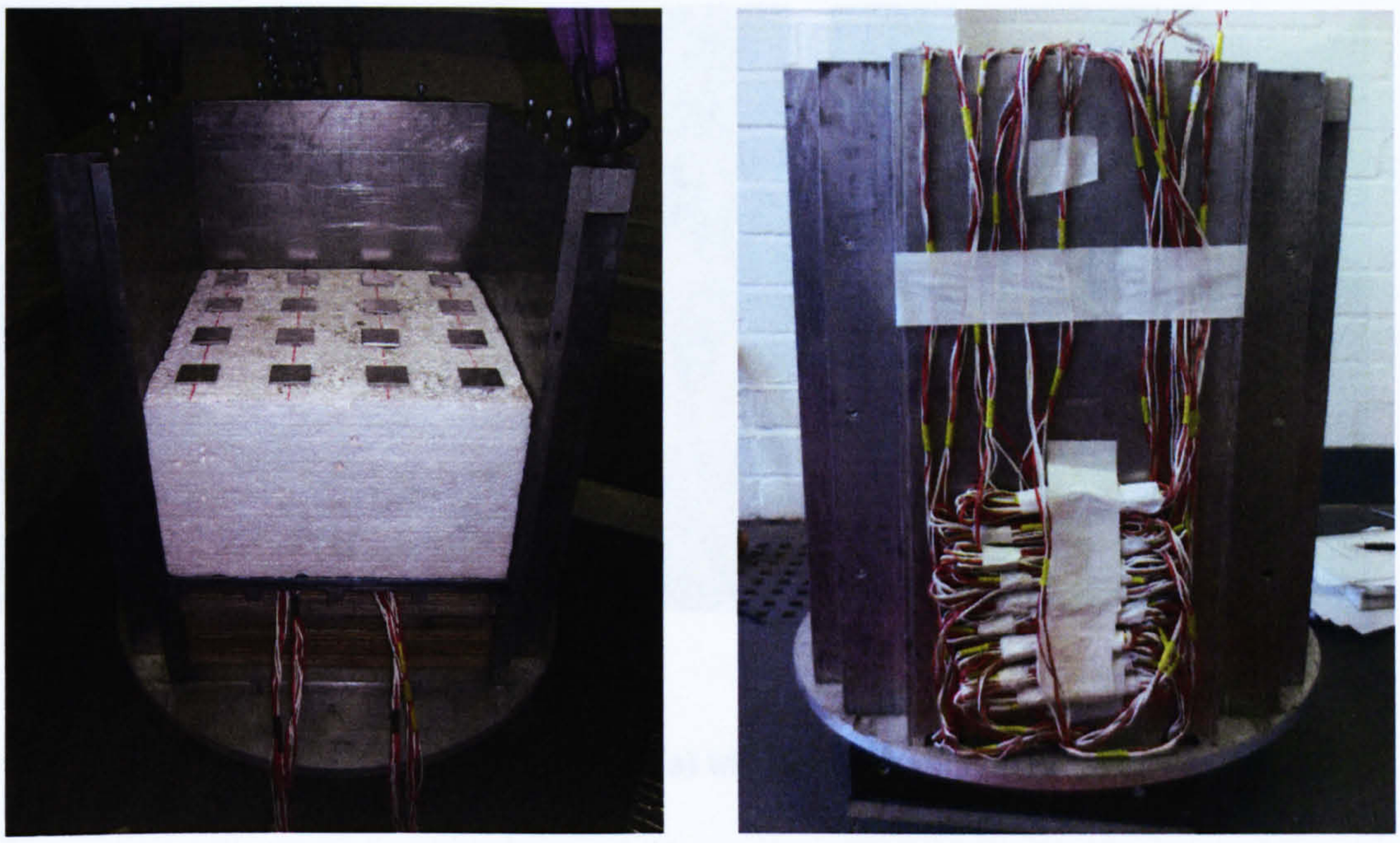

(a) (b)

Figure 3.18 - Model box: (a) containing substructure with pile caps, (b) cables from instrumented piles attached to the outside of the model box

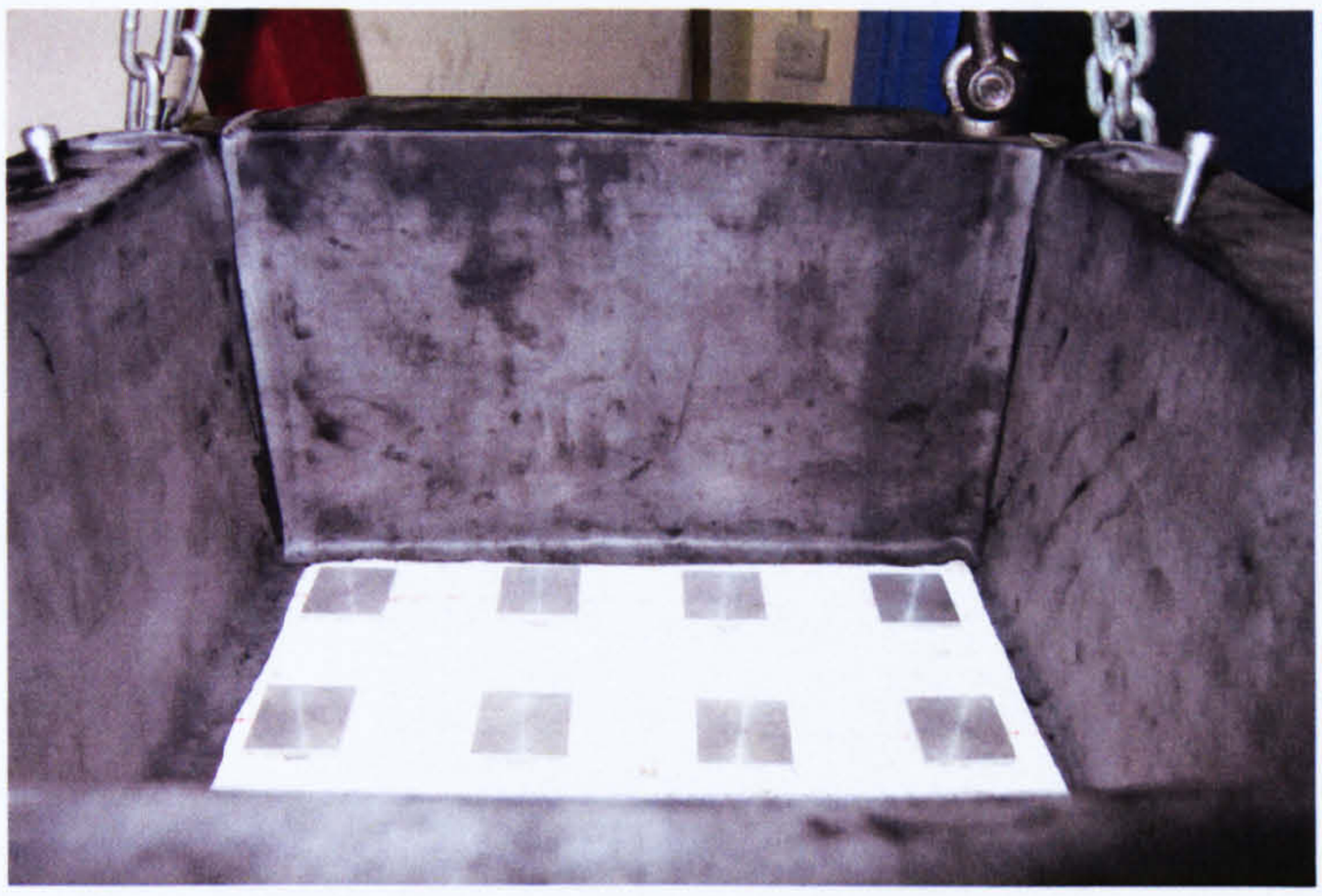

Figure 3.19 - Latex panels around the inside of the model box

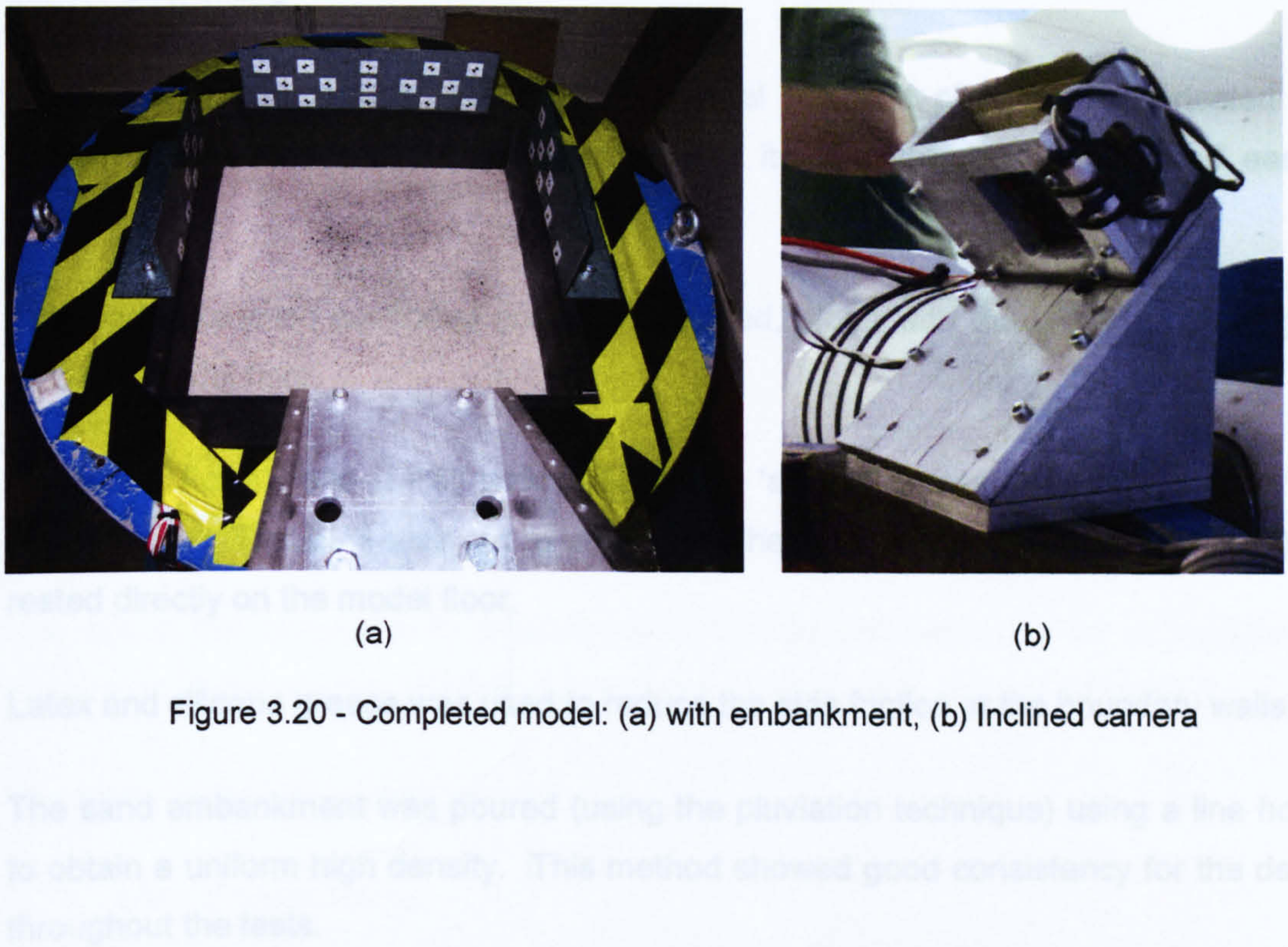

(a) (b)

Figure 3.20 - Completed model: (a) with embankment, (b) Inclined camera

3.7 Summary

All the major components, including the model box and piles, were fabricated from aluminium. Aluminium was used because of its relatively low density and ease of manufacture.

The load cells were calibrated and then installed, along with the uninstrumented piles, onto the model floor.

Expanded Polystyrene (EPS) was used as the 'subsoil' instead of soft clay due to its ease of use. The EPS was cut to shape and had holes drilled out (for the piles) and rested directly on the model floor.

Latex and silicone grease was used to reduce the side friction at the boundary walls.

The sand embankment was poured (using the pluviation technique) using a line hopper to obtain a uniform high density. This method showed good consistency for the density throughout the tests.

Images of the surface were used to assess the embankment surface settlement. The movement of 'patches' of soil were tracked using GeoPIV software, and other Matlab routines were used to translate image data to 'object space'. The photogrammetric technique performed very well as it effectively gave continuous settlement profiles for each g-level. Another advantage was that it is a non contact technique and so it did not interfere with the embankment surface.

The load cell data and settlement data was processed after the test.

CHAPTER 4

CENTRIFUGE TEST DATA - PILED EMBANKMENT EPS 70

4.1 Introduction

The aim of this chapter is to present the centrifuge test data, with some analysis and discussion of the results. Further discussion and analysis is given in Chapter 8.

The tests have been categorised as:

- piled embankments,
- piled embankment with 'working platform', and
- 'reinforced' piled embankments.

In the piled embankment tests, the pile caps are level with the top of the soft soil and the embankment layer rests directly on the top of the pile caps and the soft soil (Figure 4.1(a)). In the working platform tests, the embankment layer passes below the tops of the pile caps (Figure 4.1(b)). In fact the thickness of 'embankment' material below the pile caps represents a working platform from which the piles were constructed. However, since the embankment and working platform are likely to be similar material and the same material was used in the tests, no particular distinction is made. In the reinforced piled embankment tests, the embankment layer does not come into contact with the soft soil and its weight is transferred by the reinforcement onto the piles - there is a gap in between the soft soil and embankment layer (Figure 4.1(c)). Although this is unlikely to be the case in reality many design methods assume no support from the subsoil, and this approach is a reasonable starting point for assessing the effect of reinforcement.

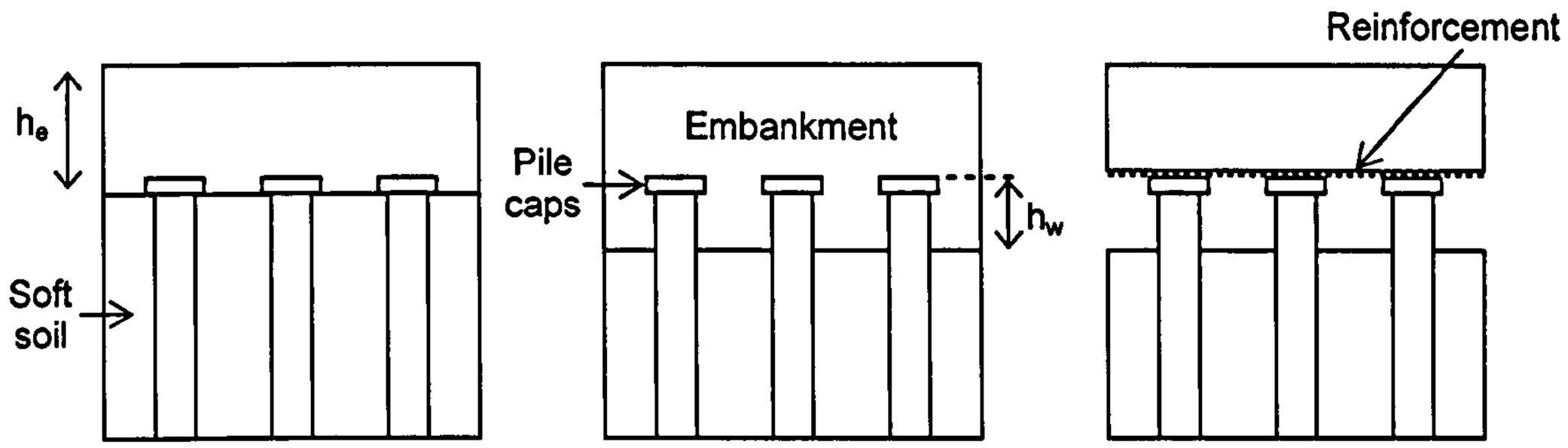

Figure 4.1 - Tests performed: (a) Piled embankment, (b) working platform, (c) reinforced piled embankment (3×3 pile group shown, not to scale)

The piled embankment tests have been further subcategorised depending on the stiffness of soft soil (EPS) used; EPS 70, presented in this chapter, and EPS 200 presented in Chapter 5.

The tests that will be considered here are shown in Table 4.1. The pile cap size, a, in all the tests is 30 mm. Two different pile spacings were used, and the tests are shown in ascending ratio of embankment thickness to pile spacing (h_e/s). The embankment height normalised by the clear spacing between pile caps $h_e/(s-a)$ is also shown.

Figure 4.2 shows an example of typical data for the load cells (from test RA21). All tests were taken up to 60g in 10g increments. Each g-level was maintained constant for typically 100-200 seconds, and the load cell data can be seen to be generally constant during these periods. Hence the plot shows 6 'steps' corresponding to the increase in g-level. 60g was reached at about 900 seconds, and following this the g-level was reduced in three 20g steps. However, the data from 'unloading' was not used. Figure 4.2 shows the load cell data 'zeroed' at the beginning of the test. This was done after the test by subtracting the initial voltage from subsequent data.

Figure 4.3(a) shows a typical 'surface plot' from test RA16, showing a 3-d view of the exaggerated deformed shape of the surface of the embankment derived from the PIV image data. The horizontal axes show plan location in the 300×300 mm model box, and the vertical axis shows 'differential settlement' relative to a nominal zero value. Note that

this is *not* absolute settlement (see discussion of processing of PIV data in Section 3.4.2). The plot shows 9 'humps', corresponding to 'imprints' of the pile caps at the surface of the embankment in red. Areas between the piles (in blue) have settled more.

Figure 4.3(b) shows a corresponding contour plot of differential settlement. The 3 × 3 grid of pile cap imprints is again clear in red/yellow. Figure 4.3(c) shows corresponding profiles along lines of constant Y. The profiles again show 3 clear maxima at the pile cap locations. The magnitude of the maxima is largest for profiles passing 'over' pile caps, but significantly smaller for profiles at locations between the pile caps. These profiles were used to manually assess the typical magnitude of differential settlement from the largest amplitude of variation. In this case a value of 1.0 mm was derived.

Test code	Embankment thickness, h_e (mm)	Pile spacing, s (mm)	h_e/s	$h_e/(s-a)$
RA07	50	100	0.5	0.7
RA15	60	100	0.6	0.9
RA16	70	100	0.7	1.0
RA17	80	100	0.8	1.1
RA18	90	100	0.9	1.3
RA19	100	100	1.0	1.4
RA06	75	75	1.0	1.7
RA20	100	75	1.3	2.2
RA21	120	75	1.6	2.7
RA22	140	75	1.9	3.1
RA23	160	75	2.1	3.6

(N.b. 1g values are presented)

Table 4.1 - Summary of EPS 70 piled embankment test series

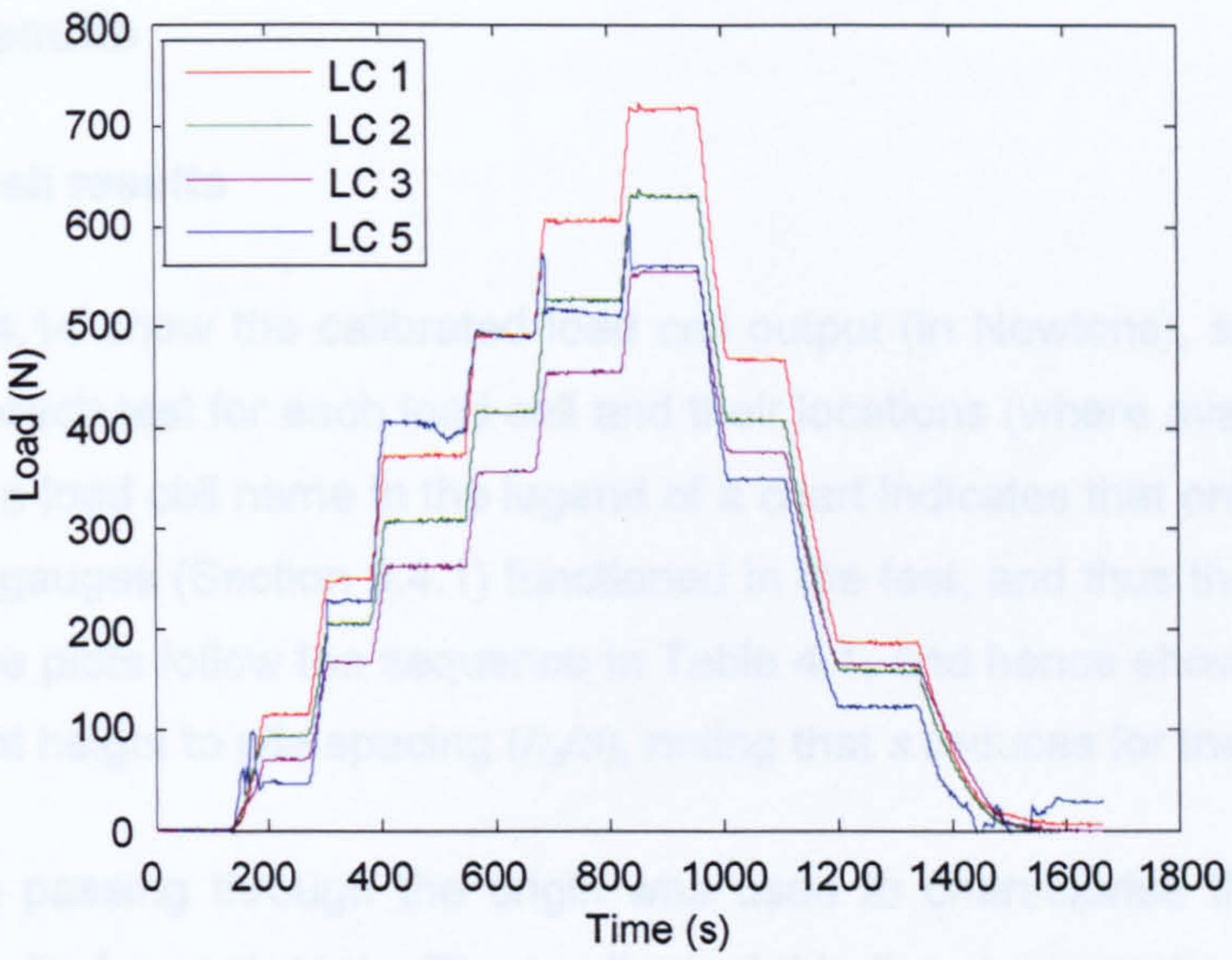

Figure 4.2 - Example of load data

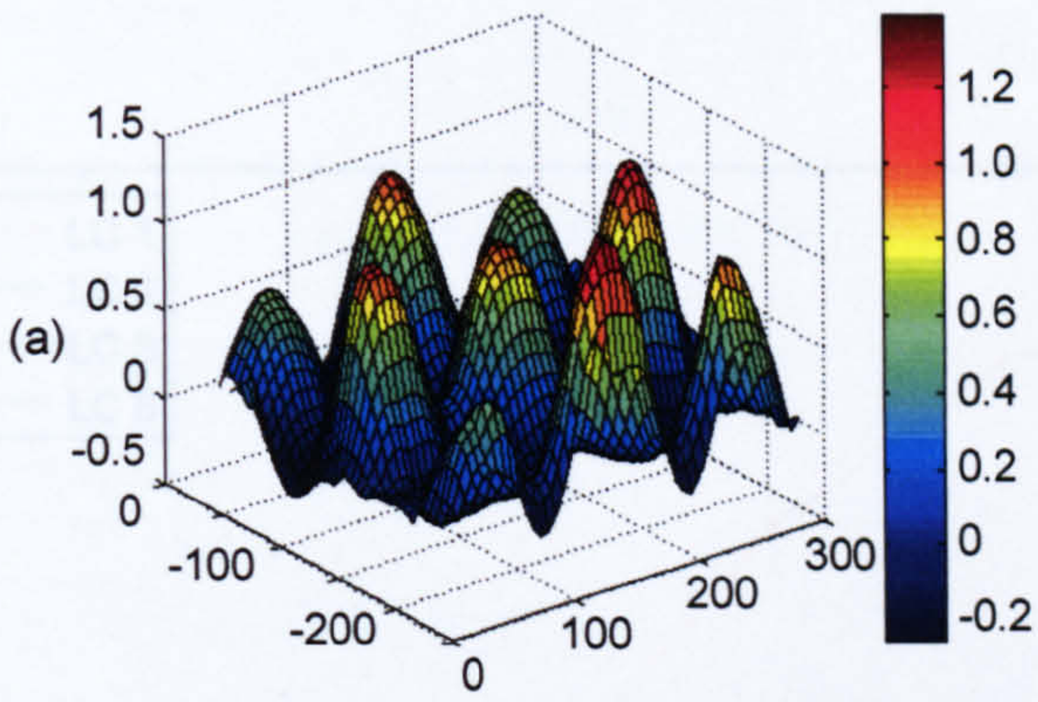

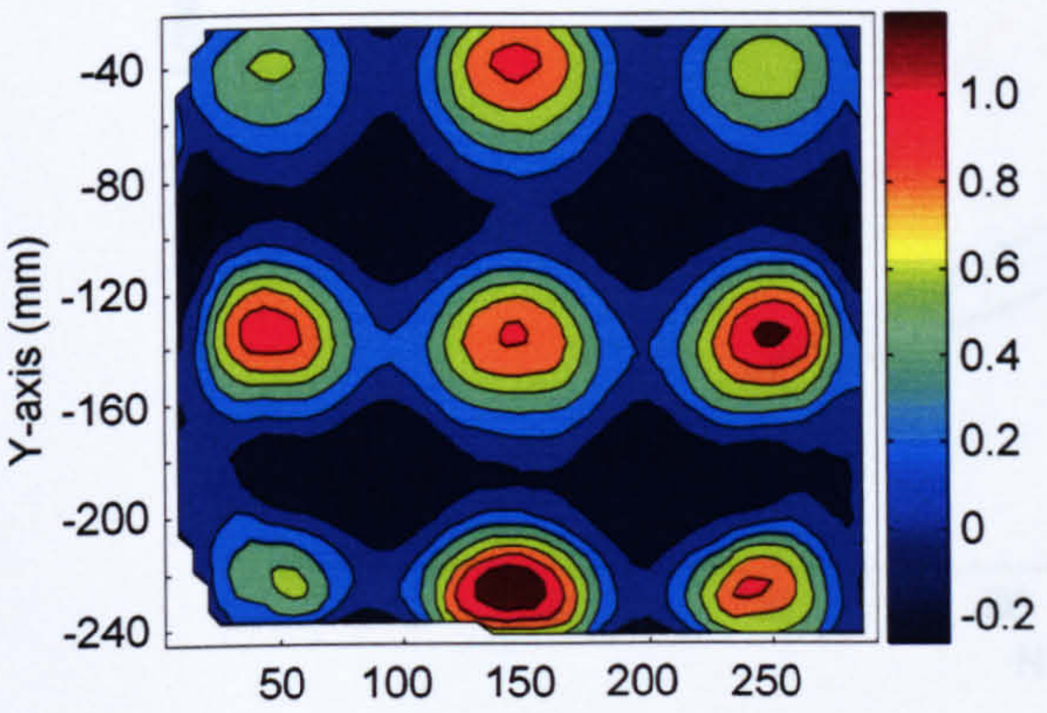

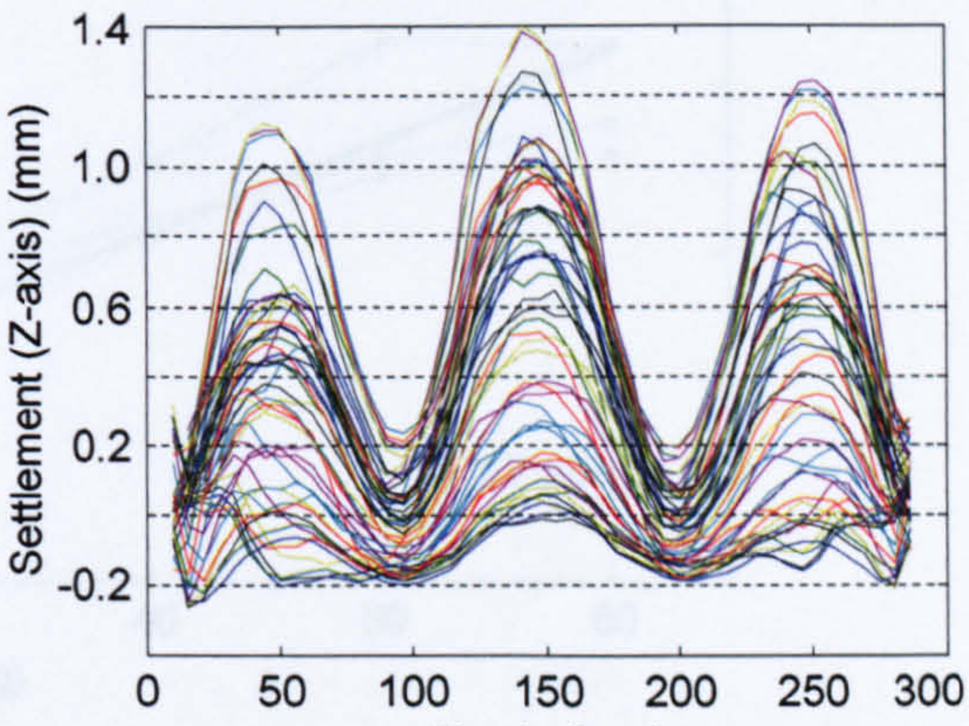

Figure 4.3 - Example of settlement data: (a) 'sin' plot,
(b) contour plot, (c) surface plot

4.2 Test results

4.2.1 Load cell results

Figures 4.4 - 4.14 show the calibrated load cell output (in Newtons), showing increase with g-level in each test for each load cell and their locations (where available). The use of '*' following a load cell name in the legend of a chart indicates that only one of the two pairs of strain gauges (Section 3.4.1) functioned in the test, and thus the results may be unreliable. The plots follow the sequence in Table 4.1, and hence show increasing ratio of embankment height to pile spacing (h_e/s), noting that s reduces for the later tests.

A straight line passing through the origin was used to characterise the results of the various load cells for each test. The gradient of this line, representing the increase in measured load per g level (N/g), is shown in the bottom right hand corner of each graph.

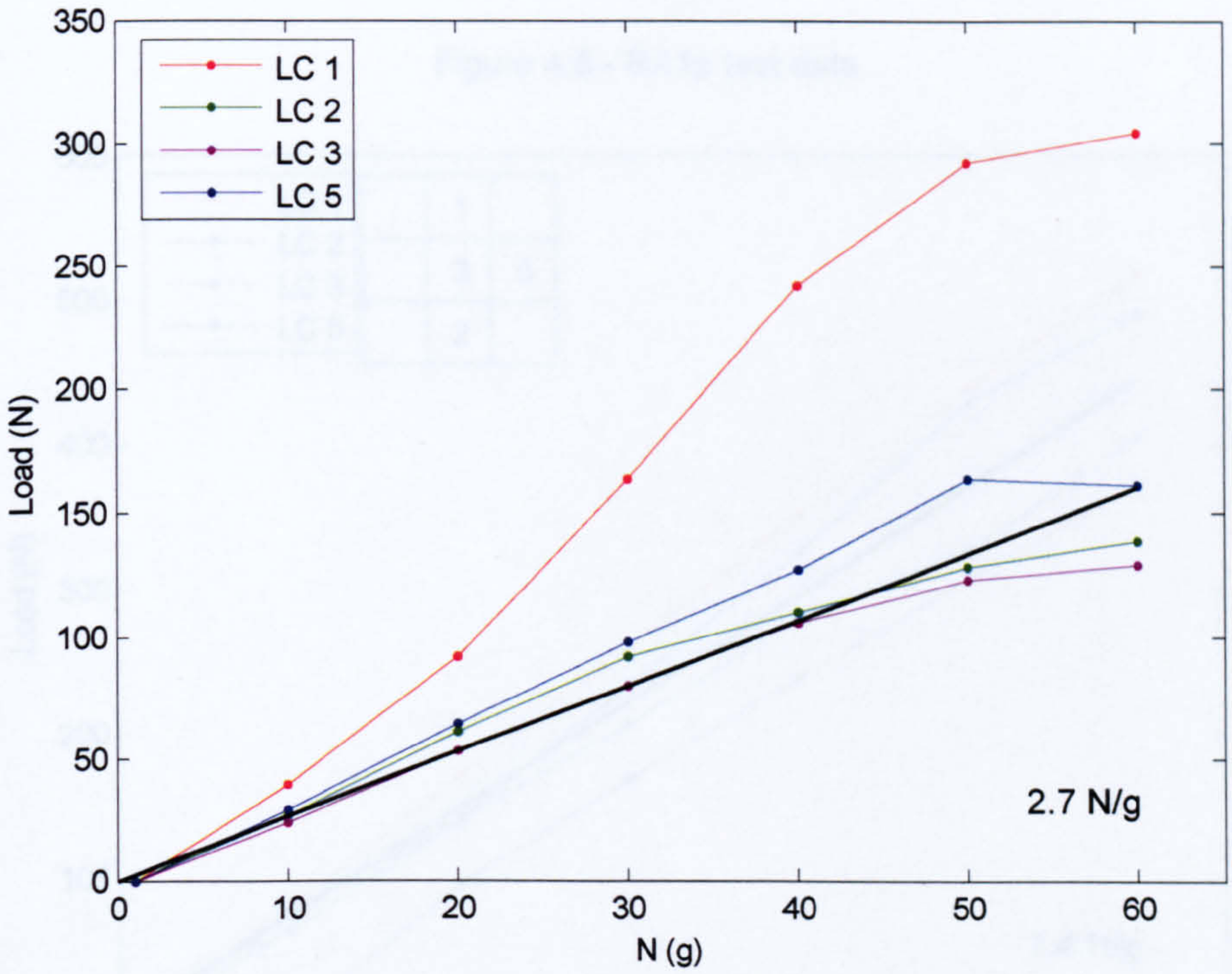

Figure 4.4 - RA07 test data

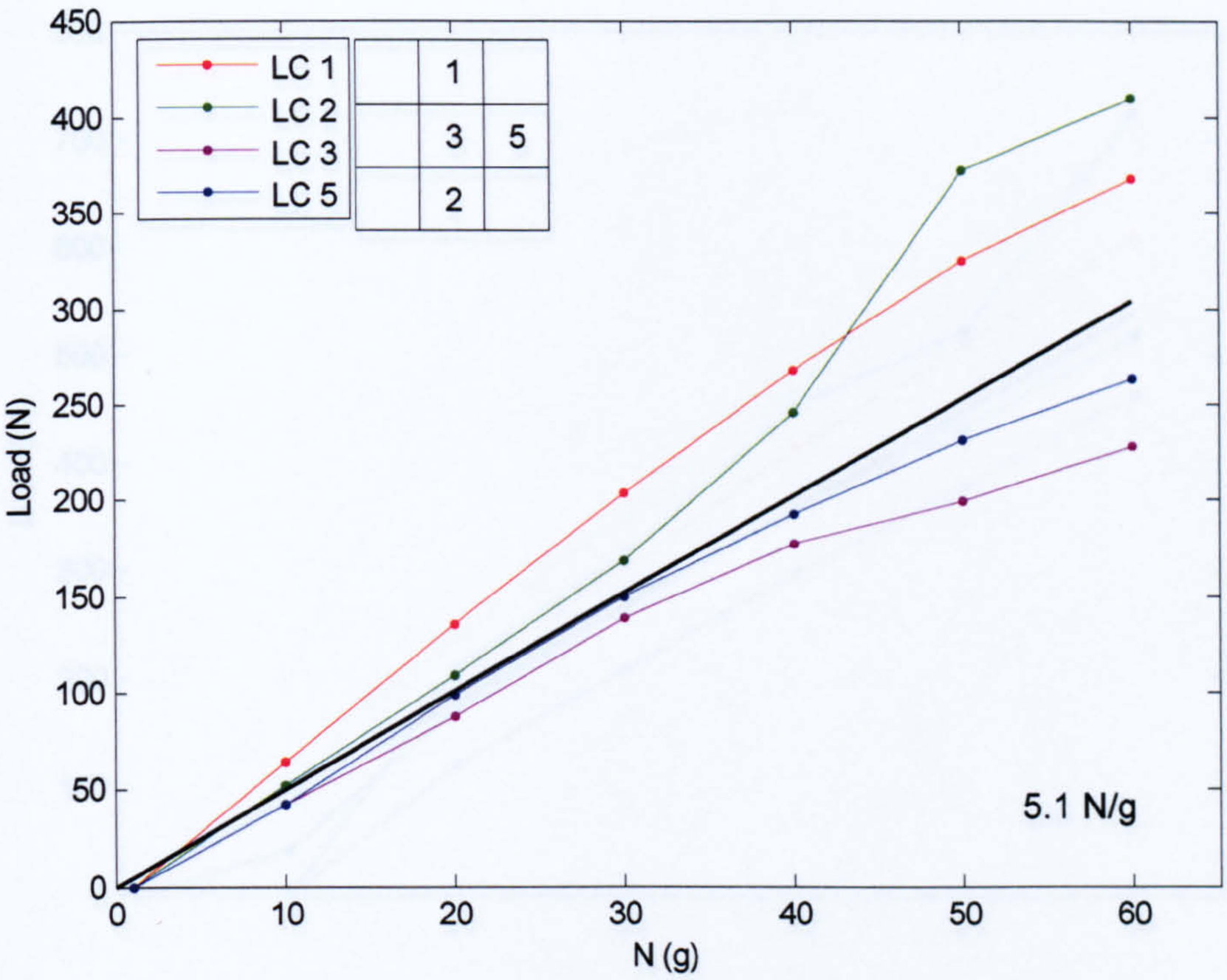

Figure 4.5 - RA15 test data

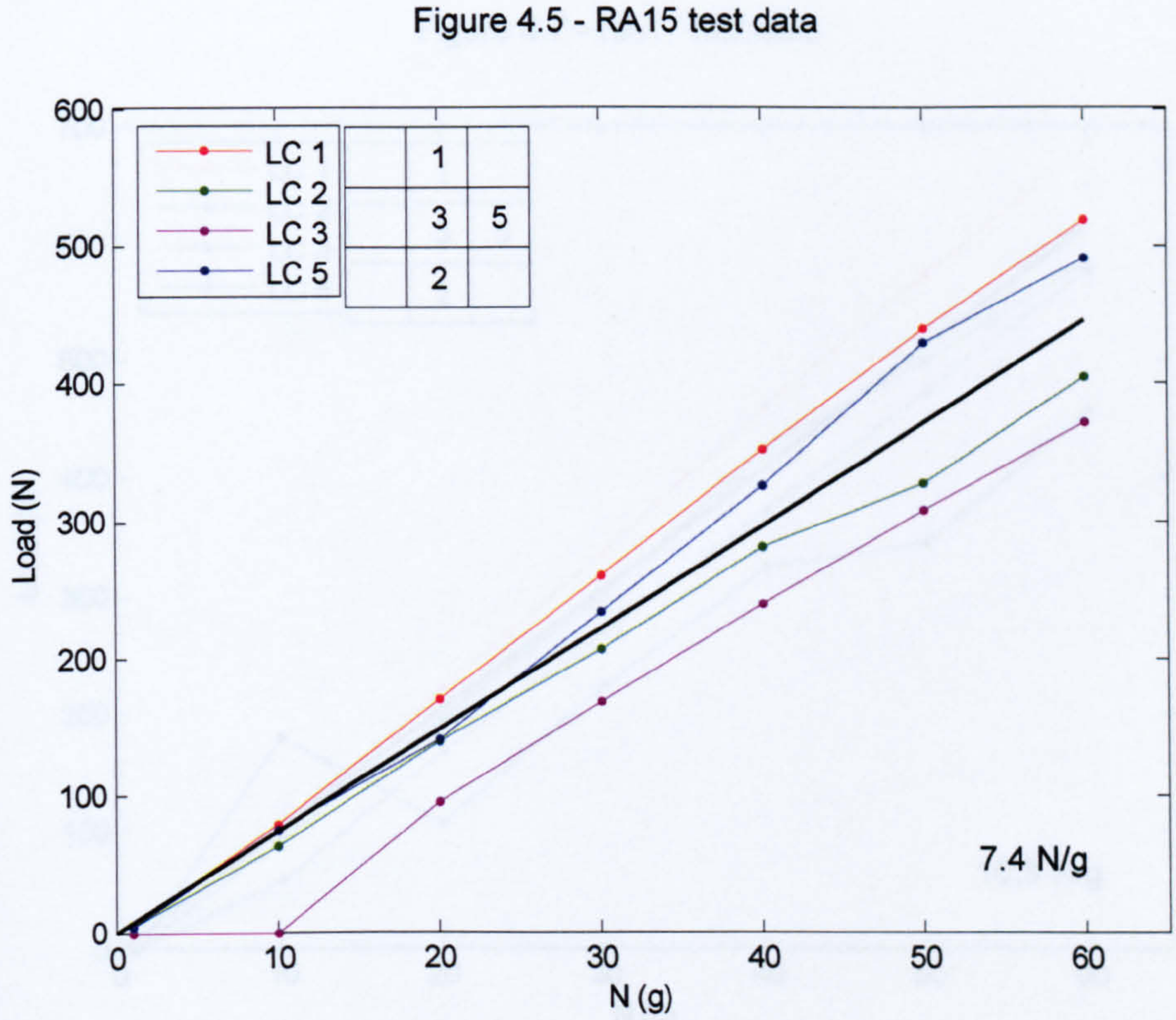

Figure 4.6 - RA16 test data

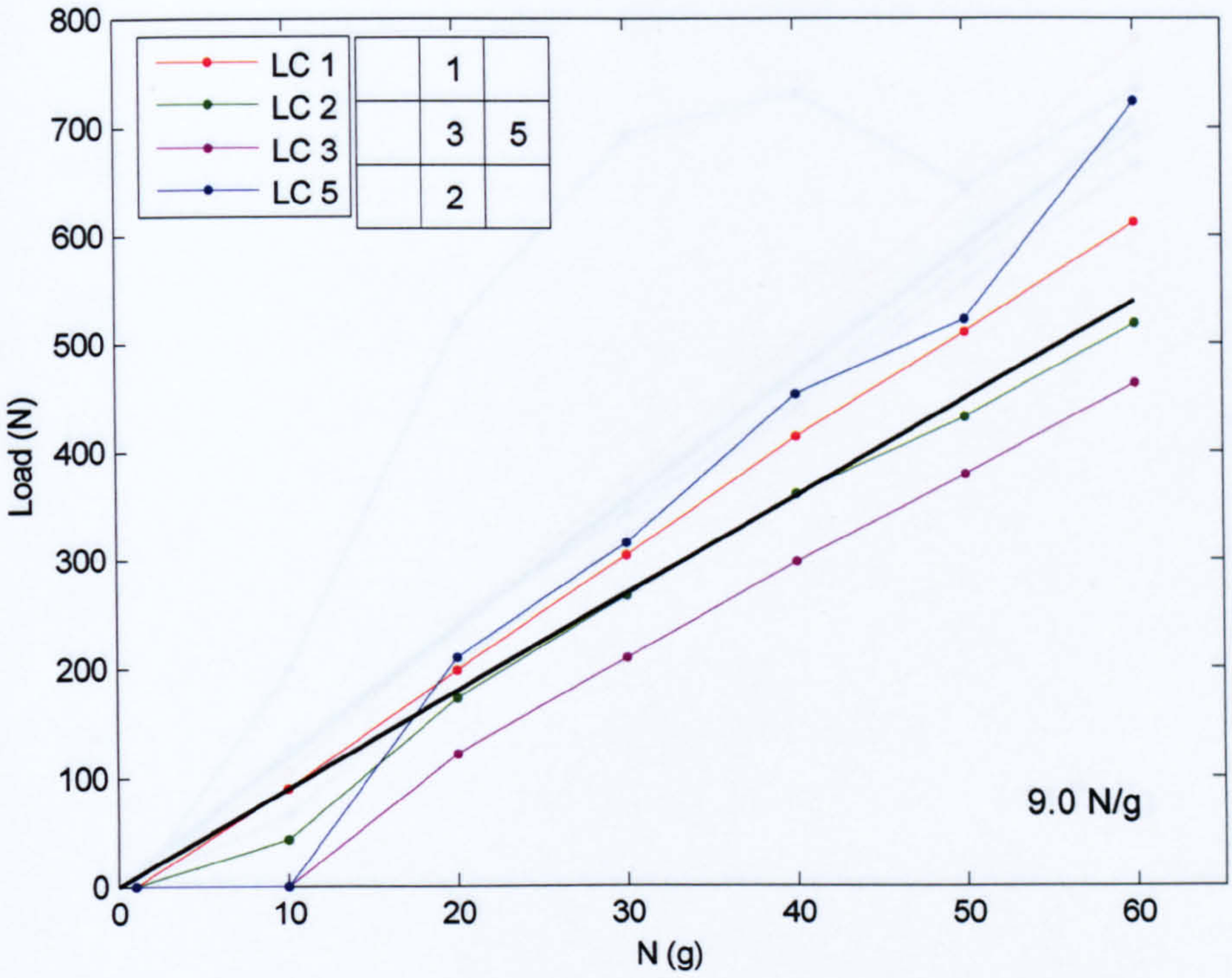

Figure 4.7 - RA17 test data

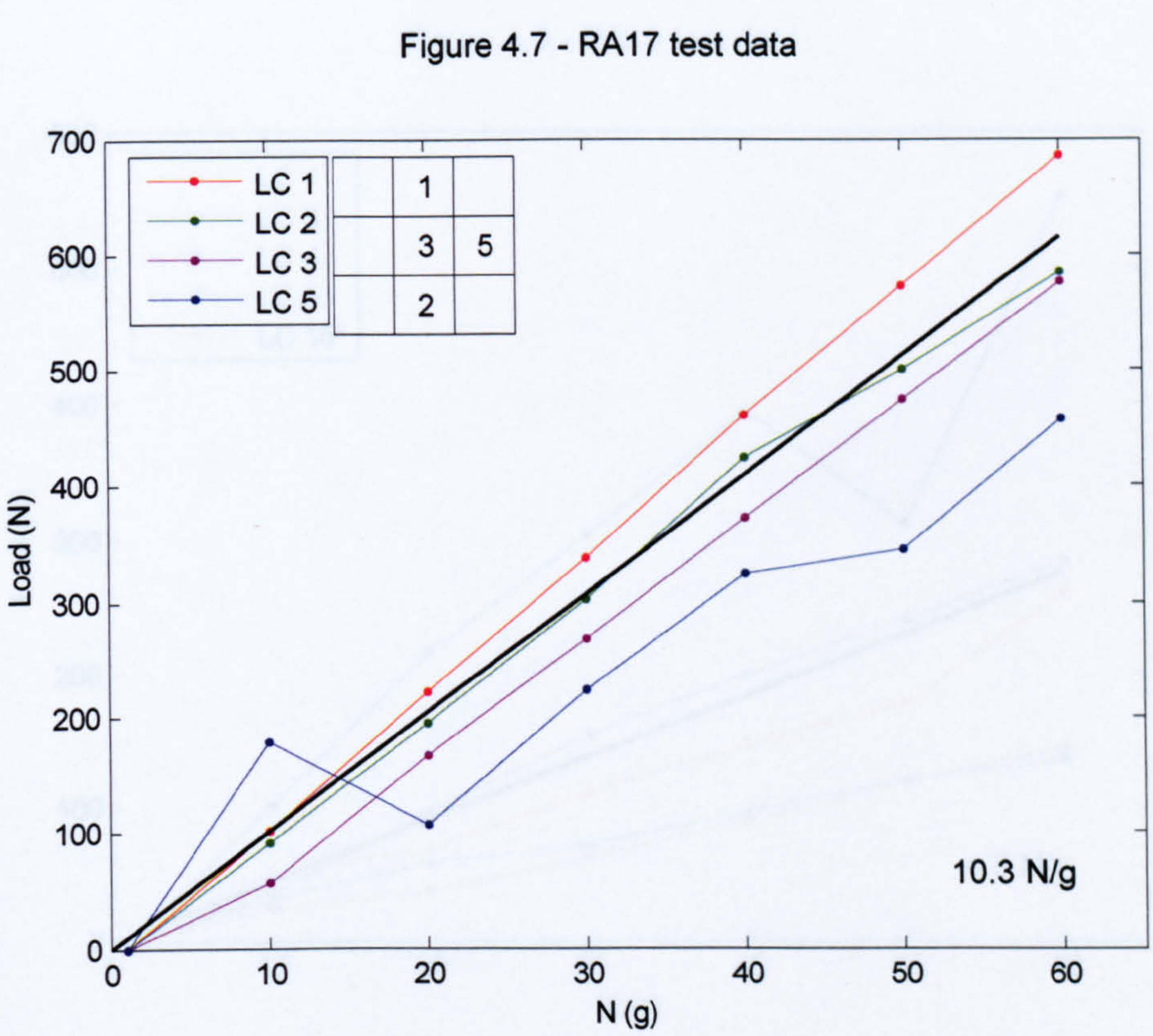

Figure 4.8 - RA18 test data

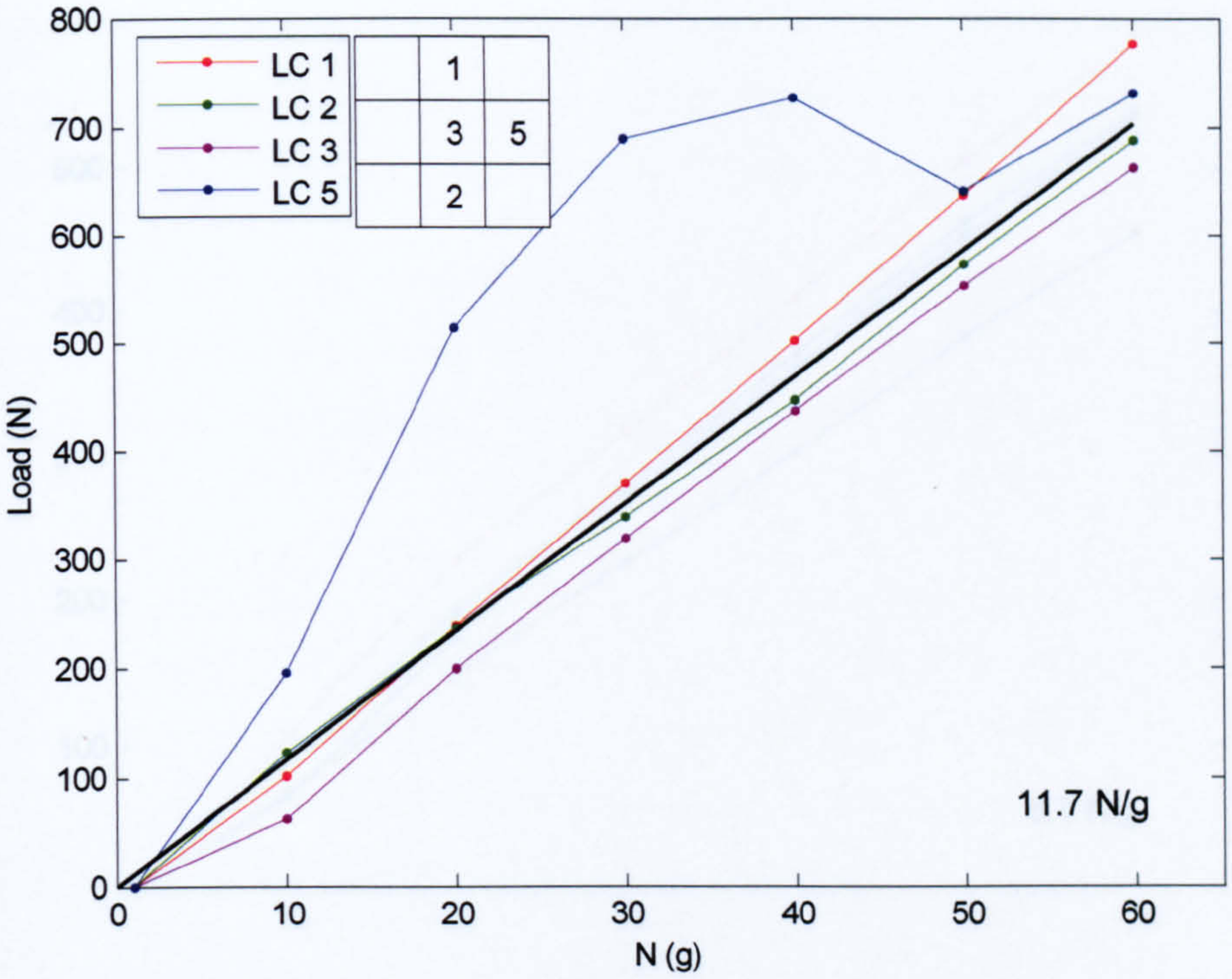

Figure 4.9 - RA19 test data

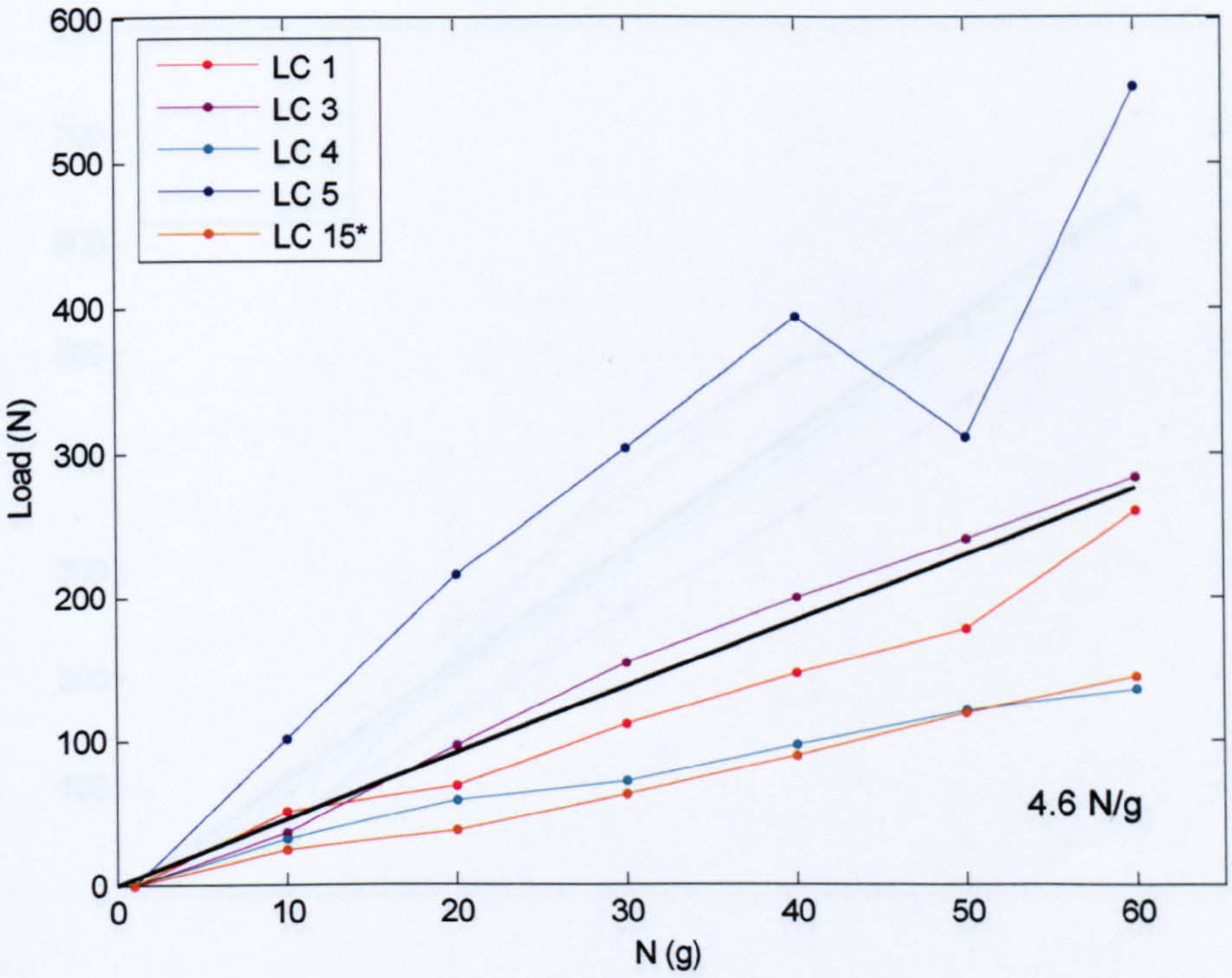

Figure 4.10 - RA06 test data

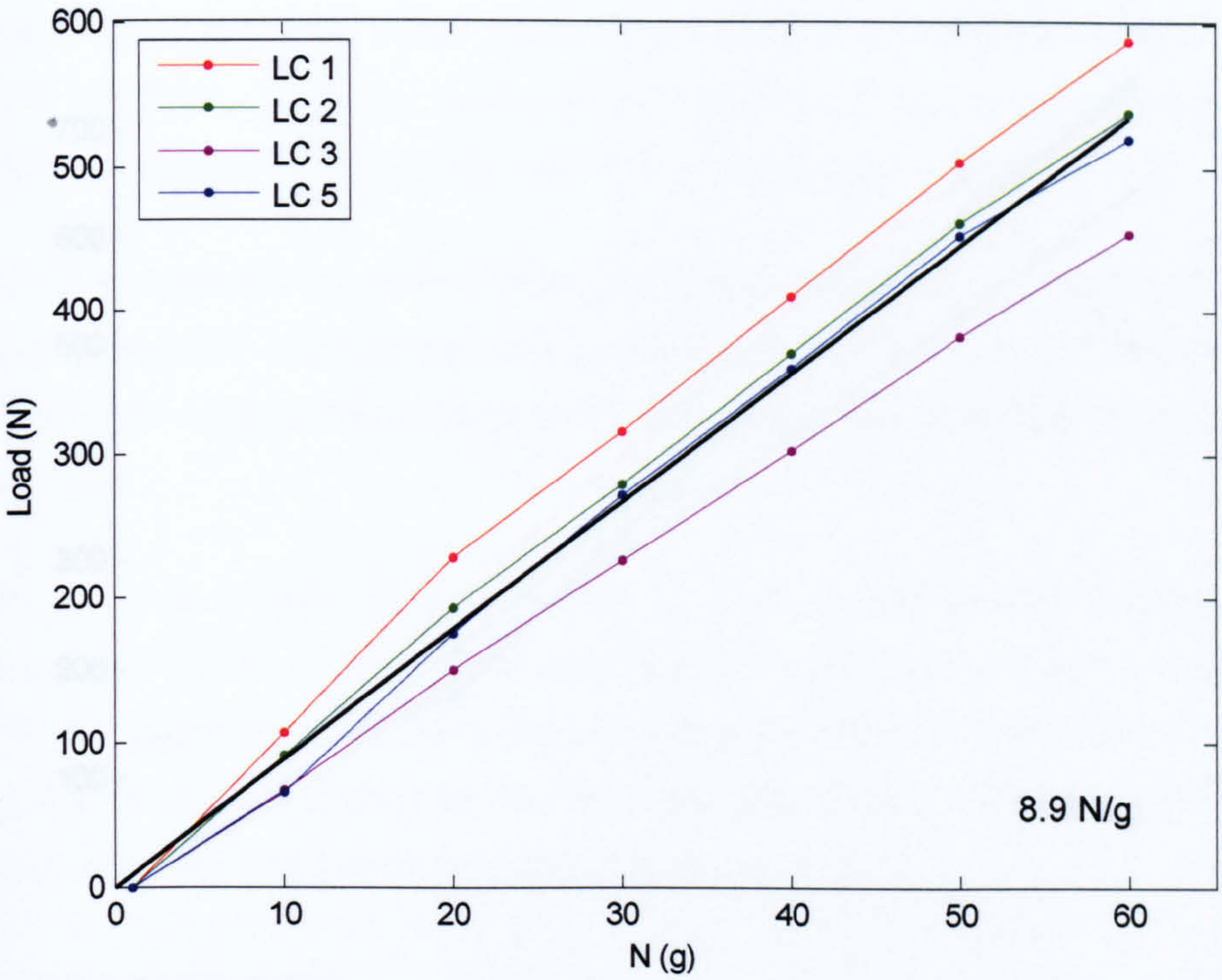

Figure 4.11 - RA20 test data

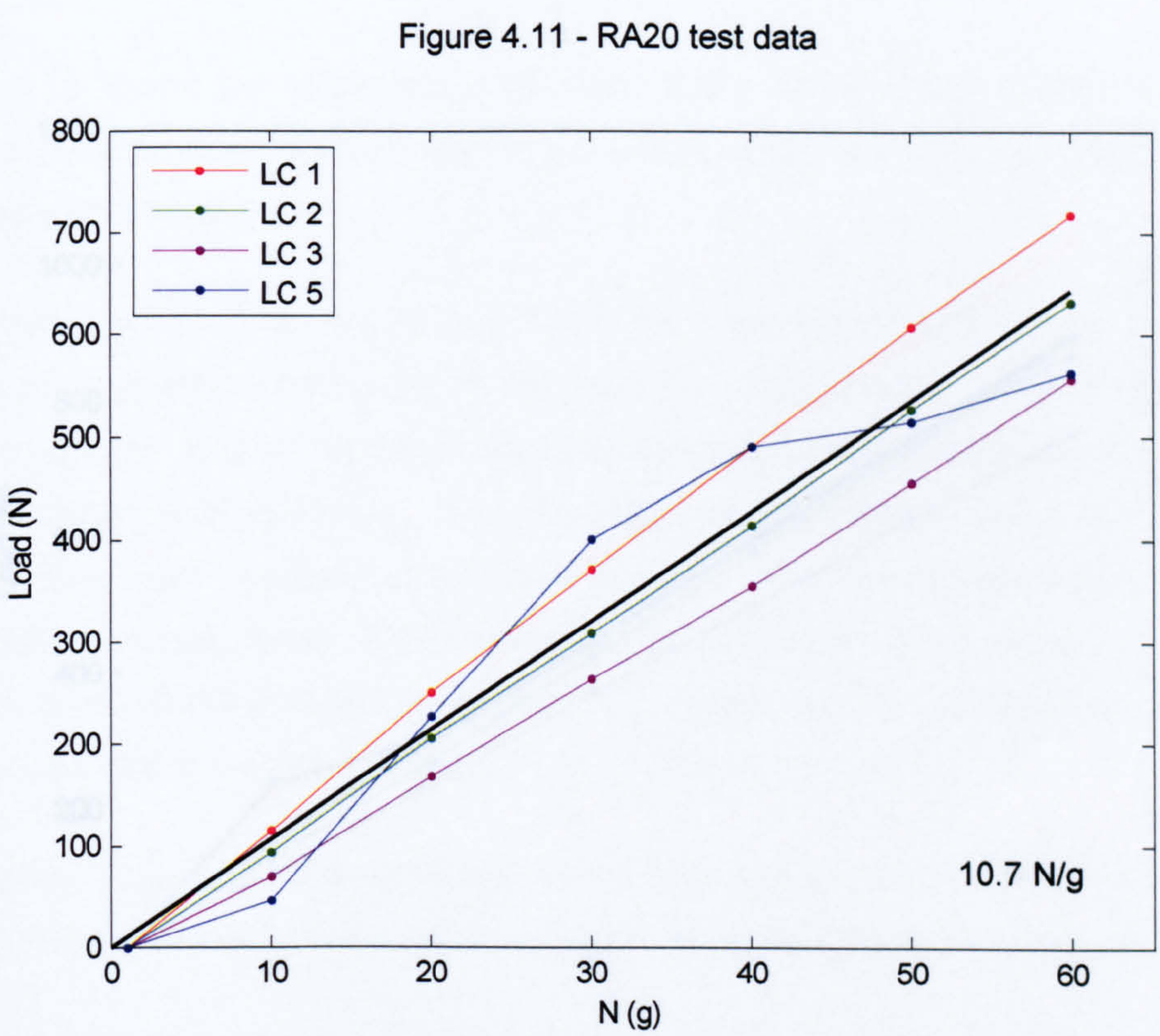

Figure 4.12 - RA21 test data

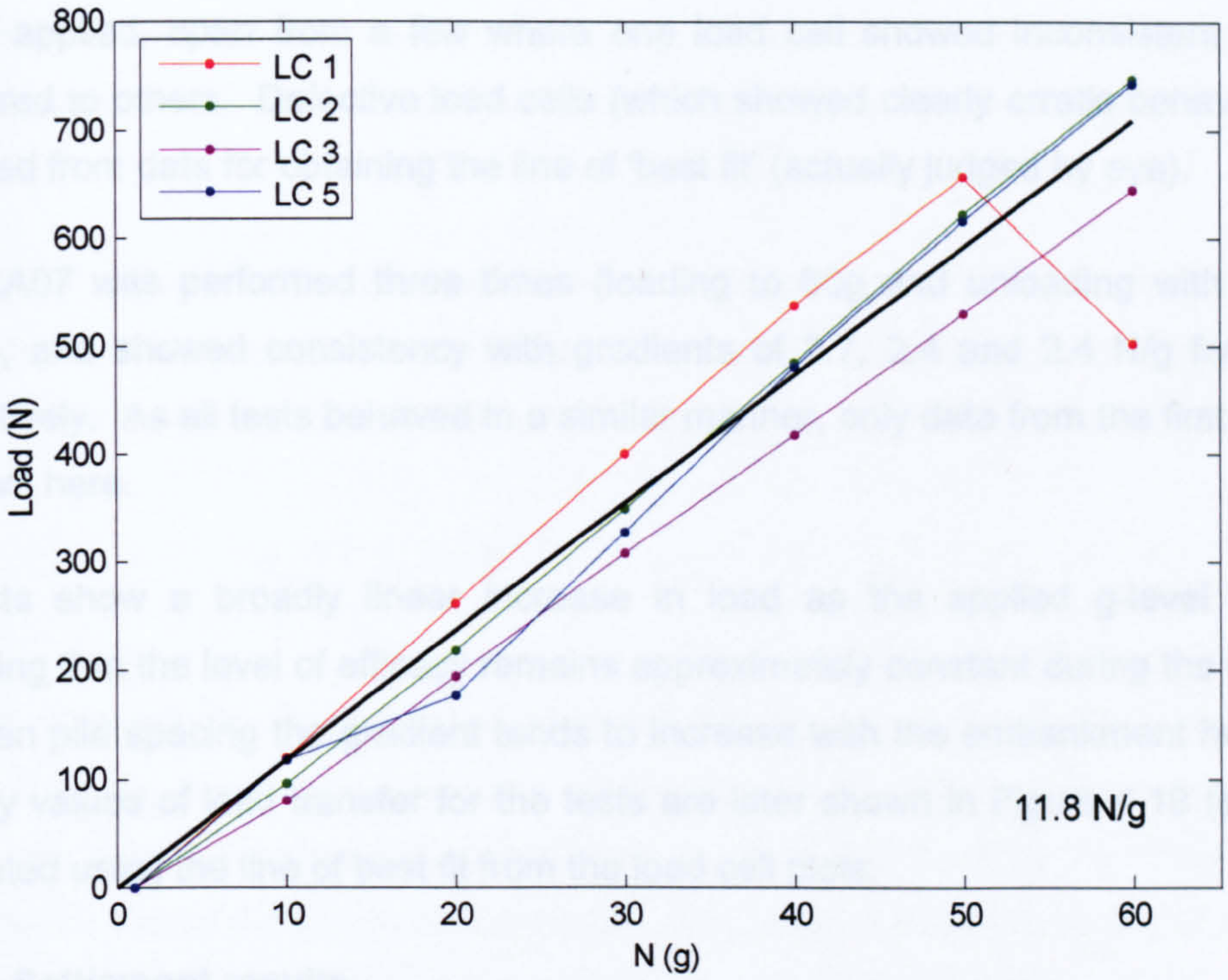

Figure 4.13 - RA22 test data

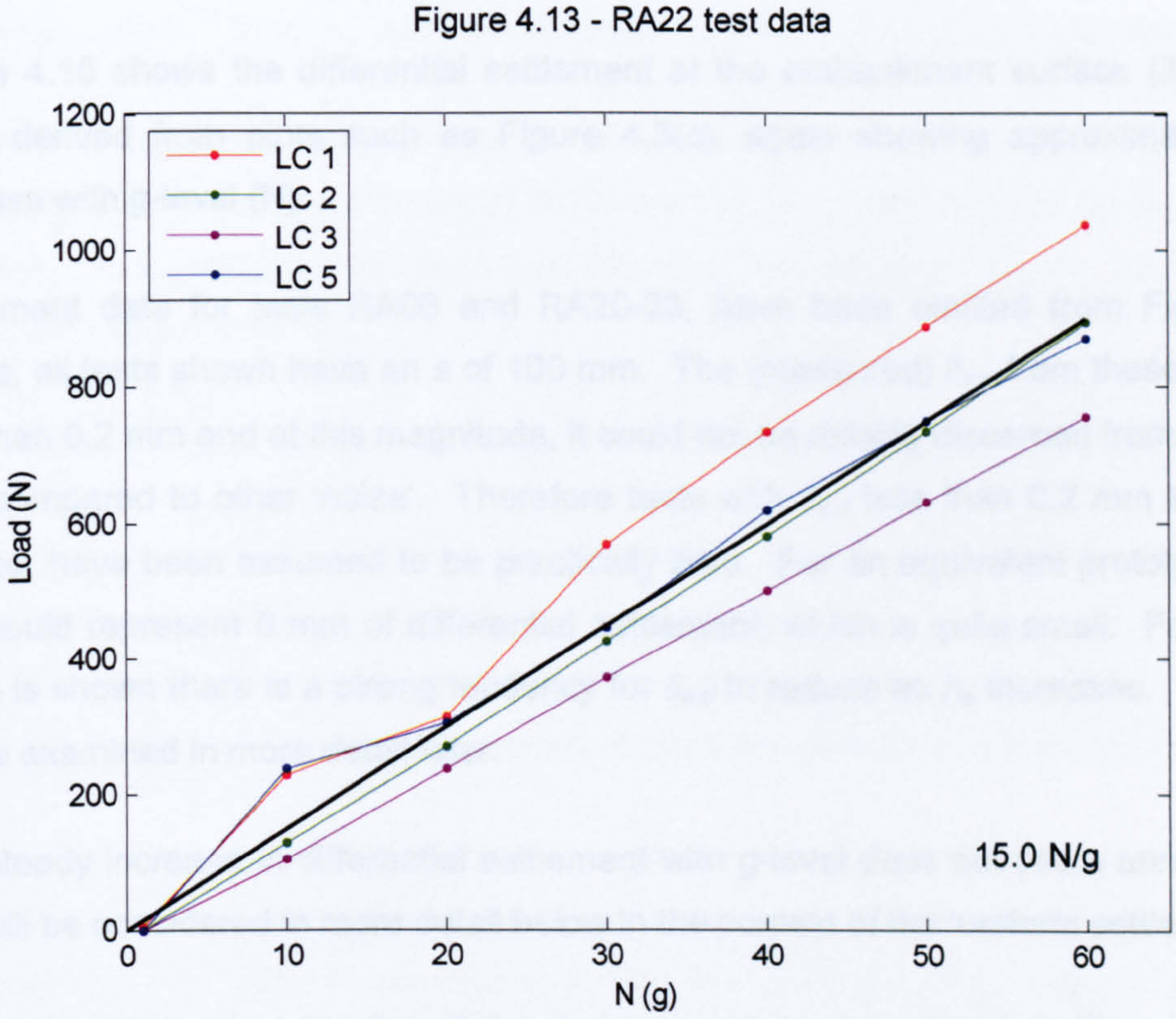

Figure 4.14 - RA23 test data

In general, all tests showed a broadly consistent load cell response to the increased g-level applied, apart from a few where one load cell showed inconsistent behaviour compared to others. Defective load cells (which showed clearly erratic behaviour) were excluded from data for obtaining the line of 'best fit' (actually judged by eye).

Test RA07 was performed three times (loading to 60g and unloading with the same model), and showed consistency with gradients of 2.7, 2.4 and 2.4 N/g for the tests respectively. As all tests behaved in a similar manner, only data from the first test RA07 is shown here.

All tests show a broadly linear increase in load as the applied g-level increases, indicating that the level of efficacy remains approximately constant during the test. Also, for given pile spacing the gradient tends to increase with the embankment height. The efficacy values of load transfer for the tests are later shown in Figure 4.19 (a), and are calculated using the line of best fit from the load cell plots.

4.2.2 Settlement results

Figure 4.15 shows the differential settlement at the embankment surface ($\delta_{e,d}$) for the tests, derived from plots such as Figure 4.3(c), again showing approximately linear increase with g-level (N).

Settlement data for tests RA06 and RA20-23, have been omitted from Figure 4.15. Hence, all tests shown have an s of 100 mm. The (measured) $\delta_{e,d}$ from these tests was less than 0.2 mm and at this magnitude, it could not be reliably discerned from the image data compared to other 'noise'. Therefore tests with $\delta_{e,d}$ less than 0.2 mm at 30g and beyond, have been assumed to be practically zero. For an equivalent prototype at 30g this would represent 6 mm of differential settlement, which is quite small. For the data which is shown there is a strong tendency for $\delta_{e,d}$ to reduce as h_e increases. This effect will be examined in more detail later.

The steady increase in differential settlement with g-level does not seem unreasonable, and will be considered in more detail below in the context of the 'uniform settlement'.

'Uniform' settlement at the top of the embankment ($\delta_{e,u}$) is shown in Figure 4.16. As described in Section 3.4.2 (processing of PIV data) a smooth 'surface' was subtracted

from the raw settlement data to give the arbitrary origin in Figure 4.3(c), and allow differential movement to be seen more clearly in isolation. The uniform settlement is the average value of this surface, which increases steadily in value with g-level throughout all tests.

Figure 4.17 schematically indicates the relationship between $\delta_{e,u}$, $\delta_{e,d}$ and $\delta_{e,c}$ (settlement at the embankment surface immediately above a pile cap - the minimum settlement of the deformed surface). As indicated on the Figure

$$\delta_{e,c} + \delta_{e,d} / 2 \quad < \quad \delta_{e,u} \quad < \quad \delta_{e,c} + \delta_{e,d} \qquad \text{Eqn. 4.1}$$

The 2-d schematic illustrates a profile passing directly over a row of pile caps. However, the peaks only occur over pile caps which occupy 10 -15 % of the total plan area. Hence the 'average' settlement representing $\delta_{e,u}$ is biased towards the troughs. This is illustrated in Figure 4.3(c) where subtraction of $\delta_{e,u}$ has caused the 'arbitrary' origin to lie considerably nearer the base of the troughs than the highest peaks (which are directly above pile caps). The lower 'peaks' are directly between pile caps but not over them.

Referring to Figures 4.15 and 4.16, it can be seen that for the lowest embankments where there is very large differential settlement ($\delta_{e,d}/\delta_{e,u}$) has a value up to about 0.7. However, as $\delta_{e,d}$ reduces this ratio also reduces, and generally $\delta_{e,u} \approx$ 1-2 mm and is significantly larger than $\delta_{e,d}$.

The uniform settlement would arise from a number of components, potentially including:

- Nett compression through the thickness of the embankment itself due to increasing self-weight (gravity level) during the test,
- Other vertical strain in the embankment due to the effects of arching,
- Settlement at the base of the embankment (the embankment-subsoil interface).

The first effect can be estimated from the average increase in vertical stress through the thickness of the embankment, and an appropriate secant one-dimensional stiffness. For a typical 100 mm thick embankment at 60g the corresponding nominal overburden stress at mid-depth (an approximate average) is about 50 kN/m^2. For the dense

granular material the stiffness might be of the order 1000 times larger than this value, and the corresponding settlement at the surface would then be of the order 0.1 mm. This is a crude estimate, but it indicates that this contribution may not be that large. Referring to Figure 4.16, it appears that in general $\delta_{e,u}$ tends to reduce as h_e increases for given s, which is not the trend which would be expected if this effect dominated the behaviour.

Referring to Figure 4.18, compressive stress will occur above the pile caps, and tensile stress beneath the arch, corresponding to increase and reduction in vertical stress respectively. It will be assumed that the pile caps do not settle significantly, and this is confirmed by calculated axial deformation of approximately 0.01 mm at typical loading. Thus $\delta_{e,u}$ could be assumed to arise primarily from the compressive strain above the pile cap, but it also seems likely that settlement of the subsoil (δ_s) will tend to increase $\delta_{e,u}$. In fact the two effects will be linked since as the subsoil settles, more load will be transferred to the pile caps, and hence compressive strain in the soil above them will increase.

Apart from the general increase in $\delta_{e,u}$ with g-level, the following trends are evident from Figure 4.16:

- Higher s leads to higher $\delta_{e,u}$,
- For given s, $\delta_{e,u}$ tends to reduce as h_e increases.

The first observation would be consistent with the hypothesis that compressive stress above the pile caps (Figure 4.18) tends to increase as the area ratio $(a/s)^2$ reduces, since the embankment load carried by the pile caps is concentrated on a smaller proportion of the total area. The second observation could be related to the tendency for arching to 'break down' and $\delta_{e,d}$ to increase at low h_e. Certainly this is the case for very low h_e, where it has already been noted that $\delta_{e,d}$ contributes significantly to $\delta_{e,u}$, whereas $\delta_{e,d}$ is much smaller than $\delta_{e,u}$ at larger h_e.

It seems reasonable that both $\delta_{e,u}$ and $\delta_{e,d}$ should increase with g-level, since the underlying strains and subsoil settlement (Figure 4.18) will all increase as stress in the model increases, even though it has already been noted that efficacy does not vary significantly with g-level in the tests.

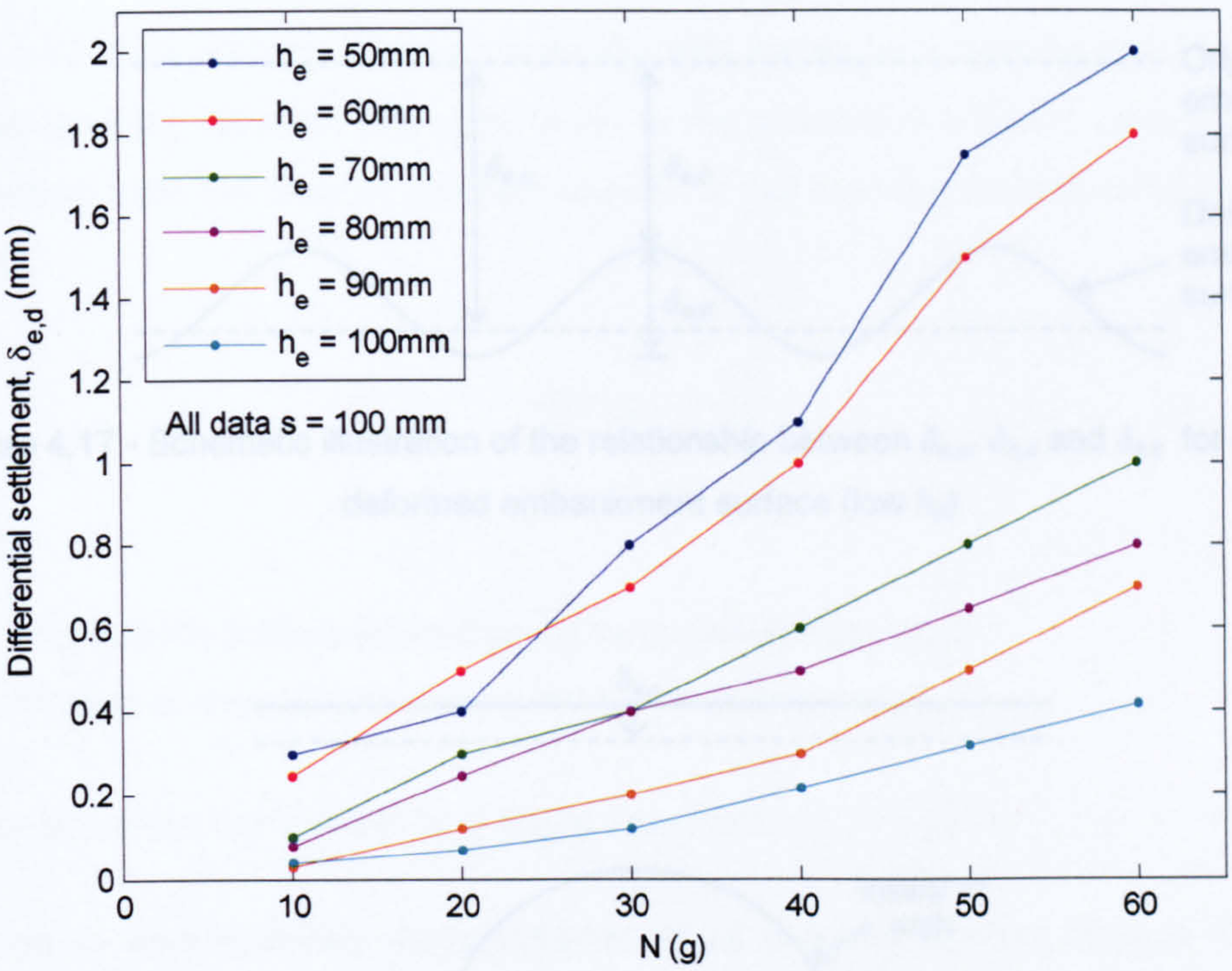

Figure 4.15 - Differential settlement at the embankment surface, $\delta_{e,d}$

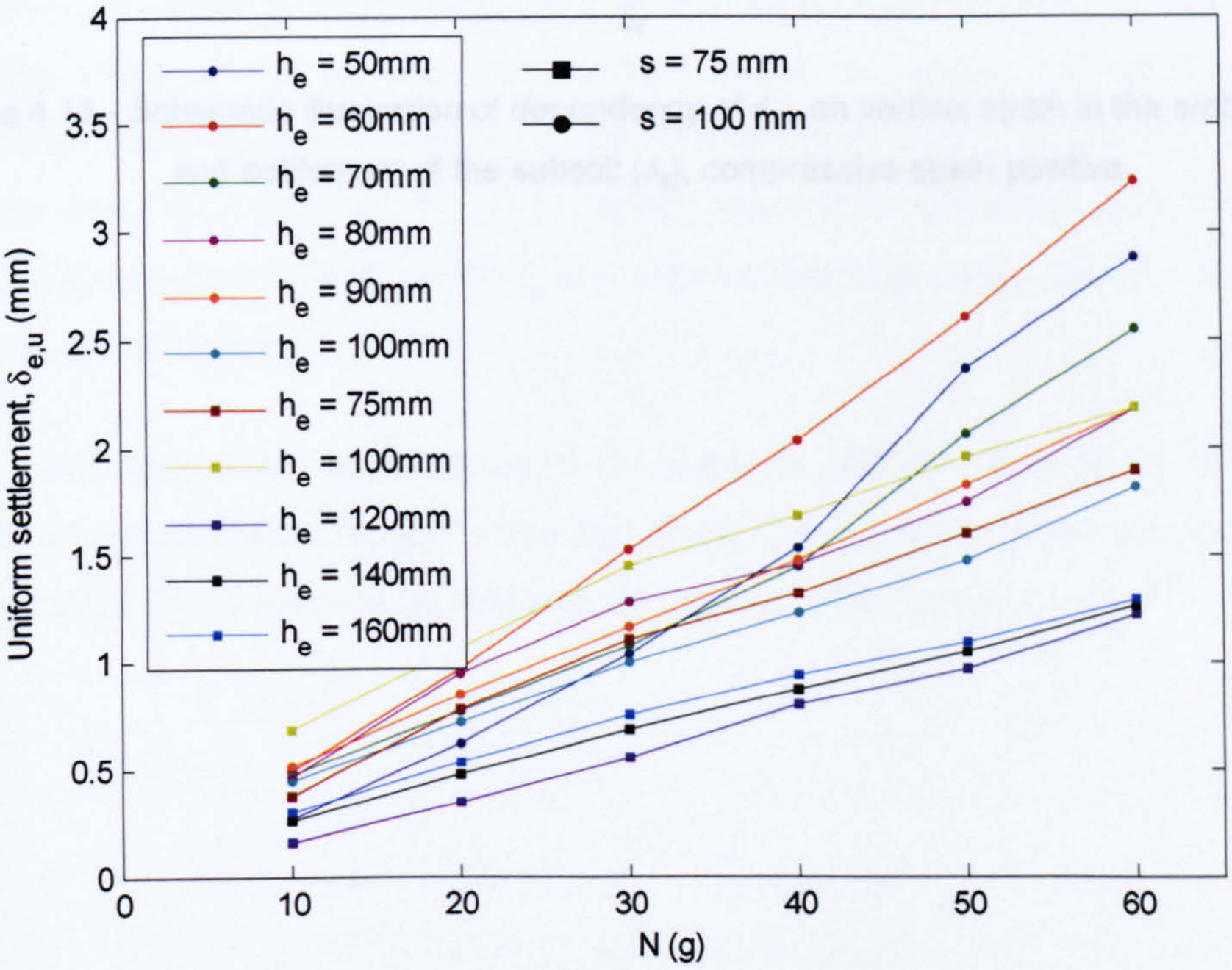

Figure 4.16 - Uniform settlement at the embankment surface, $\delta_{e,u}$

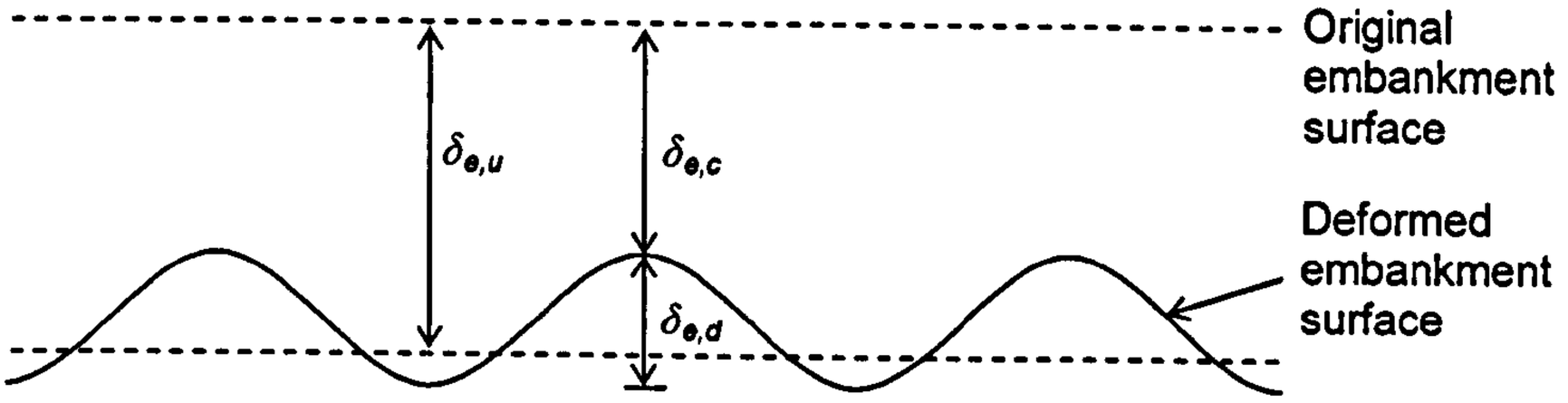

Figure 4.17 - Schematic illustration of the relationship between $\delta_{e,u}$, $\delta_{e,d}$ and $\delta_{e,c}$ for a typical deformed embankment surface (low h_e)

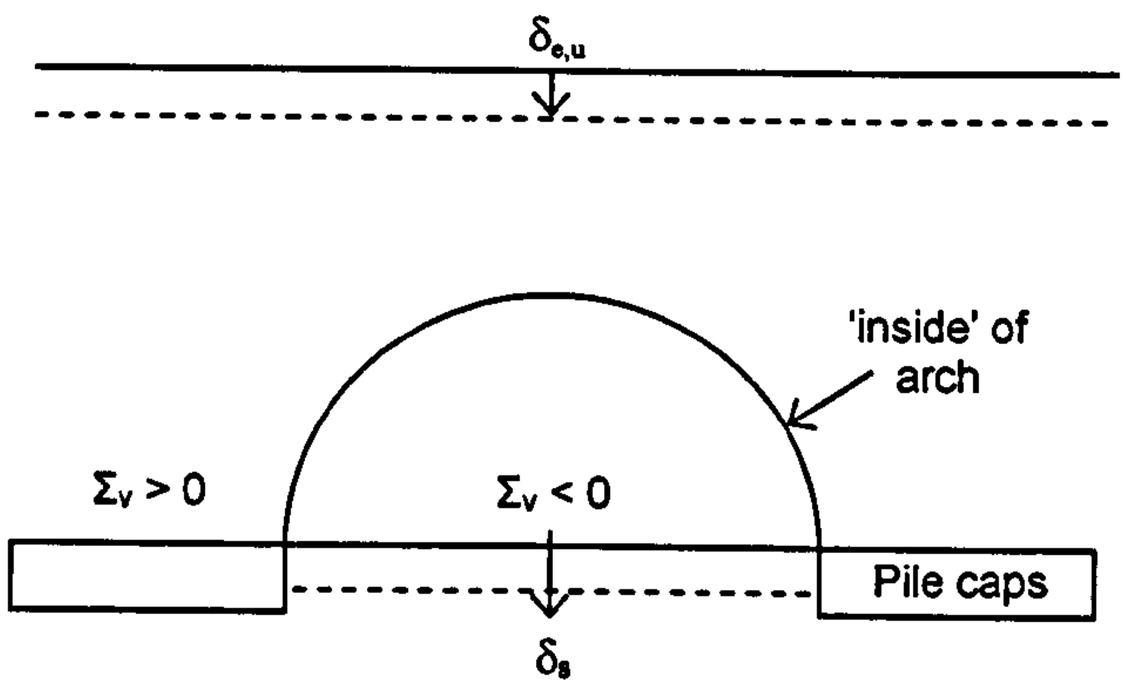

Figure 4.18 - Schematic illustration of dependency of $\delta_{e,u}$ on vertical strain in the embankment and settlement of the subsoil (δ_s), compressive strain positive

4.3 Analysis of results

Figure 4.19 plots efficacy, showing variation with the embankment height normalised by the clear spacing between pile caps (*s-a*). A representative efficacy value for each test was derived from the 'best fit' gradient shown for the load cell results using the following formula:

$$Efficacy = \frac{m_T}{W_e} \qquad \text{Eqn. 4.2}$$

Where:

m_T = Increase in measured load per g level (Newtons/g-level)

W_e = Weight of Embankment per g level (Newtons/g-level)

Both these values correspond to a single pile, hence $W_e = \rho g s^2 h_e$.

Since m_T is approximately representative of all g-levels, as has already been noted efficacy is approximately constant throughout each test.

The results in Figure 4.19(a) show the expected trend, with efficacy tending towards a maximum value of 1.0 as the embankment height increases, and arching is more effective in transmitting the majority of the embankment load onto the pile caps. The result for test RA06 ($h_e/(s-a)$ = 1.7) is slightly lower than expected, and this could be attributed to uncertainty in interpreting the data for this test, which showed an unusually large amount of scatter.

For $h_e/(s-a)$ less than (approximately) 2, there is steady increase in efficacy with normalised embankment height. After this point, the results level off as they approach the asymptote of 1.0 (with some scatter), as shown on the figure.

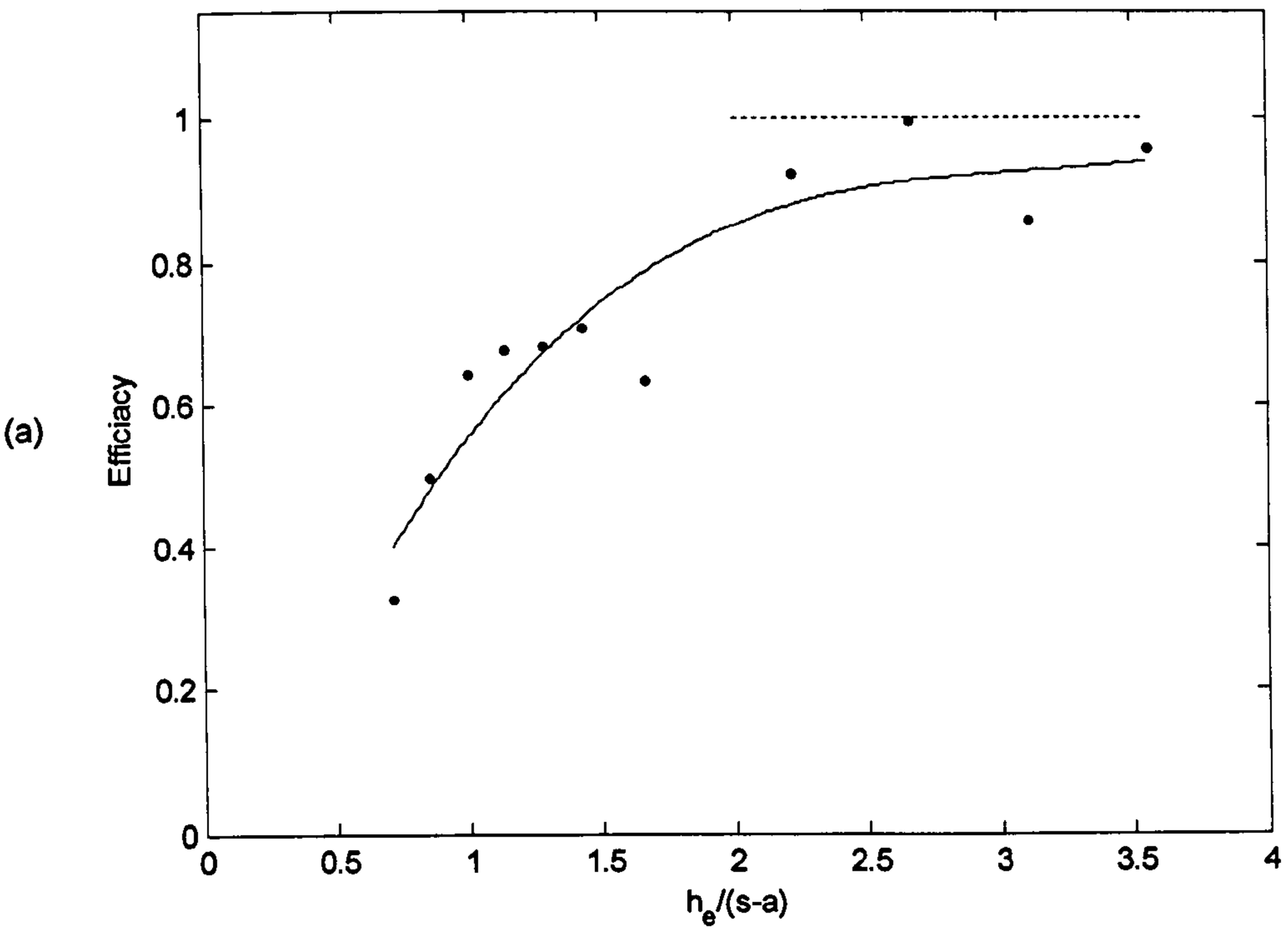

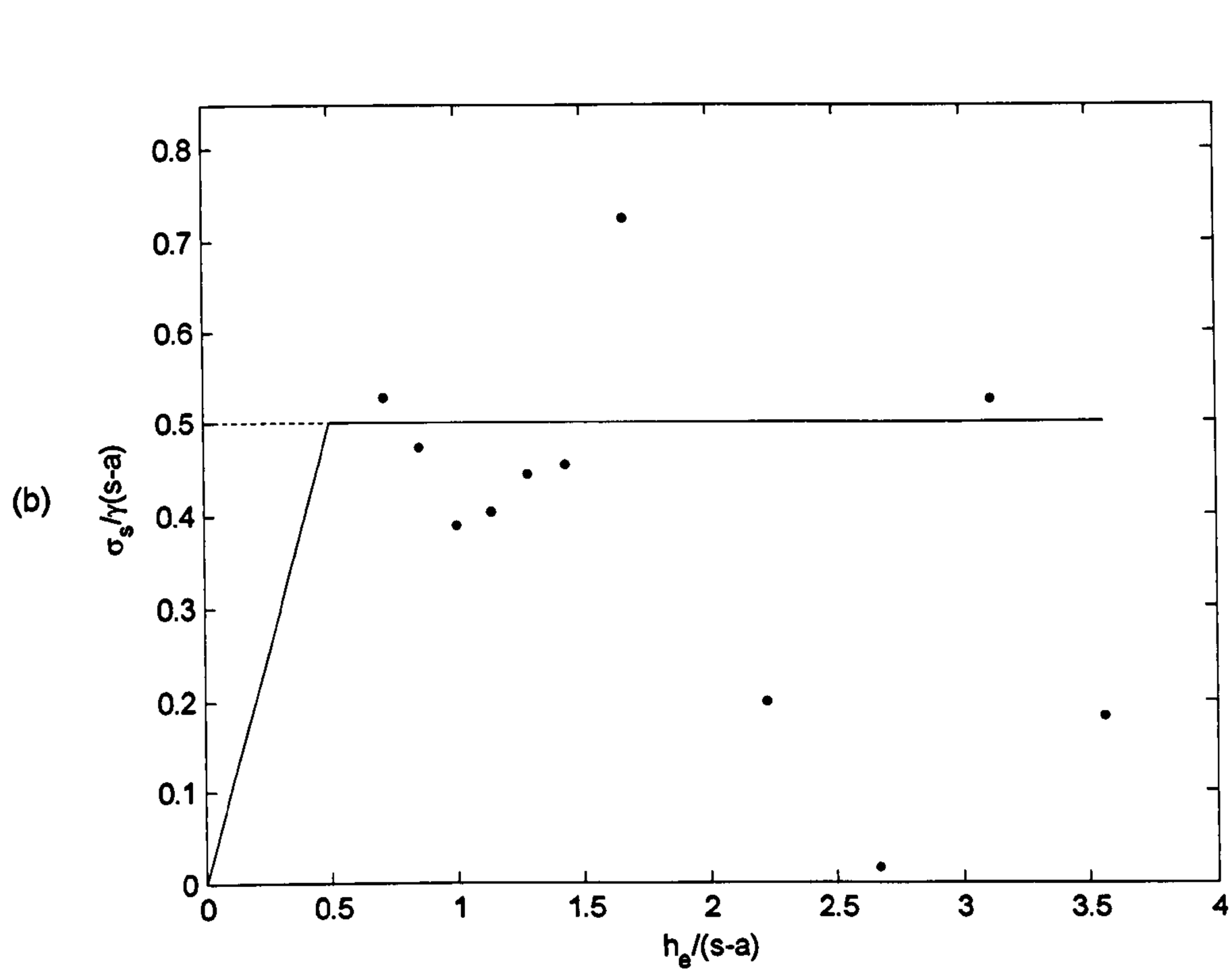

Figure 4.19 - Distribution of load between piles and subsoil: (a) Efficacy, (b) Normalised stress on subsoil

Figure 4.19(b) shows the subsoil stress σ_s, normalised by $\gamma(s\text{-}a)$. The normalising variable is based on the additional term for the weight of 'infilling sand' proposed by Hewlett & Randolph (1988), which is based on the maximum height of a 3-d dome which was $\gamma(s\text{-}a)/\sqrt{2}$ (see Section 2.4.2). The embankment height is again normalised by the clear spacing between pile caps ($s\text{-}a$). The value of σ_s was derived from the 'best fit' lines for the load cell data using the following formula:

$$\sigma_s = \frac{N(W_e - m_T)}{s^2 - a^2} \qquad \text{Eqn. 4.2}$$

Where:

σ_s = Stress acting on subsoil at Ng level (Newtons/m^2)

This formula correctly implies that the stress on the subsoil increases proportionally with g-level, but normalising by $\gamma(s\text{-}a)$, γ also increases in this way and hence the normalised value is (like W_e and m_T) independent of g-level.

For most of the tests, $\sigma_s/\gamma(s\text{-}a)$ is about 0.5, as shown by the line on the chart. The line shown for $h_e/(s\text{-}a)$ less than 0.5 indicates $\sigma_s = \gamma h_e$ – i.e. 'no arching'. As $h_e/(s\text{-}a)$ increases the results become more erratic when plotted in this way. As efficacy tends to 1.0, σ_s tends to zero, so that the value of σ_s is very sensitive to the exact proximity of efficacy to the asymptotic value of 1.0. This means that small change (or error) in the load cell data causes disproportionately large change in the inferred value of σ_s.

Disregarding these erratic values it can be proposed that when $h_e/(s\text{-}a) \approx 0.5$ there is no arching - σ_s corresponds to the unmodified overburden stress from the embankment material. As h_e increases σ_s remains approximately constant at $0.5\gamma(s\text{-}a)$.

It is now possible to estimate settlement of the subsoil (EPS 70) under this nominal load (assuming both stress and settlement are uniform). At 60g $0.5\gamma(s\text{-}a)$ = 36 kN/m^2 for $(s\text{-}a)$ = 70 mm and 23 kN/m^2 for $(s\text{-}a)$ = 45 mm. Taking the one-dimensional modulus of EPS 70 as 2 MN/m^2 (Appendix B), the corresponding settlement is 3 and 2 mm respectively. These values compare reasonably well with Figure 4.16 where the

average $\delta_{e,u}$ was 2.5 mm and 1.6 mm respectively at 60g. For the largest values of h_e there is some indication that $\delta_{e,u}$ is less than the calculated settlement of the subsoil, potentially corresponding to vertical extension of the soil below the arch as shown in Figure 4.18.

Figure 4.15 clearly showed that in tests with the same s but with varying h_e, a greater h_e gave less differential settlement ($\delta_{e,d}$). Figure 4.20 shows $\delta_{e,d}$ at 30g and 60g plotted against $h_e/(s\text{-}a)$ for the tests. The dotted line for high $h_e/(s\text{-}a)$ at 0.2 mm indicates that differential displacement less than this value could not be reliably quantified for the range of $h_e/(s\text{-}a)$ indicated. As $h_e/(s\text{-}a)$ initially increases the differential displacement drops rapidly, tending to zero from $h_e/(s\text{-}a) \approx 2.0$.

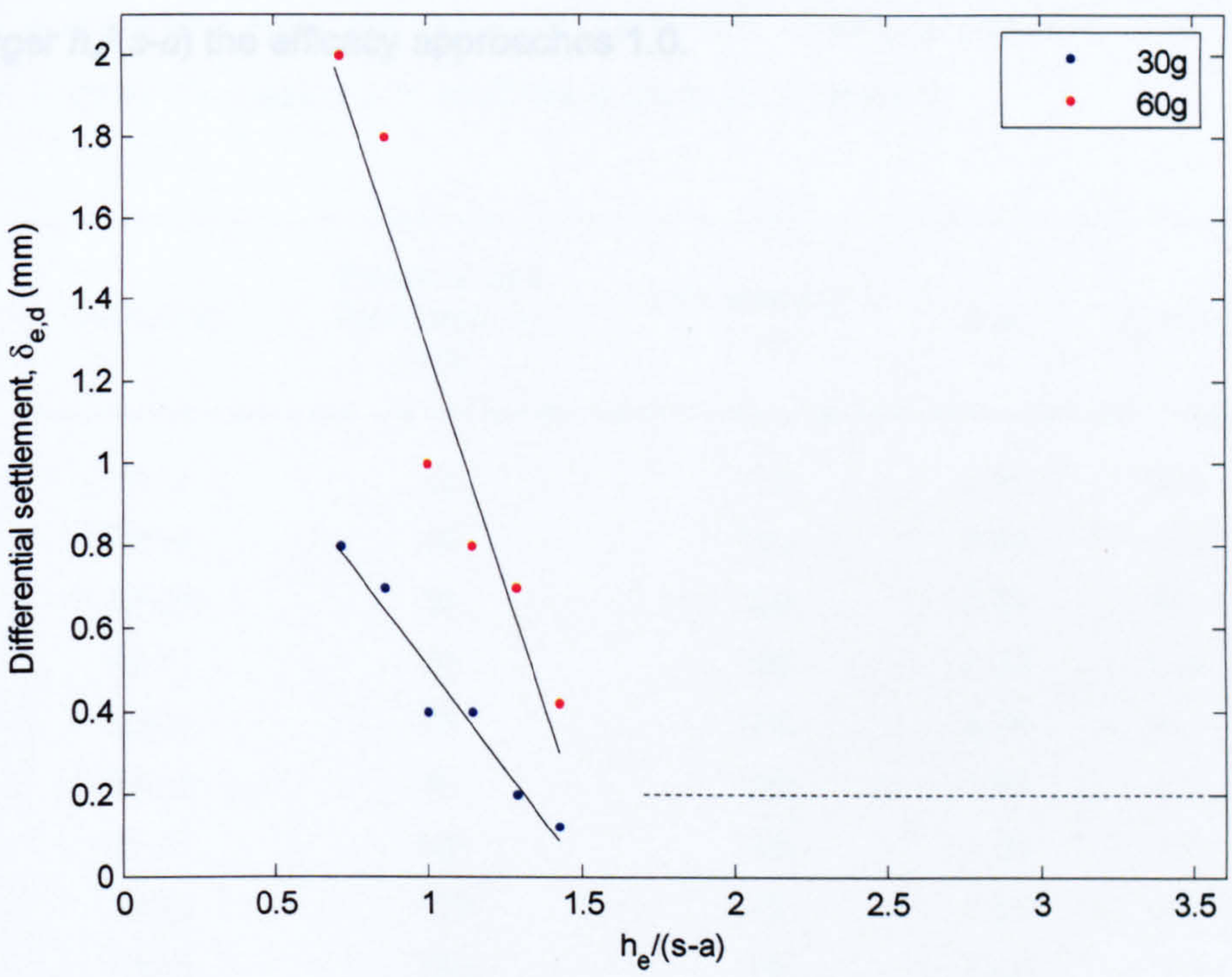

Figure 4.20 - Differential settlement, $\delta_{e,d}$

4.4 Summary

The following features of behaviour were observed for the piled embankment tests using EPS 70 as a subsoil material.

At $h_e/(s\text{-}a) \approx$ 0.5 there is no evidence of arching based on the stress acting on the subsoil, and there is very large differential settlement at the embankment surface (due to imprints of the pile caps).

As $h_e/(s\text{-}a)$ increases to 2.0 the stress on the subsoil does not increase significantly (and thus there is significant evidence of arching), and differential settlement at the embankment surface tends to zero.

For larger $h_e/(s\text{-}a)$ the efficacy approaches 1.0.

CHAPTER 5

CENTRIFUGE TEST DATA – PILED EMBANKMENT EPS 200

5.1 Introduction

The aim of this chapter is to present the centrifuge test data for the piled embankment tests using EPS 200, with some analysis and discussion of the results. The tests that will be summarised here are shown in Table 5.1. The pile cap size in all the tests is 30 mm. Further discussion and analysis is given in Chapter 8.

Test code	Embankment thickness, h_e (mm)	Pile spacing, s (mm)	h_e/s	$h_e/(s-a)$
RA11	35	100	0.35	0.5
RA14	45	100	0.45	0.6
RA08	50	100	0.50	0.7
RA12	60	100	0.60	0.9
RA09	75	100	0.75	1.1
RA13	85	100	0.85	1.2
RA10	100	100	1.00	1.4
RA24	100	75	1.33	2.2
RA25	120	75	1.60	2.7
RA26	140	75	1.87	3.1
RA27	160	75	2.13	3.6
RA05	210	75	2.80	4.7

(N.b. 1g values are presented)

Table 5.1 - Summary of EPS 200 piled embankment test series

5.2 Test results

5.2.1 Load cell results

As in Chapter 4, each model was accelerated up to 60g in 10g increments, and the results are represented by the constant load at each increment of g-level (10, 20, 30 etc). Figures 5.1 - 5.12 show the calibrated load cell output (in Newtons), showing increase with g-level in each test for each load cell and their locations (where available). The use of '*' following a load cell name in the legend of a chart indicates that only one of the two pairs of strain gauges (Section 3.4.1) functioned in the test, and thus the results may be unreliable. The plots follow the sequence in Table 5.1, and hence show increasing ratio of embankment height to pile spacing (h_e/s), noting that s reduces for the later tests.

A straight line passing through the origin was again used to characterise the results of the various load cells for each test. The gradient of this line representing the increase in measured load per g level (N/g), is shown in the bottom right hand corner of each graph.

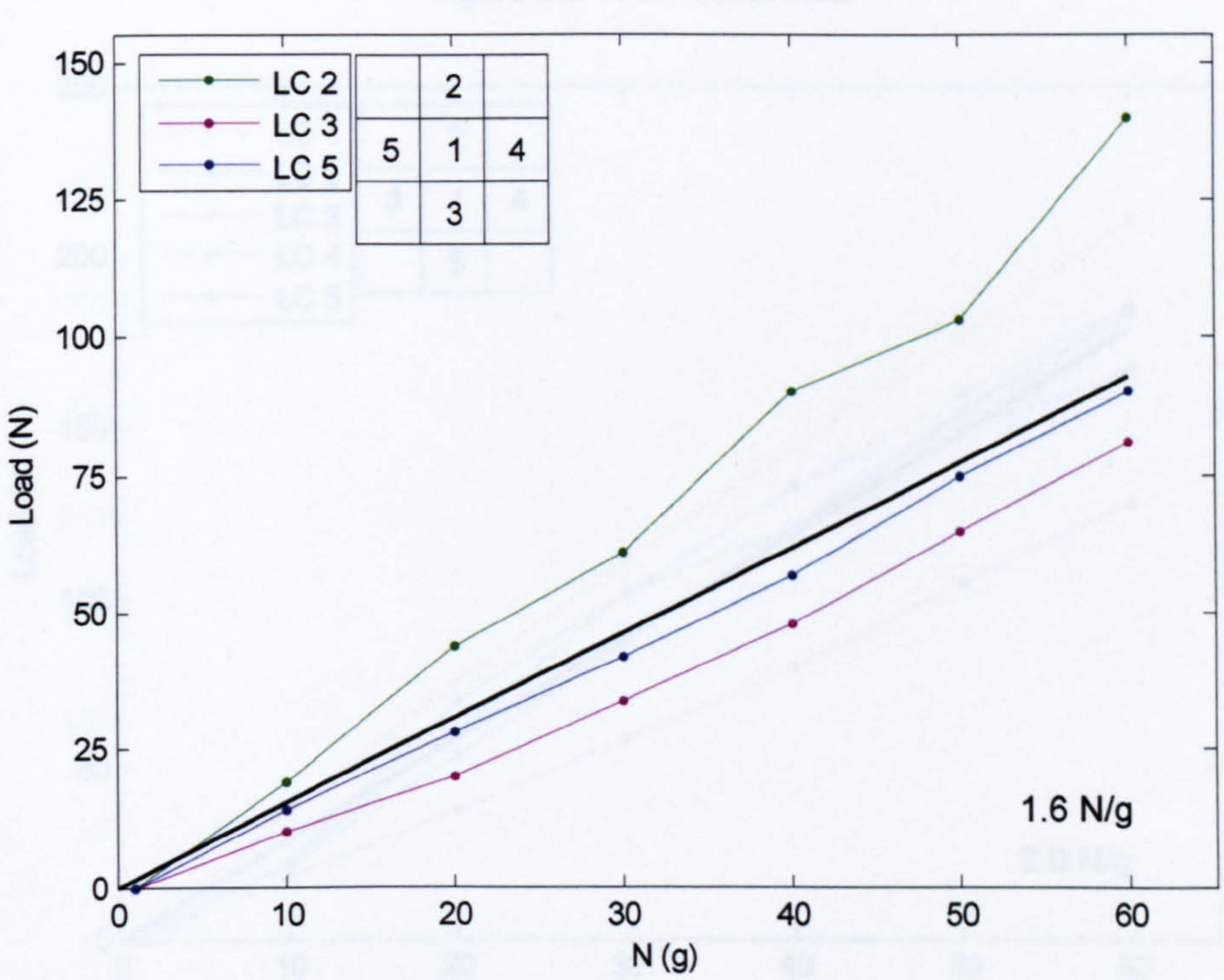

Figure 5.1 - RA11 test data

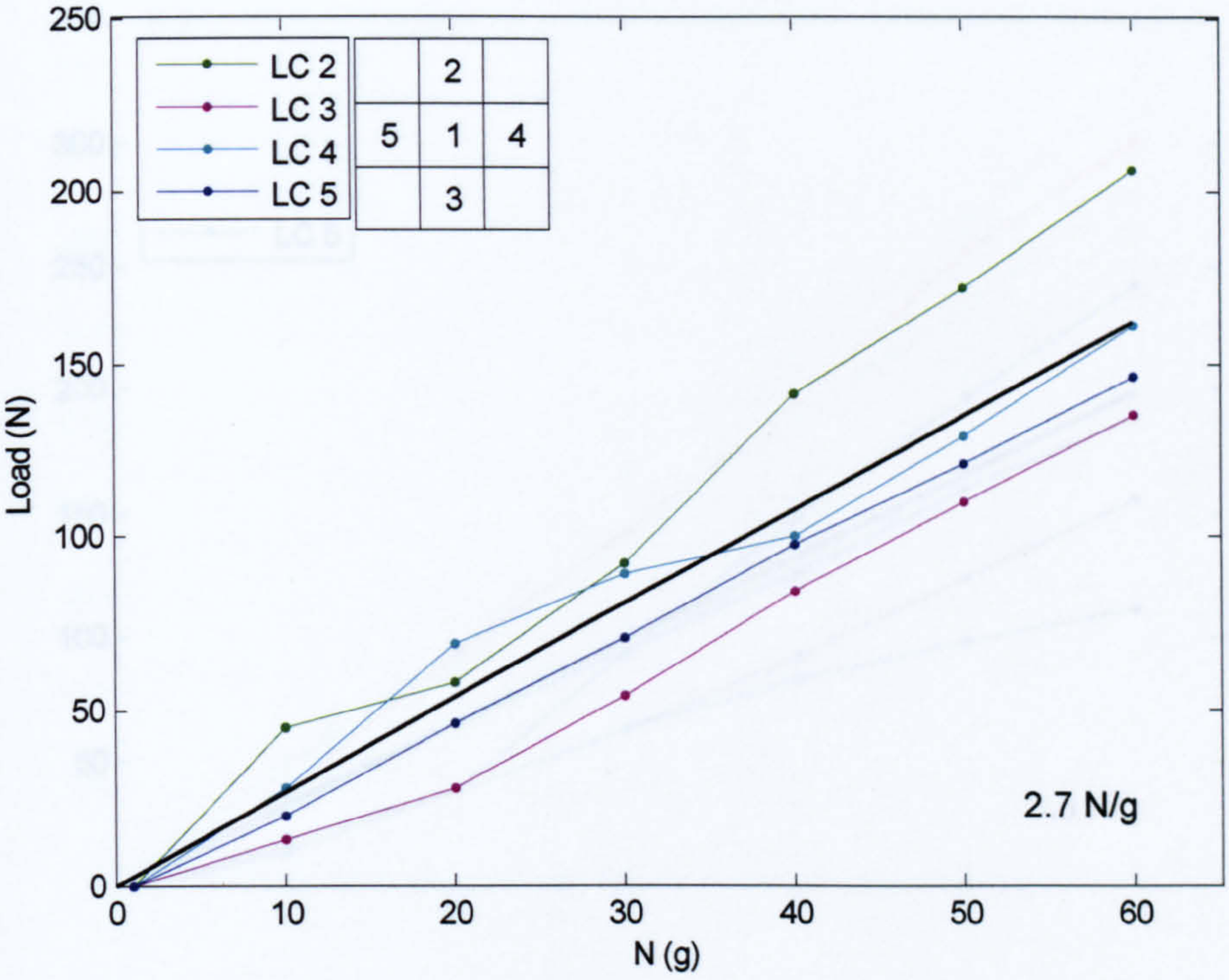

Figure 5.2 - RA14 test data

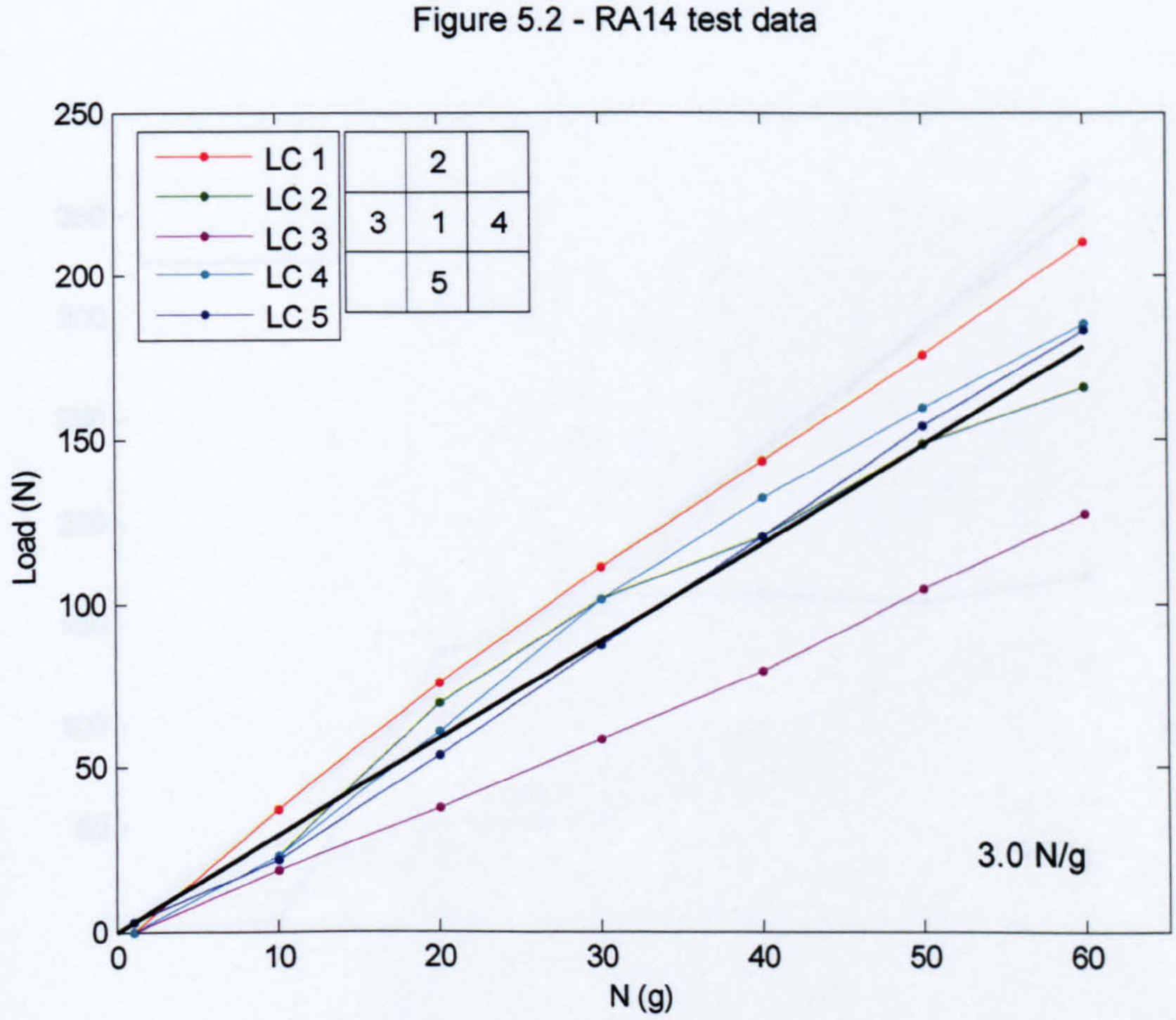

Figure 5.3 - RA08 test data

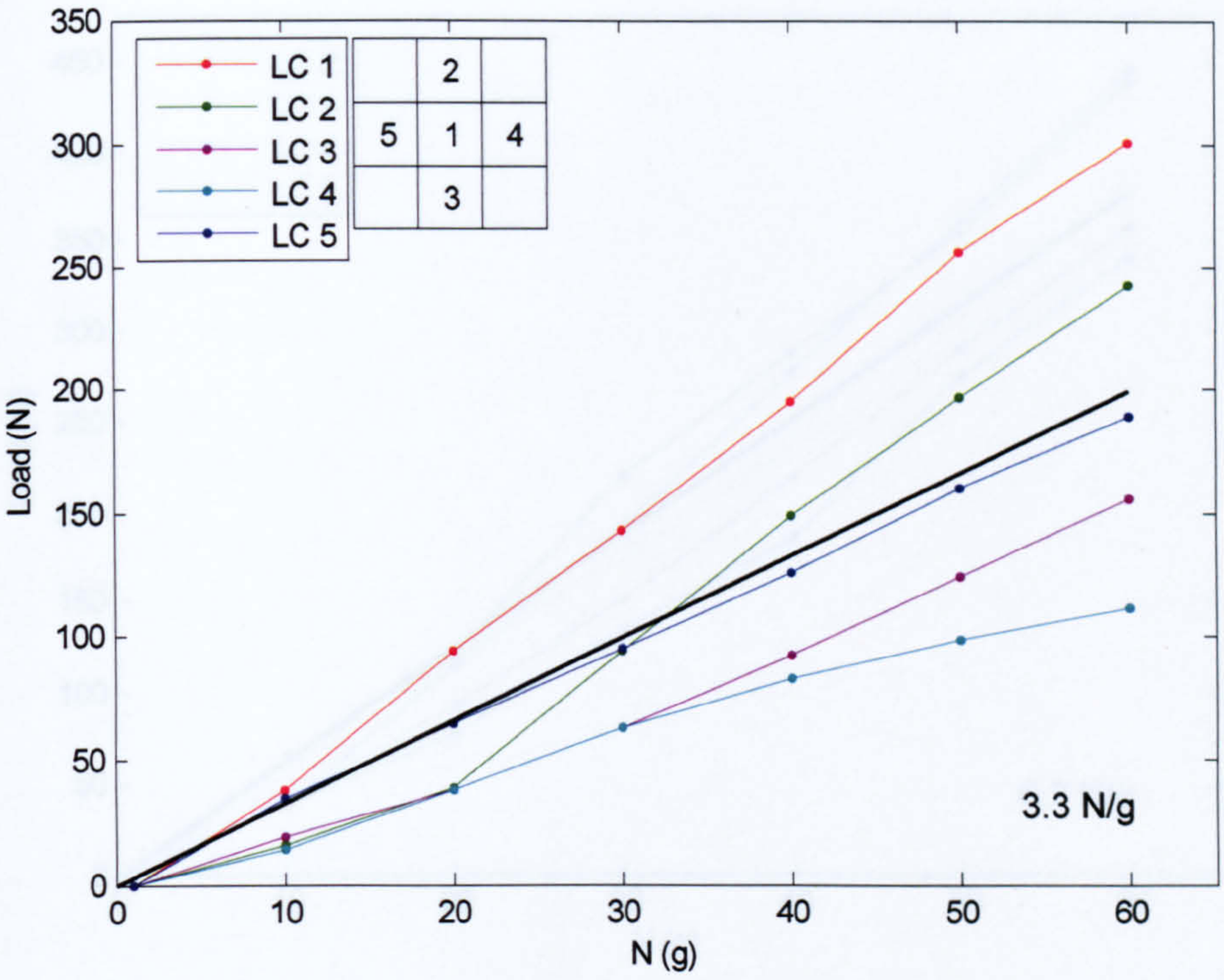

Figure 5.4 - RA12 test data

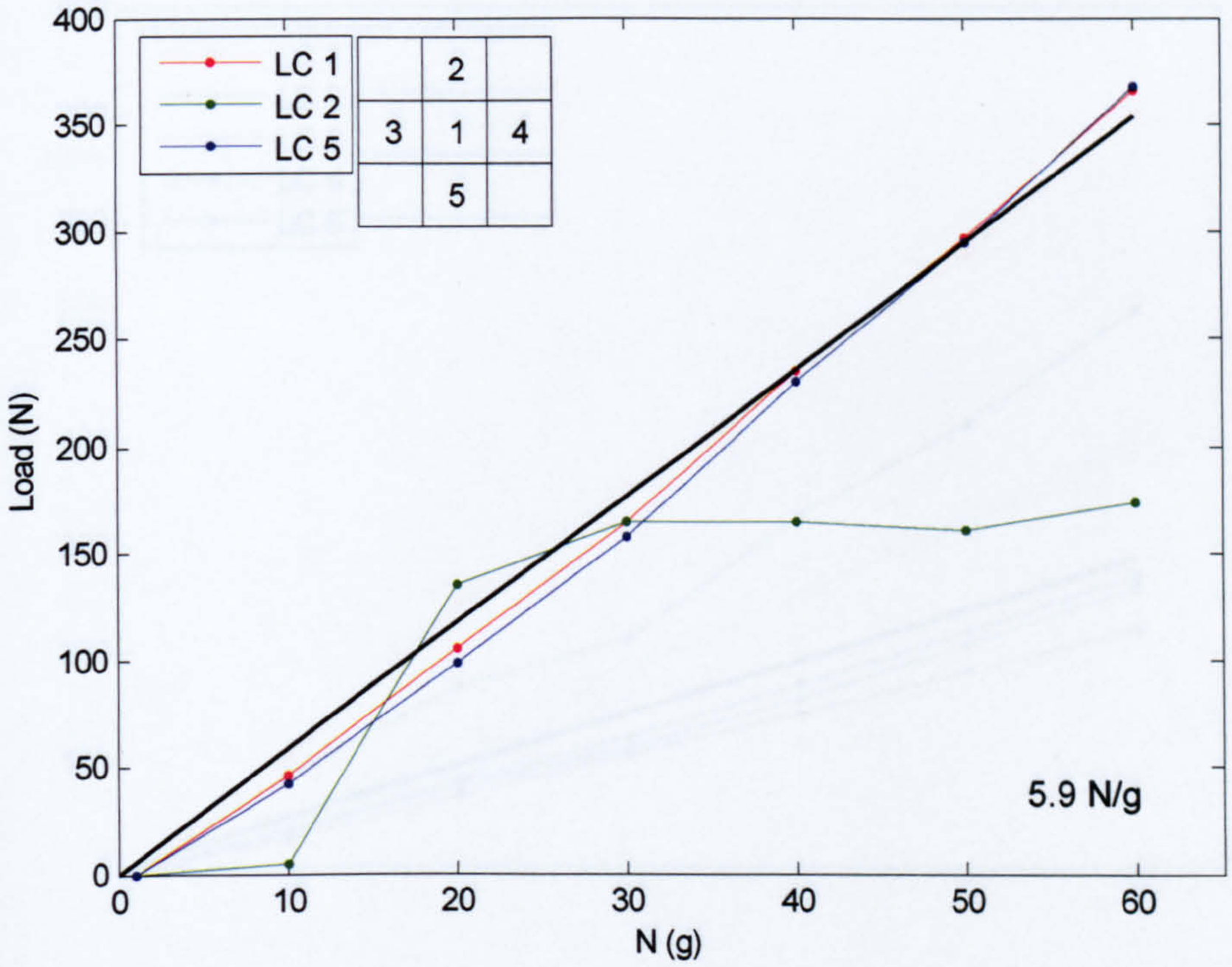

Figure 5.5 - RA09 test data

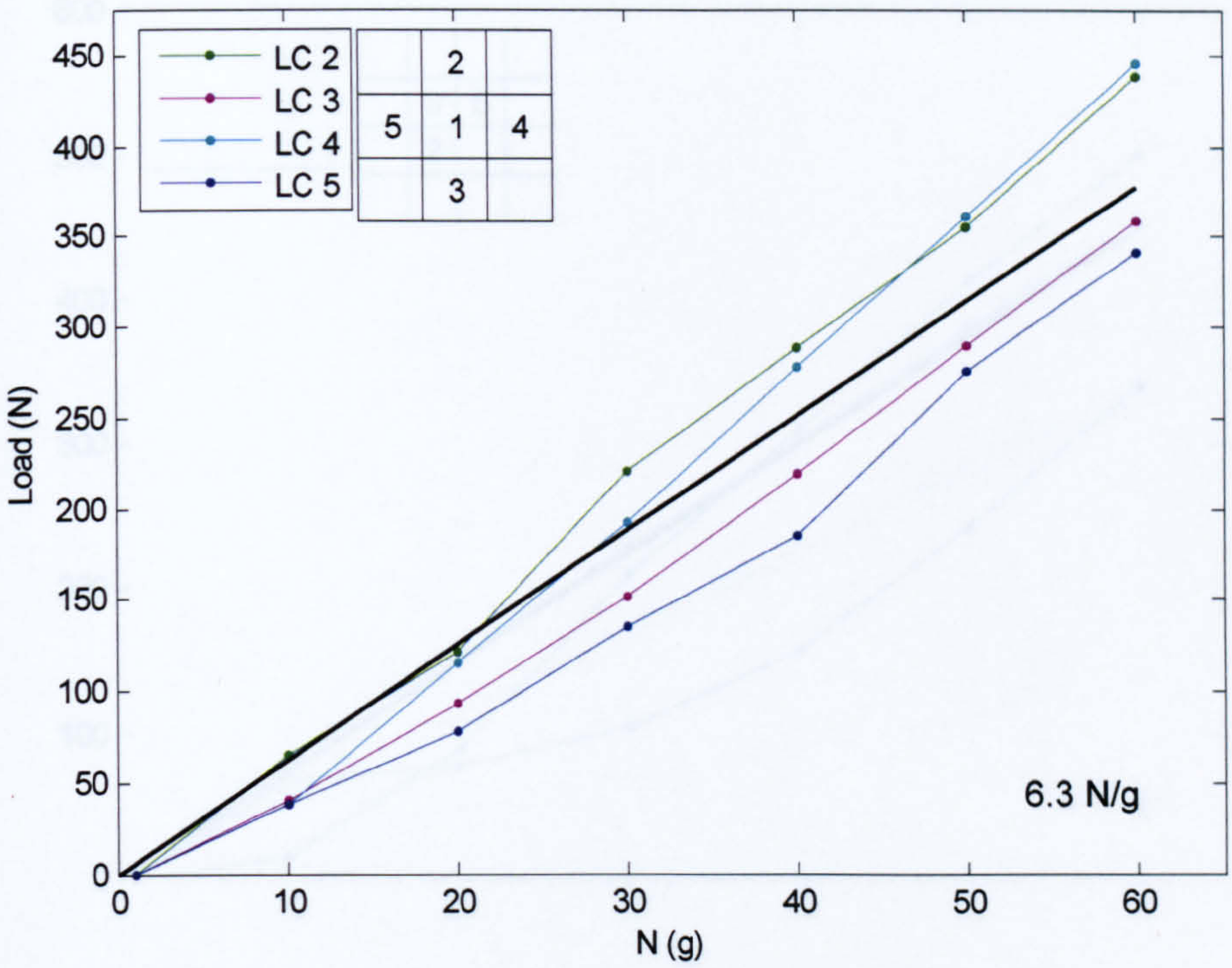

Figure 5.6 - RA13 test data

Figure 5.7 - RA10 test data

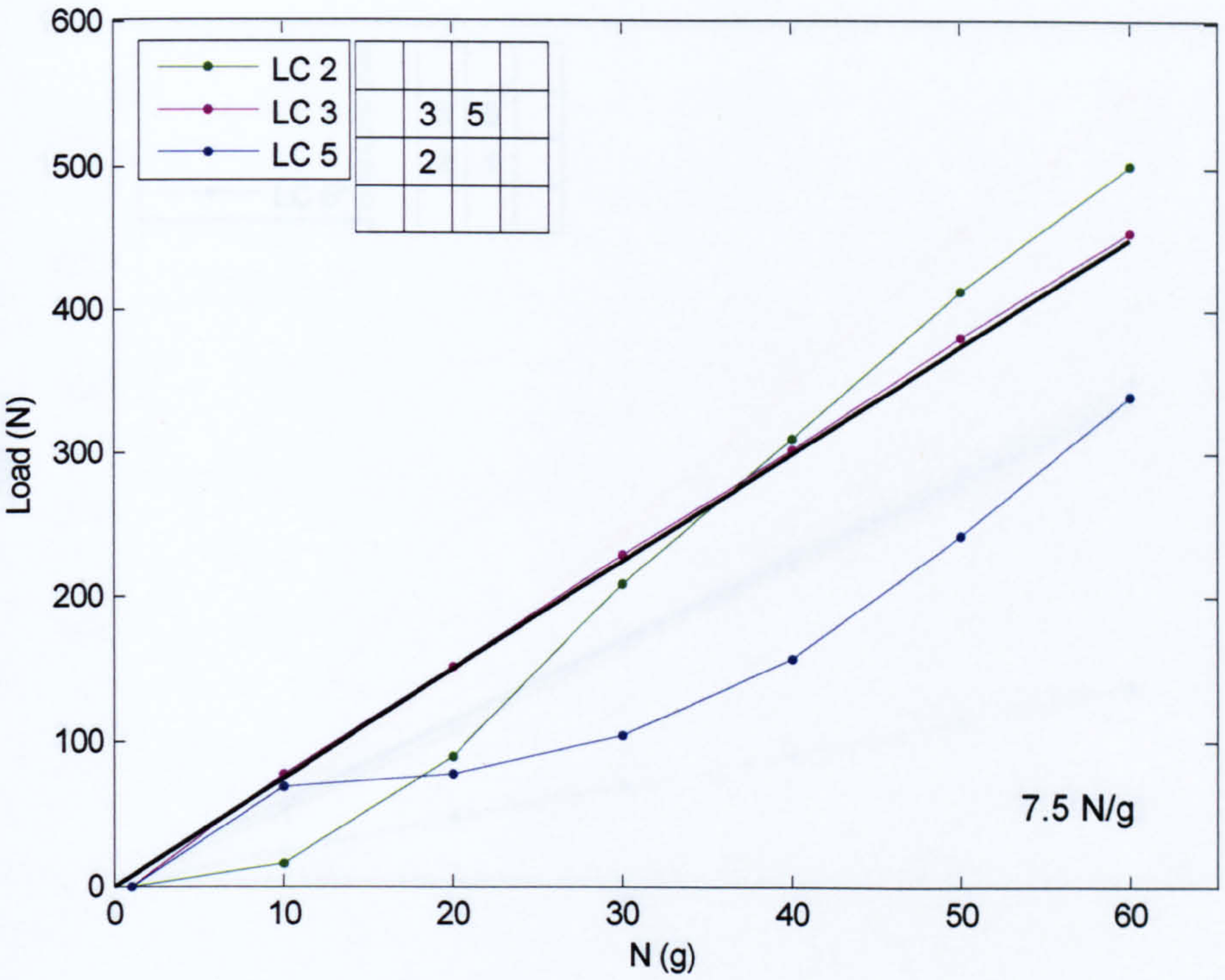

Figure 5.8 - RA24 test data

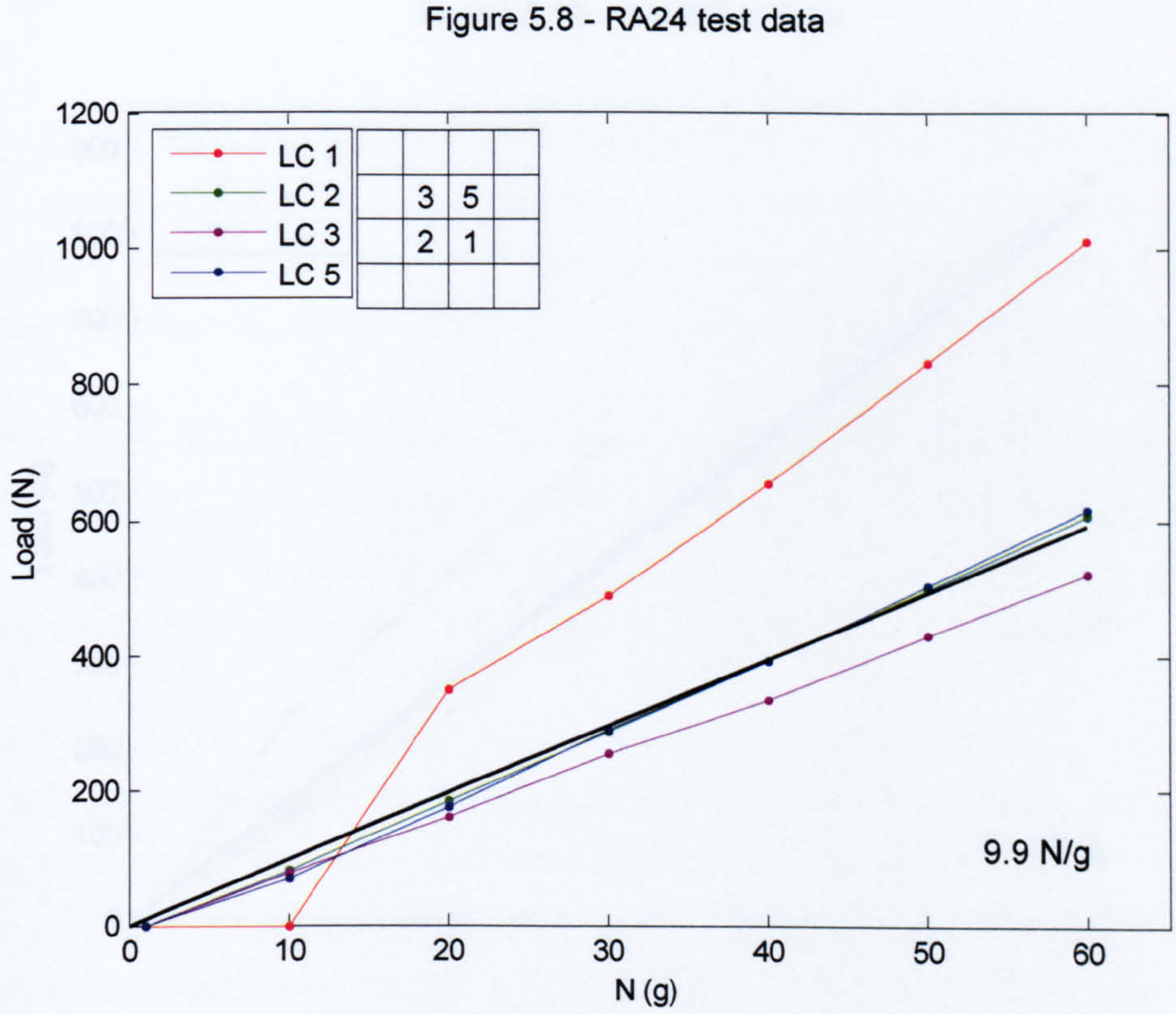

Figure 5.9 - RA25 test data

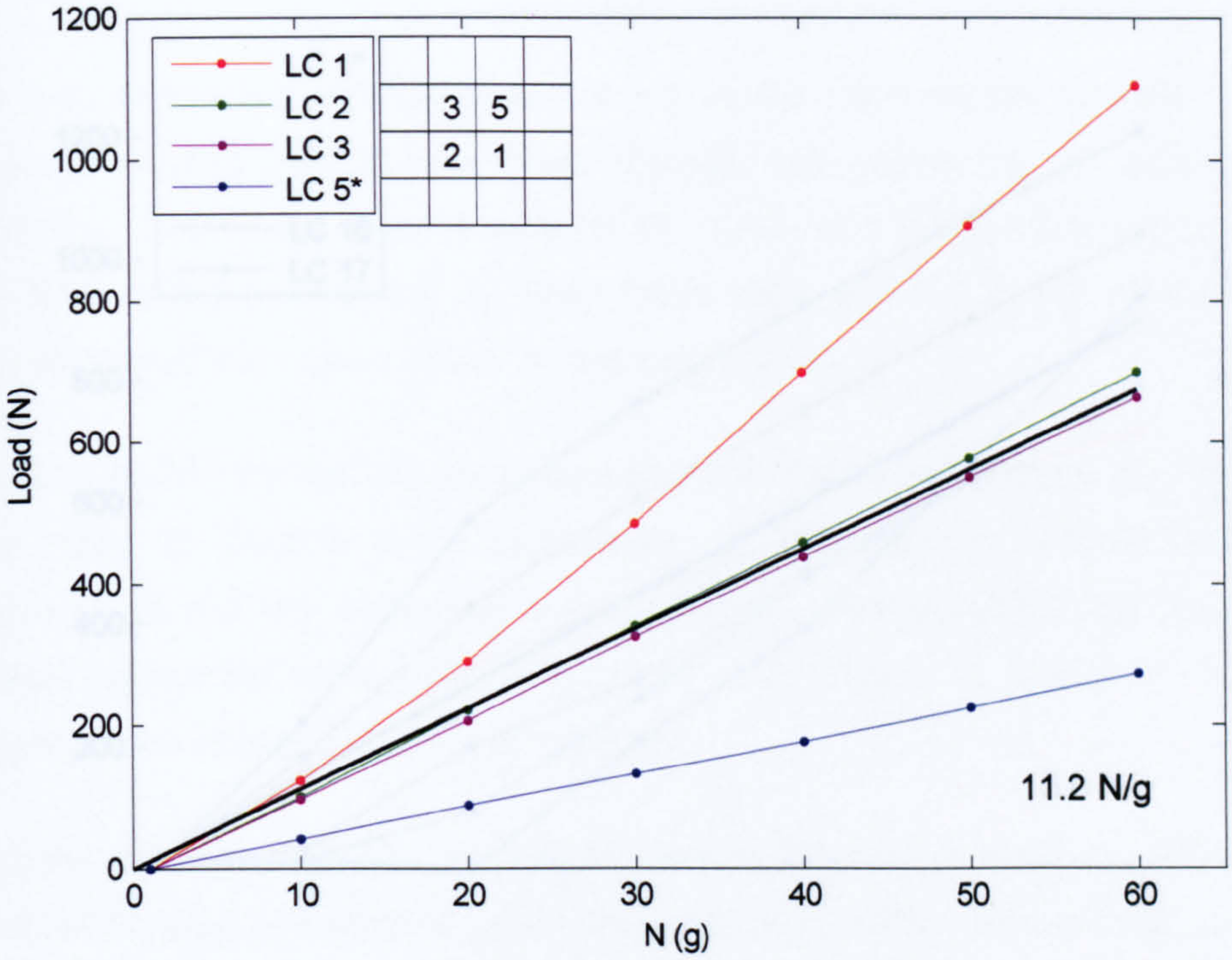

Figure 5.10 - RA26 test data

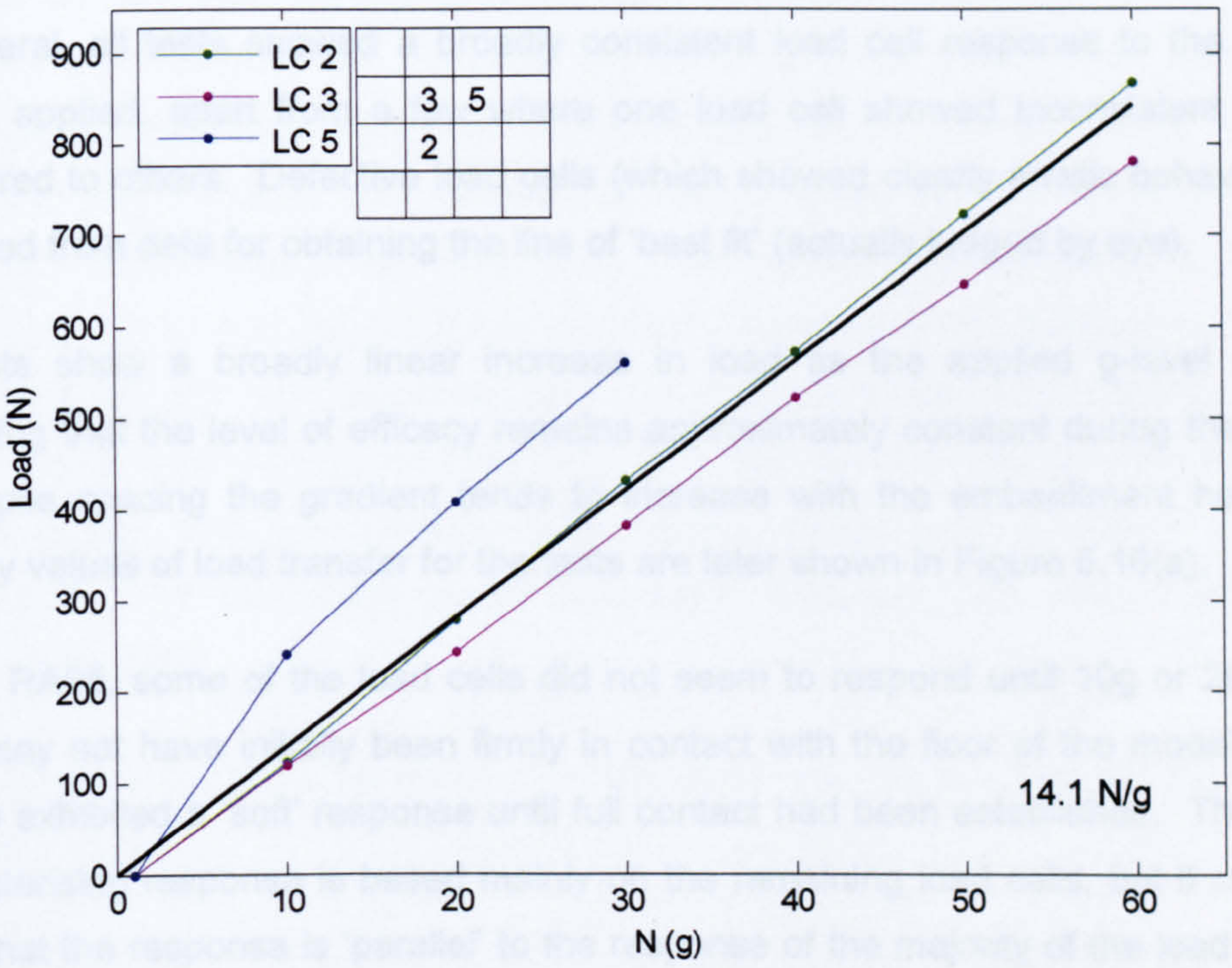

Figure 5.11 - RA27 test data

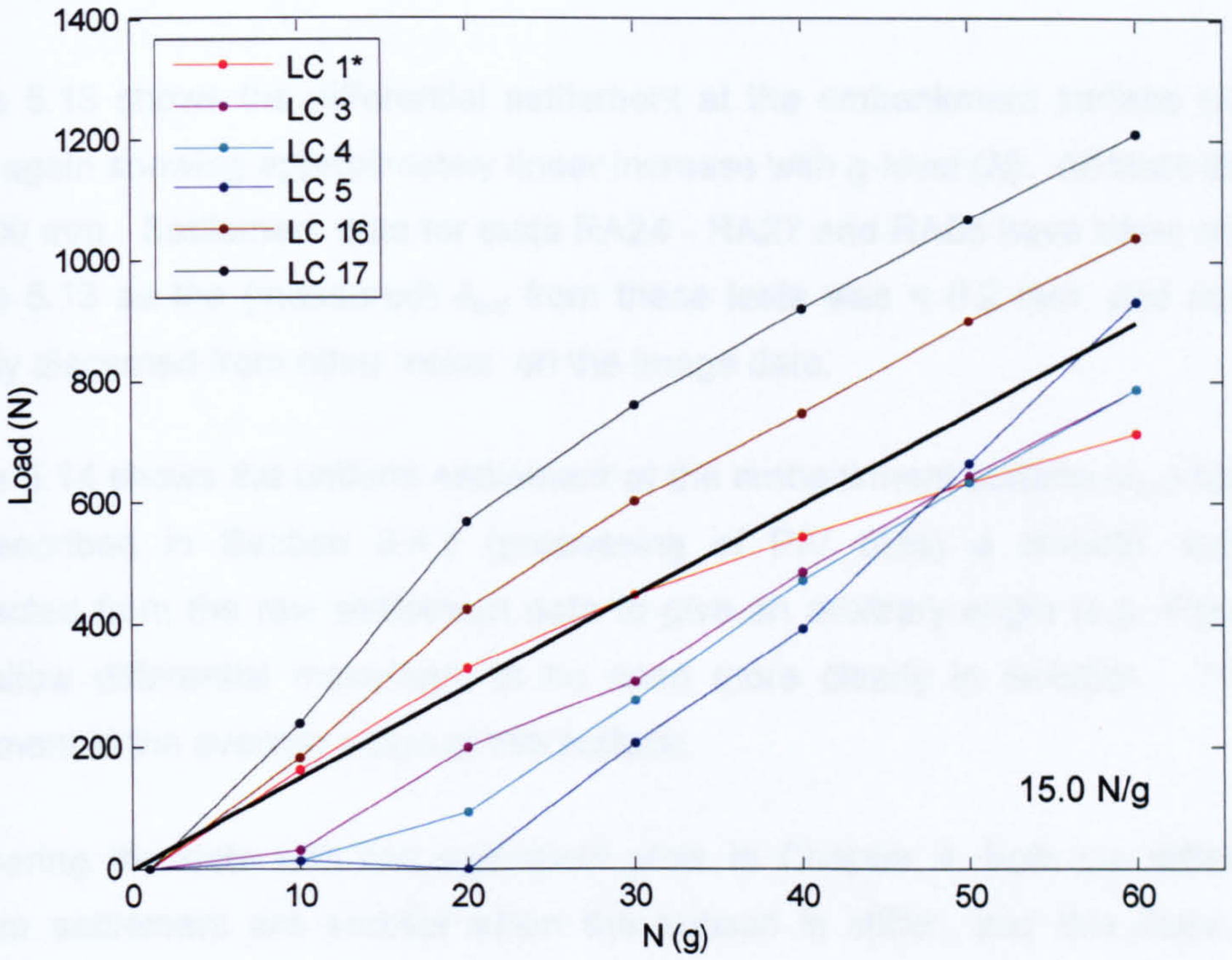

Figure 5.12 - RA05 test data

In general, all tests showed a broadly consistent load cell response to the increased g-level applied, apart from a few where one load cell showed inconsistent behaviour compared to others. Defective load cells (which showed clearly erratic behaviour) were excluded from data for obtaining the line of 'best fit' (actually judged by eye).

All tests show a broadly linear increase in load as the applied g-level increases, indicating that the level of efficacy remains approximately constant during the test. For given pile spacing the gradient tends to increase with the embankment height. The efficacy values of load transfer for the tests are later shown in Figure 5.16(a).

In test RA05, some of the load cells did not seem to respond until 10g or 20g. These piles may not have initially been firmly in contact with the floor of the model, and thus initially exhibited a 'soft' response until full contact had been established. Thus the line characterising response is based mainly on the remaining load cells, but it can also be seen that the response is 'parallel' to the response of the majority of the load cells once they had begun to register a reading.

5.2.2 Settlement results

Figure 5.13 shows the differential settlement at the embankment surface ($\delta_{e,d}$) for the tests, again showing approximately linear increase with g-level (N). All tests shown have s = 100 mm. Settlement data for tests RA24 - RA27 and RA05 have been omitted from Figure 5.13 as the (measured) $\delta_{e,d}$ from these tests was < 0.2 mm, and could not be reliably discerned from other 'noise' on the image data.

Figure 5.14 shows the uniform settlement at the embankment surface ($\delta_{e,u}$) for the tests. As described in Section 3.4.2 (processing of PIV data) a smooth 'surface' was subtracted from the raw settlement data to give an arbitrary origin (e.g. Figure 4.3(c)), and allow differential movement to be seen more clearly in isolation. The uniform settlement is the average value of this surface.

Comparing the data with the equivalent plots in Chapter 4, both the differential and uniform settlement are smaller when the subsoil is stiffer, and this does not seem unreasonable.

The test for h_e = 50 mm gives unusually high differential settlement. Three tests give unusually high uniform settlement, but this effect does not appear to be systematically related to any particular feature of the model geometry. However, these tests do all seem to exhibit an initially 'soft' response to initial g-levels, with later response becoming stiffer, and comparable to the other tests. The highest of these results is Test RA05 (s = 75, h_e = 210 mm), where it has previously been remarked that some of the piles exhibited a slightly 'soft' response, and this probably would have contributed to this effect. The (measured) $\delta_{e,u}$ for Test RA08 (s = 100, h_e = 50 mm) remained unchanged from 40 to 50g. This is unusual behaviour taking into account the increase in stress on the subsoil. The other tests are all quite tightly bunched, with uniform settlement of about 1 mm at 60g.

As in Chapter 4, $\delta_{e,d}/\delta_{e,u}$ is about 0.5 only when $\delta_{e,d}$ has it's highest values, and is otherwise lower.

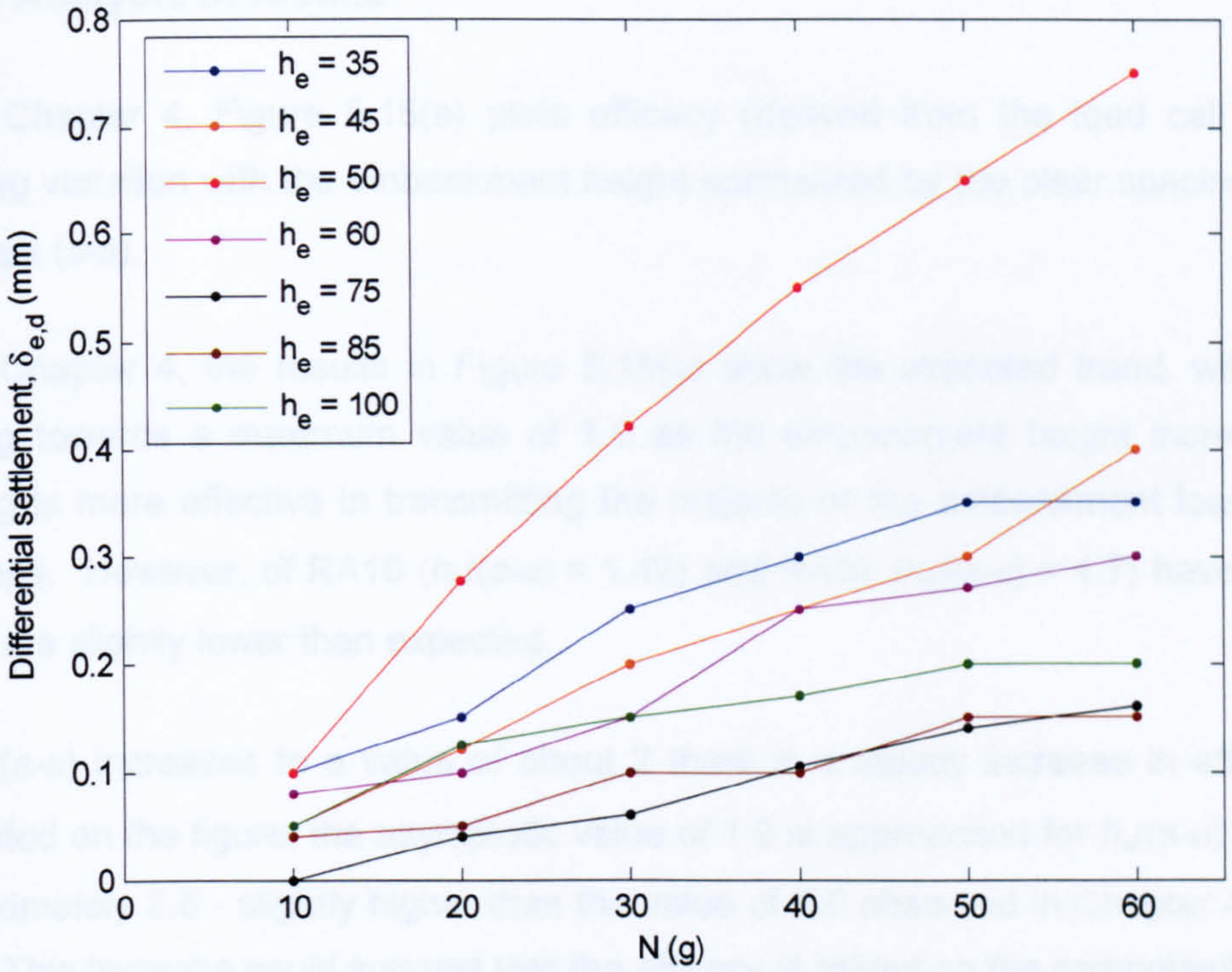

Figure 5.13 - Differential settlement at the embankment surface, $\delta_{e,d}$

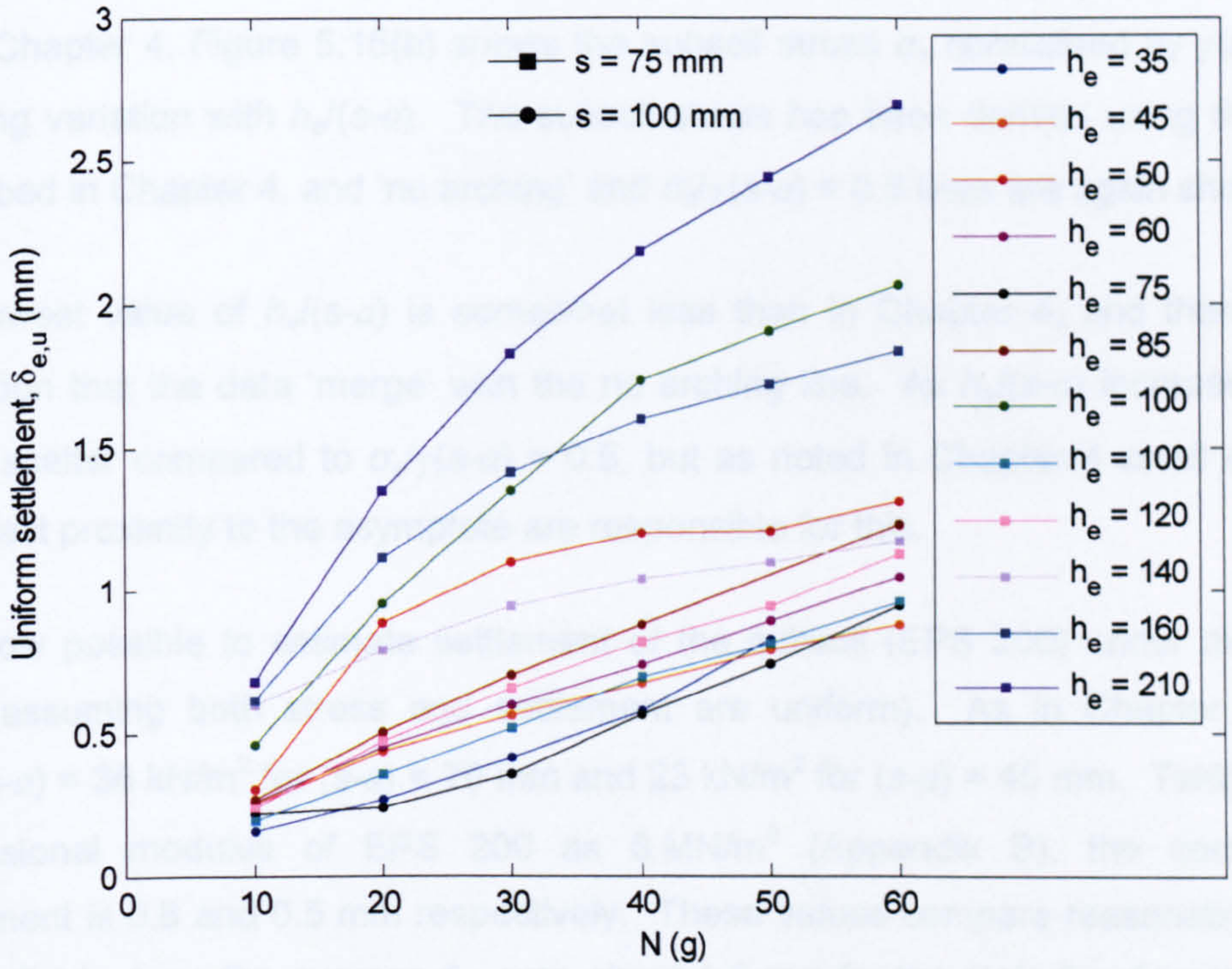

Figure 5.14 - Uniform settlement at the embankment surface, $\delta_{e,u}$

5.3 Analysis of results

As in Chapter 4, Figure 5.15(a) plots efficacy (derived from the load cell gradient), showing variation with the embankment height normalised by the clear spacing between pile caps (s-a).

As in Chapter 4, the results in Figure 5.15(a) show the expected trend, with efficacy tending towards a maximum value of 1.0 as the embankment height increases, and arching is more effective in transmitting the majority of the embankment load onto the pile caps. However, of RA10 ($h_e/(s\text{-}a)$ = 1.42) and RA05 ($h_e/(s\text{-}a)$ = 4.7) have efficacies which are slightly lower than expected.

As $h_e/(s\text{-}a)$ increases to a value of about 2 there is a steady increase in efficacy. As illustrated on the figure, the asymptotic value of 1.0 is approached for $h_e/(s\text{-}a)$ exceeding approximately 2.5 - slightly higher than the value of 2.0 observed in Chapter 4 for softer EPS. This increase could suggest that the efficacy is reliant on the compressibility of the subsoil to cause arching in the embankment.

As in Chapter 4, Figure 5.15(b) shows the subsoil stress σ_s normalised by $\gamma(s\text{-}a)$, again showing variation with $h_e/(s\text{-}a)$. The subsoil stress has been derived using the method described in Chapter 4, and 'no arching' and $\sigma_s/\gamma(s\text{-}a)$ = 0.5 lines are again shown.

The lowest value of $h_e/(s\text{-}a)$ is somewhat less than in Chapter 4, and there is some indication that the data 'merge' with the no arching line. As $h_e/(s\text{-}a)$ increases there is some scatter compared to $\sigma_s/\gamma(s\text{-}a)$ = 0.5, but as noted in Chapter 4 small changes in the exact proximity to the asymptote are responsible for this.

It is now possible to estimate settlement of the subsoil (EPS 200) under this nominal load (assuming both stress and settlement are uniform). As in Chapter 4, at 60g $0.5\gamma(s\text{-}a)$ = 36 kN/m^2 for (s-a) = 70 mm and 23 kN/m^2 for (s-a) = 45 mm. Taking the one-dimensional modulus of EPS 200 as 8 MN/m^2 (Appendix B), the corresponding settlement is 0.8 and 0.5 mm respectively. These values compare reasonably well with Figure 5.14 where the average $\delta_{e,u}$ was about 1.0 mm for the majority of tests at 60g. It

was estimated in Chapter 4 that compression of the embankment material itself due to increase in self-weight gave additional settlement of the order of 0.1 mm, so additional allowance for this effect gives good overall correspondence.

Ignoring the result from test RA08 ($h_e/(s-a)$ = 0.7), the trends shown by the data for $\delta_{e,d}$ in Figure 5.16 are similar to Chapter 4, although the magnitude of the differential displacement for given $h_e/(s-a)$ is about 4 times lower, corresponding to the ratio of subsoil (EPS) stiffness in the two cases. Again, the range of tests where differential displacement was less than 0.2 mm and thus could not be reliably established is shown.

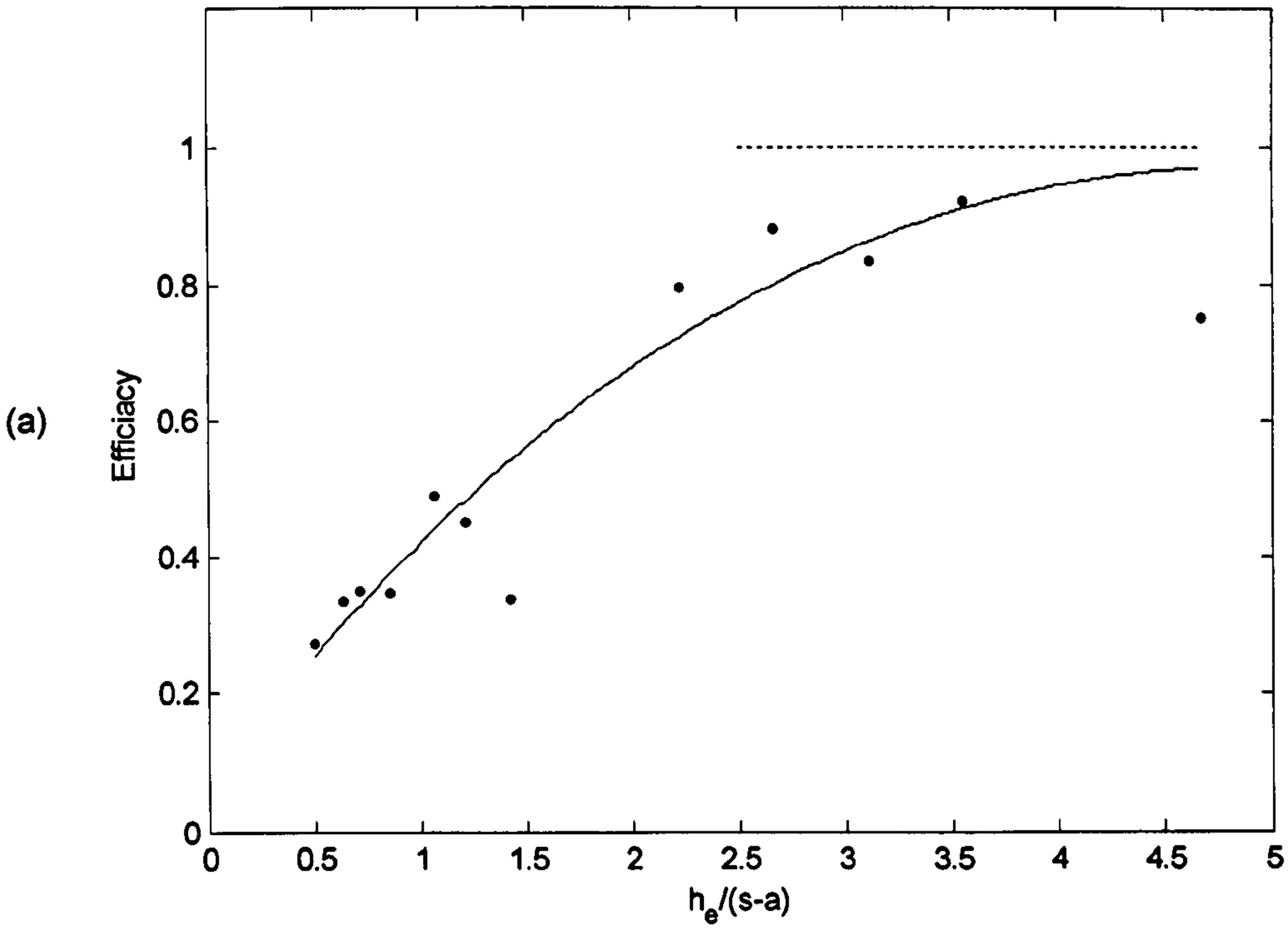

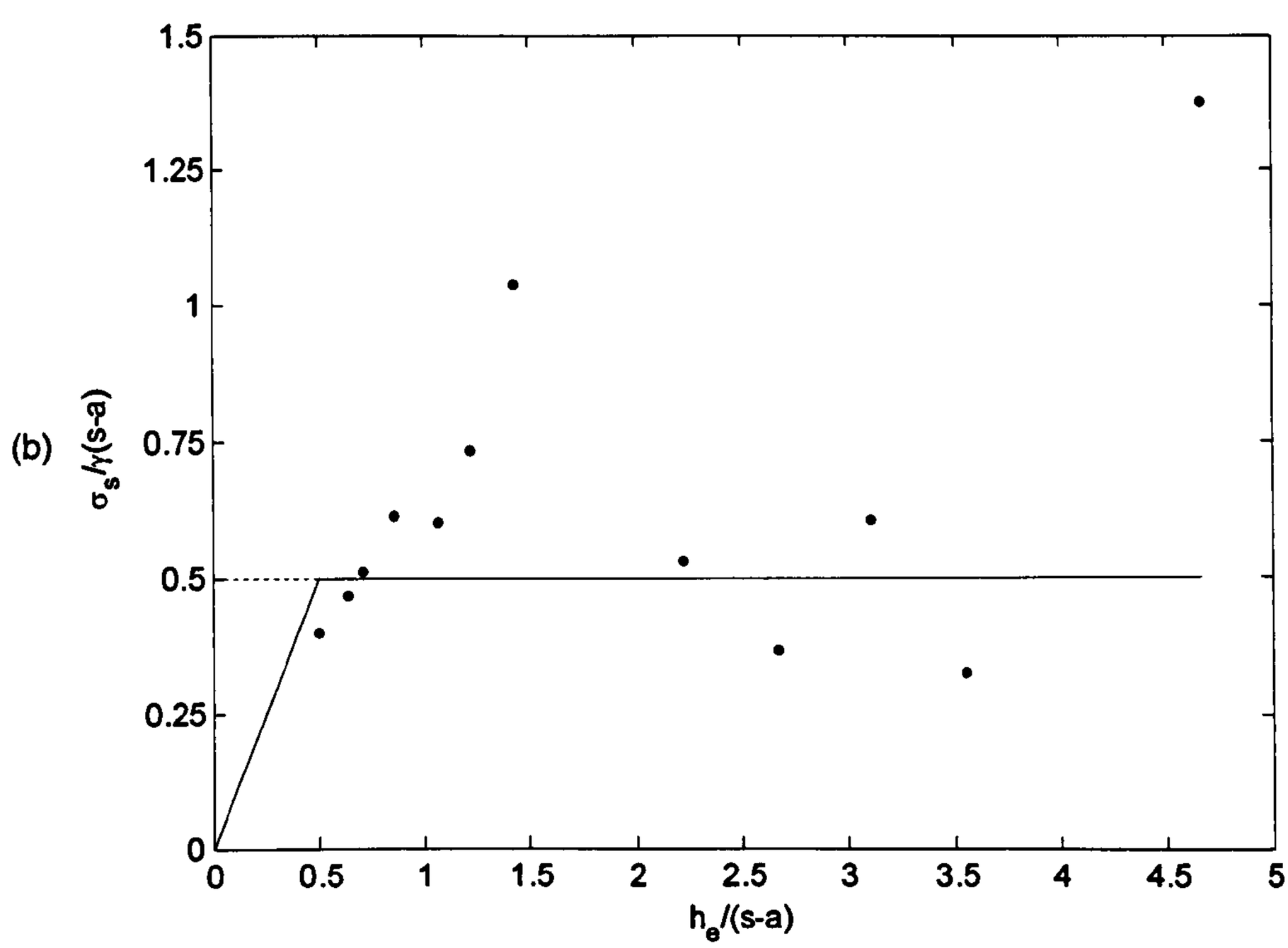

Figure 5.15 - Distribution of load between piles and subsoil: (a) Efficacy, (b) Normalised stress on subsoil

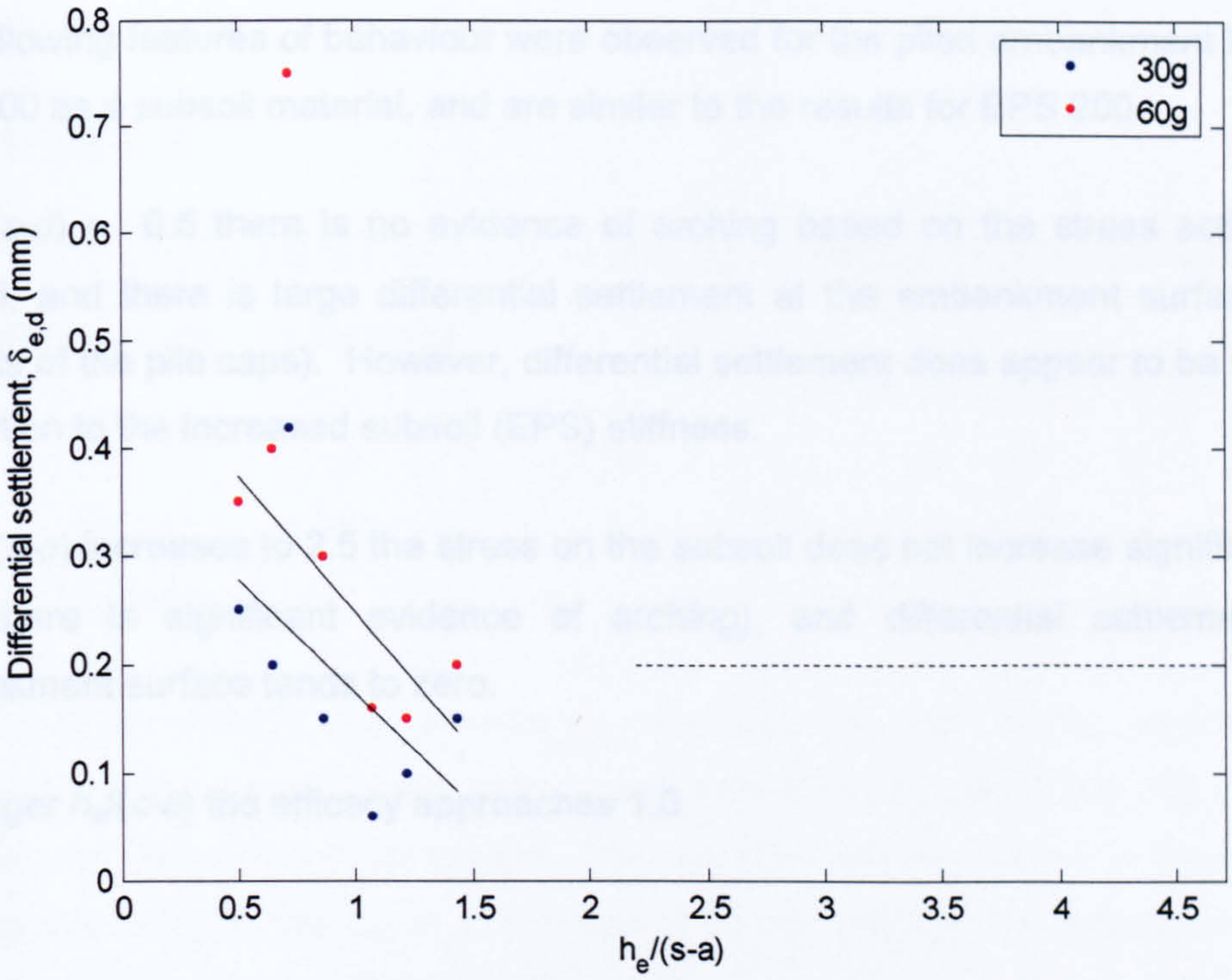

Figure 5.16 - Differential settlement, $\delta_{e,d}$

5.4 Summary

The following features of behaviour were observed for the piled embankment tests using EPS 200 as a subsoil material, and are similar to the results for EPS 200.

At $h_e/(s\text{-}a) \approx$ 0.5 there is no evidence of arching based on the stress acting on the subsoil, and there is large differential settlement at the embankment surface (due to imprints of the pile caps). However, differential settlement does appear to be reduced in proportion to the increased subsoil (EPS) stiffness.

As $h_e/(s\text{-}a)$ increases to 2.5 the stress on the subsoil does not increase significantly (and thus there is significant evidence of arching), and differential settlement at the embankment surface tends to zero.

For larger $h_e/(s\text{-}a)$ the efficacy approaches 1.0.

CHAPTER 6

CENTRIFUGE TEST DATA – PILED EMBANKMENT WITH WORKING PLATFORM

6.1 Introduction

The aim of this chapter is to present the centrifuge test data for the working platform (piling mat) piled embankment tests using both EPS 70 and EPS 200, with some analysis and discussion of the results. The relevant tests are shown in Table 6.1. The pile cap size and pile spacing in all the tests is 30 mm and 100 mm respectively. Further discussion and analysis are given in Chapter 8.

Test code	Embankment thickness, h_e (mm)	Working platform thickness, h_w (mm)	EPS	$h_e/(s-a)$
RA28	140	60	70	2.0
RA29	**270**	60	70	3.9
RA30	140	**30**	70	2.0
RA31	140	60	**200**	2.0

(N.b. 1g values are presented)

Table 6.1 Summary of working platform piled embankment test series

The feature which 'differentiates' each test is highlighted in bold. At 30g the 'standard' dimensions (RA28) correspond to pile caps of 0.9 m, spaced at 3.0 m, with a 4.2 m high embankment. The corresponding working platform thickness h_w, Figure 4.1, is 1.8 m, which is deliberately large so that the effect of this aspect can be clearly observed. Test

RA29 considers increased embankment height of 8.1 m, RA30 considers a thinner (0.9 m) working platform. The softer subsoil (EPS 70) is generally considered, but RA31 uses the stiffer subsoil (EPS 200).

6.2 Test results

6.2.1 Load cell results

Figures 6.1 - 6.4 show the calibrated load cell output (in Newtons), showing increase with g-level in each test for each load cell, and a line representing an efficacy of 1.0 based on the initial embankment height above pile cap level - it will later be noted that there was significant uniform settlement of many of the embankments considered in this chapter, hence effectively reducing this value. The locations of the load cells are also shown (where available). The results of Chapters 4 and 5 indicate that for the value of $h_e/(s\text{-}a)$ used in these tests an efficacy close to 1.0 would ordinarily be anticipated.

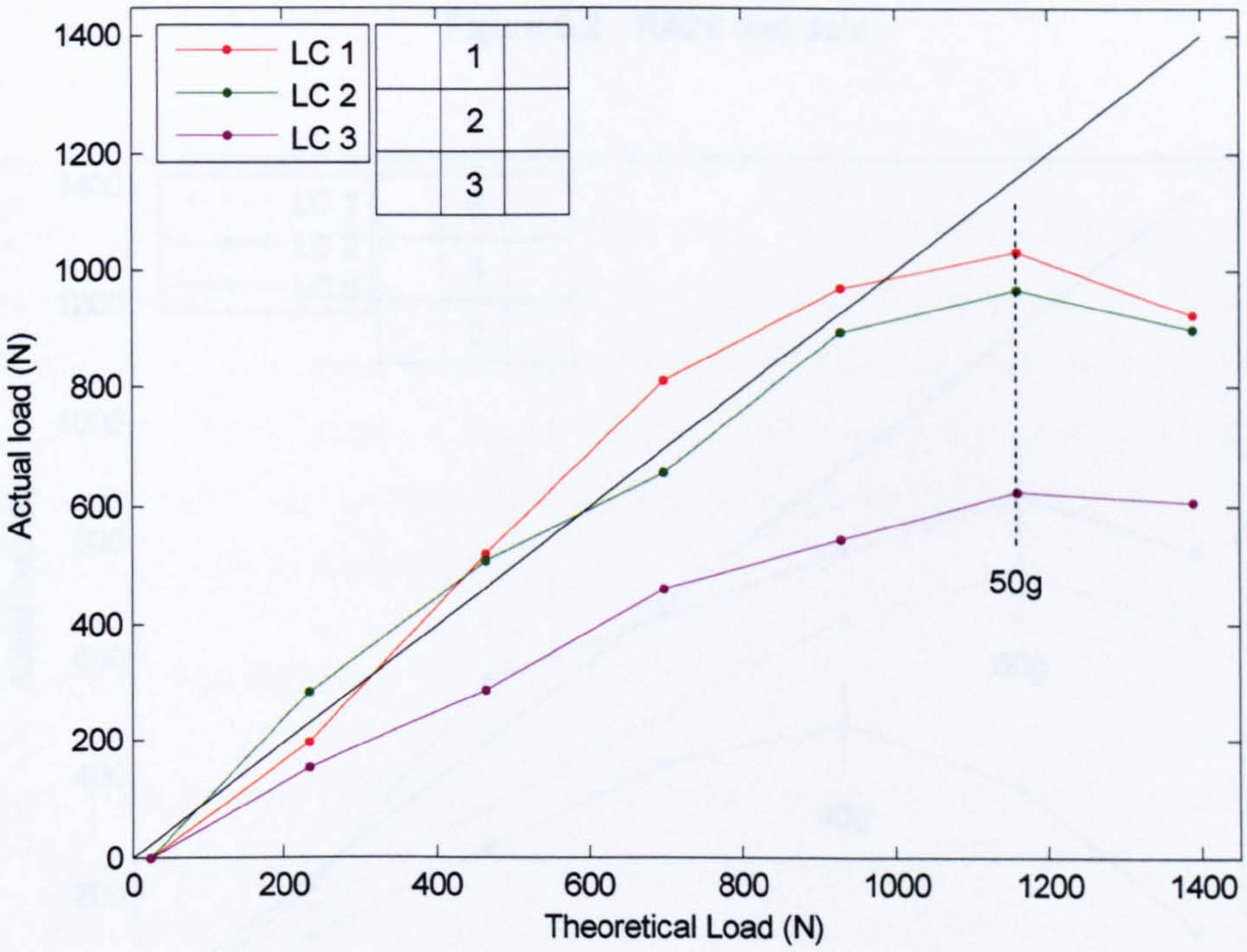

Figure 6.1 - RA28 test data

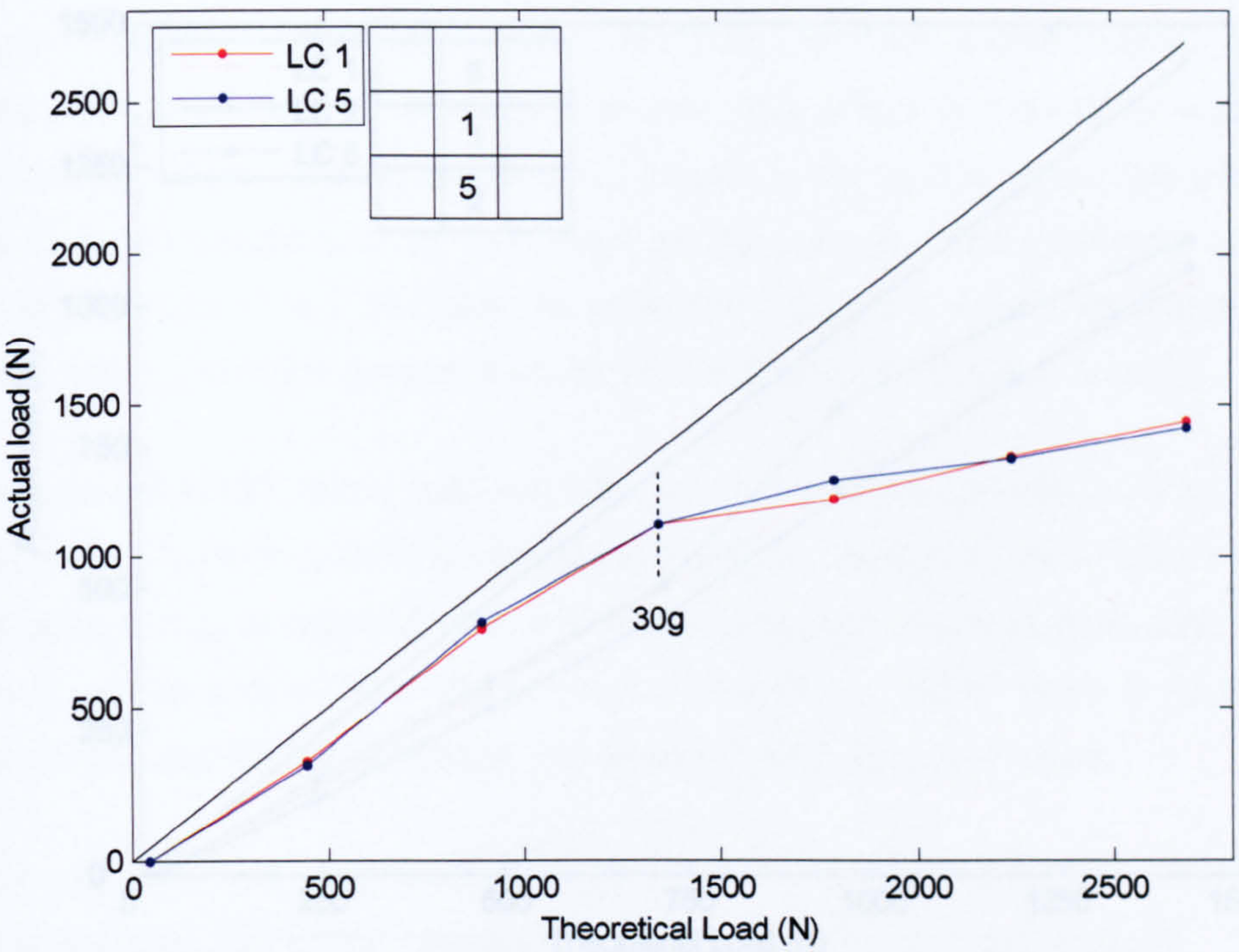

Figure 6.2 - RA29 test data

Figure 6.3 - RA30 test data

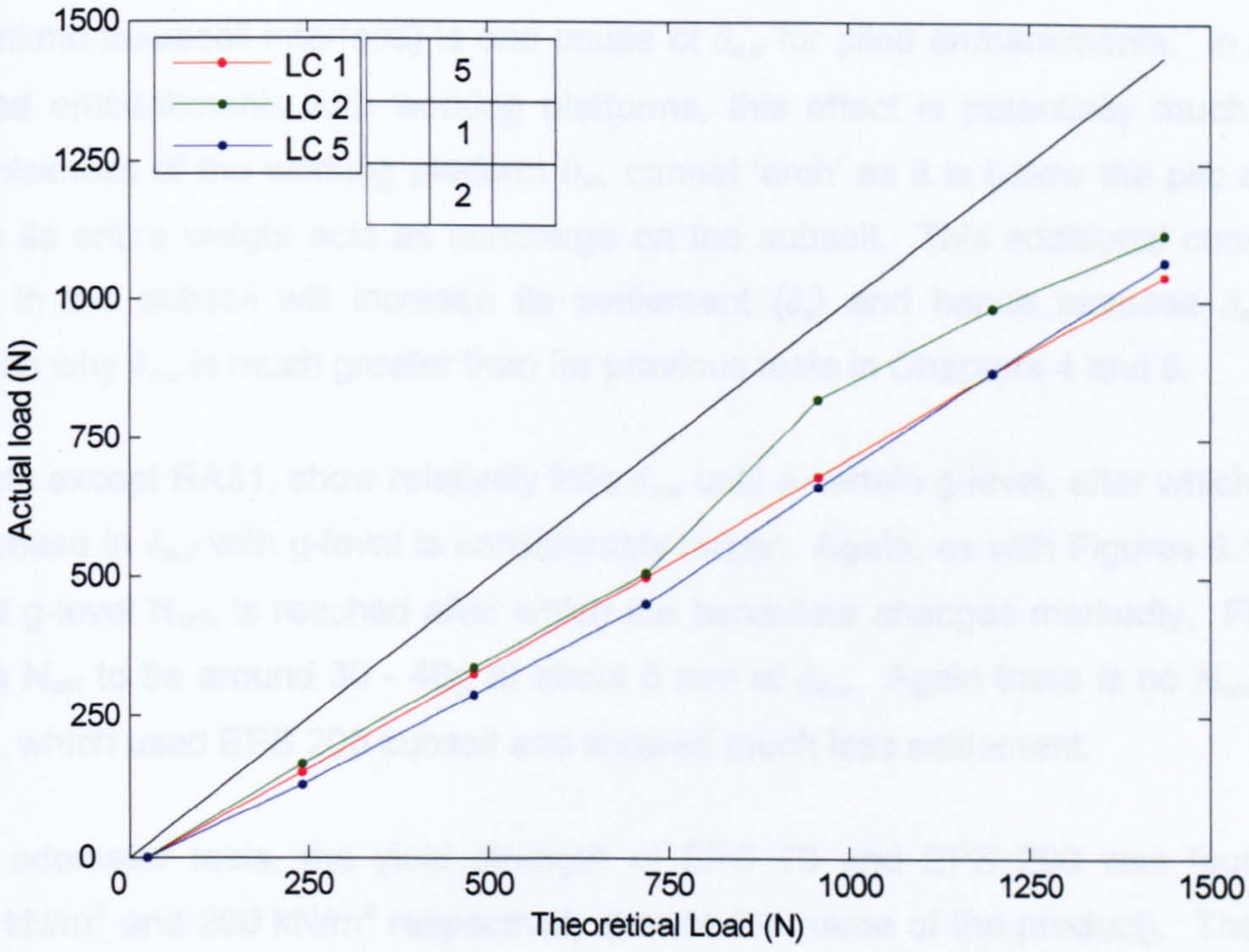

Figure 6.4 - RA31 test data

Figures 6.1 - 6.3 clearly show that after a certain g-level, the efficacy reduces from an initial value of approximately 1.0 (or slightly less). Therefore, for the purposes of these tests, an N_{crit} value has been defined and will be used to highlight the g-level at which the test behaviour changes. Test RA31 (Figure 6.4) does not have any N_{crit} as it showed linear behaviour with efficacy close to 1.0 throughout the entire test. The N_{crit} value for each load cell is shown using a dashed line, with values of 50g, 30g and 40 or 50g for RA28, RA29 and RA30 respectively.

6.2.2 Settlement results

The test series showed relatively little differential settlement at the embankment surface ($\delta_{e,d}$). The measured $\delta_{e,d}$ for RA28 was 0.5 mm at 60g and 0.4 mm for Test RA30 at 60g. $\delta_{e,d}$ in Tests RA29 and RA31 was less than 0.2 mm and hence could not be reliably discerned.

By comparison 'uniform' settlement at the top of the embankment ($\delta_{e,u}$) was generally extremely large as shown in Figure 6.5.

In Chapter 4 it was mentioned that settlement at the base of the embankment (the embankment-subsoil interface) is one cause of $\delta_{e,u}$ for piled embankments. In the case of piled embankments with working platforms, this effect is potentially much greater. The thickness of the working platform h_w, cannot 'arch' as it is below the pile caps and hence its entire weight acts as surcharge on the subsoil. This additional compressive strain in the subsoil will increase its settlement (δ_s) and hence increase $\delta_{e,u}$. This explains why $\delta_{e,u}$ is much greater than for previous tests in Chapters 4 and 5.

All tests except RA31, show relatively little $\delta_{e,u}$ until a certain g-level, after which the rate of increase in $\delta_{e,d}$ with g-level is considerably larger. Again, as with Figures 6.1 - 6.3, a critical g-level N_{crit}, is reached after which the behaviour changes markedly. Figure 6.5 shows N_{crit} to be around 30 - 40g at about 5 mm of $\delta_{e,u}$. Again there is no N_{crit} for Test RA31, which used EPS 200 subsoil and showed much less settlement.

From odometer tests, the yield strength of EPS 70 and EPS 200 was found to be $\approx$ 70 kN/m^2 and 200 kN/m^2 respectively (hence the name of the product). The change in gradient of the $\delta_{e,u}$ data in Figure 6.5 during the test seems to suggest that the EPS 70 subsoil yielded.

In Tests RA28-30, the significant increase in $\delta_{e,u}$ does not show any significant increase in the load acting on the piles (Figures 6.1 - 6.3), and at 50-60g the load on the piles actually reduces in two of the tests. This behaviour is explained in more detail later on in the context of a ground reaction curve (GRC). In these tests, considerable $\delta_{e,u}$ occurs but there is no significant $\delta_{e,d}$. According to Hewlett & Randolph (1988) in embankments which experience high $\delta_{e,u}$, the embankment fails by the piles 'punching' into the embankment fill which probably explains what is happening here as the EPS 70 subsoil yields. Figure 6.5 clearly shows that the EPS 200 subsoil is sufficiently strong enough to cope with the load exerted on it and does not reach its yield point.

Apart from the increase in $\delta_{e,u}$ with g-level, the following trends are evident from Figure 6.5 for EPS 70:

- For a given h_e, $\delta_{e,u}$ tends to increase with h_w, particularly around 40 to 50g
- For given h_w, $\delta_{e,u}$ tends to increase as h_e increases

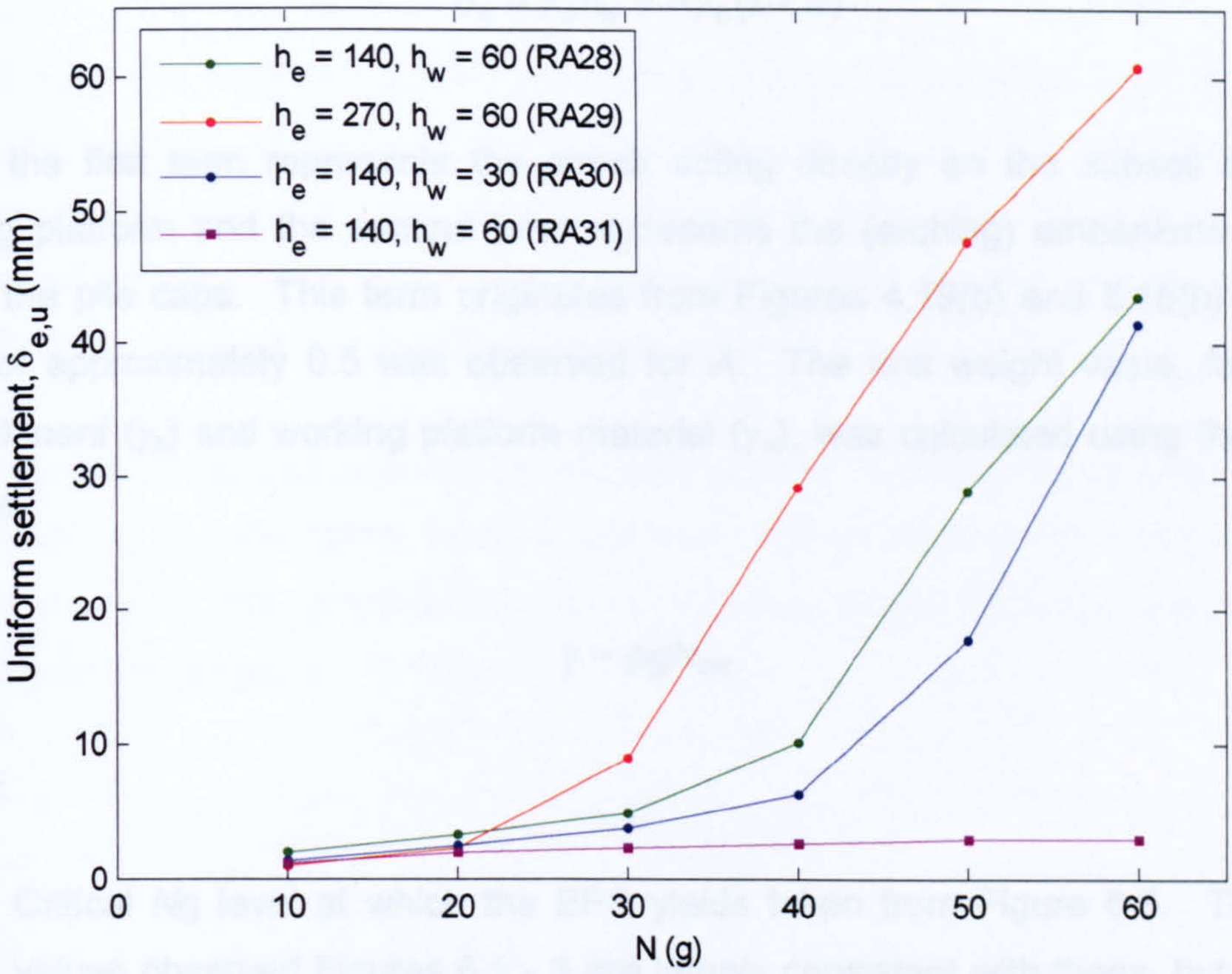

Figure 6.5 - Uniform settlement lines at the embankment surface, $\delta_{e,u}$

The first observation seems reasonable. All the weight of the working platform is transferred onto the subsoil (EPS) and therefore increase in h_w will cause more $\delta_{e,u}$. At 60g, the $\delta_{e,u}$ values for Tests RA28 and RA30 converge again. This is perhaps unexpected, but indicates significant yield of the EPS in both cases.

Once arching begins to 'break down' at large settlement (high g), the majority load of the embankment will also be transferred onto the subsoil, increasing δ_s and hence $\delta_{e,u}$. The difference in h_e for tests RA28 and RA29 is very large; 140 and 270 mm (at 60g this is nearly 8 m difference) and hence it seems reasonable that $\delta_{e,u}$ should show significant increase. There is inherently increased tendency for 'punching' of the piles into the base of the embankment for high embankments (Hewlett & Randolph, 1988), and this would be consistent with the observation that the highest embankment shows tendency for significant settlement at slightly lower g-level (30g) than the other tests.

As it is now clear that the EPS in tests RA28-29 yielded, the yield stress of the EPS can be inferred using the following formula:

$$\sigma_s = \gamma_w h_w + A\gamma_e(s-a) \qquad \text{Eqn. 6.1}$$

where the first term represents the stress acting directly on the subsoil due to the working platform and the second term represents the (arching) embankment material above the pile caps. This term originates from Figures 4.19(b) and 5.15(b) where the value of approximately 0.5 was observed for *A*. The unit weight value, for both the embankment (γ_e) and working platform material (γ_w), was calculated using the following formula:

$$\gamma = \rho g N_{crit} \qquad \text{Eqn. 6.2}$$

Where:

N_{crit}= Critical *N*g level at which the EPS yields taken from Figure 6.5. The 'critical' values observed Figures 6.1 - 3 are largely consistent with these, but tend to be slightly higher.

From equation 6.1, the apparent yield stress of EPS 70 in the tests was:

- RA28: 63 kN/m^2 (N_{crit} = 40, h_w+0.5(s-a) = 95 mm)
- RA29: 48 kN/m^2 (N_{crit} = 30, h_w+0.5(s-a) = 95 mm),
- RA30: 42-53 kN/m^2 (N_{crit} = 40-50, h_w+0.5(s-a) = 65 mm).

These values compare reasonably well with the value of 70 kN/m^2 from the odometer tests, but are somewhat lower in general. Thus there is significant evidence that 'yield' of the subsoil leads to very significant uniform settlement of the embankment surface and reduction in efficacy. It can also be noted that the settlement of about 5 mm at the point of yield (Figure 6.5) implies a strain of about 3 % in the subsoil (assuming $\delta_{su} \approx \delta_s$, Figure 4.18), corresponding well with the yield strain in the EPS.

6.3 Analysis of results

Figures 6.6 - 6.8 show the ground reaction curves (GRCs) derived from the test data (See section 2.4.2). RA31 has been omitted as the EPS did not yield in the test. The plots show the stress on the subsoil, normalised using the nominal embankment overburden stress according to Iglesia et al (1999), showing variation with $\delta_{e,u}$ normalised by the clear spacing between pile caps (s-a).

The stress on the subsoil was calculated using Equation 6.3 where the value of the load on the pile cap Q_c, was taken from the test data. Hence there is one point on the GRC per g-level. $h_{e,c}$ is the current embankment height above the pile caps (adjusted to take into account the (large) $\delta_{e,u}$ i.e. $h_{e,c} = h_e - \delta_{e,u}$).

$$\sigma_s = \frac{s^2 h_{e,c}\gamma_e - Q_c}{s^2 - a^2} \qquad \text{Eqn. 6.3}$$

The nominal overburden stress σ_o, was calculated using Equation 6.4 (again using $h_{e,c}$).

$$\sigma_o = \gamma_e h_{e,c} \qquad \text{Eqn. 6.4}$$

Where:

γ_e = $\rho_e g N$ = Unit weight of embankment fill (kN/m^2)

Figures 6.6 - 6.8 should strictly show the settlement in the embankment material at the pile cap level (normalised by (s-a)) on the x - axis, however $\delta_{e,u}$ was used as it was readily available.

The GRC plots were set to equal 1.0 on the σ_s/σ_o (y -axis) for zero $\delta_{e,u}$ in accordance to Iglesia et al (1999) corresponding to no arching.

All GRC plots show that the stress on the subsoil initially reduces very rapidly with settlement until the 'point of maximum arching'. This point occurs at a value of about 0.05 (5 %) for $\delta_{e,u}/(s$-$a)$ for all the tests (at an acceleration of 20g). This corresponds

well to Iglesia et al's (1999) findings of 2 - 6%. Test RA28 shows a very low value of minimum stress, corresponding to data which are very close to an efficacy of 1.0 (Figure 6.1). As previously noted (Chapters 4 and 5), it is difficult to reliably establish the stress on the subsoil when the efficacy is close to 1.0.

After this point the 'loading recovery stage' can be seen in all tests, referring to the transition from the maximum arching state to the ultimate state. By the end of the test a normalised stress of about 0.5 is reached. However, note that the rate of increase of stress during the recovery stage is much slower than the initial rate of reduction as arching develops.

Figures 6.6 - 6.8 clearly show the point of maximum arching is directly related to $\delta_{e,u}$ and as $\delta_{e,u}$ increases beyond this point, the effect of arching slowly decreases. As a result, it can be said that a certain amount of δ_s is beneficial to the embankment's ability to arch, but too much is detrimental.

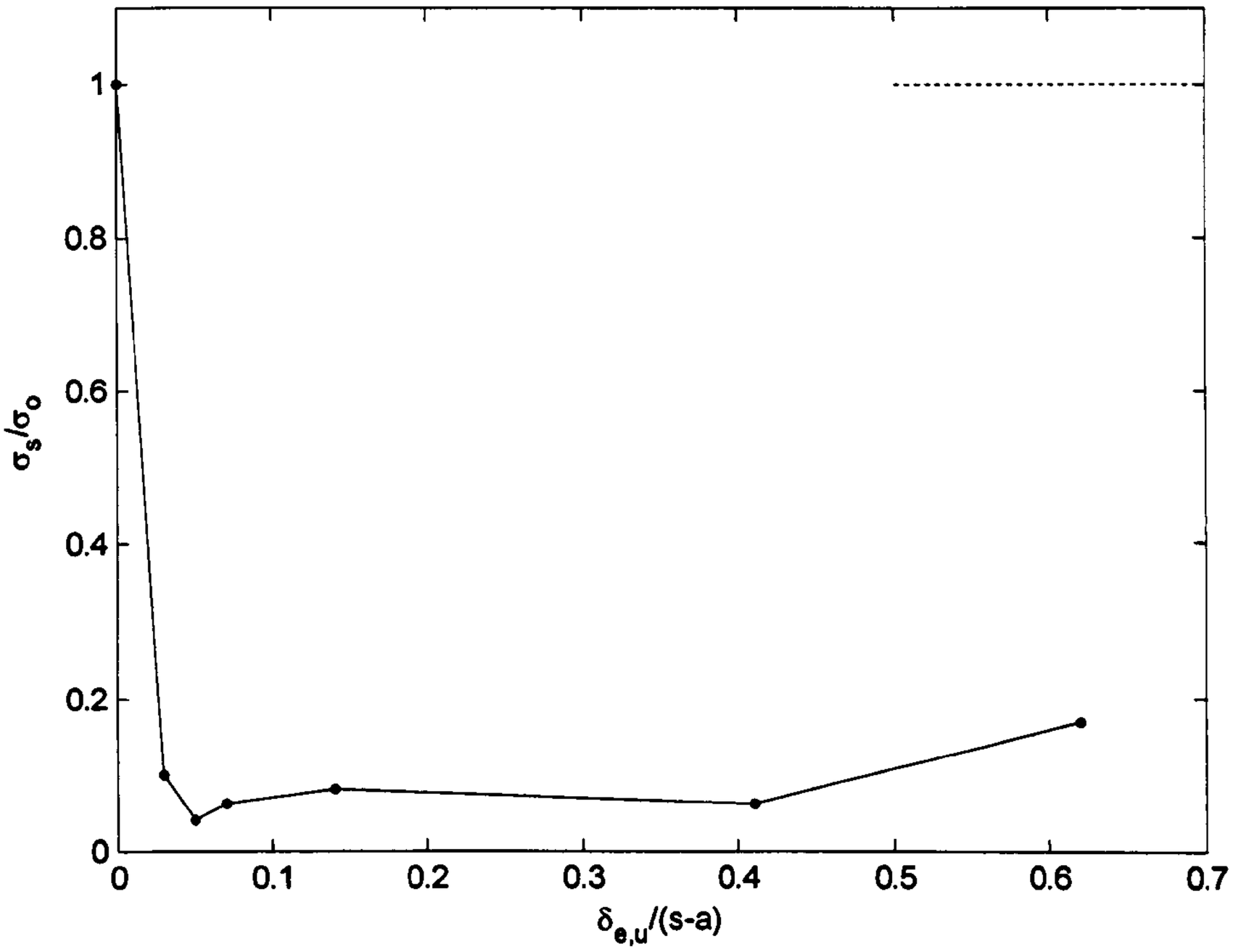

Figure 6.6 - RA28 ground reaction curve

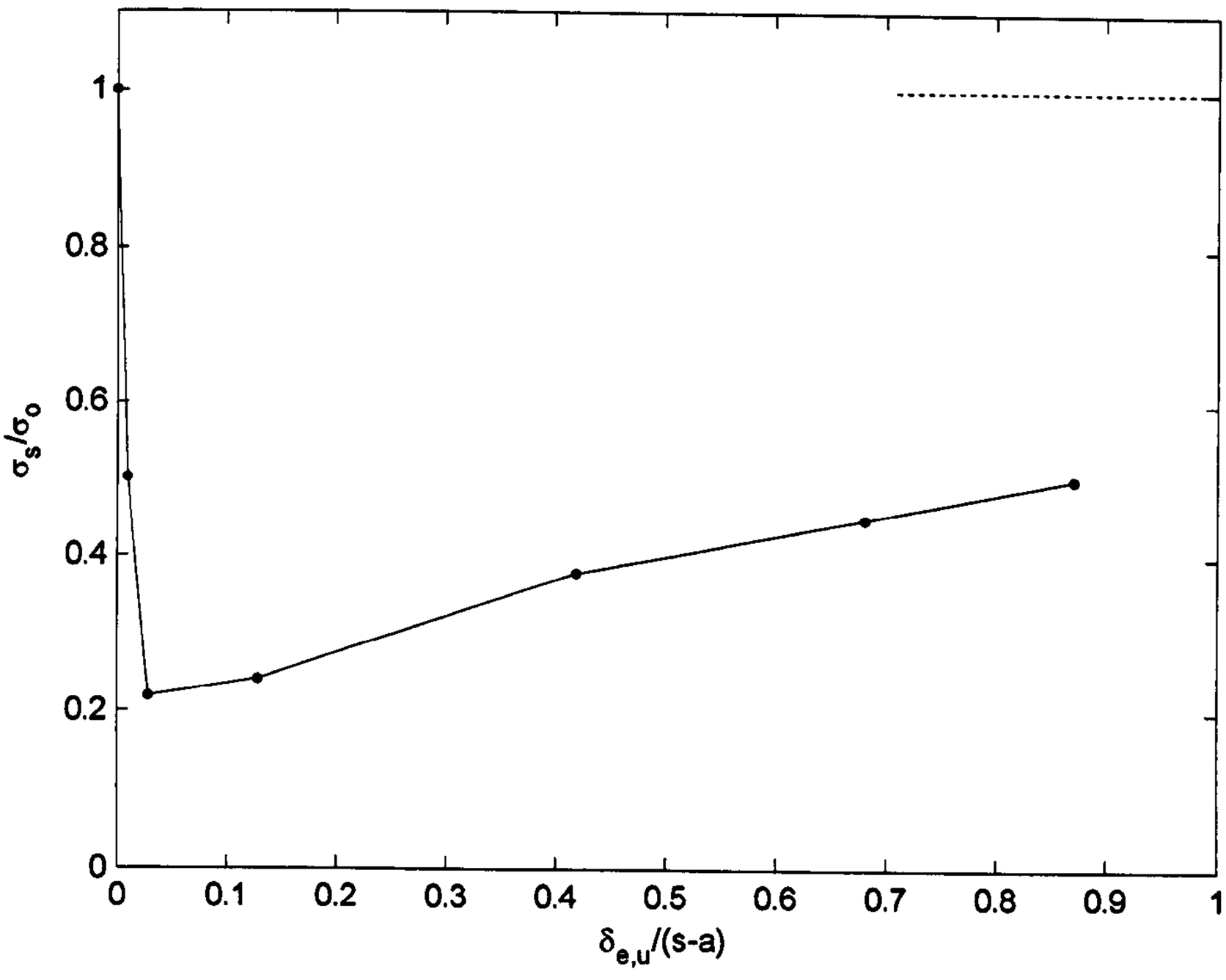

Figure 6.7 - RA29 ground reaction curve

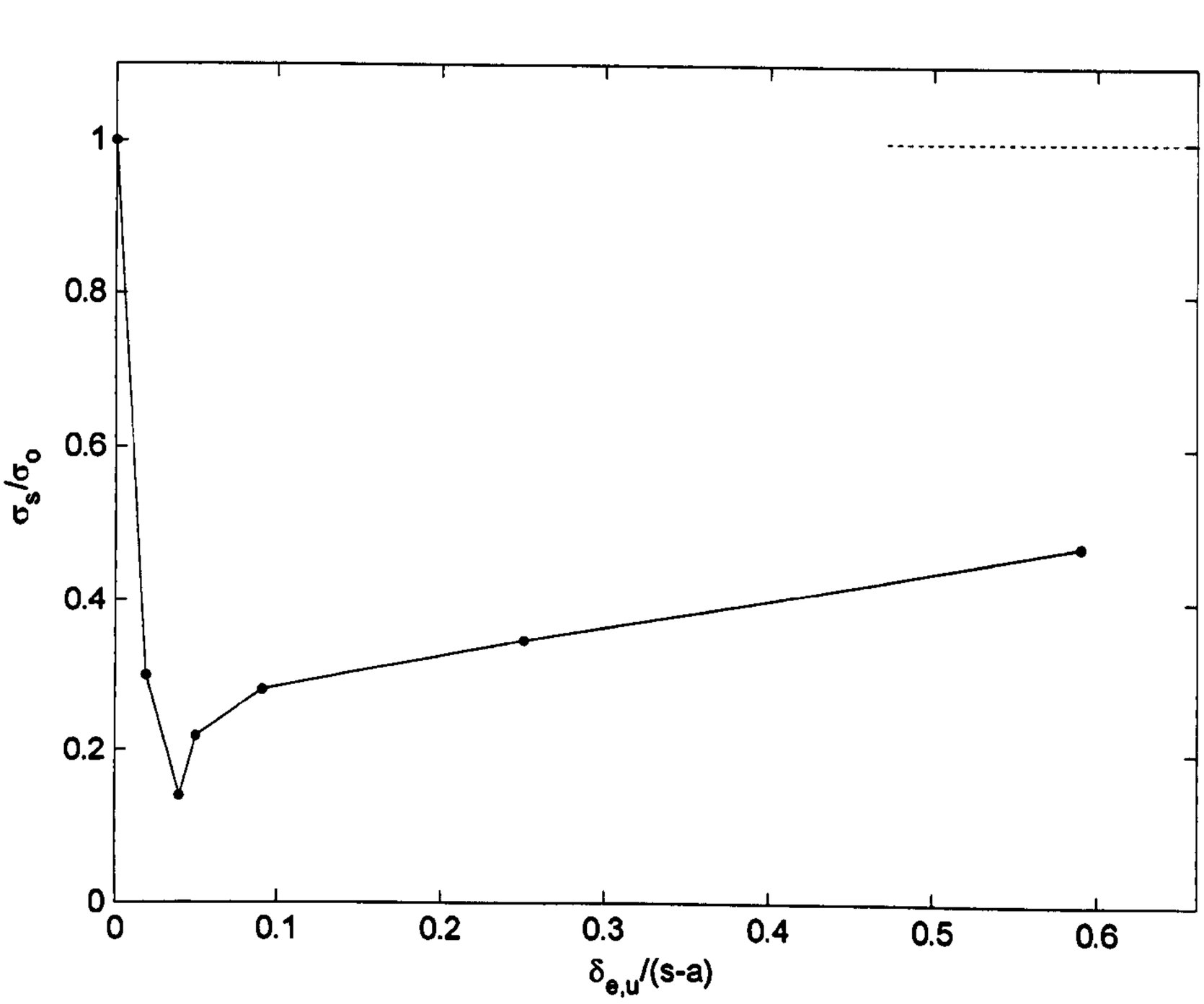

Figure 6.8 - RA30 ground reaction curve

6.4 Summary

The loading from the working platform acts directly on the subsoil and is the main cause of the large $\delta_{e,u}$ measured.

Little $\delta_{e,d}$ was observed as the embankments failed by fill material settling well below the pile cap level. It can be postulated that the piles 'punched' into the embankment fill material which, with the height of the embankments used, caused little or no $\delta_{e,d}$.

As $\delta_{e,u}/(s\text{-}a)$ increases to about 0.05, the efficacy of the embankment increases rapidly to its highest value; the 'point of maximum arching'. After this point, the efficacy slowly reduces towards an ultimate state.

CHAPTER 7

CENTRIFUGE TEST DATA – REINFORCED PILED EMBANKMENT

7.1 Introduction

The aim of this chapter is to present the centrifuge test data for the reinforced piled embankment tests, with some analysis and discussion of the results. The tests that will be summarised here are shown in Table 7.1. The pile cap size in all the tests is 30 mm. Further discussion and analysis is given in Chapter 8. The differences in the types of geogrid (G1 and G2), mainly stiffness, is discussed below.

Test code	Embankment thickness, h_e (mm)	Pile spacing, s (mm)	Geogrid type	$h_e/(s-a)$
RA32	50	100	G1	0.7
RA33	50	100	G2	0.7
RA34	50	75	G2	1.1

(N.b. model scale values are presented)

Table 7.1 - Summary reinforced piled embankment test series

As the geogrid was not in contact with the subsoil (EPS), it is assumed all the load from the embankment is transferred onto the pile caps through the geogrid. Therefore, no load cell data is shown. Indeed, the low embankment height implies that there will be little or no arching (Chapters 4 and 5), and thus the geogrid is approximately subjected to a known uniform stress. The geogrid itself will act primarily as a tensile membrane,

and the tests do not attempt to recreate any other 'composite reinforced material' action that may be associated with distributed multiple layers of geogrid.

7.2 Geogrid stiffness

As discussed in Section 3.3.6, two types of model geogrid were used.

In order to assess the stiffness parameters of the two types of geogrid, simple short-term extension tests, where the material was clamped at either end and loaded, were carried out. The results from these tests are shown in Figure 7.1 and 7.2 for G1 (where one loading test is shown) and G2 (where 4 loading tests are shown) respectively. The G1 test sample had a width of 69 mm and length of 120 mm. The G2 test sample had an average width of 50 mm except the 4th loading test which had a width of 30 mm and all had an average length of 100 mm.

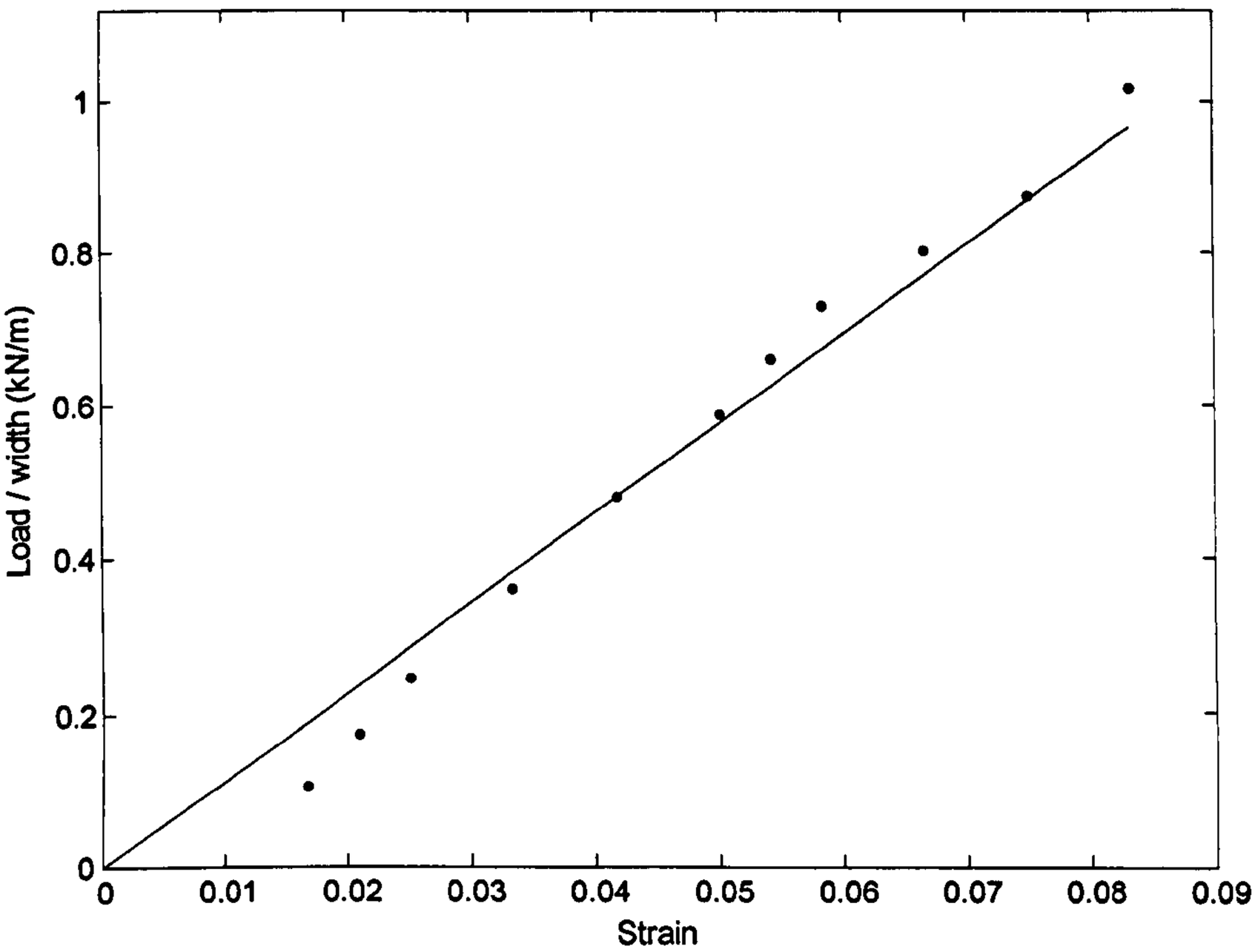

Figure 7.1 - G1 geogrid stiffness

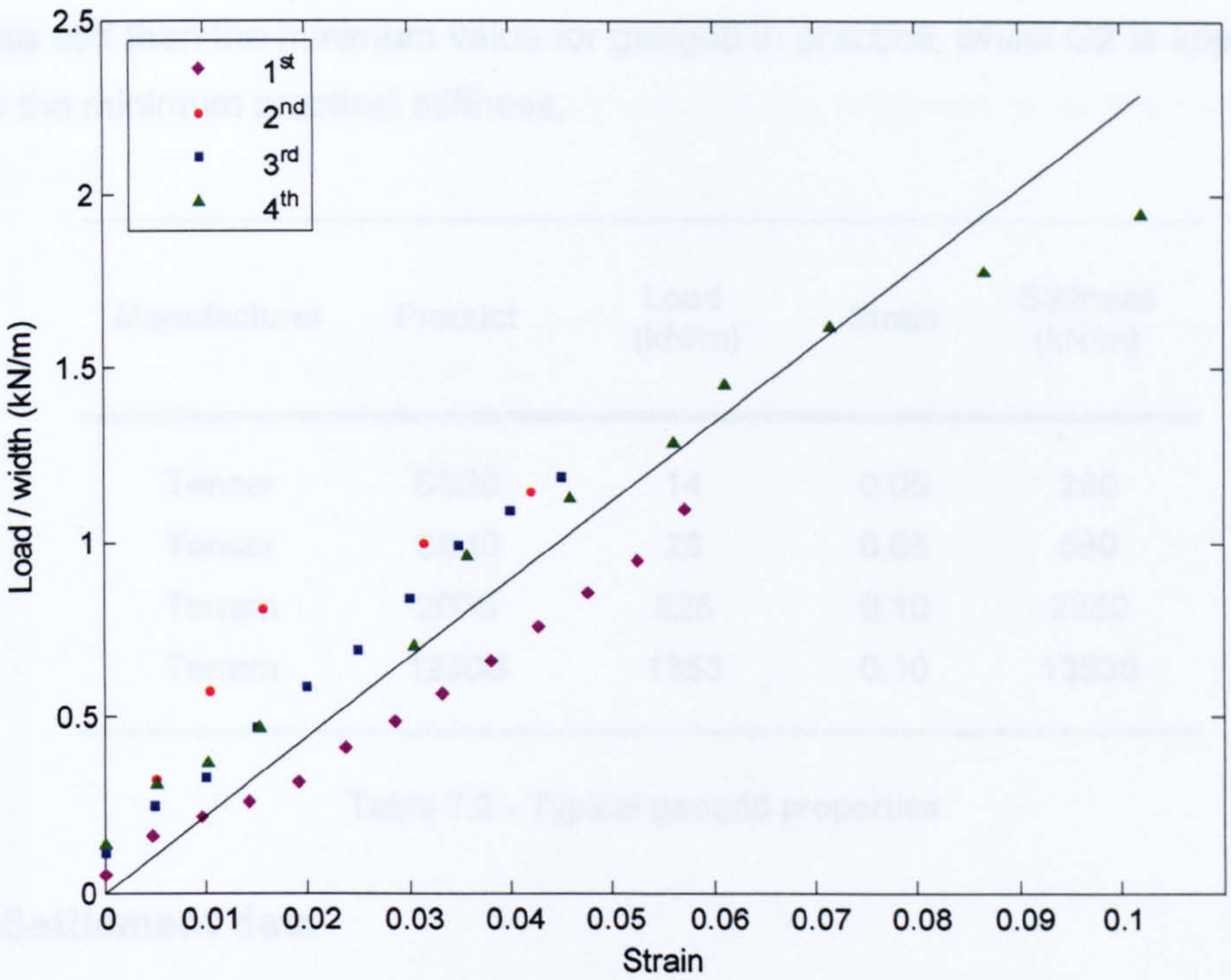

Figure 7.2 - G2 geogrid stiffness

From Figures 7.2 and 7.3, the stiffness of the geogrids (at 1g) are 12 kN/m and 26 kN/m, for G1 and G2 respectively. Therefore at 30g, these values correspond to 360 kN/m (G1) and 780 kN/m (G2), based on the scaling factor N in Table 3.1.

Table 7.2 shows typical properties for geogrids used in piled embankments. Load and corresponding strain have been taken from manufacturer's literature, and the secant stiffness calculated. It should be noted that the values presented are for short term applied loads, i.e. the material experienced no creep in testing. Therefore actual long term stiffness values may be approximately two times lower than shown.

Additionally, the Tensar geogrid would typically be used with 3 grids (distributed through the bottom 1 m of the embankment), so the values for the Tensar geogrid could be argued to be effectively three times stiffer than a single geogrid (presented) in practice.

Thus typical long-term stiffness is about 1000 kN/m or more for the actual geogrids. The values for the model grid are short-term. They are directly applicable to loading for a few minutes in the centrifuge tests, but will be compared with long-term values for actual

geogrids which are applicable to design in the field. Thus at 30g G1 would be about 3 times less stiff than the minimum value for geogrid in practice, whilst G2 is approximately equal to the minimum practical stiffness.

Manufacturer	Product	Load (kN/m)	Strain	Stiffness (kN/m)
Tensar	SS20	14	0.05	280
Tensar	SS40	28	0.05	560
Terram	200S	225	0.10	2250
Terram	1250S	1353	0.10	13530

Table 7.2 - Typical geogrid properties

7.3 Settlement data

Figure 7.3 shows the differential settlement data from the reinforced piled embankment test series. All tests have h_e = 50 mm. All data shows approximately linear increase with g-level.

During Test RA32 (s = 100 mm, G1), the tension in the model geogrid exceeded its ultimate tensile strength and tore at 50g (mainly along the edges of the pile caps) causing the embankment fill to fall to the EPS beneath. Because of this, settlement for Test RA32 (both differential ($\delta_{e,d}$) and uniform ($\delta_{e,u}$)), are only presented up to 50g.

As expected, Test RA32 (s = 100 mm, G1), with the lower stiffness geogrid, showed the most $\delta_{e,d}$. The use of the higher stiffness geogrid in Test RA33 (s = 100 mm, G2) resulted in slightly less $\delta_{e,d}$. However, the most significant impact on $\delta_{e,d}$ came from the pile spacing (s) in Test RA34 (s = 75 mm, G2). Reducing s from 100 mm to 75 mm caused a considerable reduction in $\delta_{e,d}$. As the maximum sag of the geogrid is likely to be directly related to the distance between the supports (s-a), it is no surprise that RA34 gave the least $\delta_{e,d}$. At s equal to 75, the geogrid spans considerably less distance (45 mm at 1g compared to 70 mm for s = 100 mm).

The settlement data for the reinforced piled embankment test series is large compared to the unreinforced test series reported in Chapters 4 and 5. However, there is no subsoil support in this series (the aim is to observe the response of tensile reinforcement in isolation).

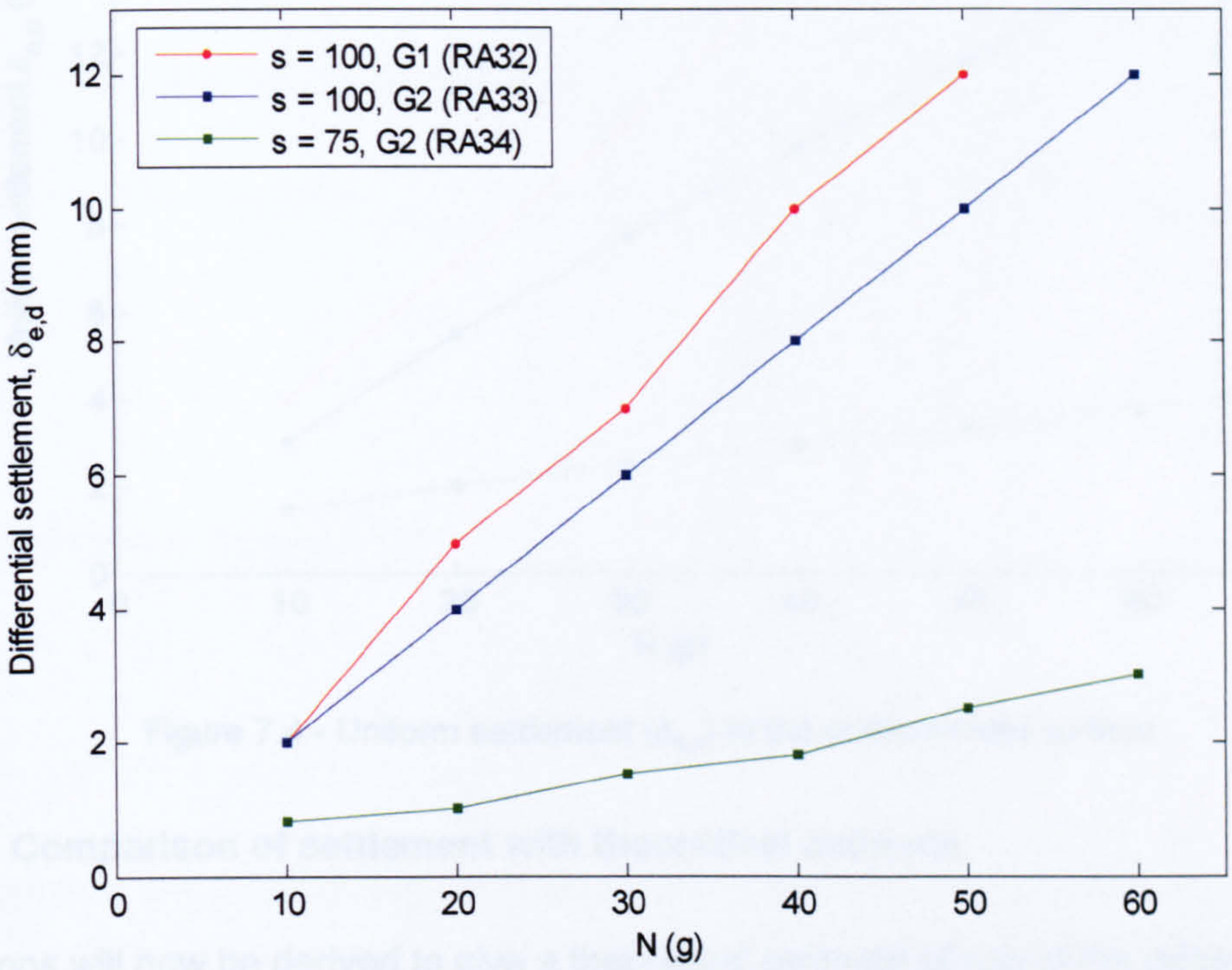

Figure 7.3 - Differential settlement ($\delta_{e,d}$) at the embankment surface

Figure 7.4 shows the uniform settlement of the embankment, $\delta_{e,u}$, for the tests. Like $\delta_{e,d}$, $\delta_{e,u}$ shows an approximately linear increase with g level all tests. Test RA32 (s = 100, G1) with the low stiffness geogrid, again showed the highest $\delta_{e,u}$. Comparing Tests RA32 and RA33 (s = 100 mm, G2), the higher stiffness geogrid again has some beneficial effect on $\delta_{e,u}$.

However, reducing s again appears to be the most beneficial method of reducing $\delta_{e,u}$. This is shown in Test RA34 (s = 75 mm, G2) which shows significantly less settlement than the other tests.

($\delta_{e,d}$ /$\delta_{e,u}$) is consistently equal to about 0.7, corresponding to a similar value in Chapters 4 and 5 for low embankments where there was little or no arching - also see Figure 4.17.

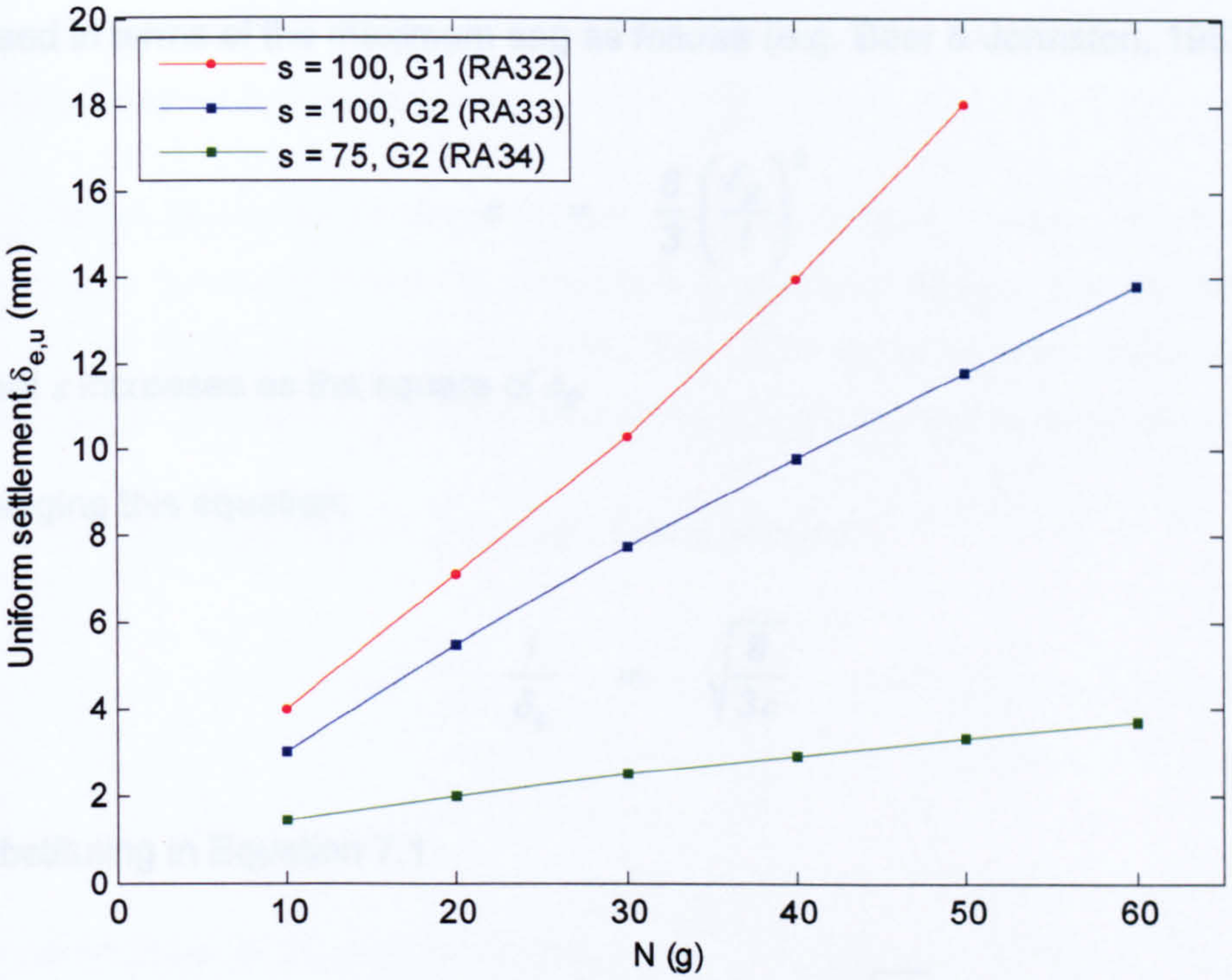

Figure 7.4 - Uniform settlement ($\delta_{e,u}$) at the embankment surface

7.3.1 Comparison of settlement with theoretical estimate

Equations will now be derived to give a theoretical estimate of sag of the geogrid.

Assuming that the geogrid is subjected to a uniform vertical load and deforms as a parabola, using a plane-strain approach the constant horizontal component of tension in it can be linked to the load acting on it (e.g. Beer & Johnston, 1987):

$$T = \frac{wl^2}{8\delta_g} \qquad \text{Eqn. 7.1}$$

where

T = the constant horizontal component of tension in the geogrid (kN/m 'into the page')
w = the uniform stress acting on the geogrid (kN/m^2)
l = the length of the span (m)
δ_g = the maximum sag (vertical deflection) of the geogrid (m)

The average strain in the geogrid (ε) derived from the total length of the parabola can be expressed in terms of the maximum sag as follows (e.g. Beer & Johnston, 1987):

$$\varepsilon = \frac{8}{3}\left(\frac{\delta_g}{l}\right)^2 \qquad \text{Eqn. 7.2}$$

Note that ε increases as the square of δ_g.

Re-arranging this equation:

$$\frac{l}{\delta_g} = \sqrt{\frac{8}{3\varepsilon}} \qquad \text{Eqn. 7.3}$$

and substituting in Equation 7.1

$$T = \frac{wl}{8}\frac{l}{\delta_g} = \frac{wl}{2}\sqrt{\frac{1}{6\varepsilon}} \qquad \text{Eqn. 7.4}$$

This equation has close analogy with the following equation from BS8006

$$T_{rp} = \frac{W_T(s-a)}{2a}\sqrt{1+\frac{1}{6\varepsilon}} \qquad \text{Eqn. 7.5}$$

where

T_{rp} = the tensile load in the reinforcement (kN/m)

W_T = the distributed vertical load acting on the reinforcement between adjacent pile caps (kN/m)

The equation specifically considers sag in the geogrid between the two caps (a strip with width a and length (s-a)), and hence:

- (W_T/a) is equivalent to w
- (s-a) is equivalent to l

There is a slight difference in the terms involving strain, which arises from the BS8006 equation accounting for the maximum actual tension in the span rather than the horizontal component (Equation 7.4).

Hence BS8006 gives slightly larger tension for given load and span. However, tension in a geogrid is generally limited to about 5 % in practical design, and at this strain the tension is only 12 % lower using Equation 7.4. This equation also offers considerably more convenience in further development of the equations, and thus will be used.

The final equation links tension and strain in the geogrid:

$$T = k\varepsilon \qquad \text{Eqn. 7.6}$$

where

k = the stiffness of the geogrid (kN/m)

Substituting for T and ε from Equations 7.1 and 7.2 respectively

$$\frac{wl^2}{8\delta_g} = \frac{8k}{3}\left(\frac{\delta_g}{l}\right)^2 \qquad \text{Eqn. 7.7}$$

This can be re-arranged to express how the load which can be carried theoretically increases with the sag:

$$w = \frac{64k}{3l}\left(\frac{\delta_g}{l}\right)^3 \qquad \text{Eqn. 7.8}$$

(Both sides of the equation have units kN/m^2)

Since the tension in the geogrid is inversely proportional to the sag (Equation 7.1), dependency on δ_g (normalised by the span) is now cubic. In fact there is dependency on l^4, supporting observations from the data that spacing of the pile caps has considerably more impact than the stiffness of the geogrid.

The theoretical settlement has been calculated assuming that all the weight of the embankment is transferred uniformly onto the geogrid (the embankments are too low to arch significantly), which causes it to deflect and support the weight purely in tension. The maximum sag of the geogrid will be taken as the uniform settlement at the top of the embankment deduced from the image data ($\delta_{e,u}$). This is an approximation but no direct measurement of the sag was available. In any case, the equations have been derived for conditions of plane strain, and therefore it is not immediately obvious which length should be taken for the span. The longest span is across a diagonal, but this is an extreme, and not an approximation of plane strain. Therefore the span is taken between adjacent pile caps - i.e. l =(s-a).

Figures 7.5 - 7.7 show the theoretical load-deflection (sag) behaviour of the geogrid from Equation 7.8 using l = (s-a) compared with data from the tests (the nominal stress from the embankment $N\rho g h_e$, and $\delta_{e,u}$).

The uniform settlement shown in Figures 7.5 - 7.7 does not consider any sag in the geogrid at 1g. $\delta_{e,u}$ is effectively assumed to be zero at 1g when the first photo is taken. However, according to Equation 7.8, the deflection of the geogrid for Tests RA32, RA33 and RA34 is 4.2 mm, 3.3 mm and 1.8 mm respectively at the beginning of the test. Although the stress at 1g is very small (0.8 kN/m^2) the nature of the equation is cubic dependency on the sag. Any increase in sag (and $\delta_{e,u}$) observed relative to the values at 1g has this sag 'built in'. Therefore, Figures 7.5 - 7.7 show two lines for the deflection of the geogrid; either passing through the origin ('inc'), or excluding the sag which had occurred at 1g ('exc'). The latter is shifted by an amount equal to the calculated sag at 1g to the left, with a stress of 0.8 kN/m^2 at $\delta_{e,u}$ = 0.

It is evident that that the experimental data do not show the cubic response of the theoretical predictions, but rather the experimental response is approximately linear. Nevertheless, general agreement with either of the predictions is good for RA32 and RA33. For RA34 the experimental results show less sag than either of the theoretical predictions.

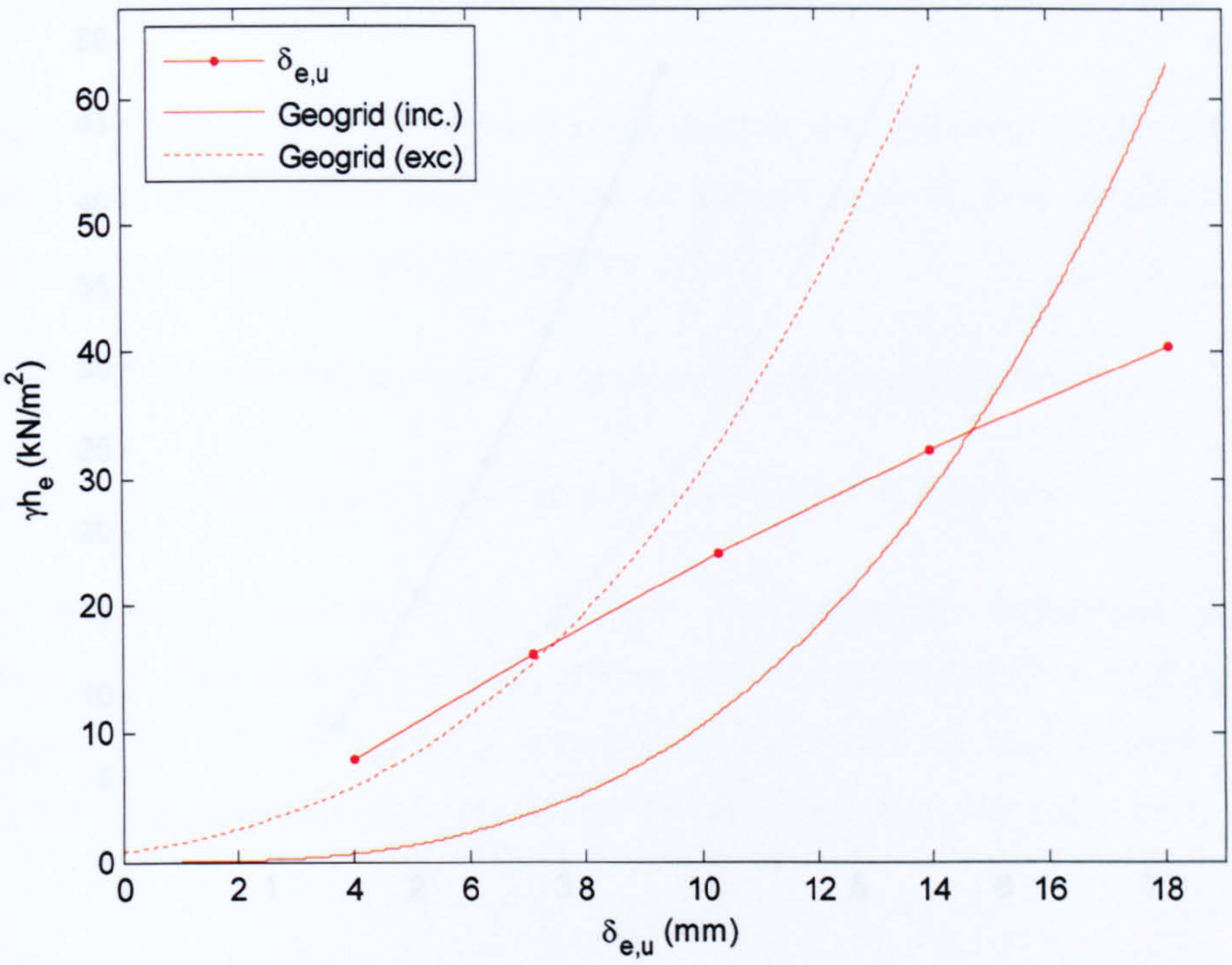

Figure 7.5 - $\delta_{e,u}$ and geogrid deflection (theoretical equation) for Test RA32

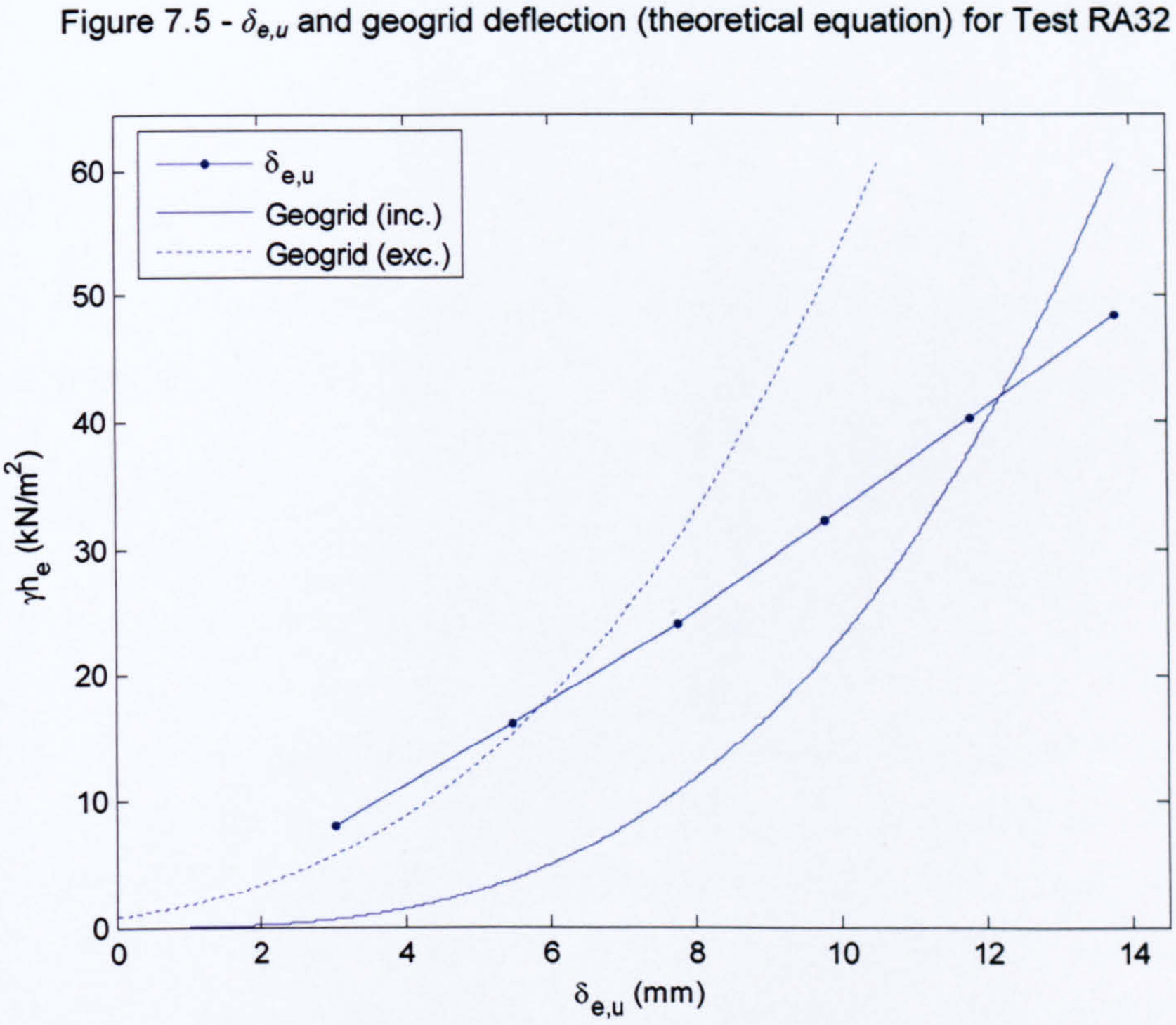

Figure 7.6 - $\delta_{e,u}$ and geogrid deflection (theoretical equation) for Test RA33

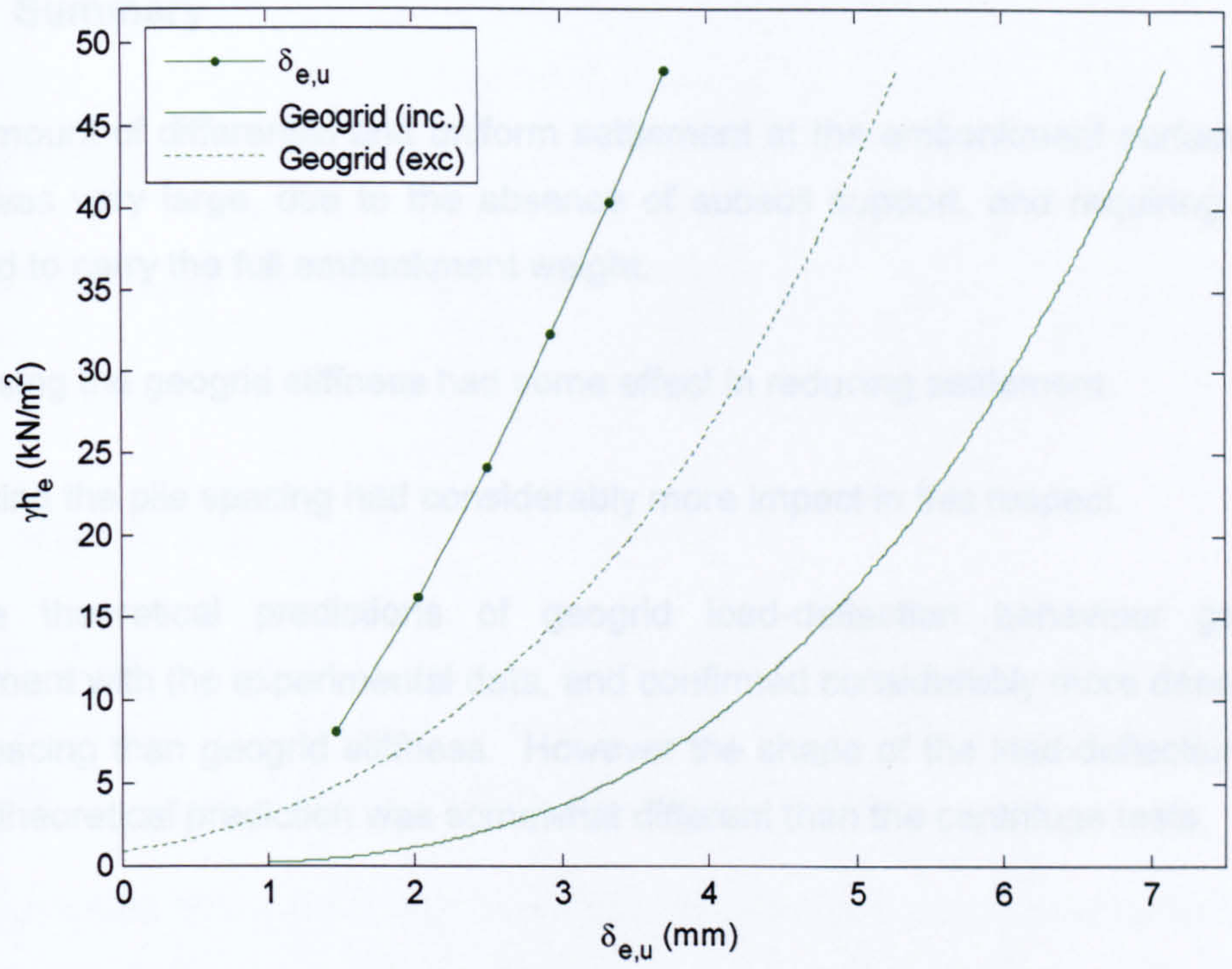

Figure 7.7 - $\delta_{e,u}$ and geogrid deflection (theoretical equation) for Test RA34

7.4 Summary

The amount of differential and uniform settlement at the embankment surface for these tests was very large, due to the absence of subsoil support, and requiring the model geogrid to carry the full embankment weight.

Increasing the geogrid stiffness had some effect in reducing settlement.

Reducing the pile spacing had considerably more impact in this respect.

Simple theoretical predictions of geogrid load-deflection behaviour gave broad agreement with the experimental data, and confirmed considerably more dependency on pile spacing than geogrid stiffness. However the shape of the load-deflection response in the theoretical prediction was somewhat different than the centrifuge tests.

CHAPTER 8

DISCUSSION OF RESULTS

8.1 Introduction

The aim of this chapter is to summarise the findings of the centrifuge tests and present further discussion of the results. This will include a comparison with the literature review presented in Chapter 2 before introducing two case studies.

The summaries of the tests have been split into the three categories of tests used in the previous chapters.

8.2 Summary of test results

8.2.1 Piled embankments

During the piled embankment test series, the following parameters were changed (pile cap size remained unchanged):

- pile spacing (s),
- embankment height (h_e) and
- subsoil stiffness (E_0') (actually modelled using EPS).

Using the ratio $h_e/(s\text{-}a)$, it was shown that for embankments with values of about 0.5, there is no evidence of arching based on the stress on the subsoil and there is significant differential settlement ($\delta_{e,d}$). As $h_e/(s\text{-}a)$ increases to 2.0, the stress acting on the subsoil (compared to the nominal overburden stress from the embankment fill) implies increasing effect of arching. $\delta_{e,d}$ also tends to reduce. For larger $h_e/(s\text{-}a)$ values, the efficacy of the embankment tends towards 1 and no $\delta_{e,d}$ was evident.

As expected, the stiffness of the subsoil proved to have an effect on settlement at the surface of the embankment - both differential ($\delta_{e,d}$) and uniform ($\delta_{e,u}$), with the softer EPS 70 giving more settlement. Furthermore, the maximum $\delta_{e,d}$ (when $h_e/(s-a) \approx 0.5$) was reduced approximately in proportion to the increase in stiffness.

In terms of the effect of the stiffness on the ability of the embankment to transfer load to the piles, the stiffness of the subsoil does not seem to have any significant effect - the $\sigma_s/\gamma(s-a)$ values for tests using both types of EPS was about 0.5.

8.2.2 Piled embankment with 'working platform'

The 'working platform' is below the elevation of the pile caps and hence arching zone. Therefore it acts as a surcharge with its entire load compressing the subsoil. This in turn increases $\delta_{e,u}$. Ground Reaction Curves (GRCs) were derived from the data, and it was shown that the settlement of the subsoil (assumed to be similar to $\delta_{e,u}$) has a direct relation with the load transfer of the embankment. As $\delta_{e,u}$ increases, the effect of arching increases until the 'point of maximum arching' where the subsoil stress was at its minimum value. This point was found to occur when $\delta_{e,u}$ was approximately 5% of $(s-a)$. After this point, the effect of arching was shown to slowly reduce with increasing subsoil settlement.

8.2.3 'Reinforced' piled embankment

The 'reinforced' piled embankment tests considered geogrid placed directly on the pile caps with no support from the subsoil. Two types of geogrid were tested (1g stiffness values; 12 kN/m and 26 kN/m). As expected the less stiff model geogrid showed higher $\delta_{e,d}$ and $\delta_{e,u}$. However, reducing the pile spacing and hence the distance between the supports of the geogrid had the most beneficial impact on reducing $\delta_{e,d}$ and $\delta_{e,u}$.

8.3 Literature review comparison

This section will compare a selection of available design methods with the test data as follows:

- Terzhagi,
- Hewlett & Randolph,
- BS8006,
- Guido,
- Kempfert et al.

The results are shown in Figures 8.4-8.8 following an introduction of each method below.

8.3.1 Terzaghi method

Equation 8.1 (Russell & Pierpoint, 1997) has been plotted (Figure 8.4) with $D = s$ to represent the frictional boundaries (shown in red) in the shape of a cruciform shown in Figure 8.1 (a), and $D = a$ where only the boundaries of the pile caps provide vertical resistance, Figure 8.1 (b).

$$\sigma_s = \frac{\gamma h_e (s^2 - a^2)}{4 h_e D K \tan\varphi}\left(1 - e^{\frac{-4 h_e D K \tan\varphi}{(s^2 - a^2)}}\right) \qquad \text{Eqn. 8.1}$$

Some difficulty arises in choice of the earth pressure coefficient for the vertical faces of the prism. Handy (1985) proposed that it could be taken as $K = (1\text{-}sin^2\varphi)/(1+sin^2\varphi)$. Figure 8.2 illustrates derivation of this formula, on the basis that frictional failure is occurring on the vertical faces. This value seems reasonable and will be used here. Figure 8.4 also shows the equation adopted by Russell et al (2003) which is essentially the same as Eqn. 8.1 with $D = a$ and with the value of K taken to be 0.5.

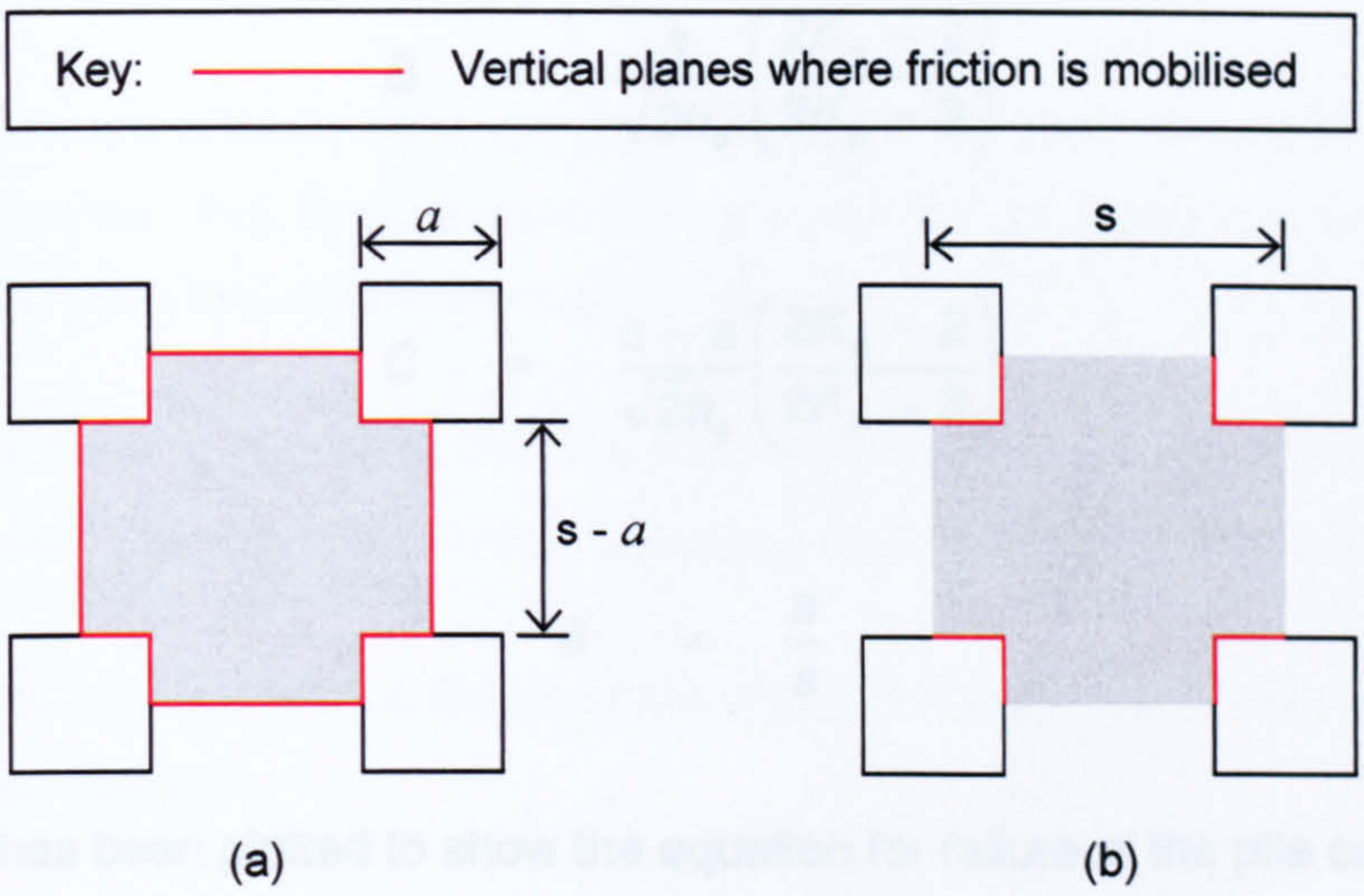

Figure 8.1 - Frictional boundaries: (a) cruciform method and (b) pile cap (boundaries) method

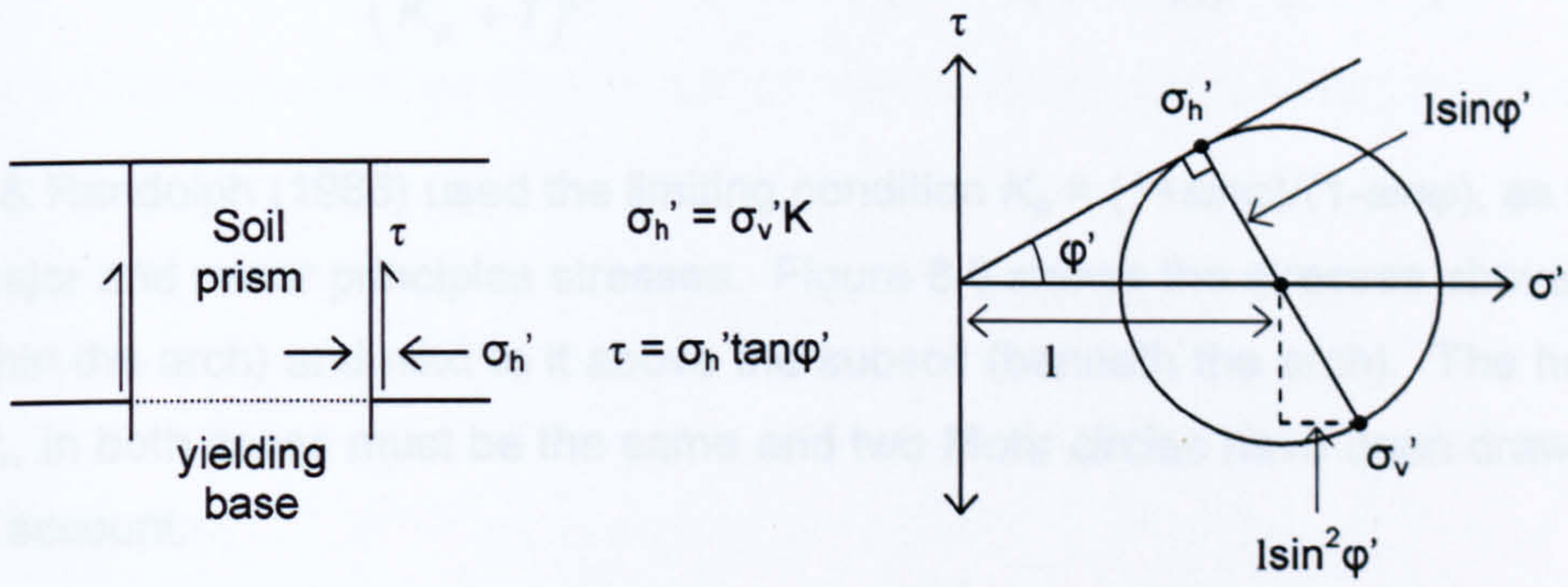

Figure 8.2 - *K* value used in Terzhagi method

8.3.2 Hewlett & Randolph method

Equation 8.2 (Love & Milligan, 2003) is plotted (Figure 8.5) to show the equation for failure at the crown of the arch.

$$\sigma_s = (A - AB + C)\gamma h_e \qquad \text{Eqn. 8.2}$$

where

$$A = (1 - \delta)^{2(K_p - 1)}$$

$$B = \frac{s}{\sqrt{2}h_e}\left(\frac{2K_p - 2}{2K_p - 3}\right)$$

$$C = \frac{s - a}{\sqrt{2}h_e}\left(\frac{2K_p - 2}{2K_p - 3}\right)$$

$$\delta = \frac{a}{s}$$

Equation 8.3 has been plotted to show the equation for failure at the pile cap.

$$\sigma_s = \frac{\gamma h_e}{\left(\frac{2K_p}{K_p + 1}\right)\left[(1-\delta)^{(1-K_p)} - (1-\delta)(1+\delta K_p)\right] + (1-\delta^2)} \qquad \text{Eqn. 8.3}$$

Hewlett & Randolph (1988) used the limiting condition $K_p = (1+sin\varphi)/(1-sin\varphi)$, as the ratio of the major and minor principles stresses. Figure 8.3 shows the stresses above the pile cap (within the arch) and next to it above the subsoil (beneath the arch). The horizontal stress σ_x, in both cases must be the same and two Mohr circles have been drawn taking this into account.

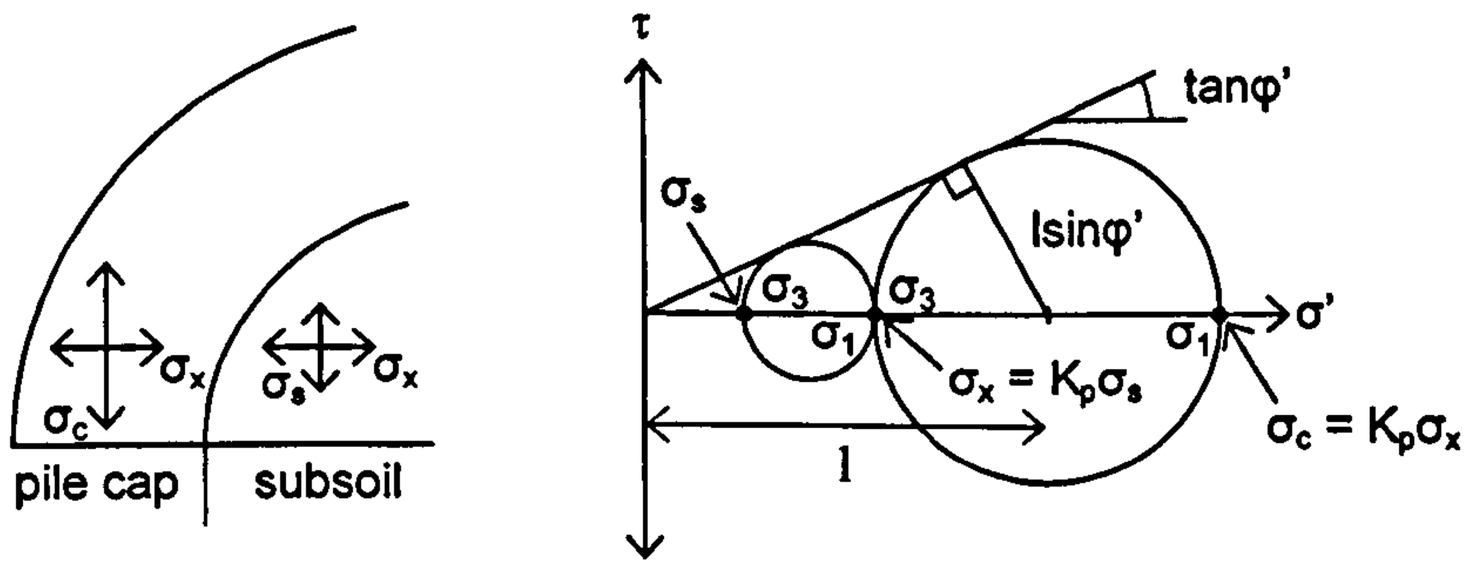

Figure 8.3 - *K* value used in Terzhagi method

8.3.4 BS8006 method

All partial factors were taken as 1 and therefore have not been shown in the equations. It has been assumed that there is no surcharge, and that the piles are 'unyielding' since this would have been the case in the centrifuge tests.

The equations have in fact been inferred from the equation for W_T (the distributed load between adjacent pile caps) in BS8006 assuming that $\sigma_s = W_T/s$ (Love & Milligan, 2003).

Equation 8.4 is used for piled embankments where $0.7(s\text{-}a) < h_e < 1.4(s\text{-}a)$ (ignoring the term for any surcharge);

$$\sigma_s = \frac{\gamma h_e}{s^2 - a^2}\left[s^2 - a^2(\sigma_c/\gamma h_e)\right] \qquad \text{Eqn. 8.4}$$

Equation 8.5 has been plotted (Figure 8.6) for piled embankments where $h_e > 1.4(s\text{-}a)$

$$\sigma_s = \frac{1.4\gamma(s-a)}{s^2 - a^2}\left[s^2 - a^2(\sigma_c/\gamma h_e)\right] \qquad \text{Eqn. 8.5}$$

σ_c is obtained from

$$\frac{\sigma_c}{\gamma h_e} = \left[\frac{C_c a}{h_e}\right]^2 \qquad \text{Eqn. 8.6}$$

where the arching coefficient C_c, for end bearing (unyielding) piles is given by

$$C_c = 1.95h_e/a - 0.18 \qquad \text{Eqn. 8.7}$$

It is worth noting that since 0.18 is generally very small compared to $1.95h_e/a$, $\sigma_c/\gamma h_e \approx 1.95^2 = 3.8$, and is virtually independent of the other geometrical factors. Similarly from the BS8006 equation for normal ('friction and other') piles $\sigma_c/\gamma h_e \approx 1.5^2 = 2.3$.

Both equations above contain the term

$$\frac{(s/a)^2 - (\sigma_c / \gamma h_e)}{(s/a)^2 - 1}$$

which has a value of approximately 0.47 for (s/a) = (75/30) and approximately 0.72 for (s/a) = (100/30) for unyielding piles. The remaining terms are proportional to h_e and (s-a) for the low and high embankments respectively. The result is indepenedent of the embankment soil strength.

8.3.5 Guido method

Equation 8.8 (Russell & Pierpoint, 1997) is used for the Guido method (Figure 8.7).

$$\sigma_s = \frac{\gamma(s-a)}{3\sqrt{2}} \qquad \text{Eqn. 8.8}$$

This results directly from the geometry of a pyramid whose square base has side length (s-a), and whose height is (s-a)/√2. The result is independent of the embankment soil strength.

8.3.6 Kempfert et al

It has been assumed that there is no surcharge, since this would have been the case in the centrifuge tests. Equation 8.9 (Kempfert et al, 2004) has been plotted (Figure 8.8) to show the stress on the subsoil.

$$\sigma_s = \lambda_1^x \gamma_e \left[h_e \left(\lambda_1 + h_g^2 \lambda_2\right)^{-x} + h_g \left(\left(\lambda_1 + \frac{h_g^2 \lambda_2}{4} \right) - \left(\lambda_1 + h_g^2 \lambda_2\right)^{-x} \right) \right] \qquad \text{Eqn. 8.9}$$

where:

$$\chi = \frac{a(K_{krit} - 1)}{\lambda_2 s}$$

$$K_{krit} = \tan^2\left[45° + \frac{\varphi'_e}{2}\right]$$

$$\lambda_1 = \frac{1}{8}(s - a)^2$$

$$\lambda_2 = \frac{s^2 + 2as - a^2}{2s^2}$$

where

φ'_e = internal angle of friction (embankment)

γ_e = unit weight of embankment fill (kN/m^3)

h_g = vault height (m) $\quad h_e \geq s/2 \rightarrow h_g = s/2$

$h_e < s/2 \rightarrow h_g = h_e$

8.4 Comparison of methods

Figures 8.4 - 8.8 show results from the five predictive methods, plotted as $\sigma_s/\gamma(s\text{-}a)$ showing variation with embankment height $h_e/(s\text{-}a)$. When plotted in this way only the ratio of geometrical variables are important in the preceding equations, not the absolute magnitude. This is consistent with approximately constant efficacy in the centrifuge tests with varying g-level. Lines labelled s = 75 and 100 mm actually refer to (s/a) = (75/30) and (100/30) respectively. A friction angle of 35° has been used in the methods which account for the embankment strength. A black line shows the general trend of the centrifuge test results, which were observed to have $\sigma_s/\gamma(s\text{-}a) \approx$ 0.5 for $h_e/(s\text{-}a)$ exceeding 0.5.

All plots (design methods), apart from Guido's, show somewhat higher values of $\sigma_s/\gamma(s\text{-}a)$ compared to the test results of 0.5. However, Guido's method gives a constant value of 0.24 (for both pile spacing's) which is less. It should be noted the Guido method inherently assumes three layers of geogrid whereas as the centrifuge tests and other design methods do not consider the effect of geogrid. The Guido method is also conceptually rather different to the other methods. The remaining design methods are potentially 'conservative' in their results compared to the centrifuge tests, but this would be preferable to unconservative results in practice.

Figure 8.4 shows that for the Terzaghi method assuming 'cruciform' frictional boundaries of total length s on each side gives better agreement with the test data than assuming that frictional boundaries only originate from the pile caps, giving a much shorter length a on each side. Initially, at low $h_e/(s\text{-}a)$ values, both plots agree well with the data (no arching) but for higher embankments the 'cap' method gives very high $\sigma_s/\gamma(s\text{-}a)$ values (tending to an asymptote of around 3) compared to the 'cruciform' method (with an asymptote of around 1). For the 'cap' method the subsoil stress tends to be higher at the wider spacing (s), which is reasonable. However, for the 'cruciform' method, the opposite is true. In fact there is actually relatively little dependency on s, and the normalisation by $(s\text{-}a)$ appears to give a smaller value when s increases. Figure 8.4 shows using a value of 0.5 for K as adopted by Russell et al (2003) does not show much difference to the Terzhagi 'cruciform' method. In fact for a friction angle of 35°, $K = (1\text{-}sin^2\varphi)/(1+sin^2\varphi) \approx 0.5$.

Figure 8.5 shows predictions from the Hewlett & Randolph method. For relatively low embankments the equation for failure at the 'crown' of the arch is critical. At low $h_e/(s\text{-}a)$ the lines for different s intersect, but beyond this point the subsoil stress is slightly higher for s = 100 mm as anticipated. In fact, both these lines indicate $\sigma_s/\gamma(s\text{-}a)$ of approximately 1, with relatively little dependency on $h_e/(s\text{-}a)$. In the derivation of the equation for equilibrium at the crown of the arch, a term $\gamma(s\text{-}a)/\sqrt{2}$ is used to account for the weight of 'infilling' material beneath the arch, and generally speaking this term appears to dominate the prediction.

For higher embankments conditions at the pile cap become more critical. As illustrated by Equation 8.3, the subsoil stress is directly proportional to h_e (and hence these lines

could be projected back to pass through the origin). These lines show quite significant dependency on (s/a), and this seems reasonable, with wider spaced caps increasing load on the subsoil. Consideration of equilibrium conditions at the pile cap is unique to this method, and hence it is the only method not to approach an asymptote for high embankments. For high embankments it was not practical to reliably estimate σ_s from the centrifuge test data as the efficacy approached 1.0. However, the Hewlett & Randolph method rationally predicts that even as the efficacy tends to 1.0, $\sigma_s/\gamma(s\text{-}a)$ will tend to increase for higher embankments.

Figure 8.6 shows predictions from BS8006. As indicated by the equations, a transition occurs at $h_e/(s\text{-}a) = 1.4$. For low embankments the subsoil stress increases in proportion to h_e, whilst for high embankments the prediction is virtually independent of h_e, with a value of $\sigma_s/\gamma(s\text{-}a) = 1.4\times0.47 = 0.66$ for $(s/a) = (75/30)$ and $1.4\times0.72 = 1.0$ for $(s/a) = (100/30)$. Consideration of 'normal' ('friction and other') piles instead of 'unyielding' piles would have given somewhat higher values.

Figure 8.8 shows predictions from Kempfert et al (2004). After the transition of $h_e = s/2$ (mentioned earlier), the plots deviate off at a steep gradient so that at high h_e the equations predict quite high stress on the subsoil.

The results can be summarised as follows for the majority of embankments heights, where $h_e/(s\text{-}a) > 0.5$:

- The methods generally predict $\sigma_s/\gamma(s\text{-}a)$ in or near the range 0.5 to 1.0, tending towards an asymptotic value for high embankments.

Exceptions to this are as follows:

- The Terzaghi 'cap' model predicts higher stress on the subsoil, particularly for high embankments.
- The Hewlett & Randolph method predicts higher stress on the subsoil for high embankments, where failure at the pile cap is critical, and this is the only method where this is specifically considered.

- The Kempfert method also predicts quite high stress on the subsoil for high embankments

- The Guido method predicts lower stress on the subsoil, but inherently considers the effect of multiple geogrid layers.

$\sigma_s/\gamma(s\text{-}a)$ in or near the range 0.5 to 1.0 is generally consistent with the centrifuge test results. However, it was not possible to verify the potential effect of failure at the pile cap for higher embankments, since the efficacy was close to 1.0.

The effect on the efficacy of the piled embankments using the different design methods is shown in Figures 8.9 (a) and (b) for s = 75 mm and s = 100 mm respectively where the four plots of efficacy are calculated using Equation 8.9 with values of $A = (\sigma_s/\gamma(s\text{-}a))$ in the range 0.5 to 2.0.

$$Efficacy = 1 - \frac{A(s-a)}{h_e}\left[1 - \left(\frac{a}{s}\right)^2\right] \qquad \text{Eqn. 8.10}$$

Figures 8.9 (a) and (b) show that as anticipated increasing subsoil stress implies reduced efficacy, particularly for low embankments. However, where the above methods (specifically Terzaghi and Hewlett & Randolph) predict $\sigma_s/\gamma(s\text{-}a)$ significantly in excess of 1.0, this tends to be for higher embankments where the efficacy tends to the asymptotic value of 1.0 for all $\sigma_s/\gamma(s\text{-}a)$.

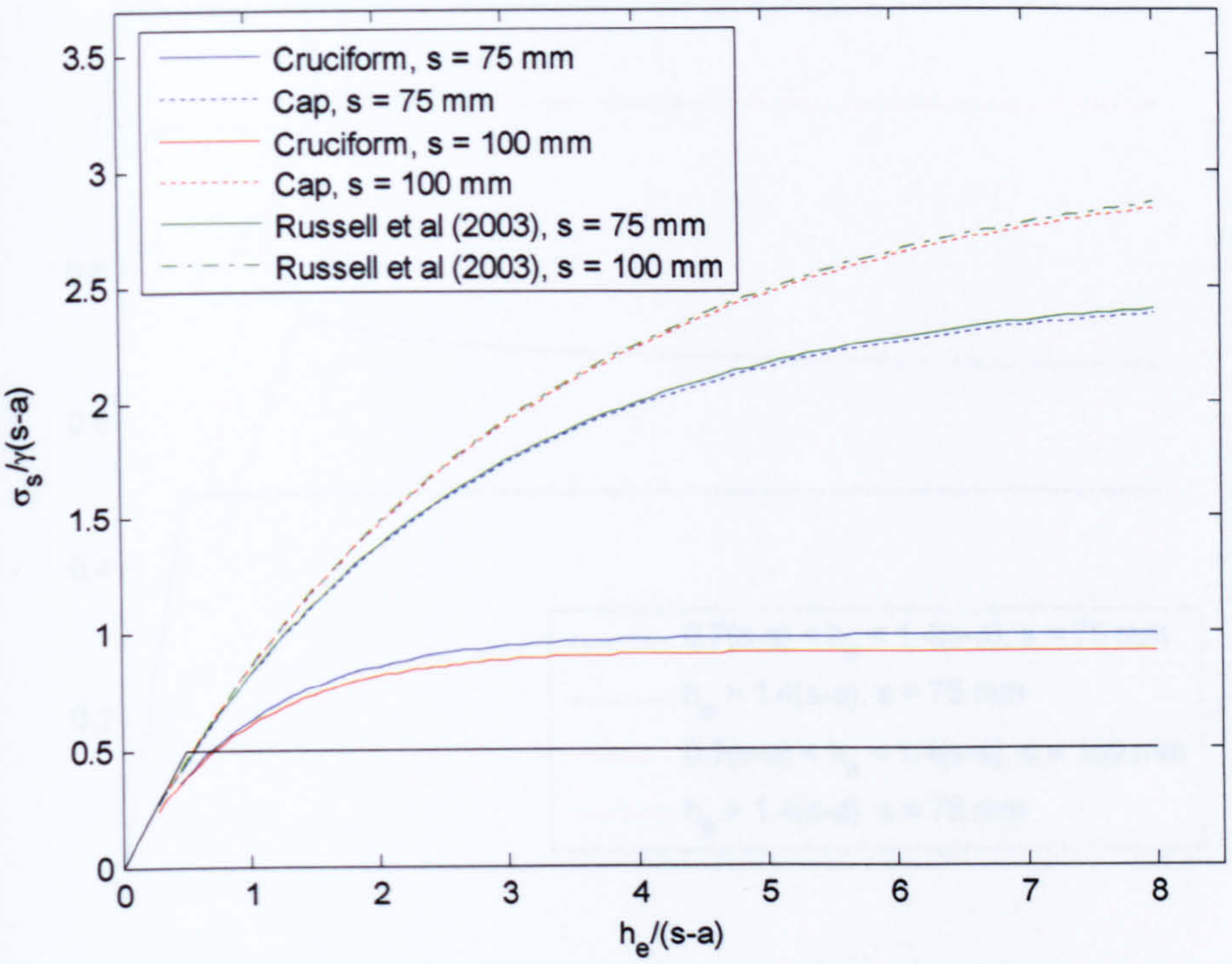

Figure 8.4 - Terzhagi design method

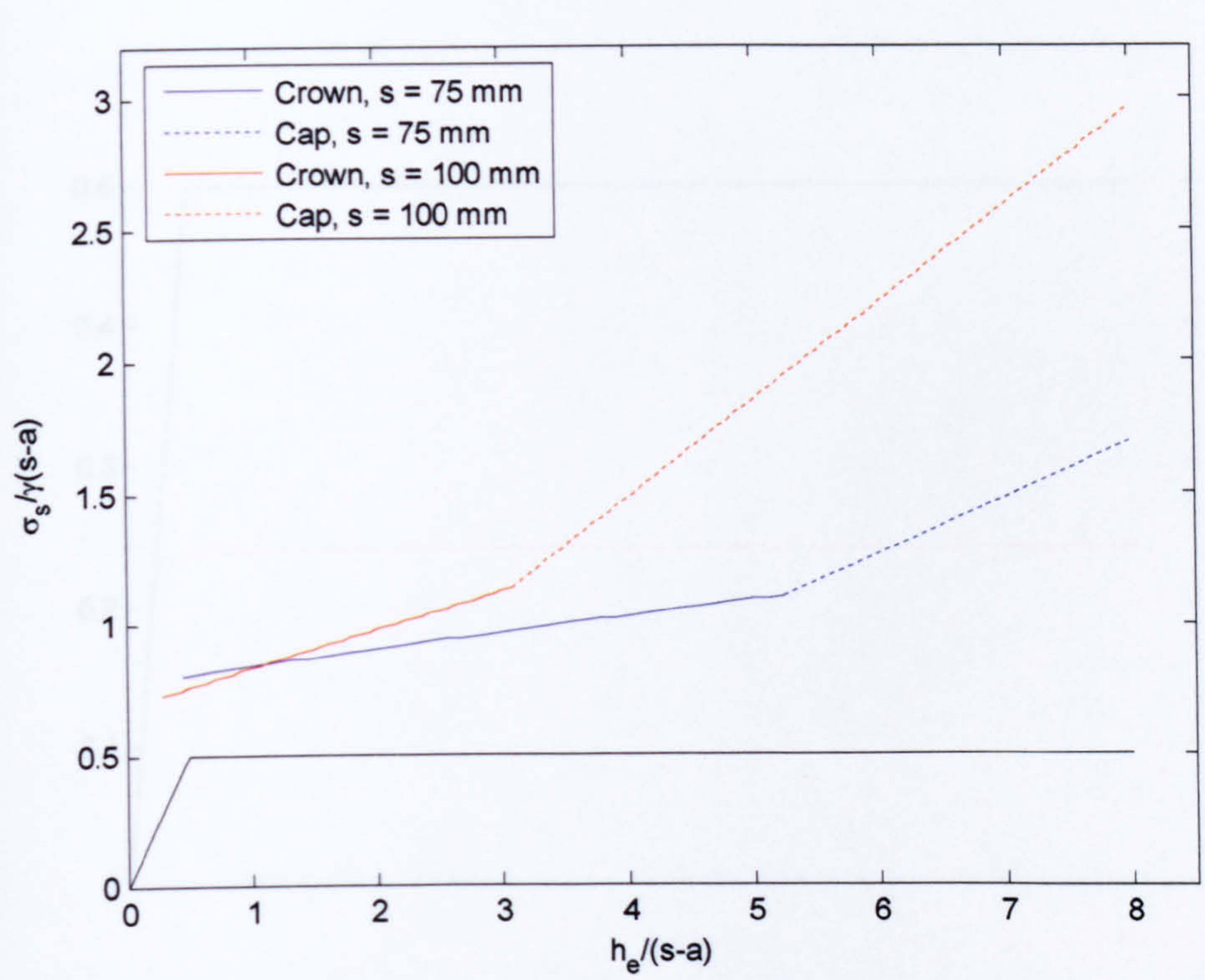

Figure 8.5 - Hewlett & Randolph design method

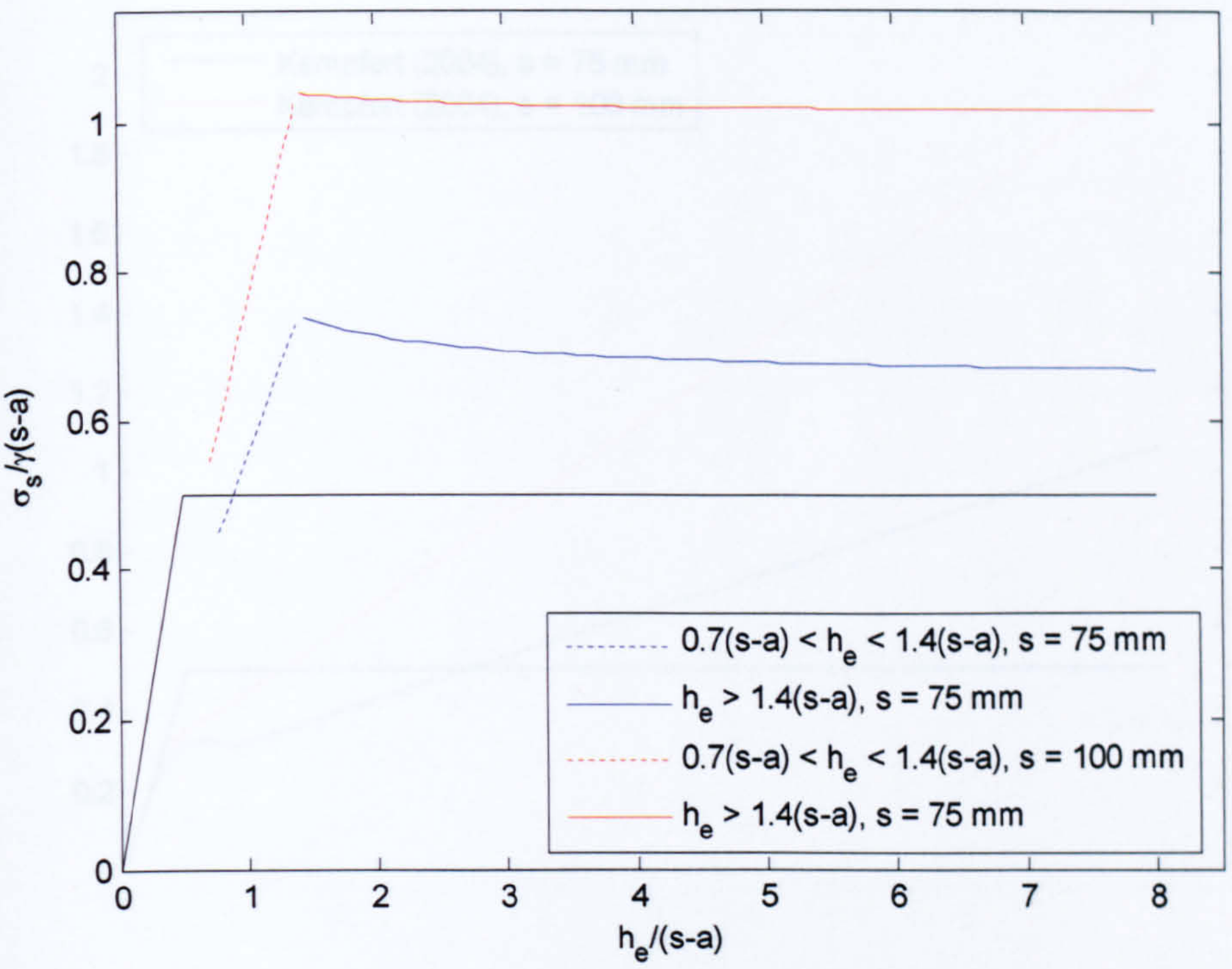

Figure 8.6 - BS8006 design method

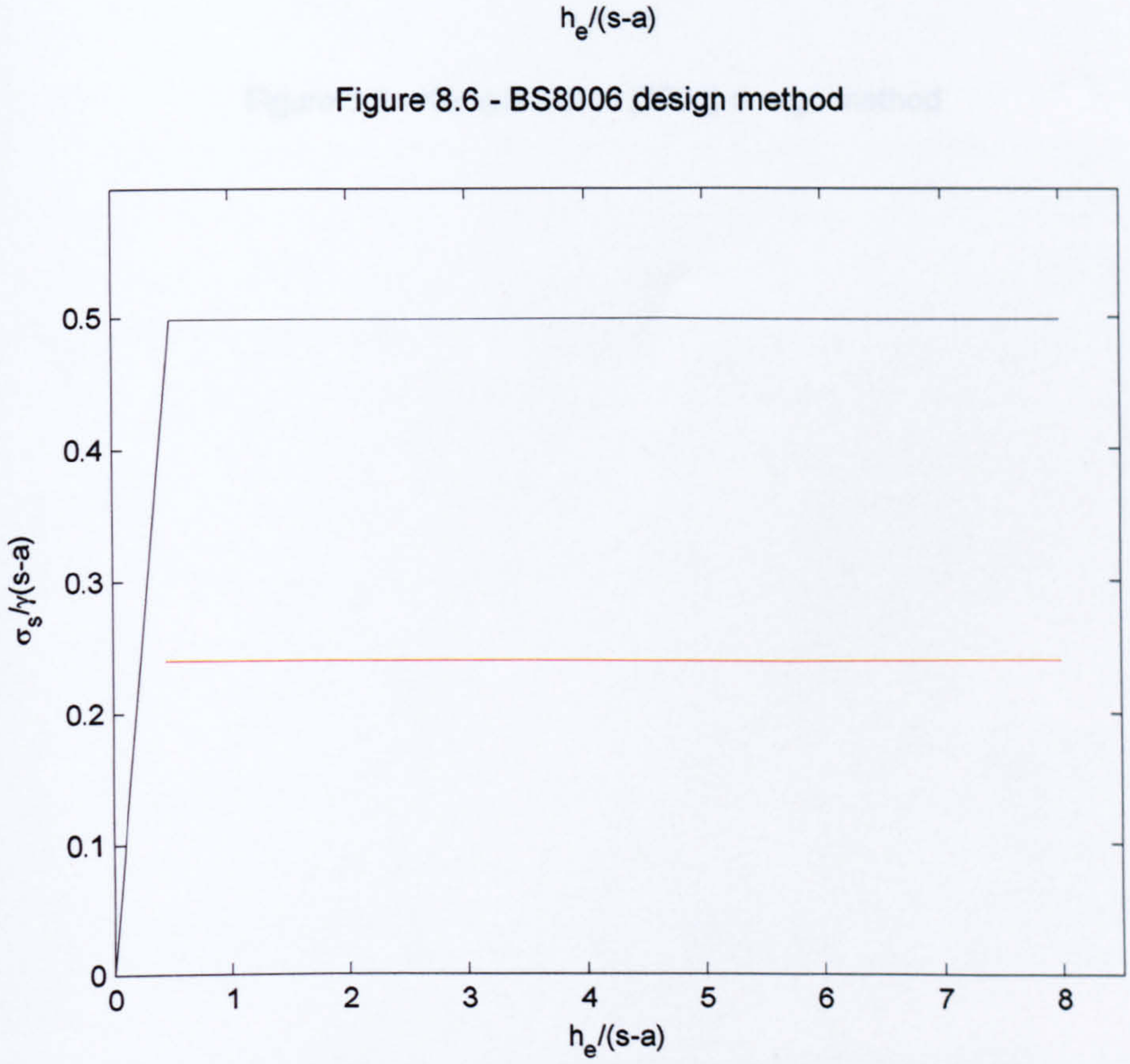

Figure 8.7 - Guido design method

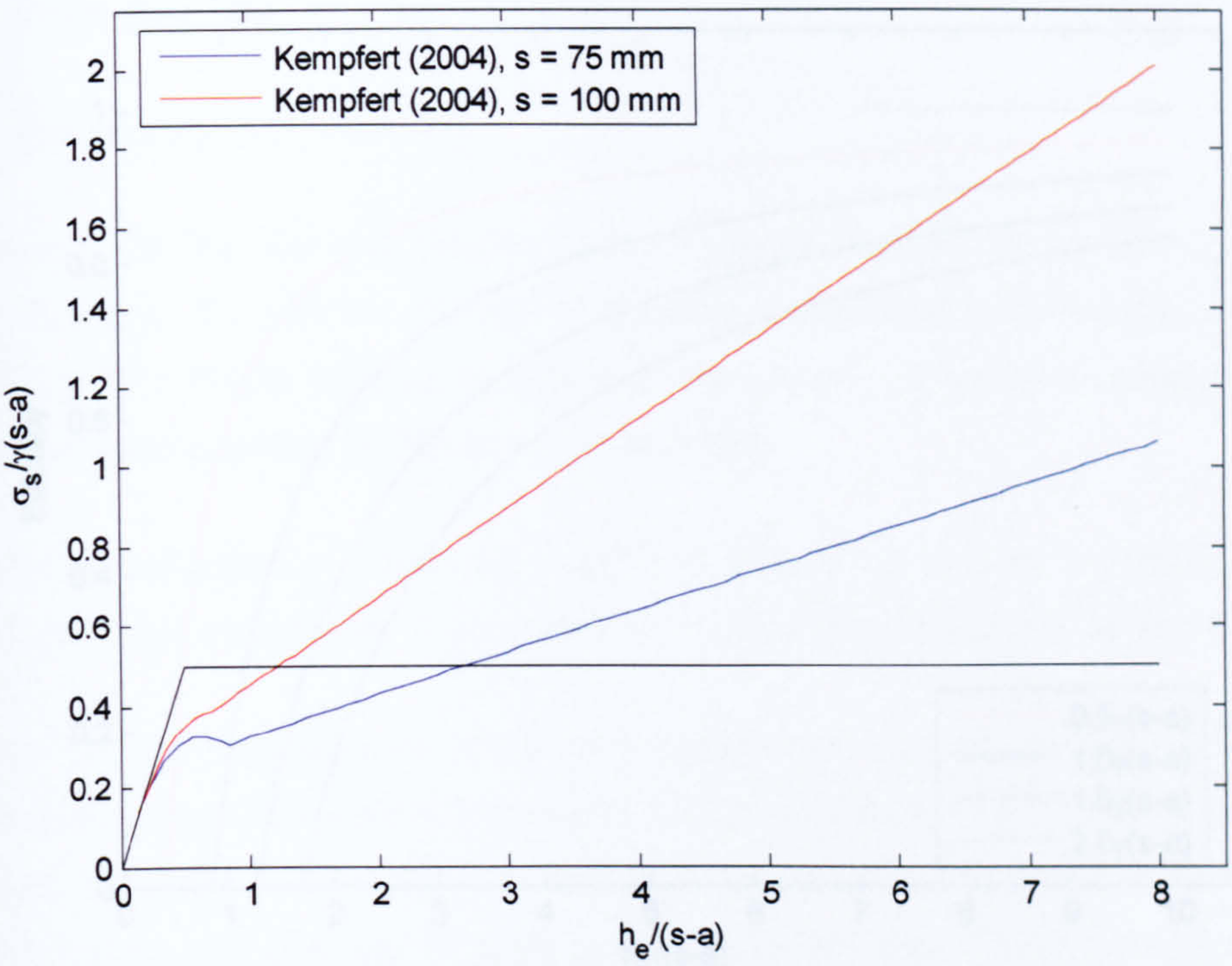

Figure 8.8 - Kempfert et al (2004) design method

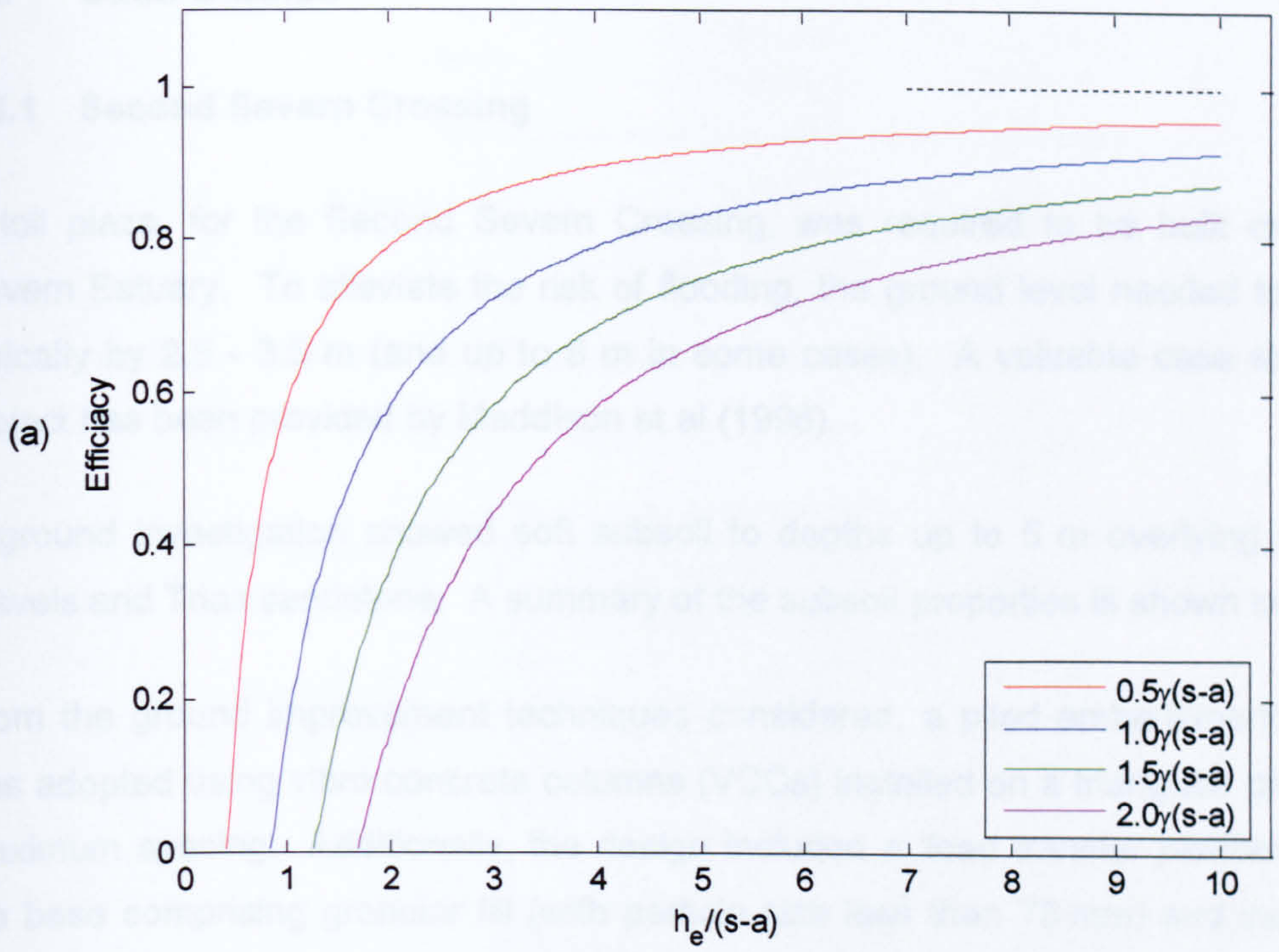

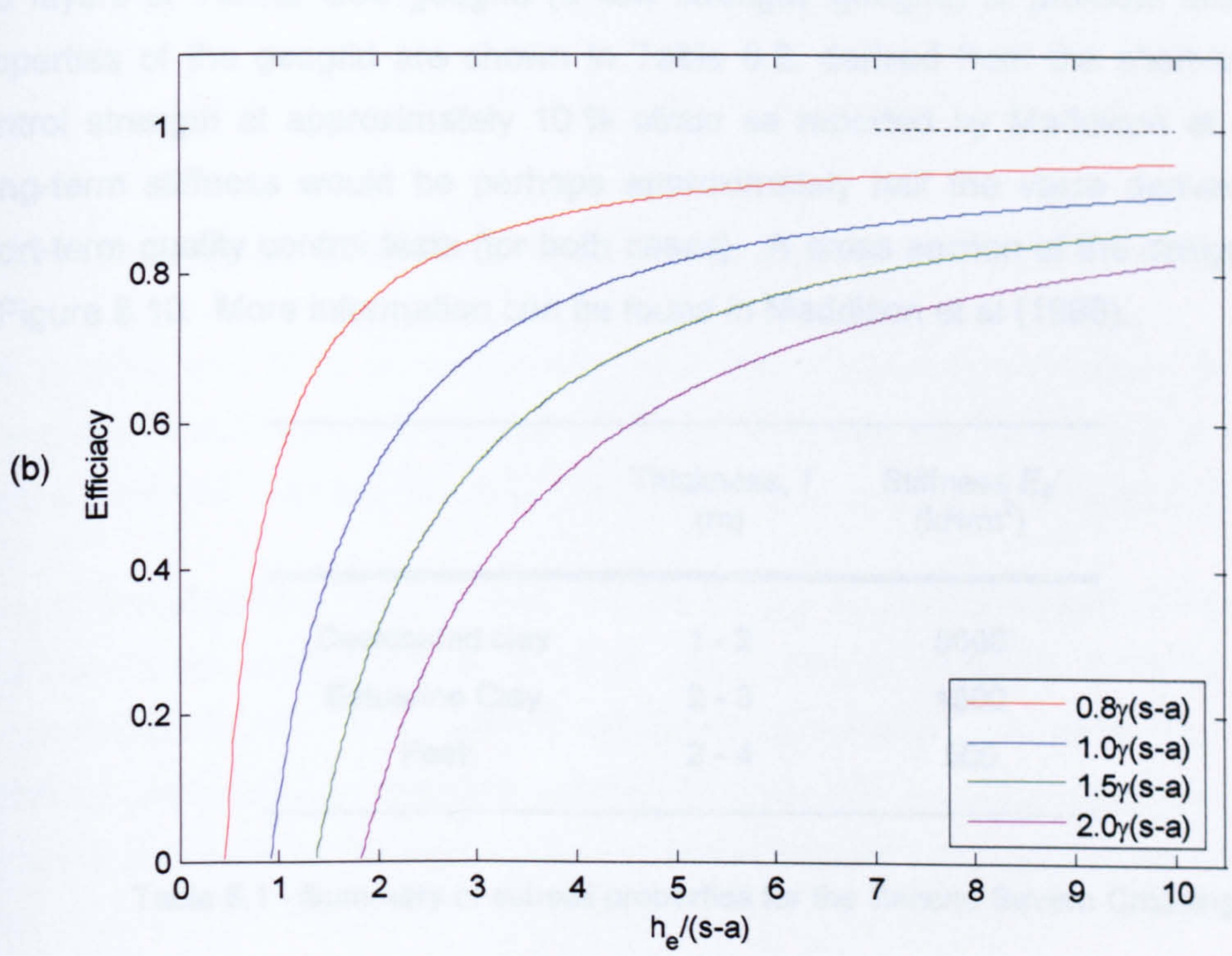

Figure 8.9 - Efficacy values of design methods for (a) *s* = 75 mm and (b) *s* = 100 mm

8.5 Case Studies

8.5.1 Second Severn Crossing

A toll plaza, for the Second Severn Crossing, was required to be built close to the Severn Estuary. To alleviate the risk of flooding, the ground level needed to be raised typically by 2.5 - 3.5 m (and up to 6 m in some cases). A valuable case study of this project has been provided by Maddison et al (1996).

A ground investigation showed soft subsoil to depths up to 5 m overlying sands and gravels and Trias sandstone. A summary of the subsoil properties is shown in Table 8.1.

From the ground improvement techniques considered, a piled embankment technique was adopted using vibro concrete columns (VCCs) installed on a triangular grid of 2.7 m maximum spacing. Additionally, the design included a 'load transfer platform' (LTP) at the base comprising granular fill (with particle size less than 75 mm) and incorporating two layers of Tensar SS2 geogrid (a 'low strength' geogrid) to promote arching. The properties of the geogrid are shown in Table 8.2, derived from the short-term quality control strength at approximately 10 % strain as reported by Maddison et al, (1996). Long-term stiffness would be perhaps approximately half the value derived from the short-term quality control tests (for both cases). A cross section of the design is shown in Figure 8.10. More information can be found in Maddison et al (1996).

	Thickness, t (m)	Stiffness E_o' (kN/m^2)
Desiccated clay	1 - 2	5000
Estuarine Clay	2 - 3	1800
Peat	2 - 4	500

Table 8.1 - Summary of subsoil properties for the Second Severn Crossing

Property	Transverse direction	Longitudinal direction
Stiffness (kN/m)	300	150

Table 8.2 - Summary of SS2 geogrid properties for the Second Severn Crossing

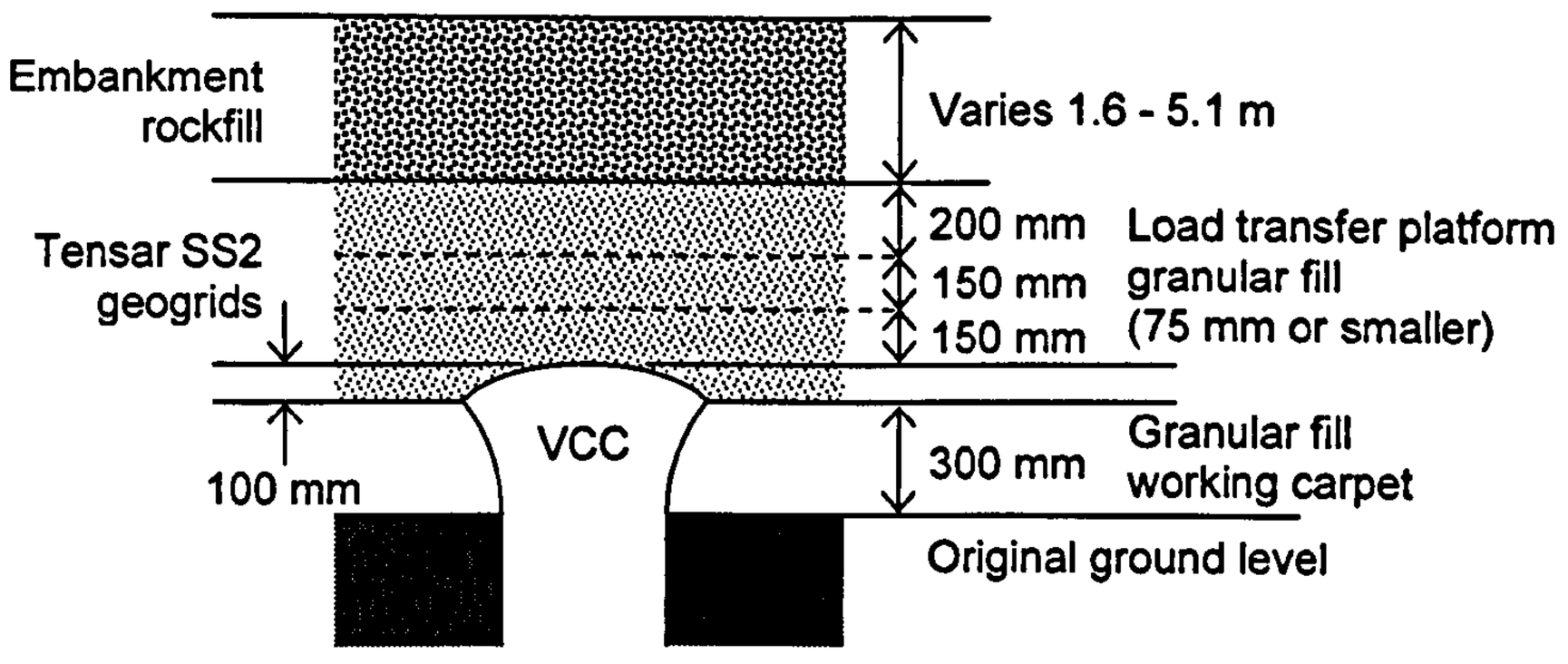

Figure 8.10 - Embankment design for the Second Severn Crossing

8.5.2 Construction of apartments on a site bordering River Erne, Northern Ireland

During 1999 and 2000 a development of 2 and 3 storey town houses and 4 storey apartment blocks were constructed on a site bordering the River Erne in Enniskillen, Northern Ireland. Various details of this project were reported by Milligan (2006).

Ground investigations showed that the underlying subsoil consisted of made ground over substantial depths of peat and soft alluvial clay of thickness of up to 10 m, and underlying glacial till. A (simplified) schematic of the site is shown in Figure 8.11. A summary of the subsoil properties is shown in Table 8.3. Note that compressibility of the subsoil is very high, for instance compared to the Second Severn Crossing case study.

	Thickness, t (m)	Stiffness E_o' (kN/m^2)
Alluvial clay	2.5 - 10	500
Peat	1 - 3	200

Table 8.3 - Summary of subsoil properties for the project in Ireland

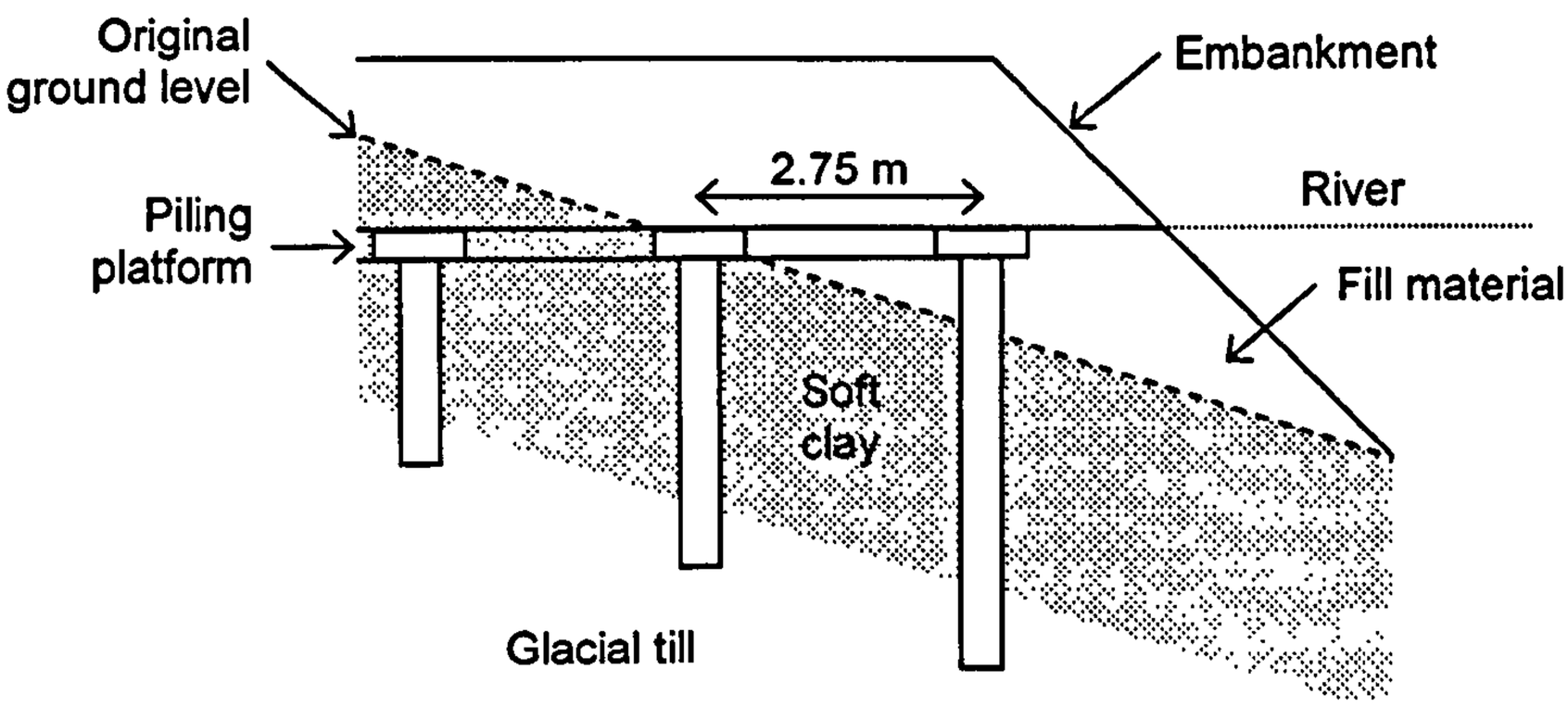

Figure 8.11 - Cross section for the project in Ireland

The site was low-lying and susceptible to flooding so the ground level for the development had to be raised by up to about 3.0 m.

Due to the poor ground conditions, a load transfer platform was constructed over the whole area of the site supported by piles into the underlying glacial till (Figures 8.11 and 8.12). The load transfer platform was used to provide the foundation for the buildings, of conventional construction with shallow strip footings, as well as for all the remainder of the site including gardens, roads and parking areas. It should be noted that there was no direct link between the building footings and piles beneath.

The piles were installed in a triangular arrangement at 2.75 m spacing with a pile cap size of 0.75 m. Beneath the pile caps was 0.5 m thickness of piling platform

(unsupported fill). Three layers of Tensar geogrid were used; SS20 (×1) and SS30 (×2) as shown in Figure 8.12. The properties of the geogrid are shown in Table 8.4 (see Chapter 7), and again long-term values are assumed to be half the short-term values in the Table.

Property	SS20	SS30
Stiffness (kN/m)	280	420

Table 8.4 - Summary of subsoil properties for the project in Ireland

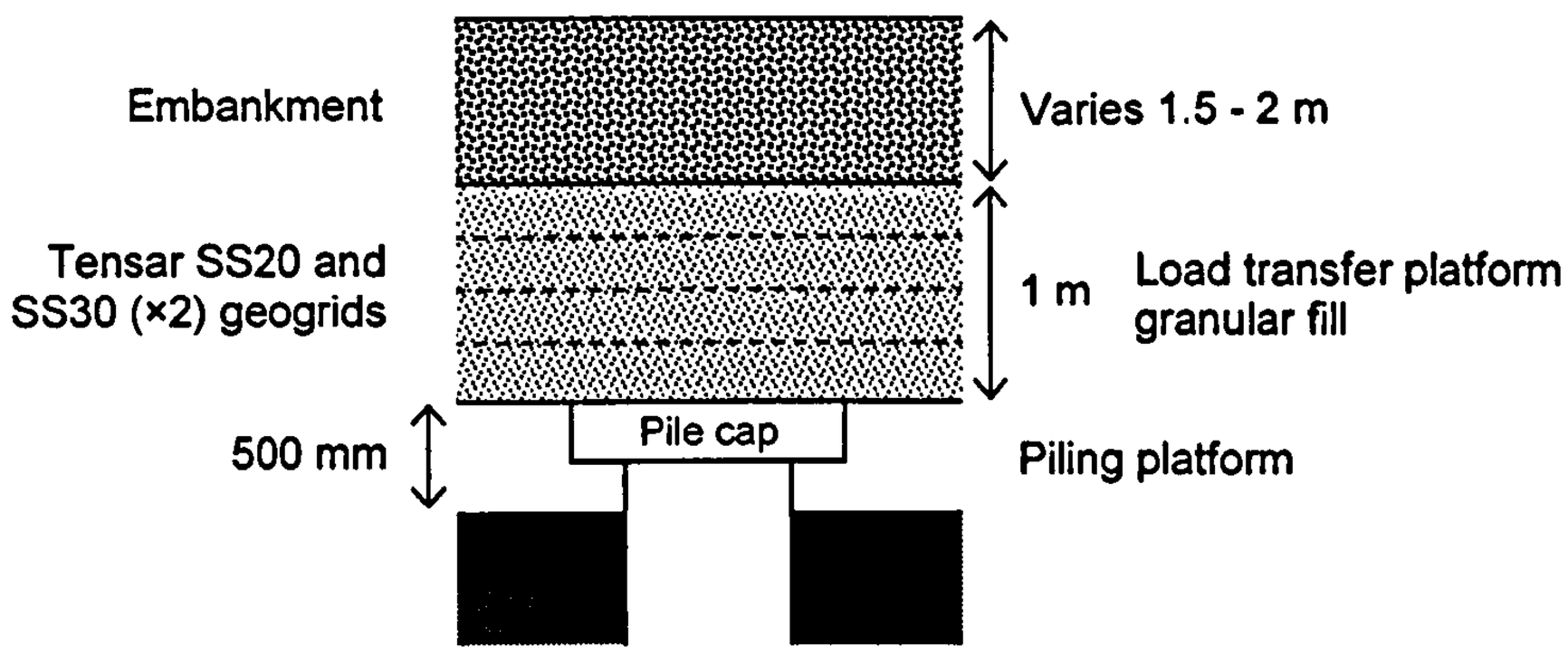

Figure 8.12 - Embankment design for the project in Ireland

8.5.3 Case study comparison

The Second Severn Crossing project has been regarded as a success in that settlement (both absolute and differential) of the embankment have remained within acceptable limits. The project in Northern Ireland however was not. Within two years of completion, ground deformations around the buildings were becoming noticeable. Some time later, pile caps 'punched' into the material above, causing significant deformation.

According to detailed investigation and assessment of the causes of failure (Milligan, 2006), the problems were caused by excessive and continuing deformation of the load transfer platform.

This section will use the findings from the centrifuge tests to back analyse the performance of the piled embankments in both cases.

The performance of the piled embankments can be understood more easily if the individual components contributing to vertical equilibrium at the interface with the subsoil are considered separately:

- Arching in the embankment
- Any load from a working platform below the elevation of the pile caps which is not affected by arching
- Contribution of geogrid(s)
- Stress carried by the subsoil

These components will be considered in conjunction with a broad measure of settlement at the interface with the subsoil.

Considering an embankments 'ability' to arch, a 'Ground Reaction Curve' (GRC) plot has been shown to relate the stress on the subsoil, σ_s, to the subsoil settlement (assumed to be similar to $\delta_{e,u}$). From the 'working platform' piled embankment tests, the GRC plots have shown a 'point of maximum arching' which is reached when $\delta_{e,u}$ is approximately 5% of (s-a). After this point, the arching of the embankment slowly reduces. From the piled embankment tests, it was shown that $\sigma_s/\gamma_e(s\text{-}a) \approx 0.5$. Using this as the 'point of

maximum arching', the stress acting on subsoil, σ_s, can be calculated using (essentially Equation 6.1 with *A* equal to 0.5):

$$\sigma_s = 0.5\gamma_e(s - a) + \gamma_w h_w \qquad \text{Eqn. 8.11}$$

The term $\gamma_w h_w$ arises from the weight of the working platform material, which acts directly on the subsoil with no effect from arching.

Equation 8.11 can be used to calculate the stress that can be carried by the geogrid in isolation. The equation only considers the contribution due to tension in the grid, and not any other interaction with the soil. Thus the effect of multiple grids is incorporated simply by assuming all grids to deform by the same amount and summing the stiffness (*k*) of the various grids. The term δ_g refers to the maximum sag of the grid, but this will be considered broadly equivalent to a more general uniform settlement. There is also some complication in selection *l*, which has been pragmatically taken as (*s*-*a*).

$$w = \frac{64k}{3l}\left(\frac{\delta_g}{l}\right)^3 \qquad \text{Eqn. 8.12}$$

where

w = the uniform stress acting on the geogrid (kN/m^2)

l = the length of the span (m)

δ_g = the maximum sag (vertical deflection) of the geogrid (m)

Equation 8.12 can be used to calculate the stress that can be carried by the (various layers of) subsoil for a given settlement;

$$\frac{\delta_s}{\sigma_s} = \frac{t_1}{E'_{01}} + \frac{t_2}{E'_{02}} + \ldots \frac{t_n}{E'_{0n}} \qquad \text{Eqn. 8.13}$$

where:

δ_s = Subsoil settlement (m)

t_n = Thickness of subsoil (m)

Generally behaviour will be dominated by any layers which have high thickness and/or low stiffness. The subsoil response could also include the preconsolidation stress of the subsoil, which would mark a considerable drop in tangent stiffness.

Table 8.5 summarises the relevant values used to plot the above formulas in Figures 8.13 and 8.14 for the Second Severn Crossing and apartments in Ireland respectively. The subsoil thicknesses are based on typical values for the least soft layers, but maximum values for the softest layer, giving a 'worst case scenario'. The plots are shown normalised in the form used for the Ground Reaction Curve.

The GRC has been plotted based on a minimum stress ('maximum arching') at the base of the embankment (Equation 8.10), assumed to occur at a normalised settlement of 5 %. Initial curvature of the GRC up to this point is indicated schematically. Since stress then increases slowly, the stress is schematically shown as constant at the minimum value. Referring to Figures 6.6 - 6.8 which show much larger normalised settlement than Figures 8.13 and 8.14, it can be seen that this is a reasonable approximation. However, it would be slightly unconservative in a design sense.

The 'geogrid' line has been plotted using Equation 8.12, summing the stiffness of numerous grids, and taking the span length as (s-*a*) as described above. Geogrid stiffnesses shown in Table 8.5 are long-term values, taken as half short-term values. The 'subsoil' line has been plotted based on Equation 8.13.

The GRC shows the reduced stress at the base of the embankment (or load transfer platform) due to arching in the embankment. This stress must be carried by the combined action of the geogrid and subsoil - hence the 'S+G' line. Equilibrium is satisfied where the GRC and S+G lines meet, at a corresponding settlement.

Referring to the Second Severn Crossing plot (Figure 8.13), the GRC line intersects the S+G line at a normalised settlement of about 9 %, corresponding to about 200 mm settlement, which is high, but potentially tolerable at the base of the embankment. The

subsoil carries the majority of the stress remaining at the point of maximum arching (about 20 kN/m^2), whilst the geogrids carry perhaps as little as 1 kN/m^2 each. Arguably the geogrid makes negligible contribution compared to the subsoil.

For Figure 8.14 (apartments in Ireland) the point of intersection is at 14 % normalised settlement (nearly 300 mm). Perhaps just as importantly, because the subsoil stiffness is so low it is implied that the layers of geogrid carry about 15 kN/m^2 of stress (between them), whilst the subsoil carries only about 10 kN/m^2. Referring to Equation 7.2 the normalised settlement implies a strain of about 5 % in the geogrid. This strain would generally be considered at the limit of acceptability. However, it has not been considered that the subsoil may have yielded (and become even less stiff), or that the distribution of load between the grids is not even (e.g. with the lowest grid carrying the most load).

The key difference between the successful and unsuccessful study appears to be the stiffness of the subsoil, and distribution of load between the subsoil and geogrid.

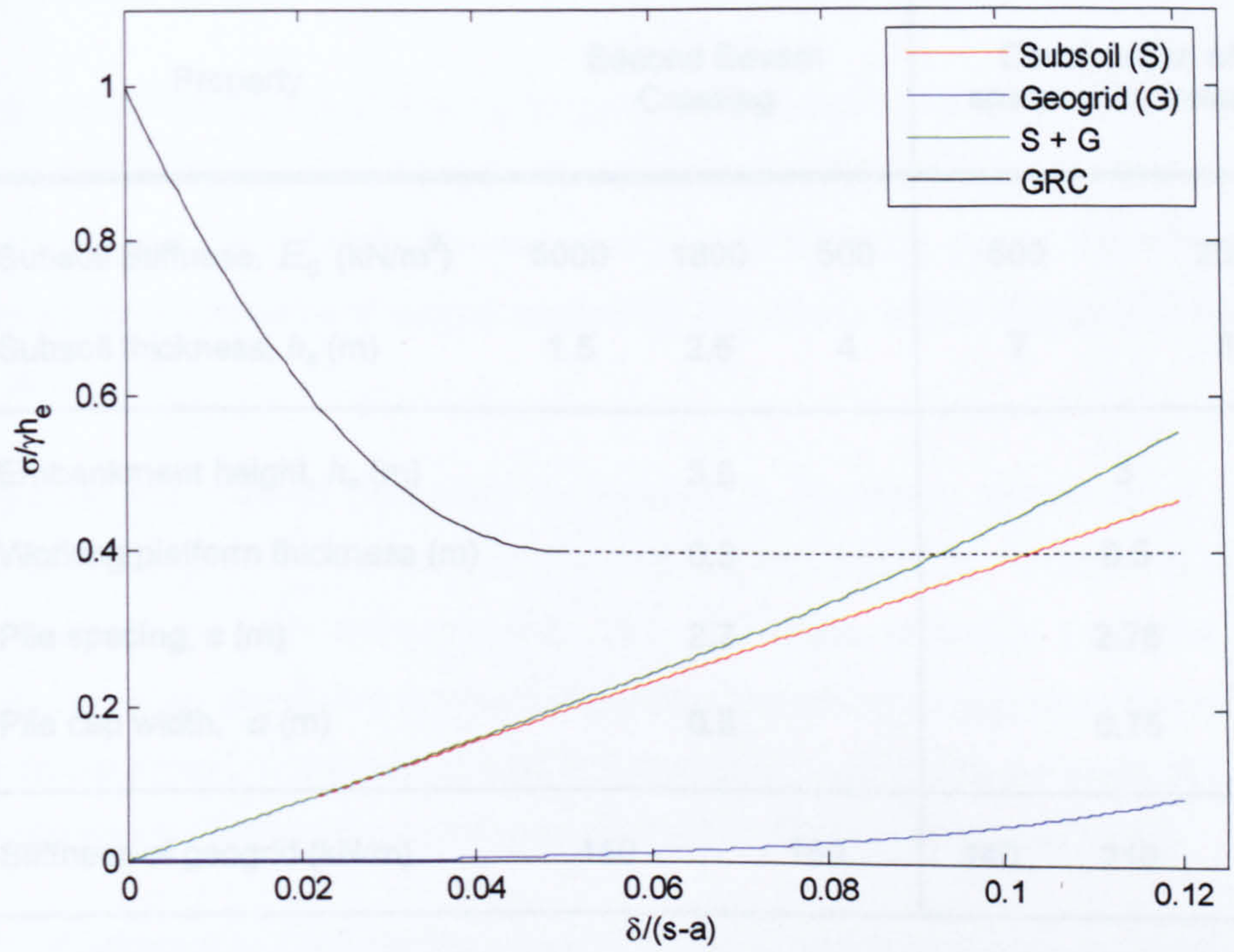

Figure 8.13 - Second Severn Crossing

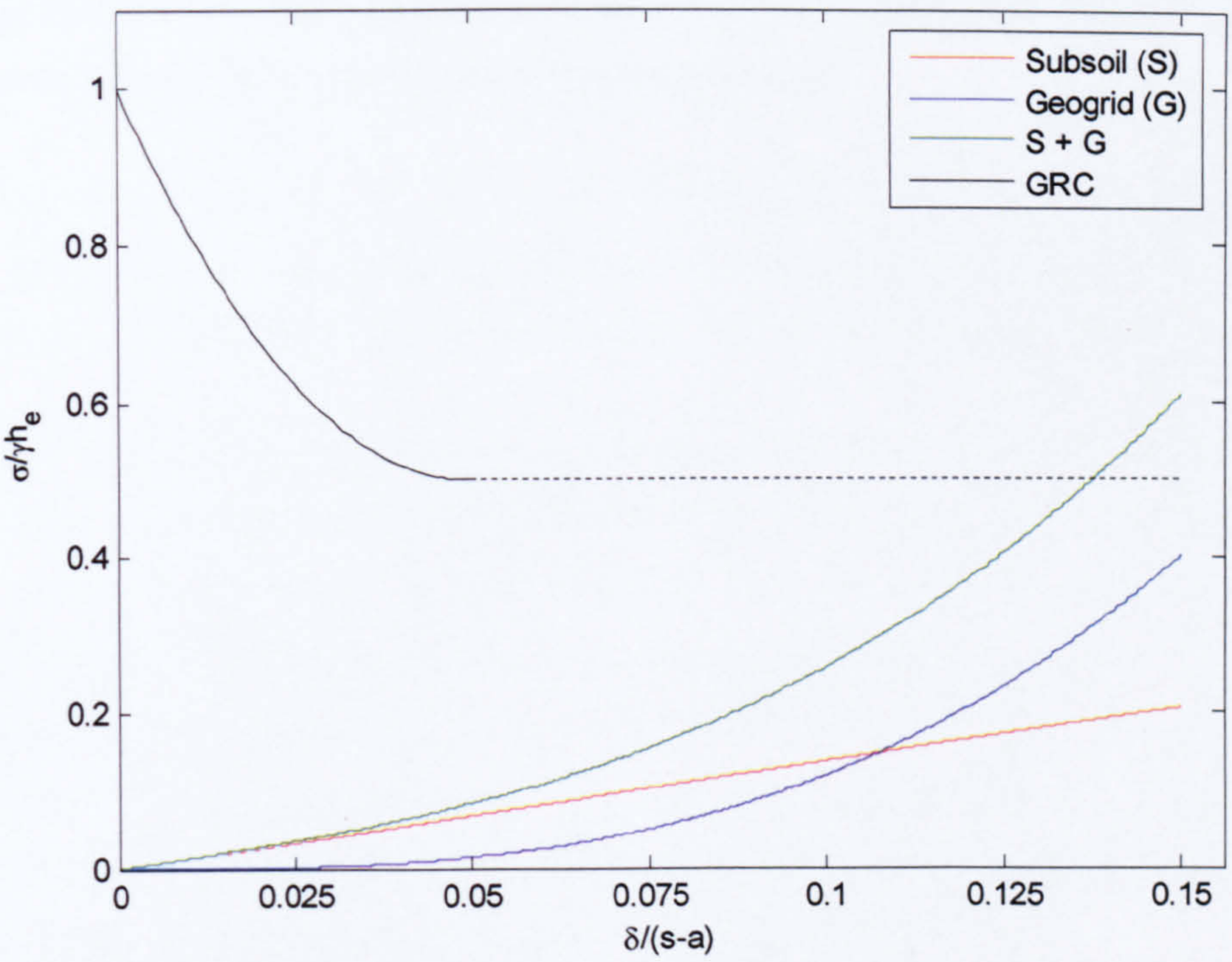

Figure 8.14 - Construction of apartments, Ireland

Property	Second Severn Crossing			Construction of apartments, Ireland		
Subsoil Stiffness, $E_0^{'}$ (kN/m^2)	5000	1800	500	500	200	
Subsoil thickness, h_s (m)	1.5	2.5	4	7	3	
Embankment height, h_e (m)	3.5			3		
Working platform thickness (m)	0.3			0.5		
Pile spacing, s (m)	2.7			2.75		
Pile cap width, a (m)	0.5			0.75		
Stiffness of geogrid (kN/m)	150		150	140	210	210

Table 8.5 - Summary of parameters used for Figures 8.9 and 8.10

8.7 Summary

Plotting results as $\sigma_s/\gamma(s\text{-}a)$ seems to give more insight into behaviour of the various methods for prediction of arching in an embankment than plotting the Stress Reduction Ratio (SRR = $\sigma_s/\gamma h_e$) which generally tends to 0 at large h_e, or the efficacy (E, the fraction of the embankment weight carried by the piles), which similarly generally tends to 1.0 at large h_e.

On balance the method proposed by Hewlett & Randolph seems most rational. It accounts for all geometrical parameters and the soil strength. It tends to predict quite large $\sigma_s/\gamma(s\text{-}a)$ for high embankments, but only when φ and/or (a/s) are low, which logically indicates significant concern regarding 'punching' of the pile caps into the base of the embankment. However, it was not possible to verify the potential effect of failure at the pile cap for higher embankments, since the efficacy was close to 1.0.

A form of 'interaction diagram' has been proposed which accounts for various potential components of a design at a compatible settlement at the base of the embankment. The equations have not been fully developed for a 3-d situation, but approximate consideration of two case studies indicates that particularly soft subsoil was likely to have been a factor in failure for one of the case studies.

CHAPTER 9

CONCLUSION

9.1 Work reported here

This thesis reports on a series of successful centrifuge tests on piled embankments and has presented useful findings.

Expanded Polystyrene (EPS) was used as the 'subsoil' instead of soft clay due to its ease of use. Some of the model piles incorporated load cells which enabled the (average) stress on the subsoil to be deduced.

Photogrammetric images of the embankment's surface were used to assess the embankment surface settlement. The photogrammetric technique performed very well as it effectively gave continuous settlement profiles. Another advantage (especially in centrifuge testing) was that it is a non contact technique and so there was no interference with the embankment surface.

All models were subjected to a range of g-levels in the centrifuge tests, but (as implied by the available predictive methods) when normalised correctly the results were largely independent of the g-level, and only related to normalised geometrical parameters.

The tests reported in Chapters 4 and 5 were for unreinforced piled embankments constructed on subsoil with one-dimensional Young's modulus approximately equal to 2 and 8 MN/m^2 respectively. In both cases at $h_e/(s\text{-}a) \approx$ 0.5 there is no evidence of arching based on the stress acting on the subsoil, and there is very large differential settlement at the embankment surface (due to imprints of the pile caps). As $h_e/(s\text{-}a)$ increases to 2.0 the stress on the subsoil does not increase significantly (and thus there is significant evidence of arching), and differential settlement at the embankment surface tends to zero. For larger $h_e/(s\text{-}a)$ ratios the efficacy approaches 1.0.

Plotting results as $\sigma_s/\gamma(s\text{-}a)$ seems to give more insight into behaviour of the various methods for predictions of arching in an embankment than plotting the Stress Reduction Ratio (SRR = $\sigma_s/\gamma h_e$) which generally tends to 0 at large h_e, or the efficacy (E, the fraction of the embankment weight carried by the piles), which similarly generally tends to 1.0 at large h_e.

On balance the method proposed by Hewlett & Randolph seems most rational. It accounts for all geometrical parameters and the soil strength. It tends to predict quite large $\sigma_s/\gamma(s\text{-}a)$ for high embankments, but only when φ and/or (a/s) are low, which logically indicates significant concern regarding 'punching' of the pile caps into the base of the embankment. However, it was not possible to verify the potential effect of failure at the pile cap for higher embankments, since the efficacy was close to 1.0.

In the 'working platform' piled embankment tests (chapter 6), the loading from the working platform acts directly on the (EPS) subsoil (which ultimately yielded) and was the main cause of the large uniform settlement ($\delta_{e,u}$) of the embankment observed in the tests. Little differential settlement ($\delta_{e,d}$) was observed as the embankments 'failed' by fill material settling well below the pile cap level. It can be postulated that the piles 'punched' into the embankment fill material which, with the height of the embankments used, caused little or no $\delta_{e,d}$. As $\delta_{e,u}/(s\text{-}a)$ increased to about 0.05, the efficacy of the embankment increased rapidly to its highest value; the 'point of maximum arching'. After this point, the efficacy reduces towards an ultimate state. There is analogy between these results and the 'Ground Reaction Curve' proposed by Iglesia et al (1999) to estimate the overburden stress on buried structures as they deform.

In the 'reinforced' piled embankment tests (chapter 7), the amount of differential and uniform settlement at the embankment surface was very large, due to the absence of subsoil support, and requiring the model geogrid to carry the full embankment weight. Increasing the geogrid stiffness had some effect in reducing settlement but reducing the pile spacing had considerably more impact in this respect. Simple theoretical predictions of geogrid load-deflection behaviour gave broad agreement with the experimental data, and confirmed considerably more dependency on pile spacing than geogrid stiffness. However the shape of the load-deflection response in the theoretical prediction was somewhat different than the centrifuge tests.

A form of 'interaction diagram' has been proposed which accounts for various potential components of a design (arching in the embankment, subsoil response to loading, and the effect of any geogrid layers) at a compatible settlement at the base of the embankment. The equations have not been fully developed for a 3-d situation, but approximate consideration of two case studies indicates that particularly soft subsoil was likely to have been a significant factor in failure for one of the case studies.

9.2 Future work

This work has given considerable insight into the arching behaviour in a piled embankment, and how this compares to the various predictive methods available. However there is still scope for further work:

- Any effect of failure at the pile cap on the subsoil stress for high embankments was not clearly discernable in the centrifuge tests, since the efficacy was close to 1.0 and hence the relatively small component of subsoil stress could not be reliably established. Physical modelling would probably need to use a different approach to overcome this problem, or numerical modelling may provide some insight.

- The idea of an interaction diagram accounting for the relative effect of various components of the system at compatible settlement at the base of the embankment has been proposed. However, significant work would be required to extend this to three-dimensions and to account for variation of settlement with location between the pile caps. The 'Ground Reaction Curve' quantifying the effect of arching in the embankment would also need to be better defined for a range of geometries, potentially also including the 'brittle' response following 'maximum arching'.

- The effect of geotextile reinforcement has not been considered beyond purely tensile response for parabolic deformation. The concept of multiple layers of geogrid giving a layer of 'composite' material has not been proved or disproved.

REFERENCES

Beer, F. P. & Johnston E. R. (1987). *Mechanics for engineers*, McGraw-Hill International editions.

BS8006, (1995). Code of practice for strengthened/reinforced soils and other fills, British Standards Institution.

Carlsson B. (1987), Reinforced soil, principles for calculation, Terratema AB, Linköping.

Cao, W. P., Chen, Y. M. & Chen R. P. (2006). An analytical model of piled reinforced embankments based on the principle of minimum potential energy, *Advances in earth structures*, *GeoShanghai 06*, pp. 217-224.

Chen, R. P., Chen Y. M. & Xu, Z. Z. (2006). Interaction of rigid pile supported embankment on soft soil, *Advances in earth structures*, *GeoShanghai 06*, pp. 231-238.

Chen, C. F. & Yang, Y. (2006). Research on bearing capacity of geosynthetic-reinforced and pile-supported earth platforms over soft soil and analysis of its affecting factors, *Advances in earth structures*, *GeoShanghai 06*, pp. 294-300.

Cox, C. (2005). The use of Matlab in conjunction with Particle Image Velocimetry (PIV) to monitor the deformations of sand surfaces, Personal correspondence.

Ellis, E. A., Cox, C. & Yu, H. S., Ainsworth, A. & Baker, N. (2006). A new geotechnical centrifuge at the University of Nottingham, UK. *ISSMGE International Conference on Physical Modelling in Geotechnics*, Hong Kong.

Giroud, J.P., Bonaparte, R., Beech J.F. & Gross B.A. (1990). Design of soil layer geosynthetic systems overlying voids, *Geotextiles and Geomembranes* (9), pp. 11-50.

Han J. & Gabr M.A. (2002). Numerical analysis of Geosynthetic reinforced and pile supported earth platform over soft soil, *Journal of Geotechnical and Geoenvironmental Engineering*, January 2002, pp. 44-53.

Handy, R. L. (1985). The arch in soil arching, *Journal of Geotechnical Engineering Vol. 111*, No. 3, pp. 302-318.

He, C., Lou, X. M. & Xiong, J. H. (2006). Arching effect in piled embankments, *Advances in earth structures, GeoShanghai 06*, pp. 270-277.

Hewlett, W. J & Randolph, M. F. (1988). Analysis of piled embankments. *Ground engineering*, Vol. 21 No. 3, pp. 12-18.

Iglesia, G. R., Einstein, H, H. & Whitman, R. V. (1999). Determination of Vertical Loading on Underground Structures Based on an Arching Evolution Concept, *Geo-Engineering for Underground Facilities*, pp. 495-506.

Jenck, O., Dias, D. & Kastner, R. (2006). Two-dimensional physical modelling of soft ground improvement by vertical rigid piles, *Physical modelling in geotechnics - 6th ICPMG*, pp. 527-532.

Kempfert, H. G., Gobel, C., Alexiew, D. & Heitz, C. (2004). German recommendations for reinforced embankments on pile-similar elements. *EuroGeo3: 3rd European Geosynthetics Conference, Geotechnical Engineering with Geosynthetics*, Munich, pp. 279-284.

Kempton, G., Russell, D., Pierpoint, N. D. & Jones, C. J. F. P. (1998). Two and three - dimensional numerical analysis of the performance of piled embankments, *Proceedings of the 6th International Conference on Geosynthetics*, Atlanta, GA, USA, pp. 767-772.

Lai, Y. P., Bergado, D. T., Lorenzo G. A. & Duangchan, T. (2006). Full scale reinforced embankment on deep jet mixing improved ground, *Ground Improvement 10*, No. 4, pp. 153-164.

Love, J. & Milligan, G. (2003). Design methods for basally reinforced pile-supported embankments over soft ground. *Ground Engineering*, March, Thomas Telford.

Low, B.K., Tang, S.K. & Choa, V. (1993). Arching in piled embankments, *ASCE Journal of Geotechnical Engineering*, Vol. 120, pp. 1917-1938.

Maddison J.D., Jones D.B., Bell A.L. & Jenner C.G. (1996). Design and performance of an embankment supported using low strength geogrids and vibro concrete columns, *Geosynthetics – Applications, Design and Construction*, De Groot, Den Hoedt & Termaat.

Milligan, G. (2006). Seminar given at the ICE setting out the findings and conclusions from a detailed investigation and assessment of the causes of failure of apartment blocks constructed on a site bordering the River Erne in Enniskillen, Northern Ireland.

McKelvey, J. A. (1993). The anatomy of soil arching, *Geotextiles and geomembranes* 13, pp. 317-329.

Naughton P. J. & Kempton, G. T. (2005). Comparison of analytical and numerical analysis design methods for piled embankments, *Contemporary issues in foundation engineering*.

Russell, D., Naughton, P. J. & Kempton, G. (2003). A new design procedure for piled embankments, *Proceedings of the 56th Canadian Geotechnical Conference and the NAGS Conference*, Winnipeg, MB, pp. 858-865.

Russell, D. & Pierpoint, N. (1997). An assessment of design methods for piled embankments. *Ground Engineering*, 30, No. 11, pp. 39-44.

Schenck, T. (1999). *Digital photogrammetry*, TerraScience.

Stewart, M. E. & Filze, G. M. (2005). Loads on geosynthetic reinforcement in bridging layers for pile-supported embankments, *Proceedings of Geo-Frontiers 2005, ASCE*, Austin.

Taylor, R N. (1995). *Geotechnical Centrifuge Technology*. Blackie Academic & Professional.

Terzahgi, K. (1943). Theoretical Soil Mechanics, John Wiley and Sons, Inc. pp. 66-76.

Thigpen, L. (1984). On the mechanics of strata collapse above underground openings. Lawrence Livermore National Laboratory, U.S. Department of Energy.

Tonks, D., Hilier, R. (1998). Assessment revisited, *Ground Engineering*, June 1998, pp 46-47.

White, D.J., Take, W.A. & Bolton, M.D. (2003). Soil deformation measurement using particle image velocimetry (PIV) and photogrammetry. *Geotechnique*, 53 (7), pp. 619-631.

Wood, H. J. (2003). The design and construction of pile-supported embankments for the A63 Selby bypass, *Foundations: Innovations, observations, deign and practice*, Thomas Telford.

Yan, L., Yang J.S. & J. Han, (2006). Parametric study on geosynthetic-reinforced pile supported embankments, *Advances in earth structures, GeoShanghai 06*.

APPENDIX A

Piled embankment EPS 70

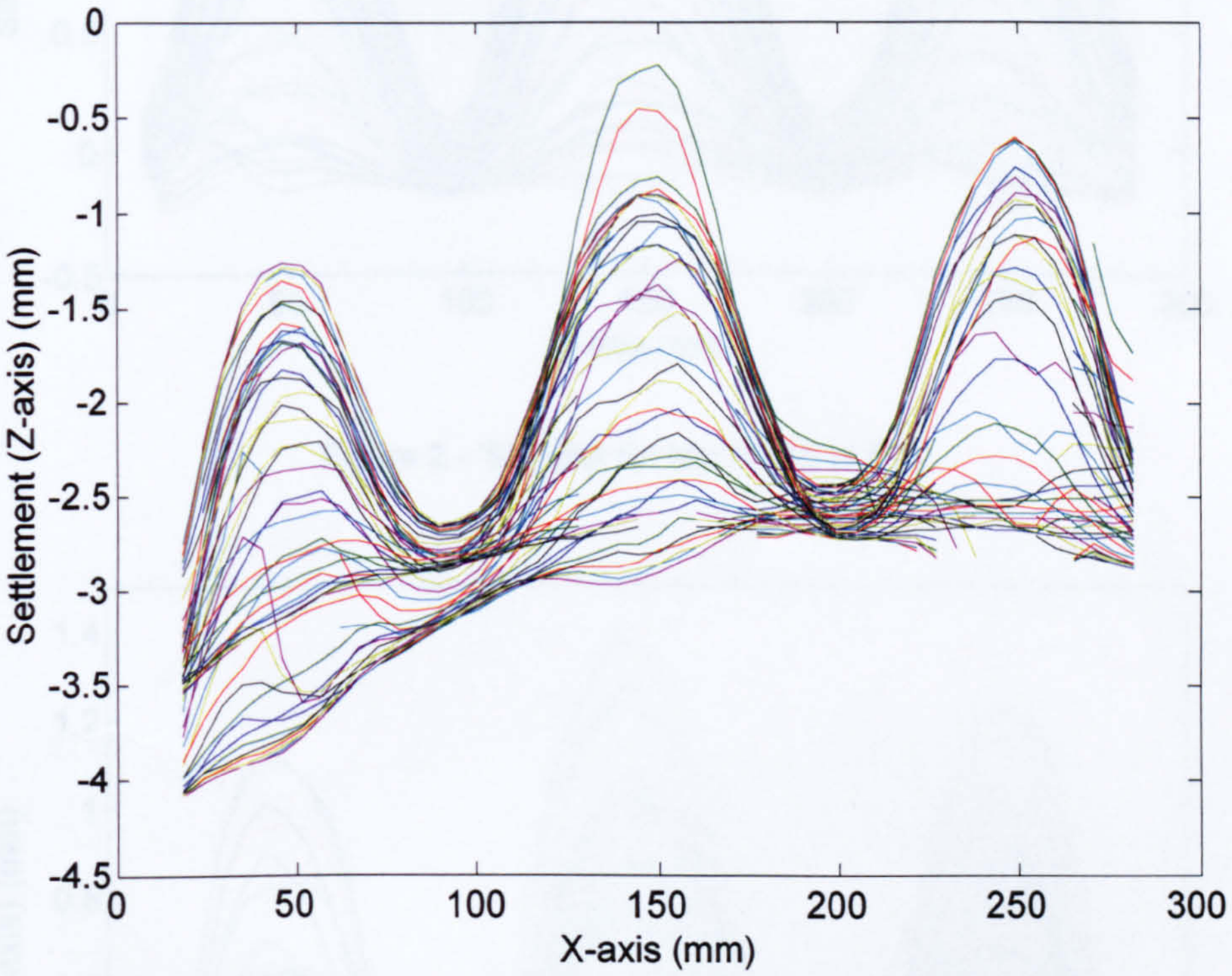

Figure 1 - 'Sin' plot for test RA07 at 60g

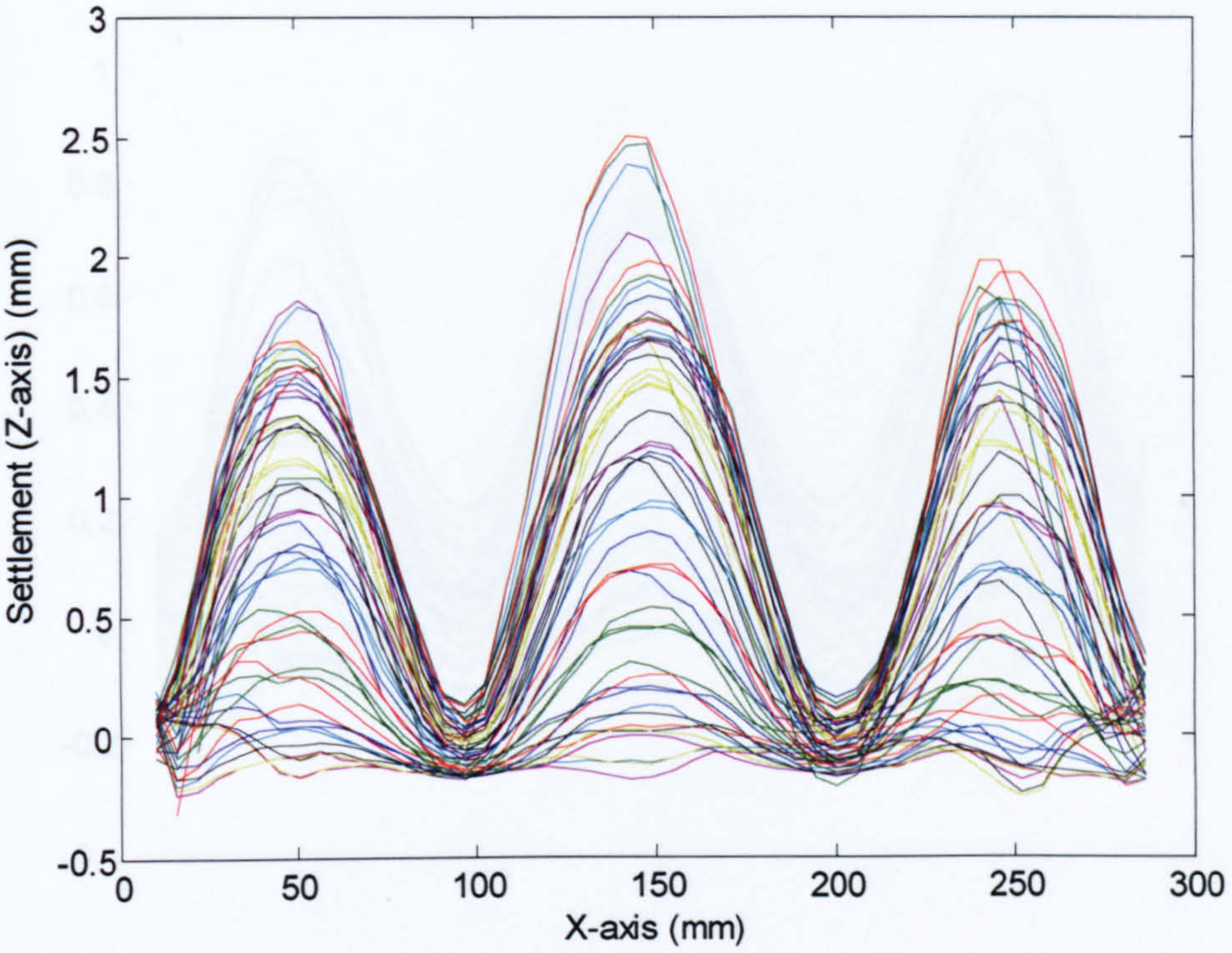

Figure 2 - 'Sin' plot for test RA15 at 60g

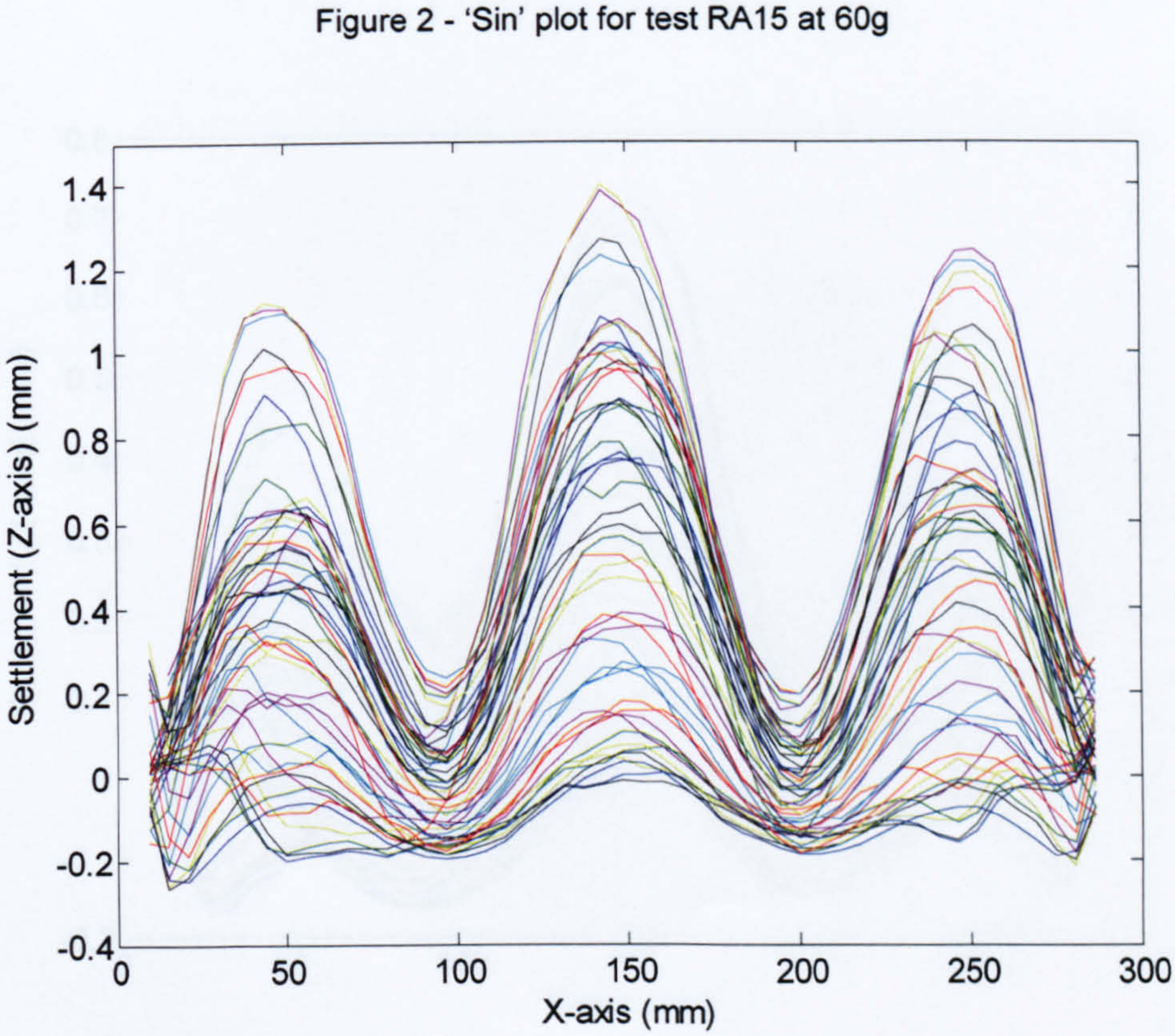

Figure 3 - 'Sin' plot for test RA16 at 60g

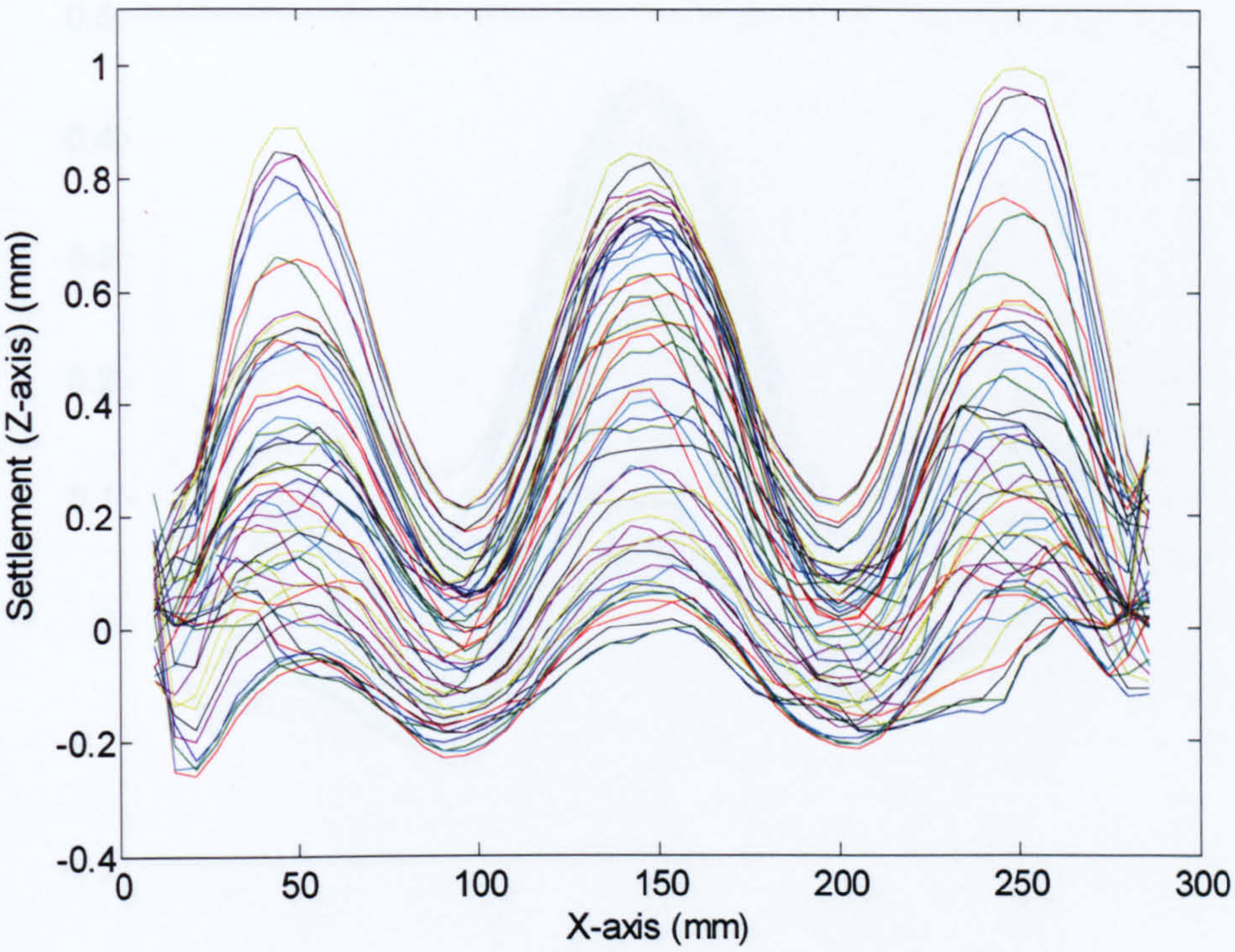

Figure 4 - 'Sin' plot for test RA17 at 60g

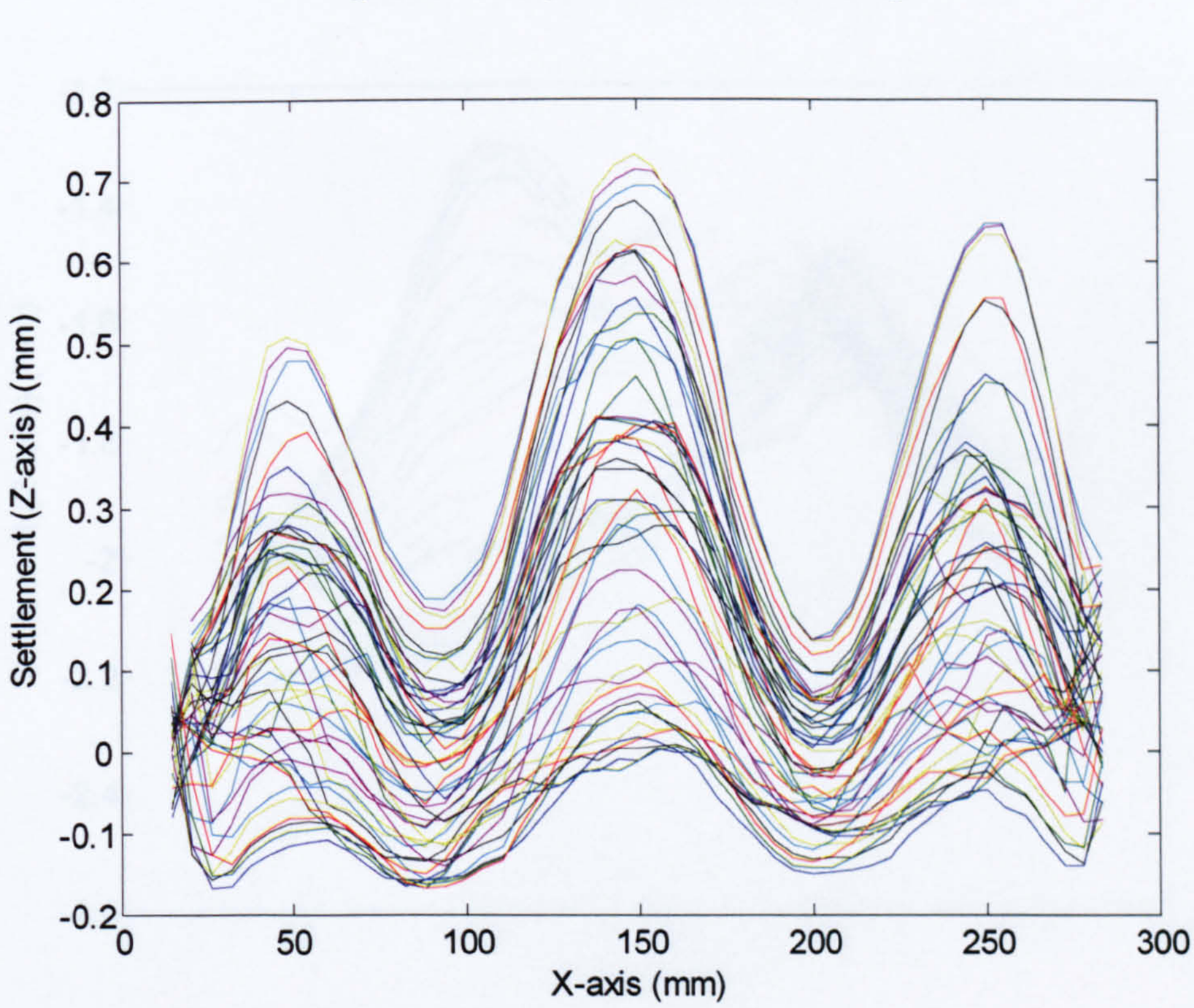

Figure 5 - 'Sin' plot for test RA18 at 60g

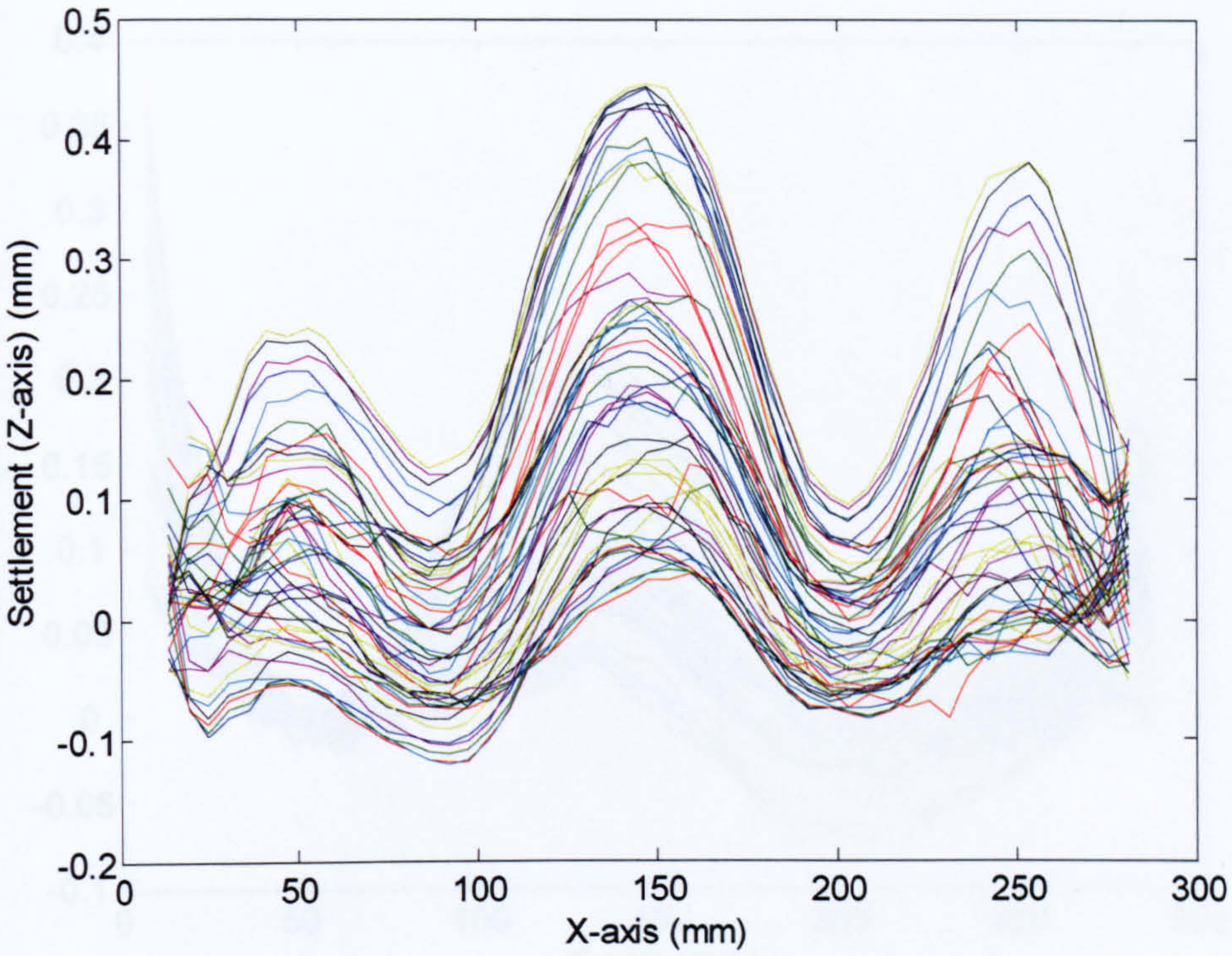

Figure 6 - 'Sin' plot for test RA19 at 60g

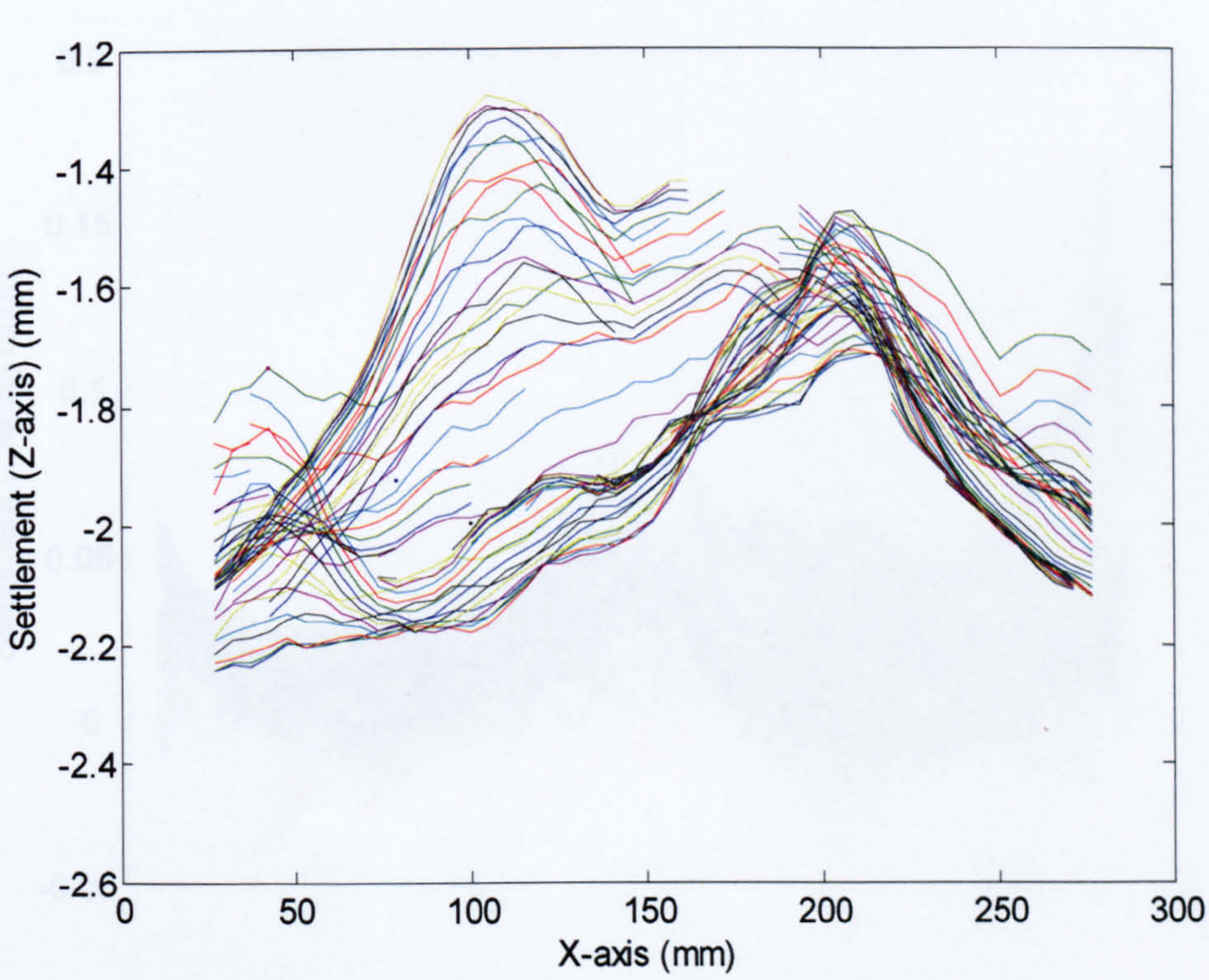

Figure 7 - 'Sin' plot for test RA06 at 60g

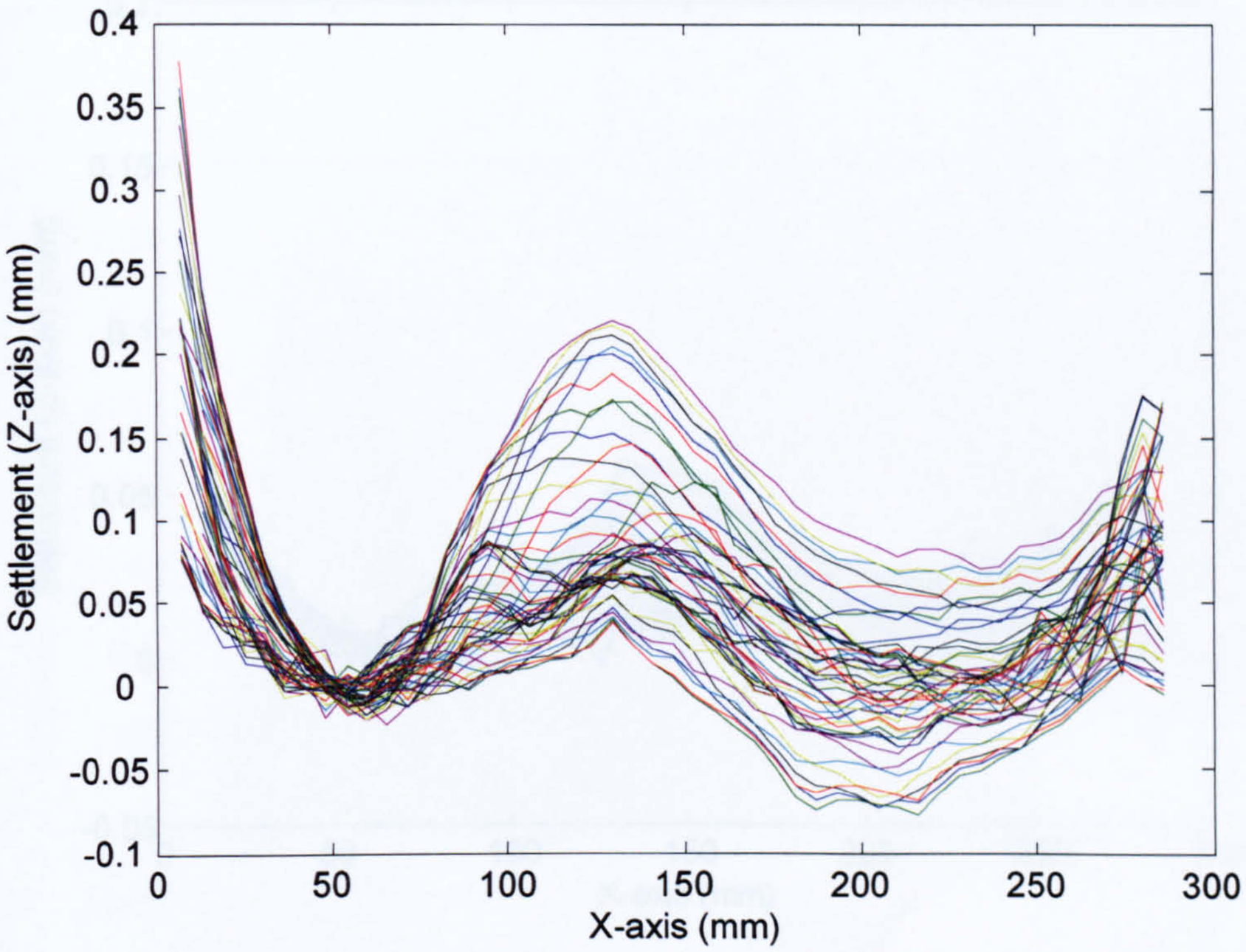

Figure 8 - 'Sin' plot for test RA20 at 60g

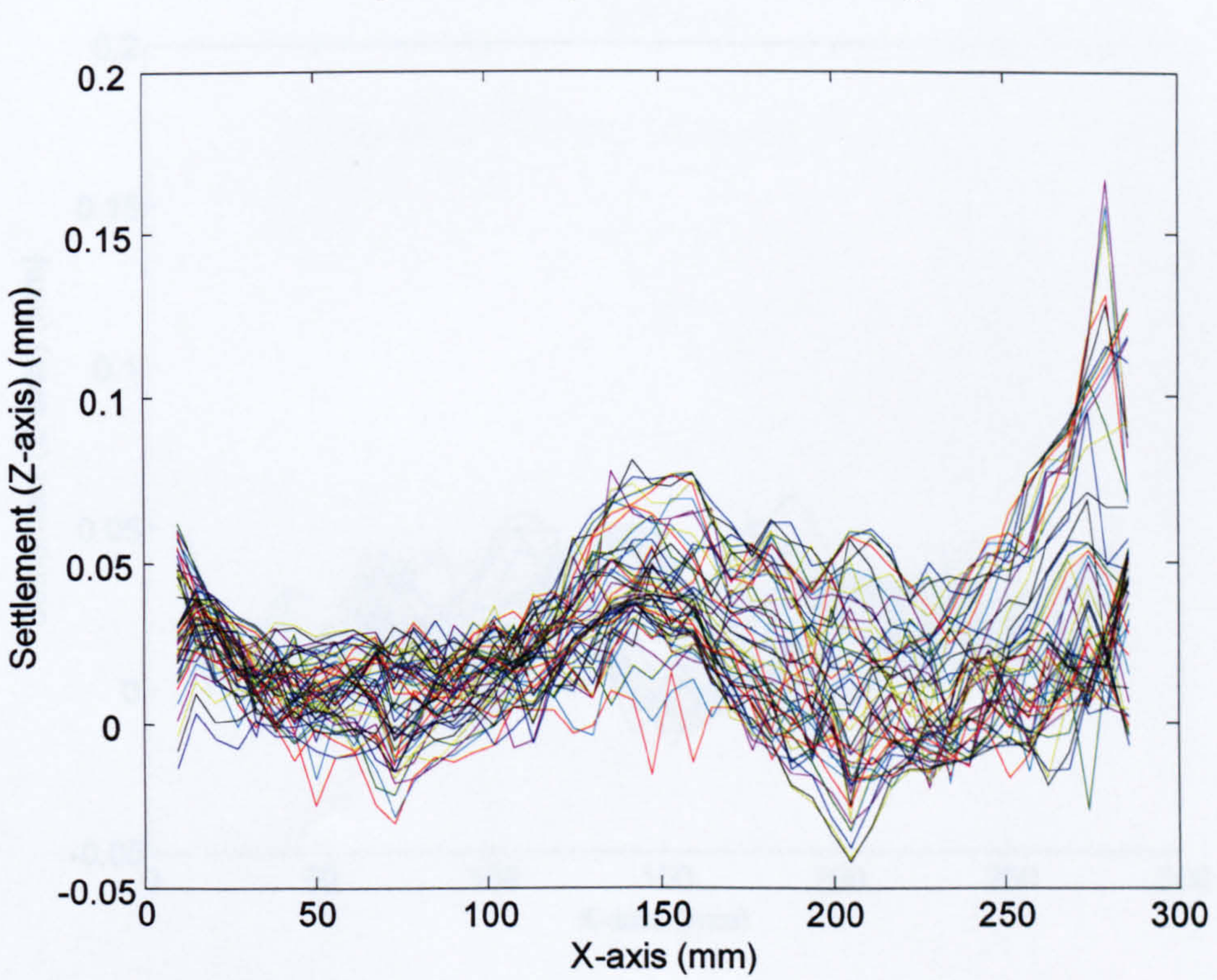

Figure 9 - 'Sin' plot for test RA 21 at 60g

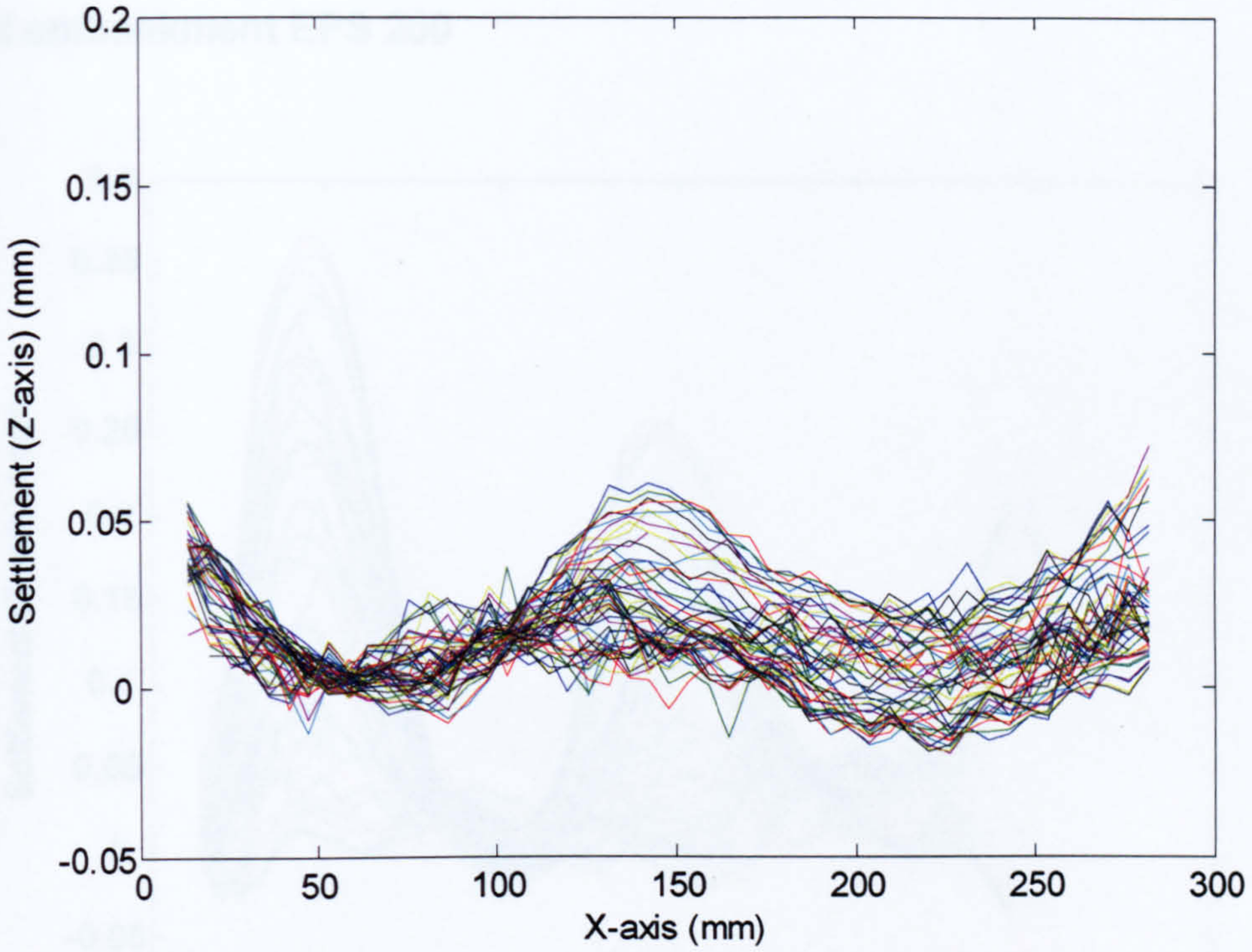

Figure 10 - 'Sin' plot for test RA 22 at 60g

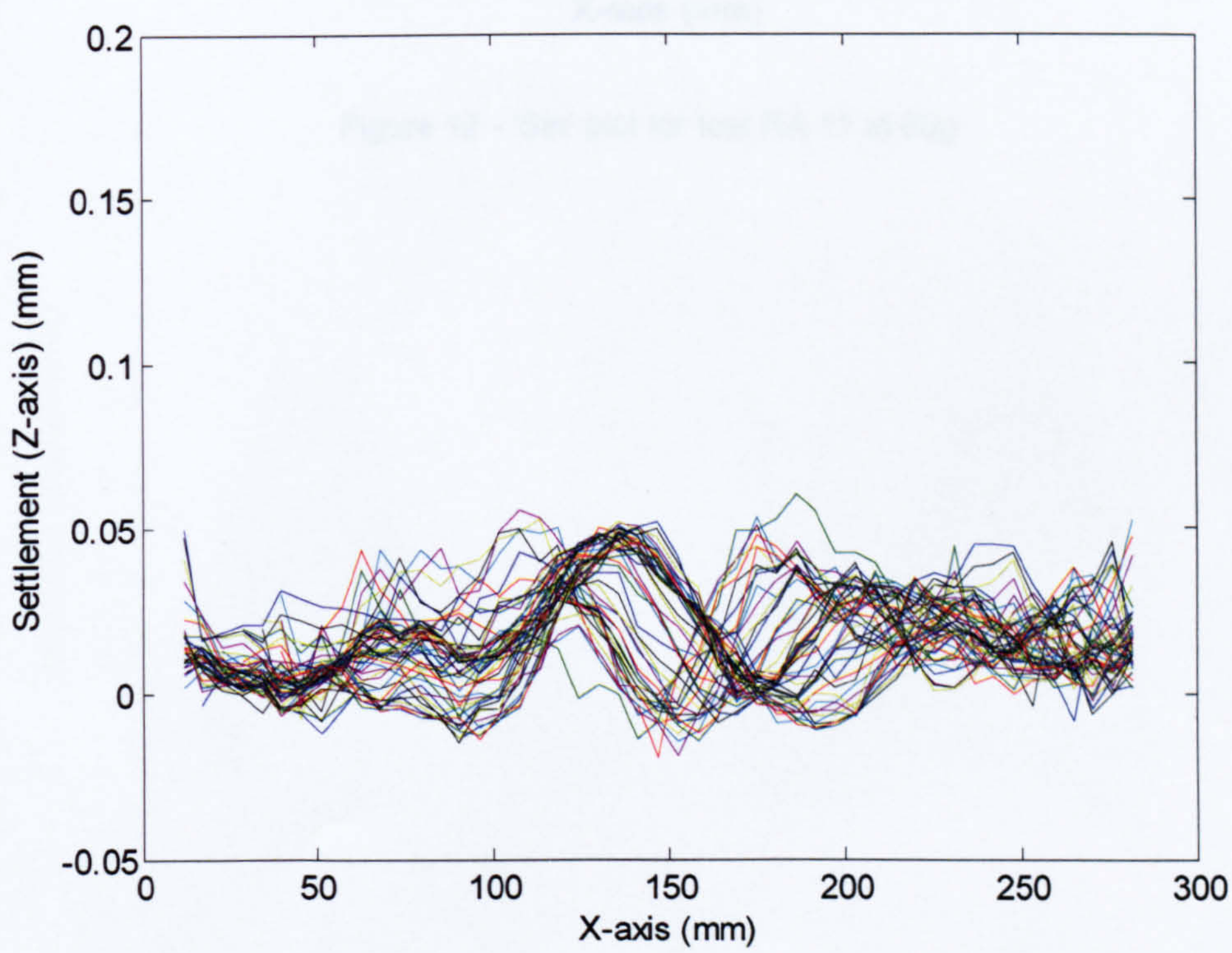

Figure 11 - 'Sin' plot for test RA 23 at 60g

Piled embankment EPS 200

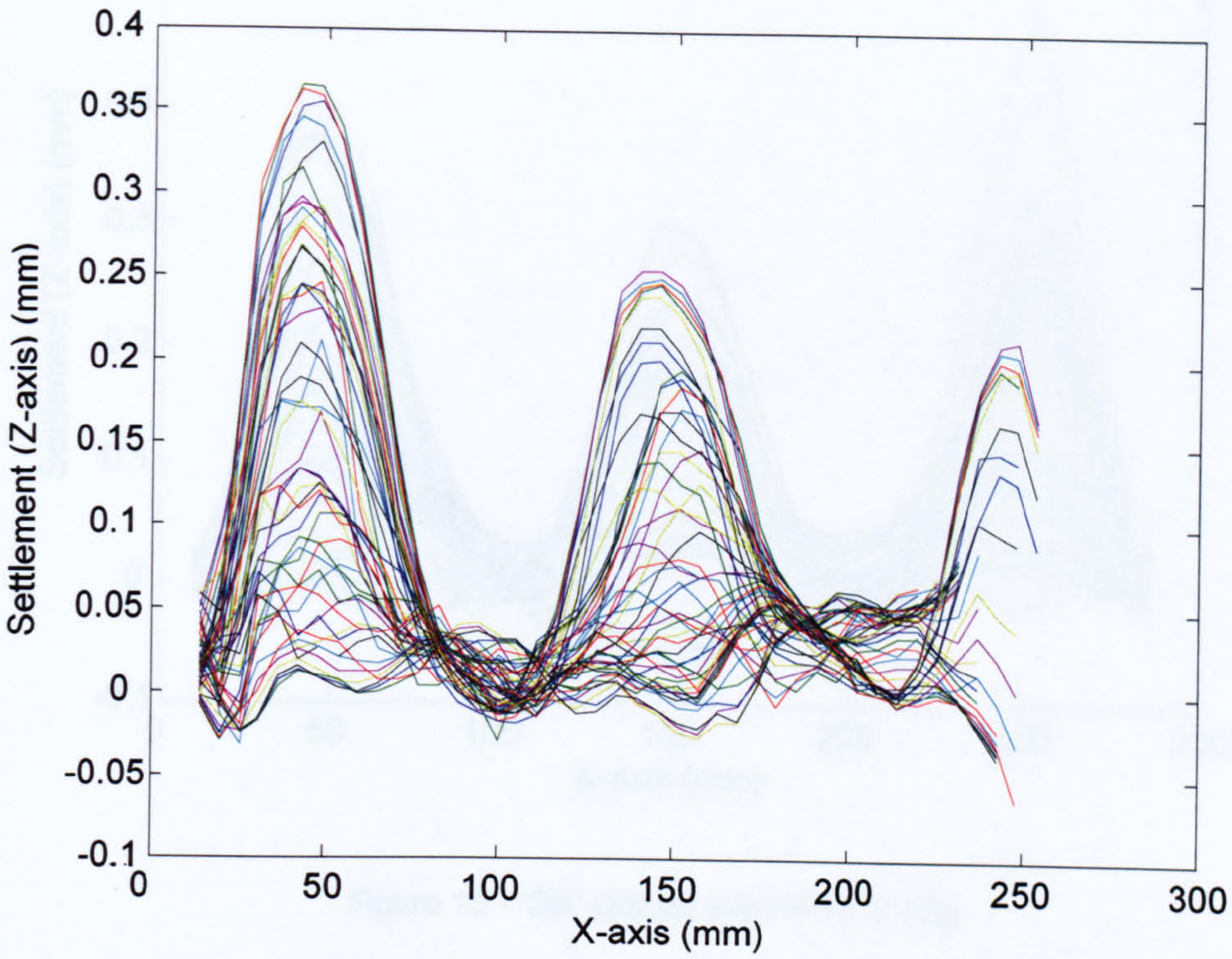

Figure 12 - 'Sin' plot for test RA 11 at 60g

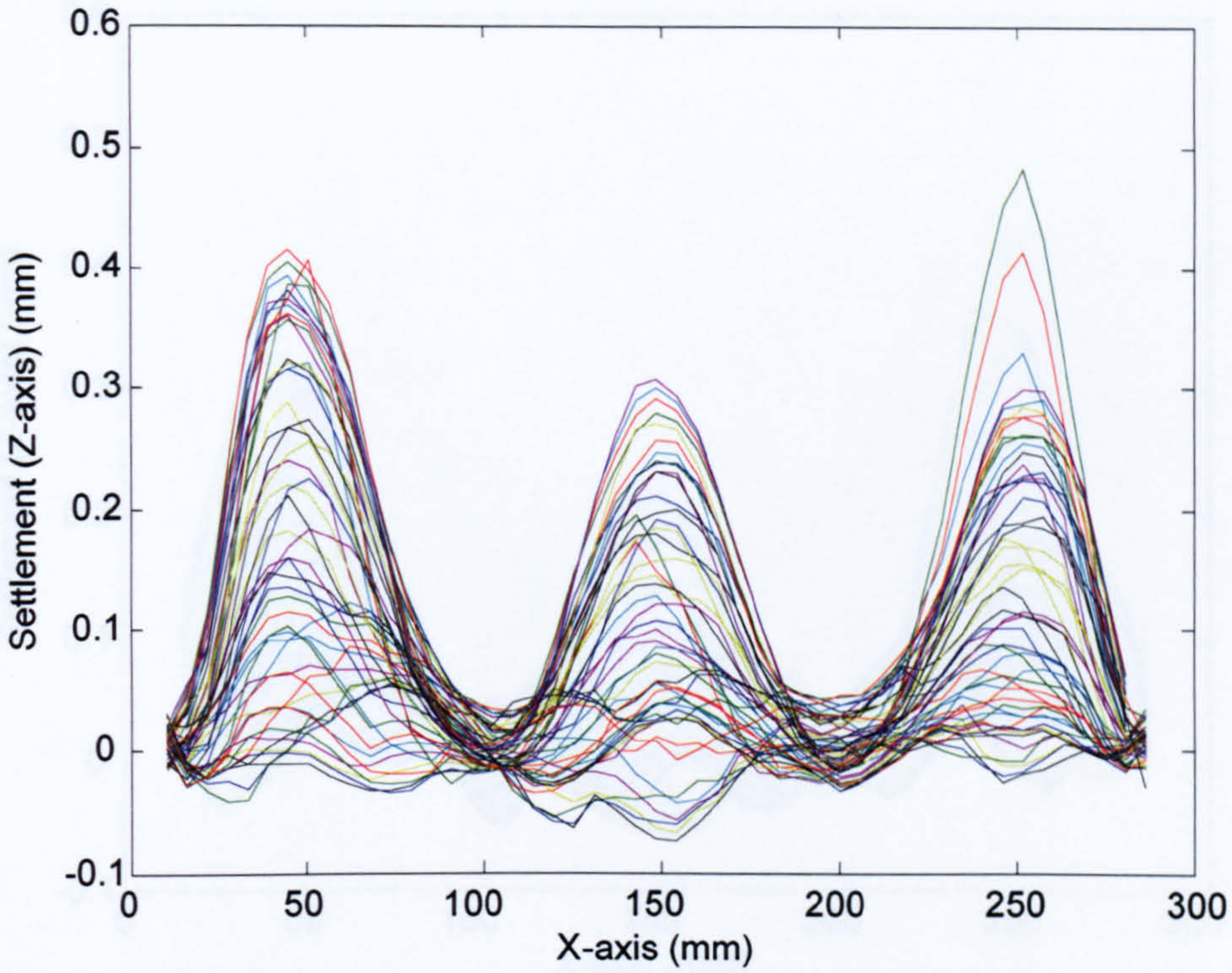

Figure 13 - 'Sin' plot for test RA14 at 60g

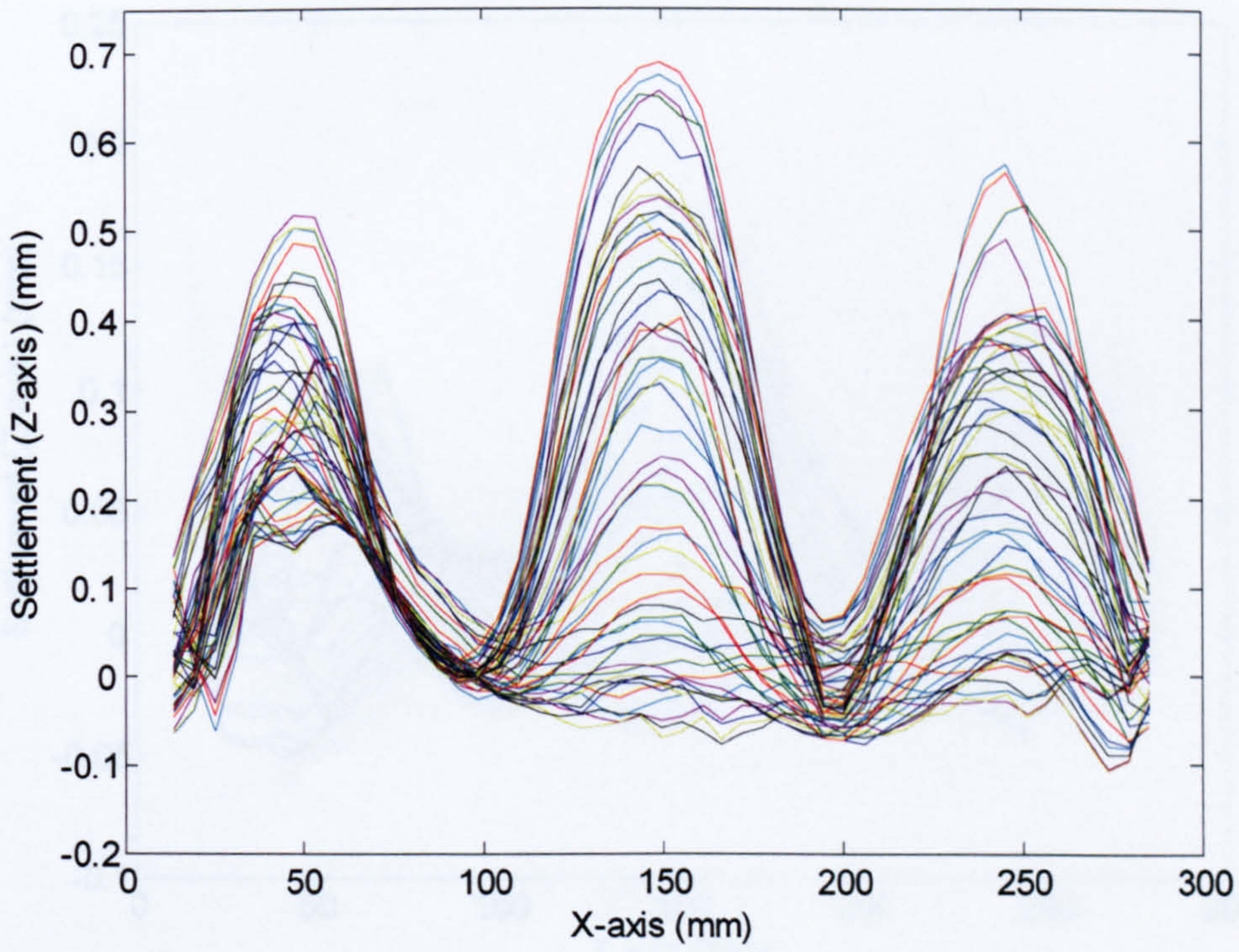

Figure 14 - 'Sin' plot for test RA08 at 60g

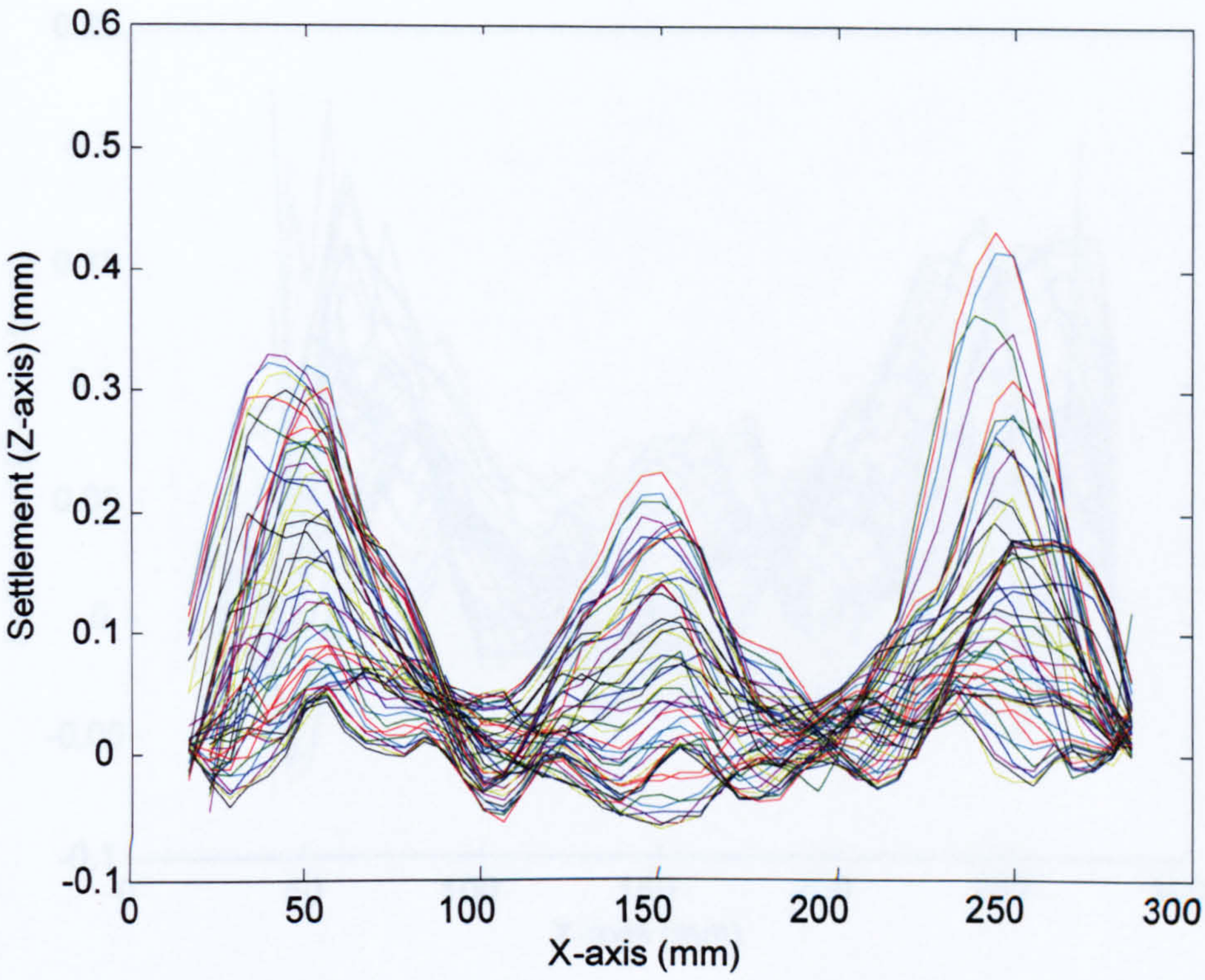

Figure 15 - 'Sin' plot for test RA12 at 60g

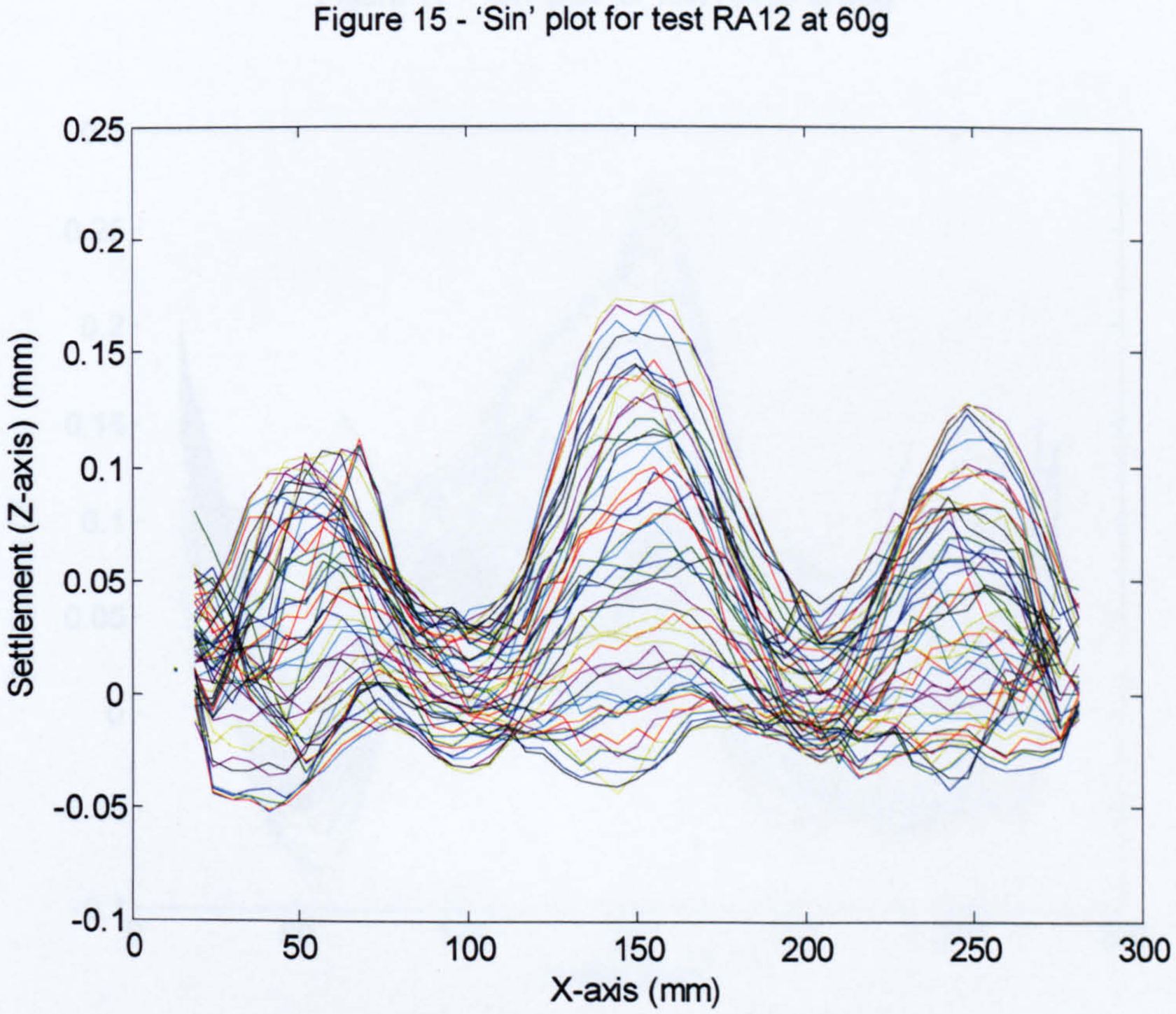

Figure 16 - 'Sin' plot for test RA09 at 60g

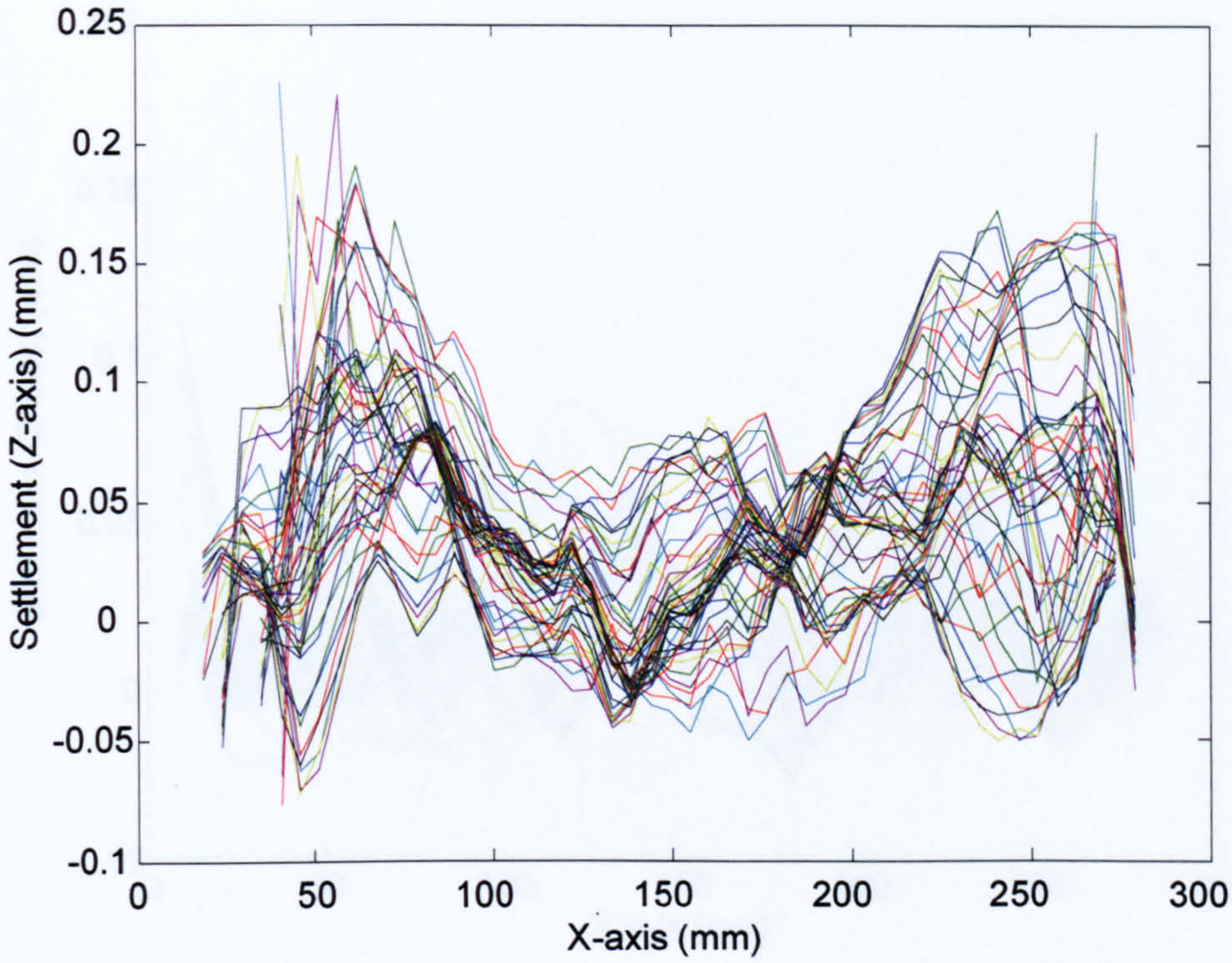

Figure 17 - 'Sin' plot for test RA13 at 60g

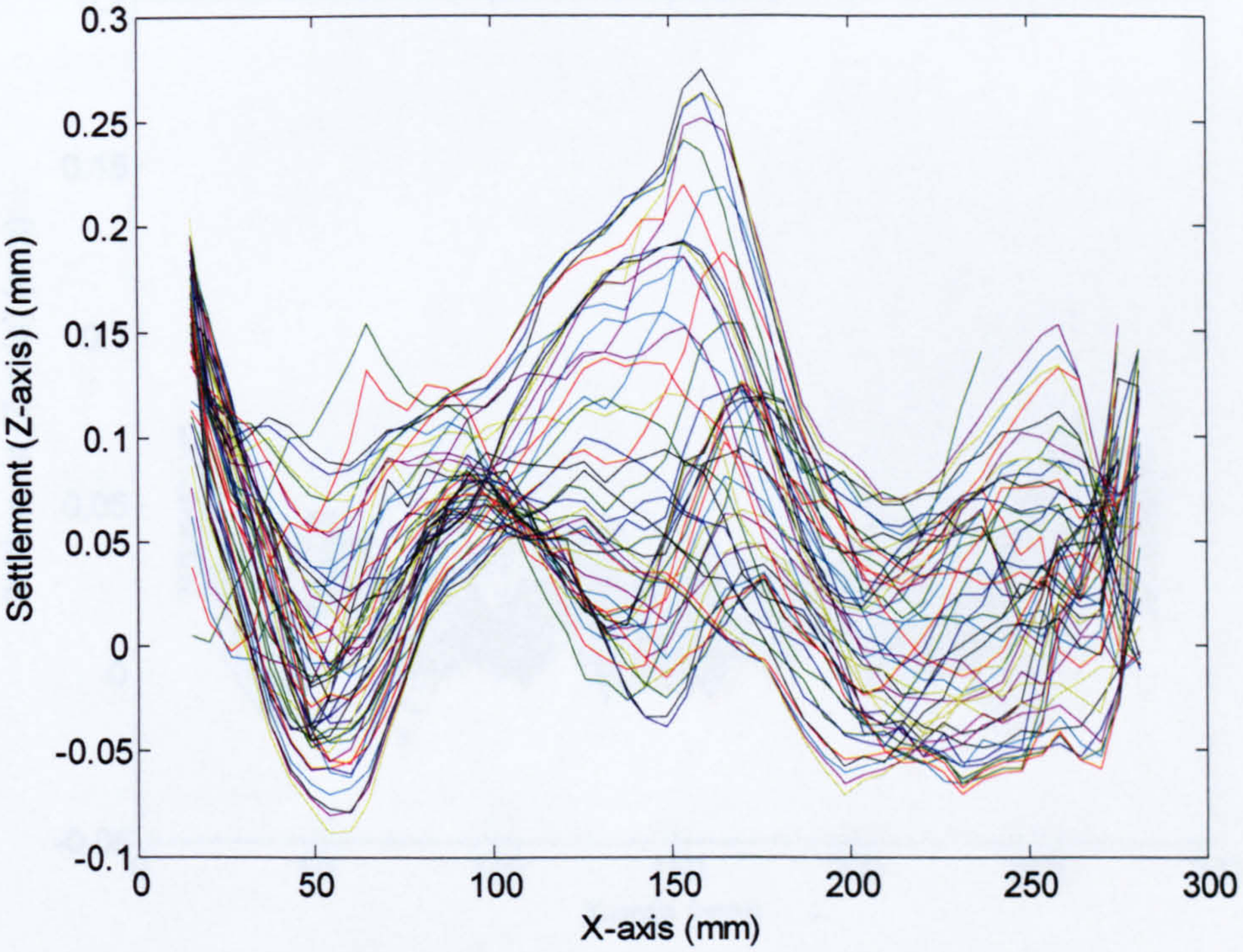

Figure 18 - 'Sin' plot for test RA10 at 60g

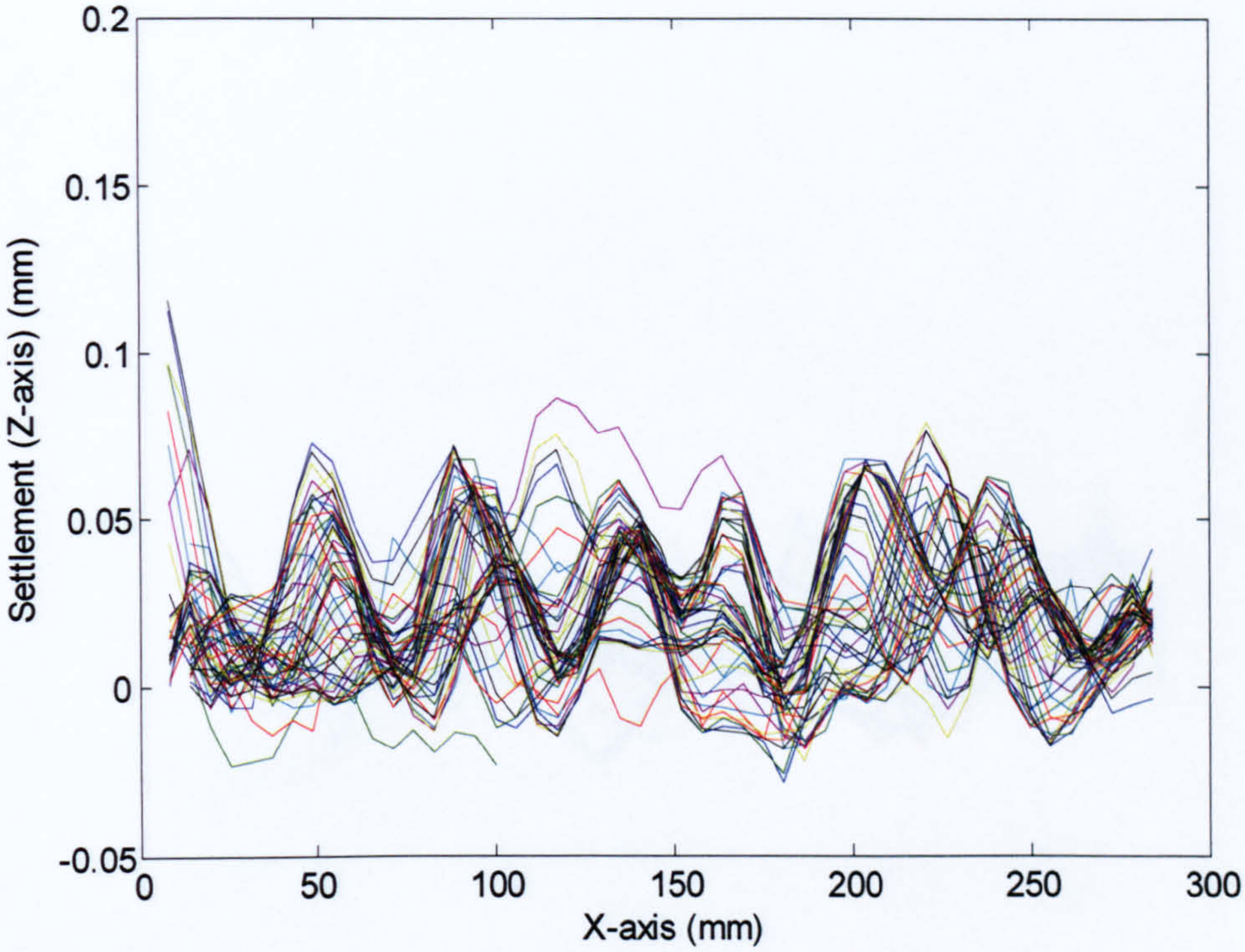

Figure 19 - 'Sin' plot for test RA24 at 60g

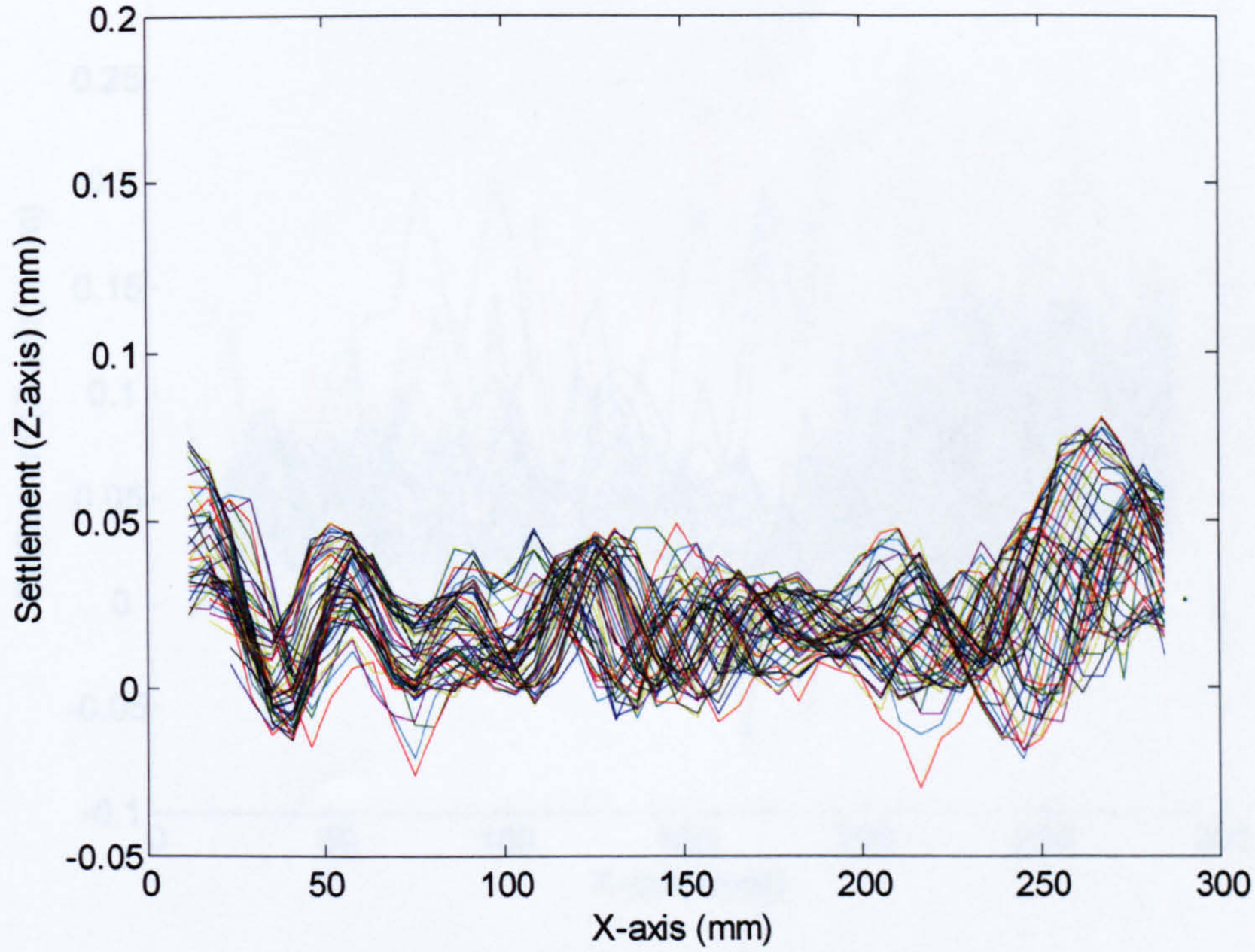

Figure 20 - 'Sin' plot for test RA25 at 60g

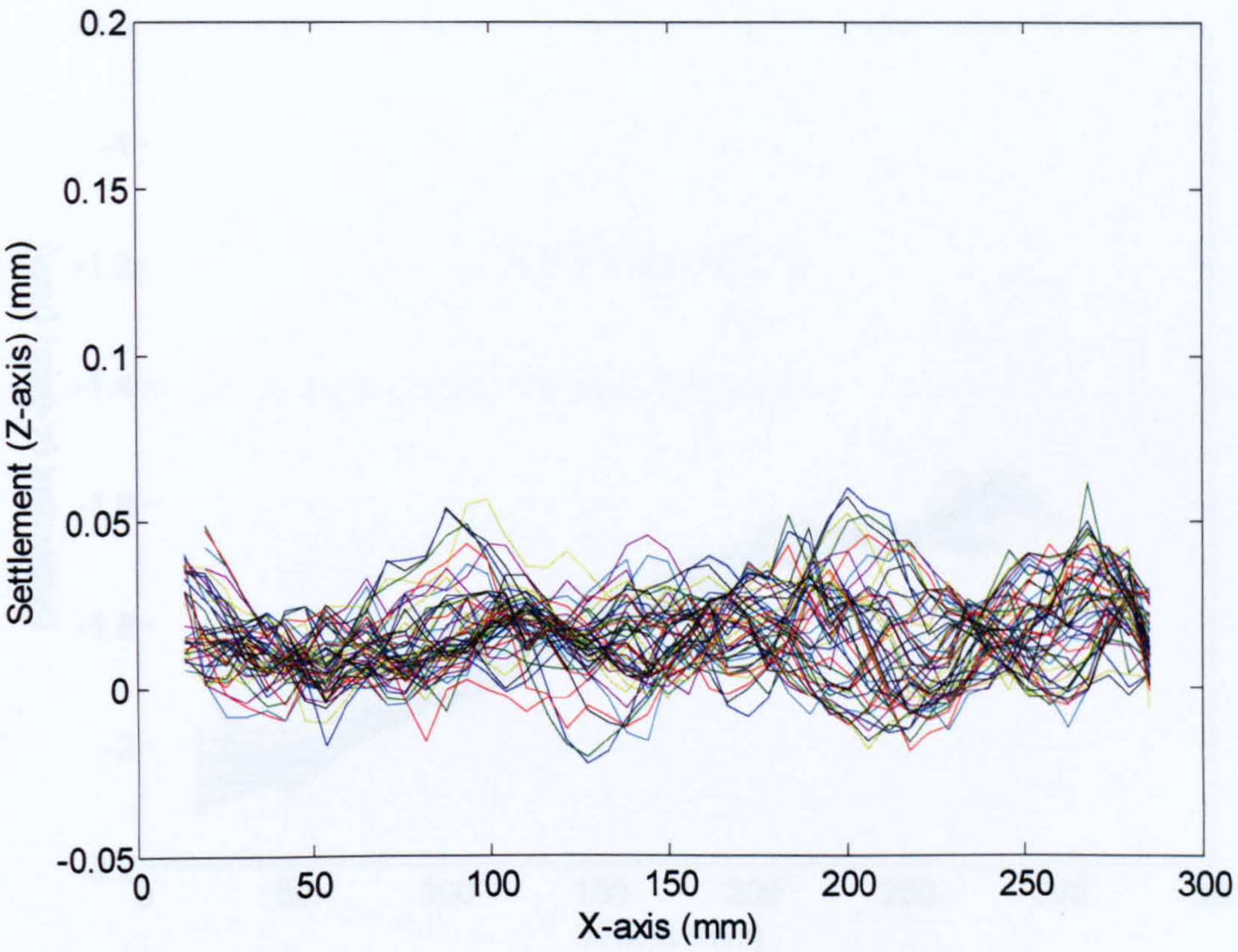

Figure 21 - 'Sin' plot for test RA26 at 60g

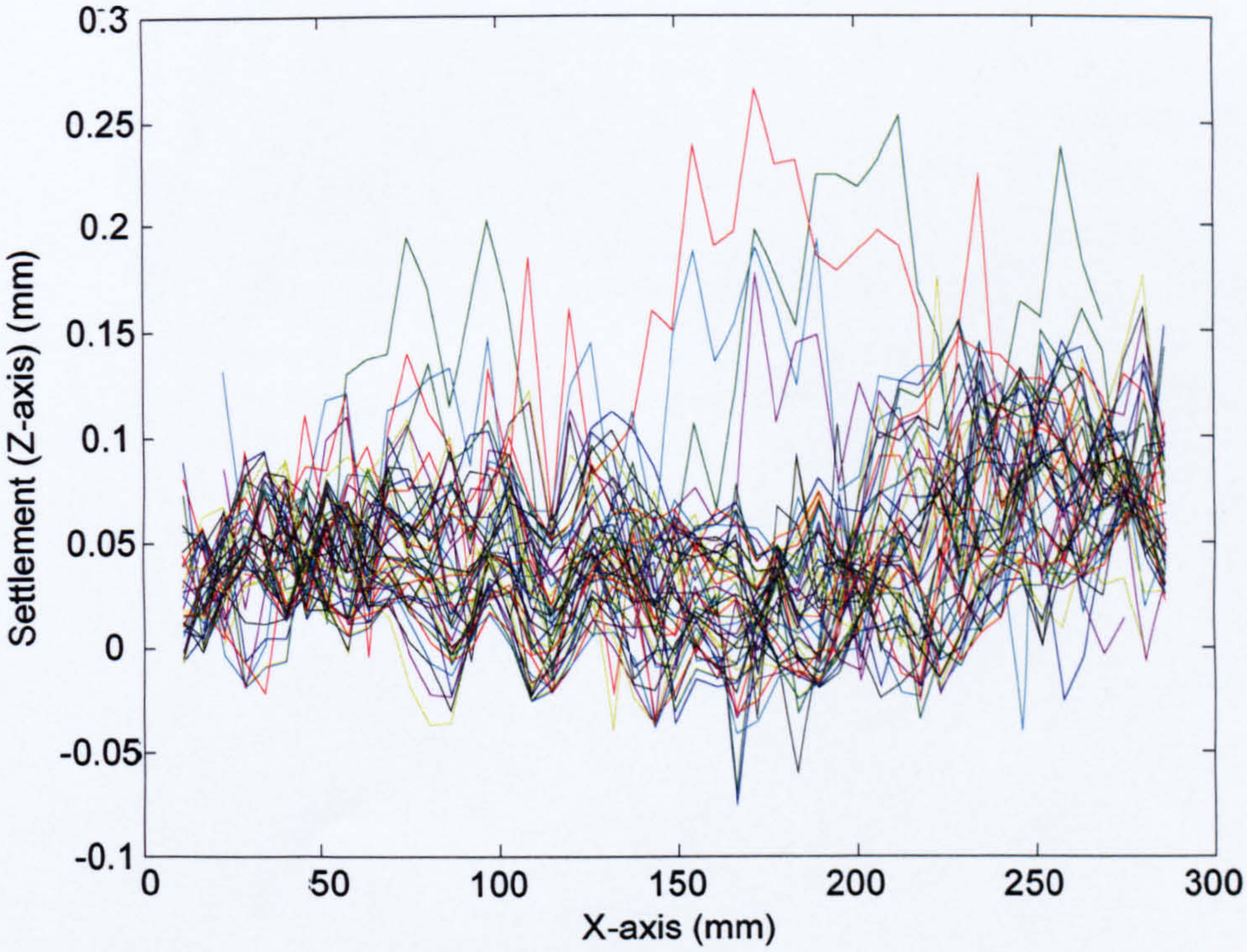

Figure 22 - 'Sin' plot for test RA27 at 60g

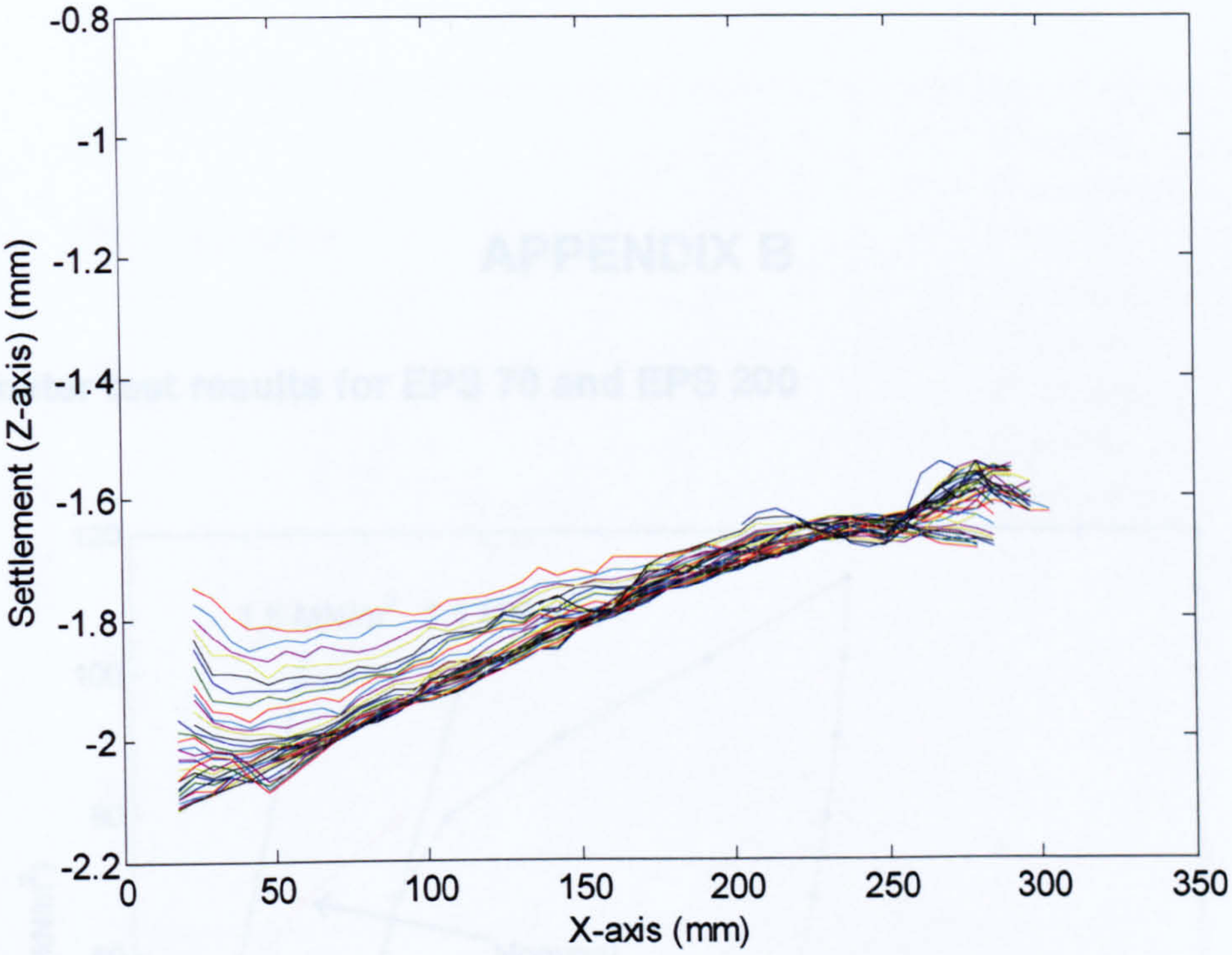

Figure 23 - 'Sin' plot for test RA05 at 60g

APPENDIX B

Odometer test results for EPS 70 and EPS 200

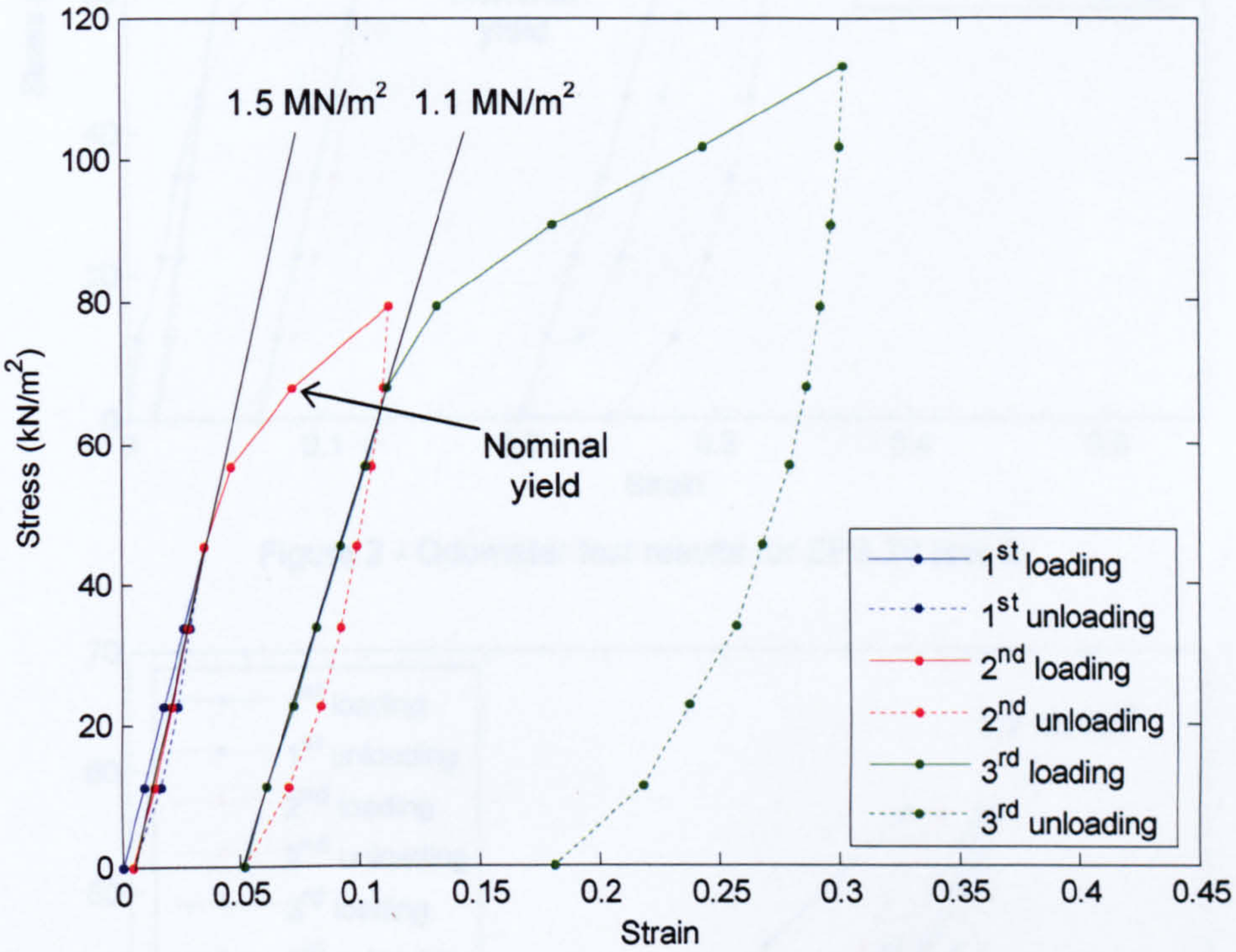

Figure 1 - Odometer test results for EPS 70 (set 1)

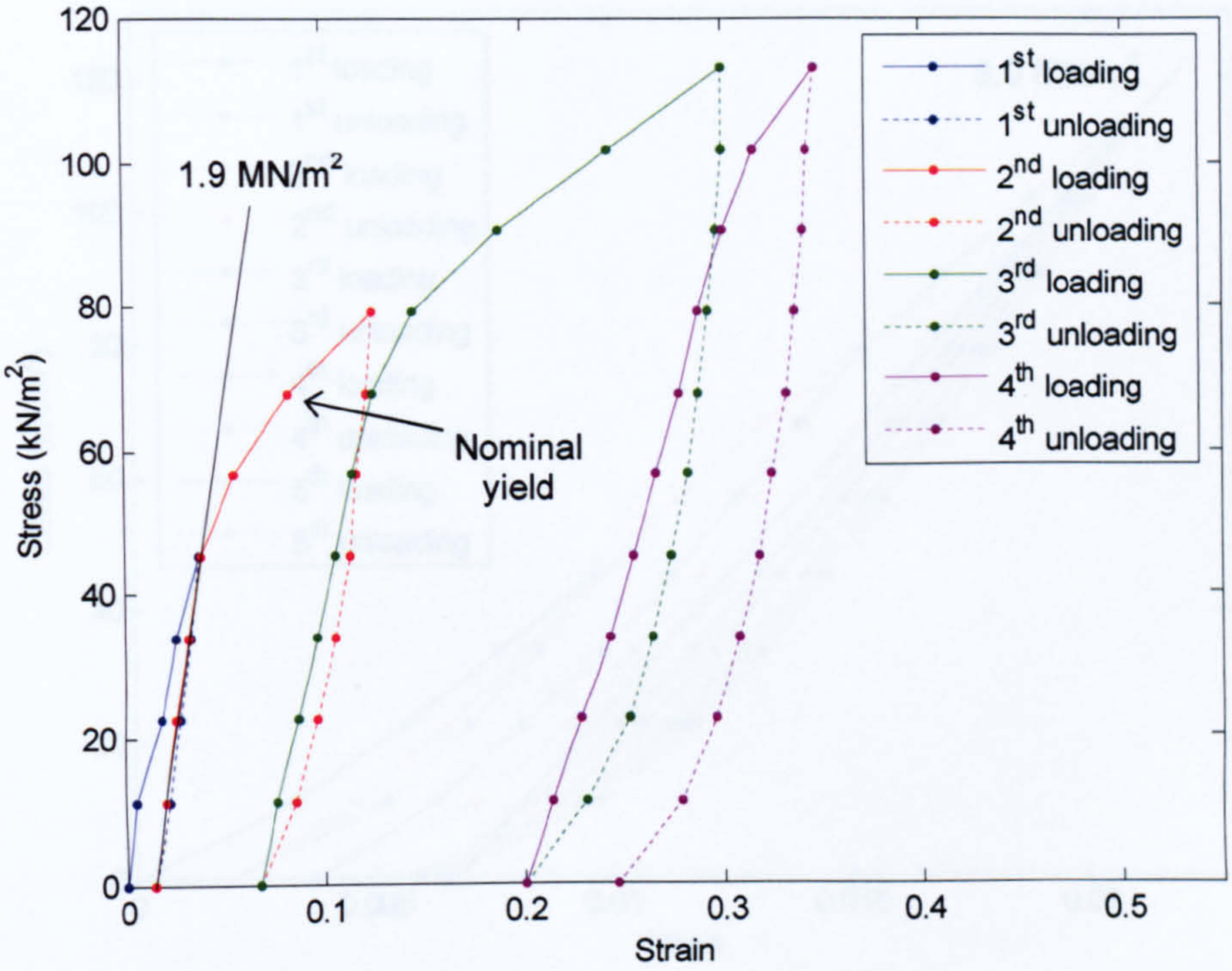

Figure 2 - Odometer test results for EPS 70 (set 2)

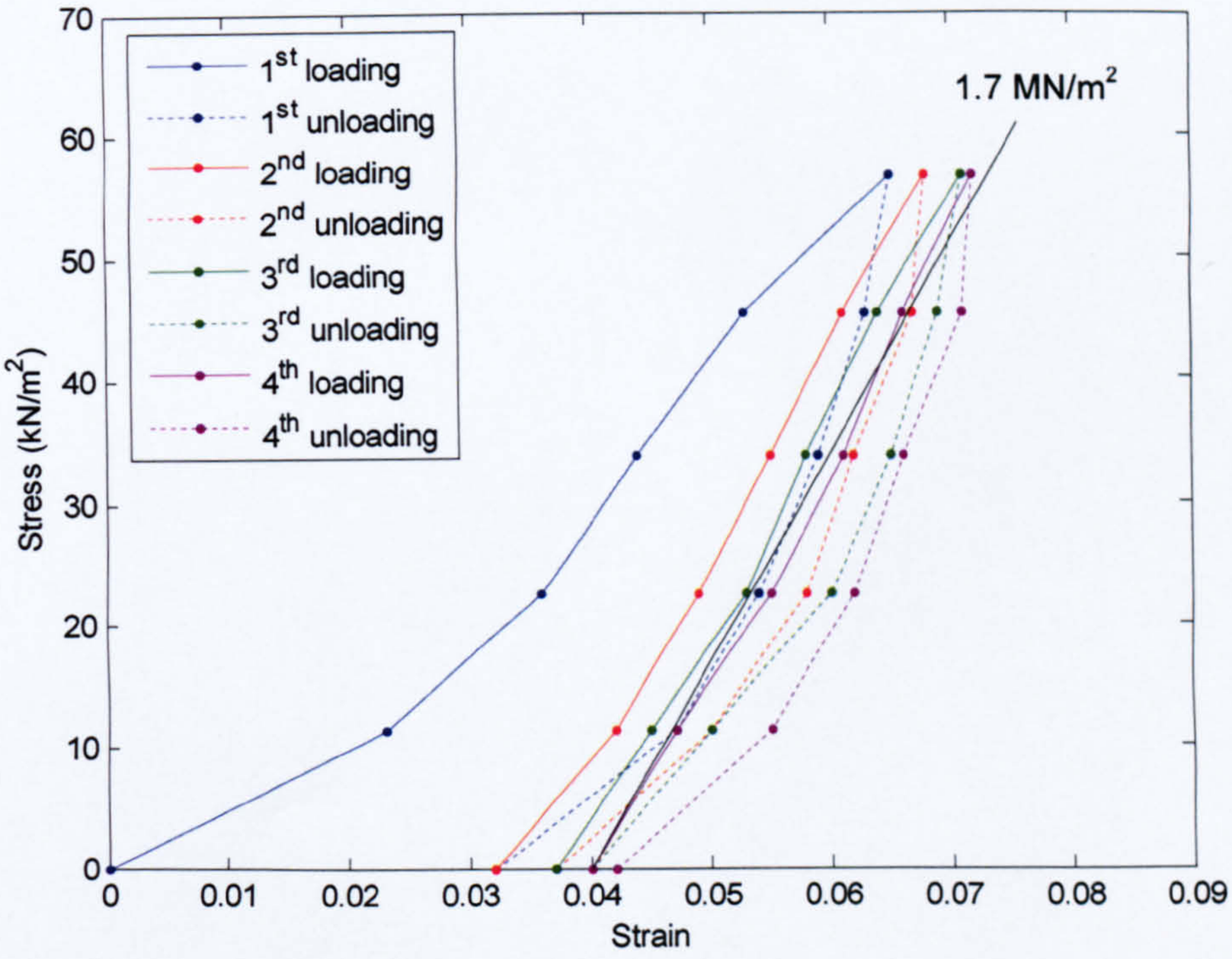

Figure 3 - Odometer test results for EPS 70 (set 3)

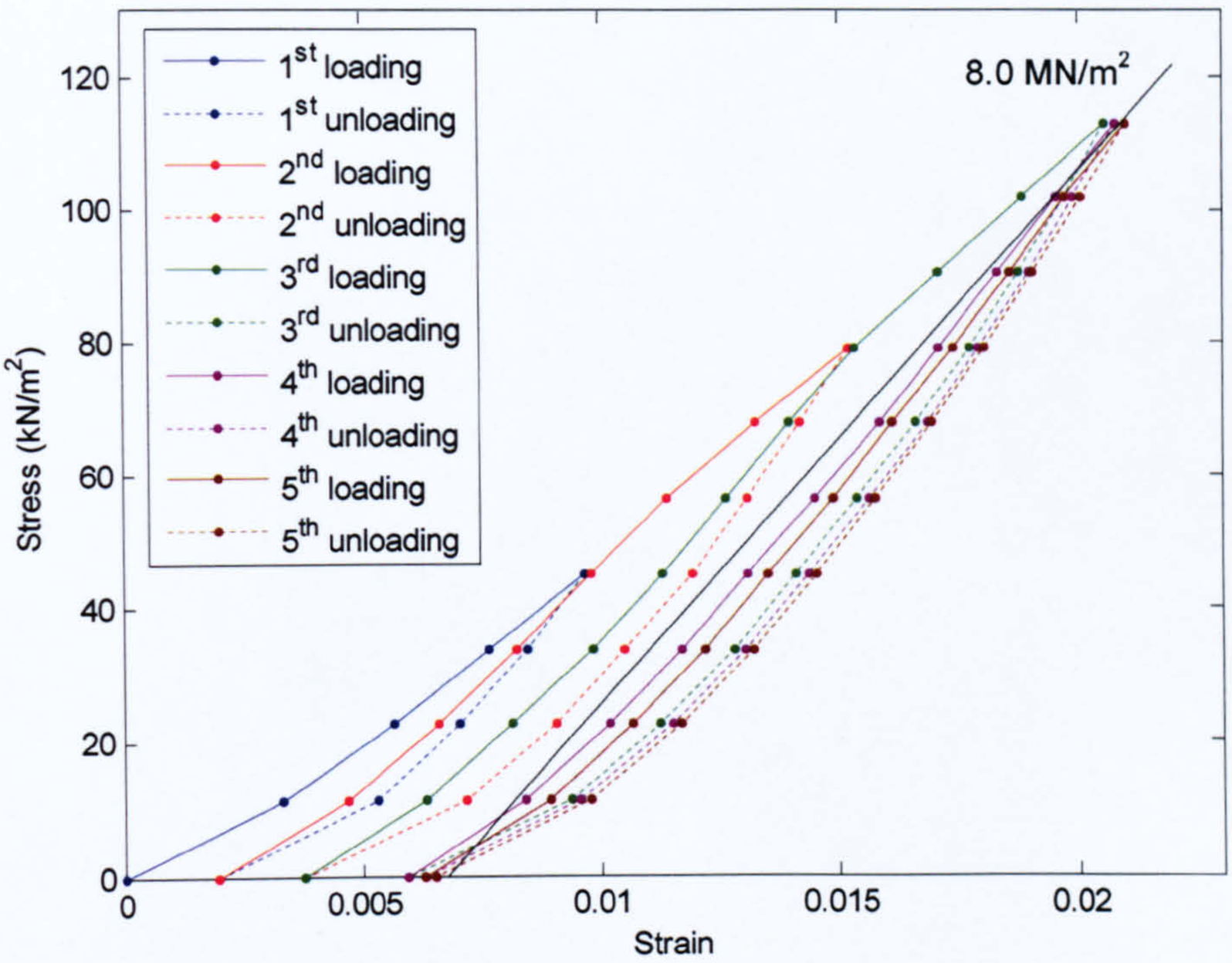

Figure 4 - Odometer test results for EPS 200